Impact of class I HDACs and their inhibitors on renal and colorectal tumor cell fate decisions

Dissertation

zur Erlangung des Grades „Doktor der Naturwissenschaften“
im Promotionsfach Chemie

am Fachbereich Chemie, Pharmazie und Geowissenschaften
der Johannes Gutenberg-Universität
in Mainz

Nicole Kiweler
geb. am 30.11.1988 in Wittlich

Mainz, Januar 2019

Dekan: [redacted]

1. Gutachter: [redacted]

2. Gutachter: [redacted]

Tag der mündlichen Prüfung: 12.07.2019

D77 (Dissertation Johannes Gutenberg-Universität Mainz)

Summary

Advanced, metastasized renal and colorectal carcinomas are difficult to treat and frequently incurable diseases. Therefore, a key focus of modern cancer research is the identification of improved chemotherapeutic treatment options. Overexpression of histone deacetylases (HDACs) is a frequent characteristic of malignant neoplasms and often correlates with disadvantageous disease progression and therapy outcome. In recent years, inhibitors of histone deacetylases (HDACi) were introduced as a new class of small-molecule anticancer therapeutics. Since HDACs deacetylate numerous histones and non-histone proteins, the inhibition of these enzymes has implications for a large number of cellular processes. As a result of the pleiotropic actions of HDACs, the precise impact of HDACi on cellular signaling pathways remains poorly understood. This work investigated the effects of HDACs and HDACi on key cellular signaling pathways in kidney and colon tumor cell lines on a global and functional scale.

Having found that HDACi induce morphological alterations in renal cell carcinoma (RCC) cells that resemble the characteristics of a mesenchymal phenotype, this work investigated individual and proteomics-based analyses of epithelial-mesenchymal transition (EMT) signaling pathways. Proteomics and GO-term enrichment analyses revealed disturbed EMT signaling and an associated loss of cell cycle control. Detailed analysis of EMT transcription factor expression by qPCR, epithelial and mesenchymal marker protein expression by Western blot, migratory potential, and β-catenin localization by immunofluorescence confirmed these findings. Furthermore, HDACi significantly induced cell death that due to caspase-mediated apoptosis. These findings were confirmed in primary renal cells. RNAi-based knockdown experiments unveiled HDAC1 and HDAC2 as mechanistic targets of HDACi.

In colorectal cancer (CRC) cells, the specific modification of HDAC2 by sumoylation affects p53- and nuclear factor kappa-light-chain-enhancer of activated B-cells (NF-κB)-dependent gene expression. The work presented demonstrates that a loss of HDAC2 sumoylation enhances CRC sensitivity towards the antimetabolite 5-fluorouracil (5-FU) as well as the DNA-crosslinker nimustine (ACNU). HDAC2 sumoylation did thereby not affect p53 activation and ATM- and ATR-dependent DNA damage signaling. In contrast, DNA damage-induced accumulation of γH2AX and γH2AX foci formation depended on HDAC2 sumoylation. Mass spectrometric analysis of global protein expression, knockdown experiments, and analyses of DNA damage repair by immunofluorescence identified the specific loss of the chromatin remodeling complex-associated DNA-helicases Brahma-related gene 1 (BRG1) and SWI/SNF-related matrix-associated actin-dependent regulator of chromatin subfamily A containing DEAD/H box 1 (SMARCAD1) as potential cause for the observed sensitization effects. Curiously, the main cytotoxic effects of 5-FU were rather based on its RNA damage than on its DNA damage. Thus, this work reveals a multitude of novel effects of commonly used chemotherapeutics.

Zusammenfassung

Fortgeschrittene, metastasierende renale und kolorektale Karzinome sind schwer behandelbare und häufig unheilbare Erkrankungen. Ein Hauptaugenmerk gegenwärtiger Krebsforschung liegt daher auf der Identifikation verbesserter chemotherapeutischer Behandlungsoptionen. Die Überexpression von Histondeacetylasen (HDACs) ist ein häufiges Merkmal maligner Neoplasien und korreliert oftmals mit einem unvorteilhaften Krankheitsverlauf und Therapieausgang. Im Laufe der letzten Jahre wurden Inhibitoren von Histondeactelyasen (HDACi) als neue Klasse niedermolekularer Chemotherapeutika vorgestellt. Da HDACs eine Vielzahl an Histonen und Nicht-Histonproteinen deacetylieren, hat die Inhibierung dieser Enzyme Auswirkungen auf zahlreiche zelluläre Prozesse. Aufgrund dieses pleiotropen Einflusses von HDACs sind die konkreten Wirkungsweisen von HDACi auf zelluläre Signalwege jedoch weiterhin kaum verstanden. Diese Arbeit untersuchte den Einfluss von HDACs und HDACi auf zentrale, zelluläre Signalwege in renalen und kolorektalen Tumorzelllinien auf globaler und funktionaler Ebene.

Nachdem gefunden wurde, dass HDACi in renalen Karzinomzellen (RCC) morphologische Veränderungen auslösen, die denen eines mesenchymalen Phänotypus ähneln, untersucht diese Arbeit individuelle und Proteom-basierte Analysen von Signalwegen der epithelial-mesenchymalen Transition (EMT). Diese zeigten eine Störung von EMT-Signalwegen sowie einen damit assoziierten Verlust der Zellzykluskontrolle. Detaillierte Analysen der Expression von EMT Transkriptionsfaktoren durch qPCR, der Expression epithelialer und mesenchymaler Markerproteine durch Western Blot, des Migrationspotentials und der β-Catenin-Lokalisation durch Immunfluoreszenz bestätigten diese Befunde. Weiterhin induzierten HDACi signifikant Zelltod durch Caspase-vermittelte Apoptose. Diese Ergebnisse wurden bestätigt in primären renalen Zellen. RNAi-basierte Knockdown-Experimente identifizierten HDAC1 und HDAC2 als mechanistischen Zielstrukturen der HDACi.

In kolorektalen Tumorzellen (CRC) beeinflusst die Modifizierung von HDAC2 durch Sumoylierung die p53- und NF-κB-abhängige Genexpression. Die vorliegende Arbeit zeigt, dass ein Verlust der HDAC2-Sumoylierung die Sensitivität von CRC gegenüber dem Antimetaboliten 5-Fluorouracil (5-FU) sowie dem DNA-Vernetzer Nimustin (ACNU) steigert. Die HDAC2-Sumoylierung beeinflusste dabei weder die p53-Aktivierung noch die ATM- und ATR-abhängige DNA-Schadenssignalisierung. Dagegen waren die schadensinduzierte Anreicherung von γH2AX und die γH2AX-Focibildung von der HDAC2-Sumoylierung abhängig. Die massenspektrometrische Untersuchung der globalen Proteinexpression, Knockdown-Experimente und Analysen der DNA-Schadensreparatur durch Immunfluoreszenz identifizierten den Expressionsverlust der DNA-Helikasen BRG1 und SMARCAD1 als potentielle Ursache der beobachteten Sensitivierungseffekte. Eigenartigerweise basierten die zytotoxischen Effekte von 5-FU eher auf dessen RNA-Schaden als auf dessen DNA-Schaden. Diese Arbeit offenbart daher eine Vielzahl neuer Effekte häufig verwendeter Chemotherapeutika.

Table of Contents

Figures

Supplementary Figures

Tables

Supplementary Tables

List of Abbreviations

53BP1	p53-binding protein 1
5'-dRP	5’-deoxyribose phosphate
5-FU	5-fluorouracil
AF488	Alexa Fluor 488
ANOVA	Analysis of variance
AP	Apurinic/apyrimidinic site
APAF-1	Apoptotic protease activating factor 1
APC	Adenomatous polyposis coli
APE1	Apurinic/apyrimidinic endonuclease 1
ATCC	American Type Culture Collection
ATM	Ataxia telangiectasia mutated
ATP	Adenosine triphosphate
ATR	Ataxia telangiectasia- and Rad3-related
ATRIP	ATR interacting protein
AU	Arbitrary units
BAX	BCL-2 associated X
BCL-2	B-cell lymphoma 2
BCL-XL	B-cell lymphoma-extra-large
BER	Base excision repair
BHD	Birt-Hogg-Dubé
BIR	Break-induced replication
BRCA1	Breast cancer 1
BRD	Bromodomain
BRG1	Brahma-related gene 1
CAPE	Capecitabin
ccRCC	Clear cell renal cell carcinoma
CDH1	Cadherin 1
CDK	Cyclin-dependent kinase
CH2THF	5,10-methylenetetrahydrofolate
CHK1	Checkpoint kinase 1
CHK2	Checkpoint kinase 2
CIMP	CpG island methylator phenotype
CIN	Chromosomal instability
CNU	Chloroethyl nitrosourea
CRC	Colorectal cancer
CtIP	CtBP-interacting protein
CTLA-4	Cytotoxic T-lymphocyte-associated protein 4
DAPI	4′,6-Diamidin-2-phenylindol
DDR	DNA damage response
DHFU	Dihydrofluorouracil
D-loop	Displacement loop
DMSO	Dimethylsulfoxide
DNA	Deoxyribonucleic acid
DNA-PK	DNA-dependent protein kinase
DPD	Dihydropyrimidine dehydrogenase
DSB	DNA double-strand break
dTMP	Deoxythymidine monophosphate

dTTP	Deoxythymidine triphosphate
dTTP	Deoxythymidine triphosphate
dUMP	Deoxyuridine monophosphate
dUTP	Deoxyuridine triphosphate
EGFR	Epidermal growth factor receptor
EMT	Epithelial-mesenchymal transition
EXO1	Exonuclease 1
FA	Fanconi anemia
FAP	Familial adenomatous polyposis
FCS	Fetal calf serum
FdUDP	Fluorodeoxyuridine diphosphate
FdUMP	Fluorodeoxyuridine monophosphate
FdUrd	Fluorodeoxyuridine
FdUTP	Fluorodeoxyuridine triphosphate
FH	Fumarat hydratase
FLCN	Folliculin
FSC	Forward scatter
FUDP	Fluorouridine diphosphate
FUMP	Fluorouridine monophosphate
FUrd	Fluorouridine
FUTP	Fluorouridine triphosphate
GO	Gene Ontology
Gy	Gray
HAT	Histone acetyltransferase
HDAC	Histone deacetylase
HDACi	Histone deacetylase inhibitor
HIF-α	Hypoxia-inducible factor α
HLRCC	Hereditary leiomyomatosis and renal cell cancer
HMGN	High mobility group nucleosome-binding
HNPCC	Hereditary nonpolyposis colorectal cancer
HPLC-MS	High-performance liquid Chromatography - mass spectrometry
HPRC	Hereditary papillary renal carcinoma
HR	Homologous recombination
HSP90	Heat shock protein 90
HU	Hydroxyurea
i.p.	intraperitoneal
ICI	Immune checkpoint inhibitor
ICL	Interstrand crosslink
IFN	Interferon
IHC	Immunohistochemistry
IL	Interleukin
IR	Ionizing radiation
IRI	Irinotecan
K	Lysin
KAT	Lysine acetyltransferase
KDAC	Lysine deacetylase
KRAS	Kirsten rat sarcoma viral oncogene homolog
LFQ	Label-free quantitation
LIG	DNA ligase

LV	Leucovorin
Mbp	Megabase pair
MET	Mesenchymal-epithelial transition
MGMT	O^6-methylguanine-DNA methyltransferase
miR	MicroRNA
MLH	MutL homolog
MMR	Mismatch repair
MRE11	Meiotic recombination 11
MRN	MRE11-RAD50-NBS1 complex
mRNA	Messenger RNA
MSH	MutS homolog
MSI	Microsatellite instability
mTOR	Mammalian target of rapamycin
NaB	Sodium butyrate
NAD$^+$	Nicotinamide adenine dinucleotide
NBS1	Nijmegen breakage syndrome 1
NER	Nucleotide expression repair
NFkB	Nuclear factor kappa-light-chain-enhancer of activated B-cells
NGS	Normal goat serum
NHEJ	Non-homologous end joining
NME1	Nucleoside diphosphate kinase
NSCLC	Non-small-cell lung cancer
O^6BG	O^6-benzylguanine
O^6-ClEtG	O^6-chloroethylguanine
OH	Hydroxyl
OPRT	Orotate phosphoribosyltransferase
OX	Oxaliplatin
PARP	Poly ADP ribose polymerase
PBS	Phosphate-buffered saline
PD-1	Programmed-death 1
PDGF	Platelet-derived growth factor
PDGFR-β	Platelet derived growth factor receptor β
PD-L1	Programmed-death ligand 1
PI	Propidium iodide
PI3K	Phosphoinositide 3-kinase
PIG3	p53-inducible gene 3
PIKK	Phosphoinositide 3-kinases-related kinases
PNK	Polynucleotide kinase
Pol	Polymerase
PRPP	Phosphoribosyl pyrophosphate
PTEN	Phosphatase and tensin homolog
PTM	Posttranslational modification
qPCR	Quantitative polymerase chain reaction
RCC	Renal cell carcinoma
RIPK	Receptor-interacting serine/threonine protein kinase
RNA	Ribonucleic acid
RNR	Ribonucleotide reductase
ROS	Reactive oxygen species
RPA	Replication protein A

rRNA	Ribosomal RNA
RT	Room temperature
SAHA	Suberanilohydroxamic acid
SCGE	Single cell gel electrophoresis
SD	Standard deviation
SDSA	Synthesis-dependent strand annealing
SDS-PAGE	Sodium dodecyl sulfate polyacrylamide gel electrophoresis
Ser	Serine
siRNA	Small interfering RNA
SIRT	Sirtuin
SMARCAD1	SWI/SNF-related matrix-associated actin-dependent regulator of chromatin subfamily A containing DEAD/H box 1
SNAI	Snail Family Transcriptional Repressor
SSB	DNA single strand break
SSC	Sideward scatter
ssDNA	Single-stranded DNA
STAT	Signal transducer and activator of transcription
SUMO	Small ubiquitin-like modifier
TBC	Tubulin cofactor
TDG	Thymidine DNA glycosylase
TdT	Terminal deoxynucleotidyl transferase
TF	Transcription factor
TGF	Transforming growth factor α
Thr	hreonine
Thy	Thymidine
TK	Thymidine kinase
TKi	Tyrosine kinase inhibitors
TLS	Translesion synthesis
TNF	Tumor necrosis factor
TNM	Tumor, node, metastasis
TP	Thymidine phosphorylase
TP53	Tumor protein p53
tRNA	Transfer RNA
TS	Thymidylate synthase
TSA	Trichostatin A
TWIST	Twist Family BHLH Transcription Factor
UDG	Uracil DNA glycosylase
UDPK	Uridine diphosphate kinase
UK	Uridine kinase
UMPK	Uridine monophosphate kinase
UP	Uridine phosphorylase
Urd	Uridine
UTP	Uridine triphosphate
UV	Ultraviolet
VEGF	Vascular endothelial growth factor
VHL	Von Hippel-Lindau
VPA	Valproic acid
XRCC	X-ray repair cross-complementing protein
ZEB	Zinc Finger E-Box Binding Homeobox
z-VAD-FMK	Pan-caspase inhibitor

1 Introduction

1.1 Cancer and carcinogenesis

Cancer poses a major and increasing global health problem against the background of a growing and aging population (Torre et al. 2015). In the United States of America, cancer is the second leading cause of death at present (Siegel et al. 2018). This global progression is closely associated with the world-wide increase in the prevalence of cancer risk factors such as obesity, physical inactivity, and smoking. These outweigh increasing treatment success and the associated reduction in cancer mortality rate in the first world (Torre et al. 2015). Research to counteract this worldwide public health problem is still hampered by the complexity of the disease with more than 100 distinct cancer types and additional subtypes in specific organs (Hanahan and Weinberg 2000). Nevertheless, it is generally acknowledged that most cancers share a common pattern of altered, acquired biological features that are essential to maintain malignant growth. This hallmark theory aids to rationalize the complexity of neoplastic disease (Hanahan and Weinberg 2000; Hanahan and Weinberg 2011). These physiological features are acquired during the course of a multistep tumorigenesis. They include self-sufficiency in growth signals, insensitivity to growth-inhibitory signals, evasion of programmed cell death, limitless replication potential, sustained angiogenesis, tissue invasion and metastasis, deregulation of cellular energy metabolism, and avoidance of immune destruction. Cellular transformation is commonly enabled by genetic instability, the subsequent formation of mutations, and a state of tumor-promoting inflammation (Hanahan and Weinberg 2000; Hanahan and Weinberg 2011). Improved understanding of these individual hallmarks of cancer outgrowth and determination of their relative importance for each individual tumor subtype is thought to prospectively enable targeted therapeutic approaches in clinical routine (Hanahan and Weinberg 2011). Thus, it is important to characterize basal signaling pathways in various cancer subtypes that contribute to the general manifestation of these cancer promoting hallmarks. Noteworthy, besides genetic alterations, chromatin and epigenetic modifications possess important functions in tumor initiation and progression. Genome wide sequencing projects report that roughly half of human cancers feature mutations in chromatin proteins and additionally exhibit broad scale changes in DNA methylation, chromatin structure, and regulatory element activity (Flavahan et al. 2017). This implication of epigenetic regulation entails the addition of a further layer of complexity to the goal of understanding the principles of cancer initiation and progression. Nevertheless, acknowledgment and commencing comprehension of these added regulatory circuits might lead to the implementation of effective epigenetic treatment schemes in oncologic practice. This approach might include the application of therapeutics targeting DNA methyltransferases, histone acetylation modifiers, and histone methylation modifiers (Flavahan et al. 2017; Kelly and Issa 2017). Along with the recent advances in cancer immunotherapy and the deeper understanding of basal mechanisms of conventional chemotherapy as well as the optimization of cost-effectiveness and applicability of tumor screening techniques, this consideration of epigenetic plasticity of cancer might significantly improve treatment efficiency to eventually counter the observed increasing global cancer prevalence.

1.1.1 Renal cell carcinoma

Renal cell carcinoma (RCC) are defined as adenocarcinomas that originate in the epithelium of the renal tubules and are thus distinct from kidney cancer of the renal pelvis or the renal medulla (Cohen and McGovern 2005; PDQ® 2018g; PDQ® 2018e). With an estimated 65.340 newly diagnosed cases and 14.970 deaths in 2018 in the United States alone, RCC is one of the most common and fatal urogenital malignancies (PDQ® 2018g). Subtypes of RCC include clear cell (~75%), papillary type 1 and 2 (16%), chromophobe (7%), translocation (1%), medullary (<0.5%), and collecting duct (<0.5%) RCC (Shuch et al. 2015). The majority of RCC is of sporadic origin with only 5 – 8% of RCC cases being attributed to distinct, autosomal dominant inherited genetic syndromes such as von Hippel-Lindau (VHL) disease, hereditary leiomyomatosis and renal cell cancer (HLRCC), hereditary papillary renal carcinoma (HPRC), and Birt-Hogg-Dubé (BHD) syndrome (PDQ® 2018e). Associated inherited susceptibility genes are the tumor suppressor genes *VHL* (in VHL disease), *FH* (fumarate hydratase; in HLRCC), *FLCN* (folliculin; in BHD syndrome) and the protooncogene *MET7* (hepatocyte growth factor receptor; in HPRC) (PDQ® 2018e). Apart from these hereditary dispositions, acknowledged risk factors for sporadic RCC include smoking, obesity, hypertension, and acquired cystic kidney disease (Chow et al. 2000; Lipworth et al. 2006; Przybycin et al. 2018). Remarkably, defects in the *VHL* gene are also causal for ~60% of sporadic clear cell RCC (ccRCC) and can thus be considered as the primary determinant of the majority of RCC (Cohen and McGovern 2005). In comparison to VHL disease, in which patients experience a predisposition for multiple benign and malignant tumors in various organ systems due to germline mutations in *VHL* (Joerger et al. 2005), patient age at sporadic tumor onset is advanced, as no predisposing one-allelic mutation is inherently present. Increasing loss of VHL protein expression reduces its inhibitory effect on hypoxia-inducible genes and their respective proteins with roles in angiogenesis (e.g. vascular endothelial growth factor (VEGF)), cell growth (e.g. transforming growth factor α (TGF-α)), glucose uptake (e.g. GLUT-1), and acid-base balance (e.g. CA9). These expression changes, taken together, generate a microenvironment that supports epithelial cell proliferation (Cohen and McGovern 2005). Furthermore, VHL protein induces ubiquitination and degradation of the key regulator of hypoxic response hypoxia-inducible factor α (HIF-α). This VHL-induced HIF-α inhibition has been shown to effectively suppress ccRCC growth in pre-clinical models (Kondo et al. 2003;

Zimmer et al. 2004; Cohen and McGovern 2005). A subpopulation of sporadic RCC, sporadic papillary RCC, carries mutations of the *MET7* gene, comparable to those observed in HPRC, that lead to enhanced expression levels of the MET receptor tyrosine kinase as a result of allele duplication (Cohen and McGovern 2005). These sporadic papillary RCC occasionally harbor translocations of the *TFE3* gene, encoding a transcription factor (TF) with relation to c-MYC, that result in fusion products with other genes (Sidhar et al. 1996; Cohen and McGovern 2005). Furthermore, it has been reported that protein levels of the crucial tumor suppressor phosphatase and tensin homolog (PTEN) were markedly reduced during early RCC genesis (Brenner et al. 2002). Additionally acquired somatic mutations in other sporadic RCC subtypes might play a role but have not been compellingly described at present. Treatment and prognosis of RCC is closely associated with the staging of the disease, which, in turn, is related to the degree of tumor spread beyond the kidney (PDQ® 2018g). RCC is commonly staged using TNM (tumor, node, metastasis) classification, which comprises four substages for RCC (TNM stage I, II, III, IV). Tumors classified as TNM stage I and II are restricted to the kidney, with tumor mass being 7 cm or smaller in its greatest dimension classified as stage I and tumor mass larger than 7 cm in its greatest dimension classified as stage II (PDQ® 2018g). For patients with stage I or II RCC either partial or radical nephrectomy offers an often curative therapeutic strategy and 5-year overall survival rates are high (93%) (PDQ® 2018g; Siegel et al. 2018). Stage III RCC have spread to regional lymph nodes, blood vessels in or near the kidney, the urine collecting ducts, or the fatty tissue surrounding the kidney (PDQ® 2018g). Nevertheless, radical nephrectomy, case-dependently accompanied by preoperative embolization or pre- and postoperative external-beam radiation therapy, represents an often curative therapy with a 5-year survival rate of 67% (PDQ® 2018g; Siegel et al. 2018). In stage IV RCC, the primary tumor has grown beyond the kidney’s layer of fatty tissue, may have spread to the adrenal gland, or has formed distant metastases in other organs or distant lymph nodes (PDQ® 2018g). Unfortunately, prognosis for stage IV disease is unfavorable and, at present, most patients are incurable due to the extensive resistance of RCC against otherwise commonly used radio- and chemotherapeutic treatment schemes (Makhov et al. 2018). At present, 5-year survival rates for RCC with distant metastases is merely 12% (Siegel et al. 2018). However, as a result of the primary asymptomatic progression of localized RCC, around 16% of patients present with metastatic disease at initial diagnosis (Patard et al. 2003; Siegel et al. 2018). Treatment options for this patient subgroup, besides prolongation of survival through local resection of the primary tumor and metastases, include several targeted therapies. Cytokine therapy with interferon-alpha (IFNα) or high doses of interleukin-2 (IL2) has been the only treatment option for more than 20 years (Makhov et al. 2018; PDQ® 2018g). Objective response rates with IFNα or IL2 were limited to approximately 15% of patients (PDQ® 2018g). Recognition of the crucial role of *VHL* mutations in RCC led to the introduction of antiangiogenic therapy with agents targeting VEGF signaling. These agents include the tyrosine kinase inhibitors (TKi) sunitinib, sorafenib, pazopanib, cabozantinib, and axitinib and the αVEGF primary antibody bevacizumab (Ghatalia et al. 2017; PDQ® 2018g). Exploitation of this strategy became standard of care in metastatic RCC and successfully increased response rates in first-line therapy but nevertheless rarely resulted in durable responses with a limited prolongation of median progression free survival to around 8.5 to 11 months (Ghatalia et al. 2017; PDQ® 2018g). The associated disease progression is mainly linked to intrinsic and acquired TKi resistance mechanisms (Makhov et al. 2018). In addition, the mammalian target of rapamycin (mTOR) inhibitors temsirolismus and everolismus are accepted treatment options in advanced RCC (PDQ® 2018g). New treatment regimens for metastatic RCC are strongly required and might have been found in the form of immune checkpoint inhibitors (ICIs), which counteract acquired immune evasion mechanisms of tumor cells (Ghatalia et al. 2017). These targeted antibody therapies comprising the ICIs nivolumab and ipilimumab have shown promising results in clinical trials and have recently been approved as single and combinatorial first- and second-line therapies in metastatic RCC (Ghatalia et al. 2017; Flippot et al. 2018). Tumor cells evade immune recognition by presenting programmed-death ligand 1 (PD-L1) on their surface. Recognition of these surface proteins by homologous, specific T lymphocyte receptors, such as programmed-death 1 (PD-1) or cytotoxic T-lymphocyte-associated protein 4 (CTLA-4), subsequently suppresses immune response as it functionally impairs T cells and blocks their activation. Nivolumab, directed against PD-1, and ipilimumab, directed against CTLA-4, inhibit these immune checkpoints and thus allow efficient targeting of tumor cells by the immune system (Buchbinder and Desai 2016; Flippot et al. 2018). Notably, several studies show that histone deacetylase inhibitor (HDACi) treatment further enhances immunotherapy efficiency with these ICIs in various solid cancer types *in vitro* and *in vivo* through augmentation of tumor antigen presentation and immune recognition (Suzuki et al. 2010; Woods et al. 2013; Kim et al. 2014; Woods et al. 2015; de Charette et al. 2016; Gameiro et al. 2016; Terranova-Barberio et al. 2017; Booth et al. 2018; Briere et al. 2018). Accordingly, several clinical studies are initiated that examine combinatorial treatment schemes of HDACi and ICI in RCC (Terranova-Barberio et al. 2016; Ghatalia et al. 2017; Flippot et al. 2018; Nuti et al. 2018). Although the advent of immunotherapy using ICIs promises a huge advancement in metastatic RCC therapy, treatment options that substantially improve overall survival and thus effectively enhance curability are still scarcely found. This is in large part still due to an insufficient understanding of the elementary molecular mechanisms that steer RCC progression and its substantial therapy resistance mechanisms.

1.1.2 Colorectal cancer

CRC arise in the intestinal epithelium of the colon and the rectum, where they predominantly develop from precancerous, asymptomatic adenomatous polyps or adenomas (Levine and Ahnen 2006; Aran et al. 2016). Colorectal cancer is estimated to be diagnosed with an incidence of 1.8 million cases worldwide in 2018. Over the same period, 881.000 patients are predicted to die from this disease. Consequently, colorectal cancer is classified as the third most commonly diagnosed form of cancer while ranking second in consideration of mortality (Bray et al. 2018). Comparable to RCC, the majority CRC cases are sporadic and can be attributed to Western lifestyle factors and advanced age, which, in turn, explains rising case rates in developing countries (Aran et al. 2016; Bray et al. 2018). A minority of around 5% can be attributed to distinct hereditary symptoms and the predominant two inherited CRC syndromes are familial adenomatous polyposis (FAP) and hereditary nonpolyposis colorectal cancer (HNPCC) (Burt and Neklason 2005). The associated mutated genes are the gene coding for adenomatous polyposis coli (*APC*, in FAP syndrome) and the DNA mismatch repair genes MutL homolog 1 (*MLH1*), MutS homolog 2, -6 (*MSH2*, *MSH6*), or *PMS2* (in HNPCC) (Burt and Neklason 2005; PDQ® 2018d). Further, less common, CRC syndromes and their respective mutated genes include oligopolyposis (*POLE*, *POLD1*), juvenile polyposis syndrome (*BMPR1A*, *SMAD4*), Cowden syndrome (*PTEN*), and Peutz-Jeghers syndrome (*STK11*) (PDQ® 2018d). Genetic testing to identify germline mutations in affected individuals has become clinical standard of care and serves to pinpoint family members at risk of disease development (Burt and Neklason 2005; PDQ® 2018d). Positive test results for inherited disease enables disease prevention in these high-risk individuals through regular colonoscopy screening, surveillance, and early detection, which significantly enhances survival outcome (Burt and Neklason 2005; PDQ® 2018b). Apart from that, several countries (e.g., the United States, Germany, the Netherlands, and the United Kingdom) established nationwide CRC screening programs for people of advanced age as preventive measure for early detection of pre-cancerous polyps or early, benign adenomatous polyps and adenomas to improve CRC disease management and to ultimately reduce CRC incidence and mortality (Brenner and Chen 2018; PDQ® 2018b; PDQ® 2018c). Early detection and prevention of CRC is feasible as, in contrast to RCC, colorectal tumors have for decades been described to grow in a continuum in which certain mutations are associated with specific histopathological features observed in the various stages of disease progression (Fearon and Vogelstein 1990; Markowitz and Bertagnolli 2009). This classic, uniform, and comparatively linear adenoma-carcinoma sequence model comprises the initial adenoma formation due to an inactivating *APC* mutation and the subsequent emergence of increasingly aggressive cancerous subclones as a result of further acquired mutations in *KRAS* and *TP53* genes (**Figure 1**) (Vogelstein et al. 1988; Jass 2007). Fundamental for this general model is an inherent genetic instability in CRC that promotes the step-wise accumulation of multiple genetic alterations within subclones of the colorectal epithelium and is a result of a loss of expression of certain DNA mismatch repair (MMR) proteins (typically MLH1 or MSH2) (Jass 2007). The succeeding MMR deficiency results in a reduced detection efficiency of DNA replication-associated base mismatches (Gelsomino et al. 2016). Repeated DNA sequences in the genome, the so-called microsatellites, are especially prone to these replication errors (e.g. base insertions or deletions) and thus become genetically instable. Should this phenomena affect the coding regions of genes whose products have crucial implications for cell faith, this microsatellite instability (MSI) might result in oncogenic transformation (Gelsomino et al. 2016).

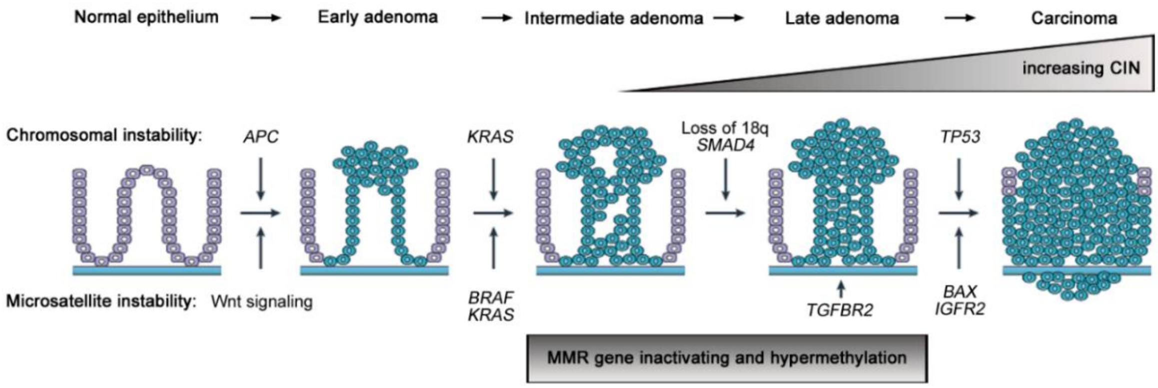

Figure 1: Adenoma-carcinoma sequence model for colorectal cancer progression. The likely oversimplified historic model of progression depicts histopathological and genetic changes in CRC with genomic instability. Initiation of tumorigenesis in cells with chromosomal instability (CIN$^+$) is marked by the early loss of *APC*. Early adenomas develop mutations in *KRAS*, lose chromosome 18q harboring *SMAD4*, and acquire *TP5*3 mutations. MSI is uncommon in early adenoma in sporadic CRC and occurs predominantly during progression by downregulation of MLH1 by promoter hypermethylation. Additional abrogation of MMR is accomplished by selection of *MSH3* and *MSH6* mutated subclones. In general, mutational profiles during cancer progression in CSI$^+$ and MSI$^+$ tumors diverge. Progression to adenoma in the MSI pathway occurs by changes in Wnt signaling pathways and *BRAF* mutations predominate over *KRAS* mutations. In progression to carcinoma, subclones with MSI induced mutations in genes coding for transforming growth factor β receptor 2 (*TGFBR2*), insulin-like growth factor 2 receptor (*IGFR2*), and BCL-2 associated X (*BAX*) are selected, providing a *TP53*-independent mechanism. Modified according to (Walther et al. 2009).

However, recent studies imply a far more heterogenous origin of CRC that cannot be explained with the historic adenoma-carcinoma sequence model. For instance, next-generation sequencing studies have revealed a remarkably high complexity of mutations in CRC, with each tumor comprising 75 individual mutations on average (Muzny et al. 2012; Punt et al. 2016). A higher complexity of CRC initiation and progression than proposed by Vogelstein in his adenoma-carcinoma sequence might explain why the understanding of patient response and relapse remains poor and why, apart from *KRAS* mutation in epidermal growth factor receptor (EGFR) targeted therapy, none of the commonly studied mutations (*KRAS*, *APC*, *TP53*) has been shown as a predictive marker in clinical practice (Vogelstein et al. 1988; Walther et al. 2009). Furthermore, solely around 15% of all CRC were tested positive for MSI, albeit MSI was previously thought to be a prerequisite for the manifestation of mutations in the tumorigenic driver genes *APC*, *KRAS*, and *TP53* (Gelsomino et al. 2016). In contrast, most

CRC show a general and intrinsic chromosomal instability (CIN) that is independent of specific mutations in MMR and has been linked to a multitude of deregulated genes with functions in chromosome segregation, telomere regulation, and DNA damage response (Pino and Chung 2010). Apart from the MSI and the CIN phenotype, a subset of CRCs has been described to show aberrant methylations of CpG islands (CGI) in the promotor region of tumor suppressor genes and is thus termed CpG island methylator phenotype (CIMP) (Toyota et al. 1999; Tse et al. 2017). Recent reports thus suggest to molecularly reclassify CRC based on the tumor's DNA MSI status (MSI-high (MSI-H), MSI-low (MSI-L), and MS stable (MSS)) as well as its CIMP (CIMP-high, CIMP-low, and CIMP-negative) to improve targeted therapy decisions (Jass 2007). Along with the shown high quantity and heterogenous nature of mutations in individual CRCs (Wood et al. 2007; Muzny et al. 2012; Punt et al. 2016), these diverse mechanisms of genetic instability and associated specific mutations demonstrate that CRC must be acknowledged for its heterogenous background to prospectively accomplish targeted therapy development and to effectively improve subsequent tumor classification and patient stratification. Thus, the definition of key CRC driver genes as possible biomarkers, their associated pathways, and their respective influence on the CRC phenotype remains a task for the ongoing CRC research (Fearon 2011). Comparable to RCC, prognosis and treatment options for CRC are dependent on the tumor's histopathological classification, which is distinguished using the TNM classification that results in four primary disease stages (stage I, II, III, IV) (Brenner et al. 2014). While the T stage defines the local invasion of the primary tumor, N stage describes the lymph node involvement, and M indicates the presence of distant metastases (Brenner et al. 2014). In stage I and II disease, the primary tumor infiltrates different layers of the colon without affecting regional lymph nodes or forming distant metastases (corresponds to T1/2/3/4N0M0) (Markowitz et al. 2002; Brenner et al. 2014). Surgical resection of the affected colon constitutes an effective therapeutic option for the 39% of patients that present with localized stage I and II disease and results in a 90% 5-year survival rate (Siegel et al. 2018). Stage III disease is characterized by the involvement of one to more than seven regional lymph nodes (corresponds to T1/2/3/4N1/2M0). Patients with stage III CRC, and possibly also with high-risk stage II CRC, were shown to benefit from adjuvant chemotherapy consisting of 5-FU, leucovorin (LV), and oxaliplatin (FOLFOX) as their recurrence risk decreases while overall survival increases (Andre et al. 2015). However, recent critical reports question the additional benefit of adjuvant chemotherapy in stage II CRC and isolated cases of stage III CRC, as surgical techniques and preoperative staging have been remarkably improved over the last decades (Påhlman et al. 2016). Consequently, this enhanced standard of care might have nowadays reduced recurrence risk to a level at which adjuvant chemotherapy could not be recommended as it provides no additional, absolute benefit while being concurrently associated with an inherent morbidity (Påhlman et al. 2016).

Advanced targeted therapy schemes that include the monoclonal antibodies bevacizumab (inhibiting VEGF) or cetuximab (inhibiting EGFR) had no impact on disease free or overall survival in resected localized or regional stage II or III CRC (Alberts et al. 2012; Allegra et al. 2013; Punt et al. 2016). Classification of advanced CRC as stage IV disease indicates the presence of at least one metastasis in a distant organ, lymph node or the peritoneum (corresponds to T1/2/3/4N1/2M+) (Markowitz et al. 2002; Brenner et al. 2014). Prognosis for the 21% of patients presenting with distant disease is dismal as 5-year survival rates are merely 14% (Siegel et al. 2018). An important step in the treatment of advanced CRC is the surgical resection of the primary tumor and of its metastases as far as it is feasible (Aran et al. 2016; Punt et al. 2016). Conventional chemotherapy is predominantly based on the administration of 5-FU, which is applied in diverse combinatorial treatment schemes in clinical practice and trials (**Table 1**).

Table 1: Chemotherapy and targeted therapy in stage IV and recurrent CRC. Table depicts current treatment options for metastatic CRC, applied in single or combinatorial treatment schemes. Due to high diversity of dosage, order, and general combination of various available drugs in clinical routine, listed combinatorial treatment schemes can only represent examples. In addition, targeted therapeutics can be applied alone or, more regularly, treatment schemes are extended by additional application of one or more of the targeted therapeutics. Information in this table was compiled from (Aran et al. 2016; Giuliani and Bonetti 2018; PDQ® 2018a; PDQ® 2018f; Shinagawa et al. 2018). *for specificities regarding dose, application sequence, and timing see (PDQ® 2018a; PDQ® 2018f).

Individual therapeutics	
Drug	**Function**
5-Fluorouracil (5-FU)	nucleic base analogue and thymidine synthase inhibitor
Irinotecan (IRI)	topoisomerase I inhibitor
Oxaliplatin (OX)	DNA inter- and intra-strand crosslinker
Leucovorin (LV)	folinic acid; enhancer of thymidine synthase inhibition
Capecitabine (CAPE)	oral 5-FU prodrug
Bevacizumab	αVEGF antibody
Panitumumab	αEGFR antibody
Cetuximab	αEGFR antibody
Aflibercept	VEGF inhibitor
Ramucirumab	αEGFR antibody
Regorafenib	multiple tyrosine kinase inhibitor
TAS-102	combination of nucleic base analogue and thymidine phosphorylase inhibitor
Pembrolizumab	αPD-1 antibody
Nivolumab	αPD-1 antibody
Combinatorial treatment schemes	
Drug combination	**Regimen***
5-FU, LV, IRI	AIO, Douillard, FOLFIRI, IFL
5-FU, LV, OX	FOLFOX-4, FOLFOX-6, FUFOX
CAPE, OX	CAPOX, XELOX
5-FU, LV, IRI, OX	FOLFOXIRI
5-FU, OX	FUOX
5-FU, LV	FL

Treatment schemes in metastatic disease include the addition of antibodies targeting VEGF (bevacizumab) or its receptor (aflibercept, ramucirumab) to standard therapy. Yet, there are no valid biomarkers in clinical routine to select patients with highest expectable benefit from VEGF-directed therapy (Hurwitz et al. 2004; Van Cutsem et al. 2012; Sinicrope et al. 2016). Interestingly, MMR deficient cancers were shown to express an increased number of mutation-associated antigens on their surface and accordingly immunotherapeutic approaches with the anti-PD1 antibodies pembrolizumab and nivolumab showed favorable results in this CRC subgroup (Goswami and Sharma 2017; Le et al. 2017; Overman et al. 2017). Although the achieved therapeutic and surgical improvements over the last 20 years did not significantly enhance overall survival rates of metastatic CRC, they nevertheless yielded a substantial prolongation of survival from 5 - 6 months to about 30 months. In order to prospectively further prolong survival or even enhance overall survival rates of stage IV disease, it is thus of the utmost importance to further investigate molecular pathways that determine CRC initiation, progression, and resistance to identify new starting points for therapeutic strategies. Increased acceptance of the discussed highly heterogenous nature of CRC will also provide the foundation to define advanced biomarkers that might enable improved patient assignment to therapeutic strategies and thus forward abandonment of the hitherto largely applied one-size-fits-all therapeutic approach.

1.2 Cellular response pathways governing cell death decisions

The execution of limited cell death is crucial in normal tissue homeostasis. Systematic elimination of specific cells can serve to control tissue characteristics and cell turnover in different developmental stages, to prevent tumorigenesis in case of mutagenic events, and thus to, in general, ensure the well-functioning of multicellular organisms. With regard to these fundamental implications, it is of no surprise that multiple separate and intertwined mechanisms have evolved to govern and control decisions between cell survival and death. A selection of these pathways is going to be outlined in the following sections.

1.2.1 Apoptosis

Apoptotic cell death is a programmed mechanism to eliminate cells during normal cell turn-over in the maintenance of tissue homeostasis (Los et al. 1999). Furthermore, apoptosis is triggered by genotoxic damage levels that exceed cellular repair capacity in order to prevent mutagenesis and subsequent tumor initiation and progression (Roos et al. 2015). Morphologically, apoptotic cells undergo a multitude of alterations including chromatin condensation, loss of cell adhesion, shrinking of the cell body, and extensive plasma membrane blebbing (Elmore 2007). Finally, apoptotic bodies consisting of cytoplasm and tightly packed organelles are formed, that are subsequently phagocytosed and degraded by macrophages (Elmore 2007). Inflammatory reaction is effectively prevented throughout the apoptotic process by the tight containment of cellular components within intact plasma membranes, the immediate processing of apoptotic vesicles by surrounding cells, and the absence of cytokine production (Elmore 2007). Mechanistically, two different pathways of apoptotic effector caspase activation can be separated – the intrinsic, mitochondrial pathway and the extrinsic, death receptor pathway. The intrinsic pathway is essentially regulated by members of the B-cell lymphoma 2 (BCL-2) protein family that govern mitochondrial membrane permeability. Upon either extracellular stimuli or intracellular signals, changes in the expression of BCL-2 family members enhance the permeability of the outer mitochondrial membrane for internal cytochrome *c*. In response, cytochrome *c* is released into the cytoplasm and triggers the assembly of apoptotic protease activating factor 1 (APAF-1) and pro-caspase 9 to form the so-called apoptosome. This subsequently leads to the execution of a caspase signaling cascade that culminates in cellular apoptosis (Ouyang et al. 2012). On the other hand, the extrinsic pathway involves transmembrane, receptor-associated signaling dependent on members of the tumor necrosis factor (TNF) receptor family, also termed death receptors, and their respective ligands (e.g. FASL/FASR, TNF-α/TNFR1, APO3L/DR3, APO2L/DR4, APO2L/DR5) (Elmore 2007). Upon ligand binding, downstream signaling pathways finally result in the induction of caspase 8 and subsequent activation of caspase cascades comparable to the intrinsic pathway. Receptor-dependent, cytoplasmic signaling pathways are best characterized for FASL and FASR, which form a so-called death complex upon ligand binding. This death complex subsequently recruits death domain-containing proteins (FADD) and pro-caspase 8. It aggregates to form the death-inducing signaling complex (DISC), that effectively triggers caspase 3 cleavage downstream (Ouyang et al. 2012). In summary, both pathways of apoptosis initiation culminate in the dimerization and activation of either the initiator caspase 8 (extrinsic pathway) or the initiator caspase 9 (intrinsic pathway), which subsequently trigger cleavage and activation of the downstream executioner caspases caspase 3, -6, and -7 and promote apoptotic cell death (McIlwain et al. 2013).

1.2.2 Necrosis and necroptosis

In contrast to the programmed induction of cell death via apoptosis, cell death induction via necrosis is thought to be accidental and uncontrolled in response to chemical or physical insults. Necrosis is morphologically characterized by cell swelling, membrane rupture, and an uncontrolled loss of intracellular content that may trigger an inflammatory response (Chaabane et al. 2013; Feoktistova and Leverkus 2015). However, in recent years, studies showed that several forms of necrosis can be considered as regulated cell death. One of these regulated necrosis pathways is termed necroptosis, which was particularly initiated in response to death receptor stimulation when intracellular apoptotic signaling was inhibited (through caspase or IAP inhibitors). Central to necroptosis are the kinases receptor-interacting serine/threonine protein kinase (RIPK) 1 (RIPK1) and 3 (RIPK3) that, dependent on the inducing stimuli, form two different complexes – the ripoptosome or the necrosome (Feoktistova and Leverkus 2015). RIPK1 activates RIPK3 which in turn activates the pseudokinase mixed-lineage kinase domain-like protein (MLKL) and induces necroptosis. Apart from RIPK1/RIPK3/MLKL-dependent necroptosis, two further regulated necrosis pathways were described – MPT-regulated necrosis and parthanatos (Feoktistova and Leverkus 2015).

1.2.3 Autophagy

The term autophagy encompasses three different molecular mechanisms: macroautophagy, microautophagy, and chaperone-mediated autophagy (Mizushima and Komatsu 2011). Macroautophagy (hereafter autophagy) represents the major type of autophagy and describes a catabolic cellular process that serves to eliminate cellular components such as protein aggregates and organelles by engulfment in autophagosomal vesicles. Subsequent fusion of these autophagosomes with lysosomes to form autolysosomes results in degradation of the incorporated cytoplasmic components (Fuchs and Steller 2015). This highly organized mechanism serves as a dynamic recycling process that provides new building blocks and energy for further cellular processes (Mizushima and Komatsu 2011). Unsurprisingly, it is thus linked to major physiological processes including cell survival, cell death, cell metabolism, development, infection, immunity, and aging (Chaabane et al. 2013). Although autophagy is mostly considered to promote cell survival by suppression of necrotic cell death and through enhanced availability of energy and molecular building blocks under stressful or even tumorigenic conditions (Esposti et al. 2010), it is additionally still debated as possible cell death mechanism that is characterized through extensive autophagic vacuolization of the cytoplasm in the absence of apoptotic chromatin condensation (Yu et al. 2004).

1.3 Posttranslational modification of proteins

The term posttranslational modification (PTM) encompasses all chemical modifications that are covalently introduced at the side chains of amino acids after protein synthesis at the ribosomes. These modifications serve to regulate the protein’s activity. PTMs can transform inactive apoproteins into functional enzymes, regulate enzymatic activity and intracellular localization of proteins, mark proteins for degradation by the proteasome, enable or prevent protein interactions, and furthermore directly or indirectly influence three-dimensional protein structure (Knorre et al. 2009; Chuh et al. 2016). Thus, PTMs provide the means to dynamically adjust cellular signaling pathways independently of transcriptional and translational regulation in response to various internal and external stimuli. Prominent examples for reversible PTMs with extensive implications for protein function and regulation are phosphorylation, glycosylation, ubiquitination, sumoylation, prenylation, methylation, and acetylation (Krueger and Srivastava 2006). These PTMs do not only function in an isolated fashion, but rather form a regulatory network to coordinately accomplish functional and structural diversity that extends beyond the provided genomic information (Chuh et al. 2016). To ensure functionality and reversibility of PTMs, evolution provided specific enzymatic domain types that serve as writer, eraser, and reader of each PTM. For instance, tyrosine phosphorylation, a PTM that is well studied for its importance in intracellular signaling cascades, is written by tyrosine kinases, erased by tyrosine phosphatases, and read by proteins containing Src Homology 2 (SH2) domains (Beltrao et al. 2013).

1.3.1 Histone deacetylases and their inhibitors

Protein acetylation through covalent addition of an acetyl residue from acetyl-coenzyme A to the ε-amino group of lysine is a widely distributed PTM throughout the proteome. The writers of protein acetylation are termed histone acetyltransferases (HATs), while the erasers are termed histone deacetylases (HDACs). Those two protein groups catalyze the acetylating and deacetylating reaction as described in **Figure 2**. Proteins that possess the ability to recognize acetylated lysine residues contain bromodomains (BRD) to enable identification and binding of this PTM (Jain and Barton 2017). The human genome encodes 46 of these BRD containing proteins, which display a wide range of functionality in the regulation of chromatin structure and gene transcription. Among others, these proteins function as HATs, TFs, chromatin remodelers, ATPases, transcriptional silencers, or methyltransferases (Gil et al. 2017; Jain and Barton 2017).

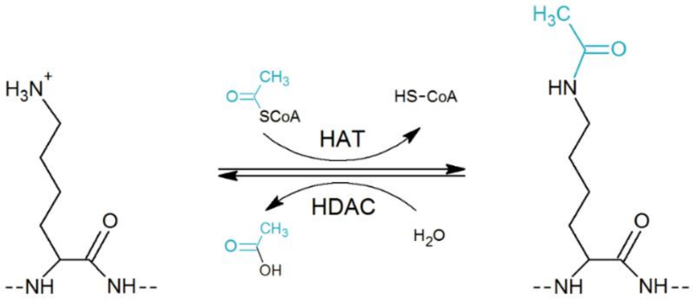

Figure 2: Acetylation and deacetylation of lysine residues by HATs and HDACs. HATs catalyze the transfer of acetyl groups from acetyl-coenzyme A to the ε-amino group of a lysine residue. Conversely, the deacetylation of lysine is catalyzed by Zn^{2+}-dependent HDACs. Addition of an acetyl group neutralizes the positive charge of this residue and can thus result in structural alterations of the protein and additionally prevent further modifications of the same residue.

HATs were initially grouped into two classes depending on their nuclear or cytoplasmic localization. The cytoplasmic HATs KAT1 and HAT4 modify freshly synthesized histones prior to their translocation to the nucleus. Nuclear HATs are additionally subcategorized into three families and further HATs that function as transcriptional co-activators (KAT4, KAT12) or steroid receptor co-activators (KAT13A, KAT13B, KAT13C, KAT13D). The GNAT family includes the members KAT2A and KAT2B, while the MYST family consists of KAT5, KAT6A, KAT6B, KAT7, and KAT8. The p300/CBP family members are KAT3A and KAT3B. All HAT isoenzymes display individual substrate specificity for histones and non-histone proteins, which is further modulated through the incorporation of HATs as catalytic cores in multi-subunit protein complexes (Wapenaar and Dekker 2016). On the other hand, the 18 known HDACs are grouped into four classes. Class I, II, and IV contain eleven HDACs that are dependent on a core Zn^{2+} ion to catalyze their enzymatic activity (**Figure 3**). Class I HDACs, namely HDAC1, -2, -3, and -8, structurally resemble the yeast enzyme Rdp3, while class II HDACs are homologous to Hda1 in yeast and are further subdivided into class IIa (HDAC4, -5, -6, -7, and -9) and class IIb (HDAC6 and -10). Class IV consists of HDAC11 that displays sequence similarity with class I as well as class II HDACs. In contrast to class I, II, and IV HDACs, seven of the known 18 HDACs are dependent on NAD^+ instead of Zn^{2+} as cofactor for their catalytic activity. They thus share sequence similarity with the yeast enzyme Sir2. These class III deacetylases are consequently termed sirtuins (SIRTs) (Li and Seto 2016). At present, a plethora of different natural and synthetic molecules shows verified inhibitory activity for HDACs. HDACi display different basic chemical structures and are thus grouped into the following classes: hydroxamates, benzamides, aliphatic acids, and cyclic peptides. In general, HDACi of class I, II, and IV accomplish their function by binding to the catalytically active pocket of the enzyme and subsequent interference with the crucial Zn^{2+} central ion (Li and Seto 2016; Olzscha et al. 2016). Common HDACi for class I, II, and IV HDACs are the benzamide entinostat (MS-275), the aliphatic acid valproic acid (VPA), and the hydroxamates panobinostat (LBH-589) and vorinostat (suberanilohydroxamic acid (SAHA)) (**Figure 3**).

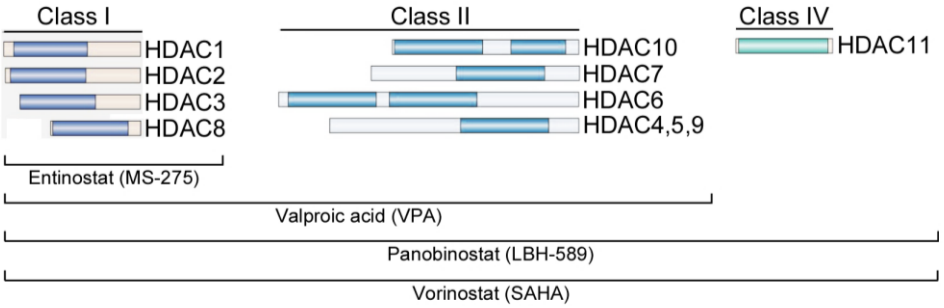

Figure 3: Zn^{2+}-dependent histone deacetylases and their inhibitors. Catalytic domains of the three classes of Zn^{2+}-dependent HDACs are represented in color. Catalytic domains display a high degree of homology, while accessory domains, that mainly execute regulatory functions, are variably structured. Figure shows selectivity of particular HDACi. Outlined are the commonly used benzamide entinostat (MS-275), the aliphatic fatty acid valproic acid (VPA), and the two hydroxamic acids panobinostat (LBH-589) and vorinostat (SAHA). Depiction of HDACs is modified according to (Minucci and Pelicci 2006). HDACi selectivity is according to (Li and Seto 2016).

HATs and HDACs not only modify histones but also a large number of non-histone proteins including essential proteins, such as the tumor suppressor p53, the transcription factors E2F, STAT3, NF-κB, and CREB, the repair proteins thymidine DNA glycosylase (TDG) and KU70, as well as α-tubulin and heat shock protein 90 (HSP90) (Minucci and Pelicci 2006). Due to the high number of acetylation sides found in non-histone proteins through quantitative proteomics analysis it was even concluded that lysine acetylation contributes to the regulation of the majority of nuclear functions in mammalian cells (Choudhary et al. 2009). To account for this increasing substrate spectrum, efforts have been made to introduce an amended nomenclature that would rename HATs and HDACs as KATs and KDACs based on their role as general lysine (K) modifiers (Allis et al. 2007). Apart from that, acetylation and deacetylation of histones themselves is directly associated with the compaction of chromatin as acetylation of histone tails abrogates their positive charge and subsequently hampers histone interaction with the negatively charged DNA phosphate backbone (Hong et al. 1993; Glozak and Seto 2007). According to this model, histone acetylation by HATs relaxes chromatin, while histone deacetylation through HDACs enhances chromatin condensation and thus impedes accessibility of the DNA for transcription, replication, or repair processes (Eberharter and Becker 2002; Glozak and Seto 2007). Furthermore, HDACs have also been described as being part of multiprotein complexes with transcriptional repressor and chromatin remodeling functions (mSin3, NuRD, N-CoR, CoREST). This indicates a higher complexity of transcriptional regulation by HDACs than mere polarity changes in histone tails (Grozinger and Schreiber 2002; Yang and Seto 2008). Given these implicated regulatory functions of lysine acetylation in a wide variety of cellular processes, it is of no surprise that a deregulation of the homeostasis of HAT and HDAC expression and function has been linked to cancer development and progression. Lower global levels of histone acetylation or certain histone acetylation patterns have been found to be predictive for poor prognosis, treatment response, and increased recurrence rates in tumors of different origin (Fraga et al. 2005; Seligson et al. 2005; Elsheikh et al. 2009; Seligson et al. 2009; Manuyakorn et al. 2010). Furthermore, overexpression of all members of class I HDACs has been found in different cancer types (Weichert et al. 2008; Weichert 2009; Barneda-Zahonero and Parra 2012). Analysis of patient derived tumor samples has shown that HDAC1 is frequently overexpressed in breast, lung, gastric, pancreatic, hepatocellular, and prostate carcinomas and that this overexpression is often associated with dismal prognosis (Choi et al. 2001; Halkidou et al. 2004; Zhang et al. 2005; Minamiya et al. 2011). Joint high expression of HDAC1, -2, and -3 has been reported in tumor tissue derived from urothelial, colorectal, and renal cancer as well as Hodgkin’s lymphoma (Fritzsche et al. 2008; Weichert et al. 2008; Adams et al. 2010; Pinkerneil et al. 2016). On the other hand, in a large-scale tissue microarray series of mesenchymal tumor samples, HDAC2 was found to be expressed more strongly than HDAC1 and to be associated with the pathogenesis of sarcoma (Pacheco and Nielsen 2011). Nonetheless, class I HDACs can also prevent tumorigenesis in healthy tissue due to a stabilizing effect on genomic integrity. For instance, loss of HDAC1/2 activity promotes acute myeloid leukemia (Santoro et al. 2013), spontaneous formation of epidermal tumors (Winter et al. 2013), and neoplastic transformation in the thymus (Dovey et al. 2013; Heideman et al. 2013). These findings affirm the crucial importance of a tared balance between acetylating and deacetylating mechanisms for tissue homeostasis. Additionally, the implication of HDAC class I overexpression in malignant transformation offers possibilities for therapeutic interventions, as, in contrast to other carcinogenic transitions such as the irreversible loss of tumor suppressor proteins or the accumulation of tumorigenic mutations, unfavorable variances in the acetyl code are reversible and can be targeted with HDACi. Fittingly, HDACi have been widely described as executing an antineoplastic effect through the initiation of apoptotic cell death and the induction of growth inhibition. For instance, HDACi were shown to induce intrinsic and extrinsic apoptosis pathways in diverse tumor cells through upregulation of BCL-2 family members (such as BID, BAD, BIM, BAX), APAF-1, and PUMA (Vrana et al. 1999; Ruefli et al. 2001; Zhang et al. 2004; Zhao et al. 2005; Jung et al. 2012; Bolden et al. 2013; Feng et al. 2013; Kim et al. 2013) or through upregulation of death receptor (such as DR5, FAS) signaling pathways and their respective ligands (such as TRAIL, FAS-Ligand) (Kwon et al. 2002; Insinga et al. 2005; Nebbioso et al. 2005; Fulda 2008; Schuler et al. 2010; Bangert et al. 2012). These p53-dependent and -independent cell death pathways might be interchangeably or concurrently executed (Vrana et al. 1999; Sonnemann et al. 2014; Zhang and Zhong 2014). Furthermore, HDACi were shown to impede tumor growth through the induction of proliferation arrest in various phases of the cell cycle. G1-phase arrest by HDACi is accomplished via upregulation of the cyclin-dependent kinase (CDK) inhibitor p21, which blocks the mandatory heterodimer formation of cyclins and CDKs (cyclin D:CDK4/6 and cyclin E:CDK2) and thus prevents G1/S transition (Vrana et al. 1999; Richon et al. 2000; Sandor et al. 2000; Finzer et al. 2001; Ocker and Schneider-Stock 2007; Mateen et al. 2012; Hao et al. 2015; Li et al. 2016; Gilardini Montani et al. 2017). Fundamental for this CDK inhibitor upregulation is the finding that catalytically active HDAC1 and HDAC2 negatively regulate the expression of p21 by direct binding to the promotor region of its encoding gene (Yamaguchi et al. 2010). Furthermore, in the absence of HDAC activity, p53 is increasingly acetylated and able to enhance p21 gene and protein expression (Zhao et al. 2006). Additionally, expression of cyclin D was found to be downregulated by HDACi either as a result of proteasomal degradation or enhanced acetylation and subsequently reduced DNA binding activity of its associated TF NF-κB (Hu and Colburn 2005; Alao et al. 2006). Alternate cell cycle arrest in G2/M-phase in response to HDACi treatment might be caused by a downregulation of mitosis-initiating cyclin B (Noh and Lee 2003). Moreover, HDACi mediate downregulation of key players of mitotic chromatin condensation, the Aurora kinases (Cha et al. 2009), and their substrates (Li et al. 2006) which might impede G2/M progression. Furthermore, HDACs and their inhibitors have implications in cellular mechanisms with crucial relevance for carcinogenesis and therapy such as epithelial-mesenchymal transformation (EMT), cellular migration, and metastasis formation as well as DNA damage response. However, for reasons of clarity, these influences and their ensuing consequences are outlined in separate, specific chapters (see **1.5**, **1.6**).

1.3.2 HDAC2 sumoylation in the regulation of p53- and NF-κB-dependent target gene expression

HDACs crucially control central cell signaling pathways by modulating the acetylation patterns of their histone and non-histone target proteins (Müller and Krämer 2010). Albeit the given structural homology of over 80% and the comparable catalytic mechanism of HDAC1 and HDAC2 (Montgomery et al. 2007), HDAC2 has furthermore been shown to possess exclusive, isoenzyme specific functions (Krämer 2009). The specific regulation of synaptic plasticity and memory function by HDAC2 (Guan et al. 2009), the pivotal role of HDAC2 in controlling murine brain development (Hagelkruys et al. 2014), and the presence of nonredundant functions of HDAC1 and HDAC2 in cell proliferation and tumor development (Jurkin et al. 2011) support a tissue- or cell type-dependent grade of functional redundancy between HDAC1 and HDAC2. However solely a combined loss of HDAC1 and HDAC2 activity is sufficient to provoke phenotypic deviations in cardiomyocytes, neuron precursors, oligodendrocytes, B cells, embryonic epidermis, and T cells (Ma and Schultz 2016). This phenomenon is consistent with a commonly reported, concurrent, and compensatory upregulation of the respective HDAC paralogue in HDAC1 or HDAC2 knockout or knockdown systems that masks the depleted phenotype (Moser et al. 2014; Göder et al. 2018; Kiweler et al. 2018). Nevertheless, as elevated HDAC2 expression levels have been implied as independent markers of dismal prognosis in diverse cancer types (Krämer 2009; Wagner et al. 2014), it is of crucial importance to specifically exploit HDAC2-dependent signaling pathways in tumor biology. HDAC2 is ubiquitously expressed, predominantly localized in the cellular nucleus, and comprises four functionally active domains that are partially common to other HDAC enzymes (Ma and Schultz 2016). N-terminally located is a HDAC association domain (HAD; green), that is crucial for homo- and heterodimerization of HDACs (**Figure 4**). The histone deacetylase domain (blue) includes more than 300 amino acids and is commonly transcribed in all class I HDACs to convey catalytic enzyme activity (**Figure 4**). A further domain contains an IACDE amino acid motif (yellow), that is essential for HDAC2 interaction with the pocket protein or retinoblastoma protein family members Rb, P107, and P130 (**Figure 4**). Furthermore, the HDAC2 protein contains a coiled coil domain (orange) at its C-terminus that potentially enables specific protein-protein associations (**Figure 4**). Additionally, a variety of PTMs of amino acid residues in the polypeptide chain of HDAC2 is described (**Figure 4**). These PTMs of HDAC2 include the addition of chemical moieties through nitrosylation or phosphorylation at the indicated tyrosine, cysteine, and serine residues as well as the covalent attachment of small ubiquitin-like modifier (SUMO) proteins to lysine 462 in the protein’s coiled coil domain (**Figure 4**). This

C-terminal lysine residue is embedded in a typical ΨKXE sumoylation consensus motif (..VK^{462}EE.. for HDAC2) (Brandl et al. 2012). Sumoylation of HDAC2 is likely dependent on a cascade comprising the enzymatic activity of an E1-activiating enzyme (SAE1/2), an E2 SUMO-conjugase (UBC9), and an E3 SUMO-ligase (Brandl et al. 2012).

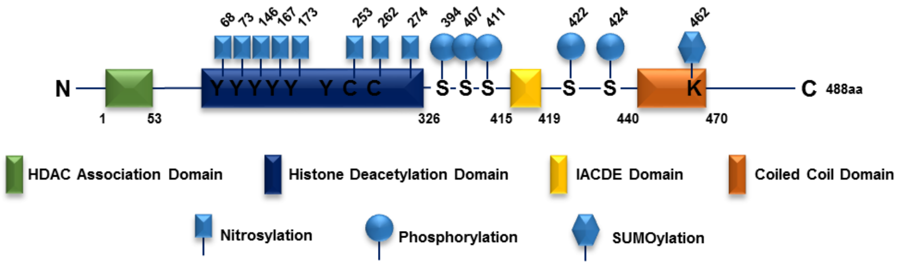

Figure 4: HDAC2 structure and posttranslational modifications. The four functional domains of HDAC2 are depicted along with the protein's numerous posttranslational modifications. Further details are given in the text. Figure is modified according to (Ma and Schultz 2016).

Using a CRC cell system that either recombinantly expresses wild-type HDAC2 (HDAC2^{wt}) or a sumoylation-deficient mutant of HDAC2, our group demonstrated the crucial significance of HDAC2 sumoylation for p53 and NF-κB activation and target gene expression (Brandl et al. 2012; Wagner et al. 2015). Elimination of HDAC2 sumoylation was achieved through charge-conserving mutation of the lysine residue at position 462 to arginine (HDAC2^{K462R}). Using this system, it has been demonstrated that HDAC2 sumoylation is essential for the interaction of HDAC2 with p53 and subsequent deacetylation of p53 at lysine 320 (K320) (Brandl et al. 2012). Acetylation of p53 at this lysine residue, that is located in the tetramerization domain of p53, is conferred by the HAT KAT2B/PCAF and induced upon DNA damage to regulate the DNA binding capability and transcriptional activity of p53 (Kruse and Gu 2008). Diminished acetylation of p53 at K320 reduces its DNA binding affinity and impairs consecutive transcriptional regulation of p53 target genes (Brandl et al. 2012; Wagner et al. 2014). Congruently, basal transcription and protein expression of the proapoptotic p53 target genes BCL-2 associated X (BAX), p21, and p53-inducible gene 3 (PIG3) as well as of the cell cycle inhibitor p21 are diminished in the presence of wild-type HDAC2 (Brandl et al. 2012) (**Figure 5**). Simultaneously, p53 mediated suppression of the apoptosis inhibitor survivin is disabled, which results in heightened survivin protein expression (**Figure 5**). In contrast, HDAC2 and p53 interaction is impeded in CRC cells expressing the sumoylation-deficient HDAC2^{K462R} protein, which prohibits HDAC2 mediated p53 deacetylation and in turn leads to augmented p53-dependent proapoptotic gene expression (**Figure 5**). In summary, the site-specific sumoylation of HDAC2 determines its deacetylase activity for p53 at K320 and represents a crucial posttranslational switch guarding p53 activity and p53-dependent gene expression. Furthermore, HDAC2 sumoylation controls the expression of antiapoptotic NF-κB target genes in a p53 and ribosomal S6 kinase 1 (RIPK1)- dependent manner (Wagner et al. 2015) (**Figure**

5). This induction of NF-κB-dependent gene expression results in the augmented concentration of cytoplasmic, antiapoptotic B-cell lymphoma-extra-large (BCL-X_L) and survivin as well as in the enhanced nuclear concentration of NF-κB in cells expressing wild-type HDAC2 (**Figure 5**). Sumoylation-deficient HDAC2, on the other hand, does not influence NF-κB-dependent gene expression. Consequently, cells expressing wild-type HDAC2 display a reduced basal susceptibility for apoptotic stimuli and augmented stress resistance when compared with cells expressing sumoylation-deficient HDAC2^{K462R} (Brandl et al. 2012; Wagner et al. 2015). Hence, site specific HDAC2 sumoylation ultimately provides a regulatory mechanism of central cell death decisions in the presence of genotoxic stress due to changes in basal expression of crucial apoptosis and cell cycle regulatory proteins. In general, as HDAC2 sumoylation is lost upon prolonged genotoxic damage, subsequent upregulation of p53 acetylation and p53-dependent proapoptotic gene expression also allows for a functional cell death response in the presence of wild-type HDAC2 (Brandl et al. 2012).

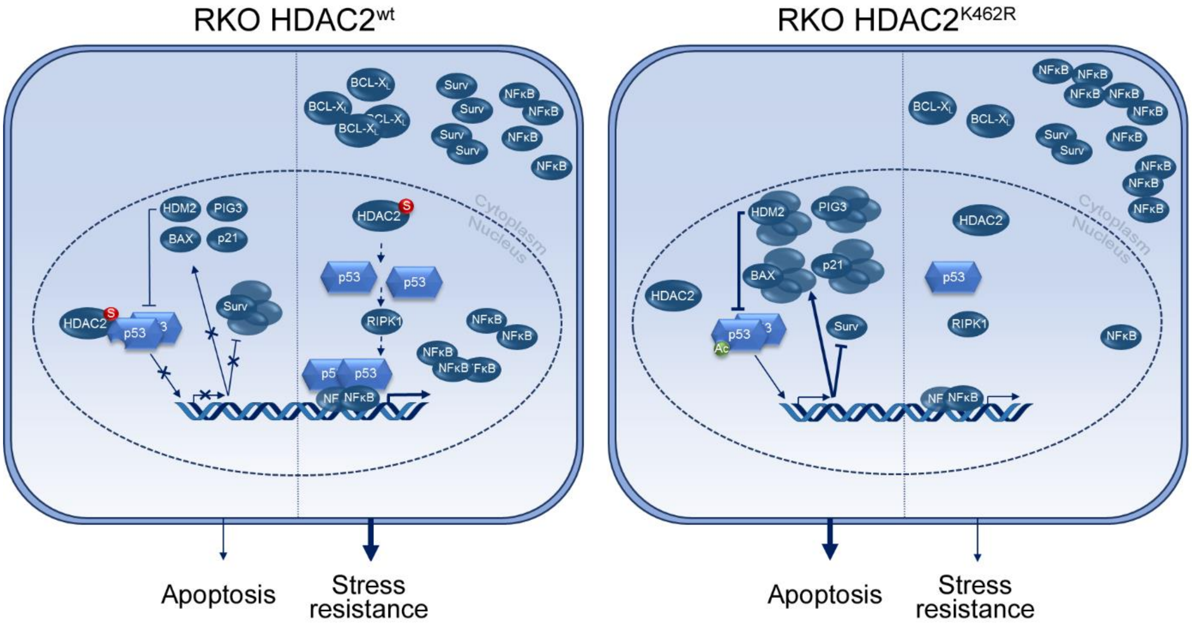

Figure 5: HDAC2 sumoylation in the regulation of p53 and NF-κB transcriptional activity. Catalytically active, sumoylatable HDAC2 in RKO HDAC2^{wt} cells inactivates p53 and p53-dependent gene expression through deacetylation of p53 at K320, thereby reducing the expression of proapoptotic factors (BAX, PIG3), the cell cycle inhibitor p21, and the E3 ubiquitin-ligase HDM2 and preventing p53 mediated suppression of antiapoptotic survivin (Surv). Furthermore, HDAC2 sumoylation triggers NF-κB mediated antiapoptotic gene expression in a p53- and RIPK1-dependent manner, which results in the heightened expression of BCL-XL and Surv and in the enhanced nuclear localization of NFκB. In contrast, in sumoylation-deficient RKO HDAC2^{K462R} cells, p53 remains acetylated due to reduced binding activity of HDAC2 for p53 and, subsequently, expression of proapoptotic and cell cycle inhibitory target genes is enhanced. Antiapoptotic NF-κB target gene expression and nuclear NF-κB expression is diminished. Hence, RKO HDAC2^{K462R} cells display augmented susceptibility for apoptotic cell death and low stress resistance compared to RKO HDAC2^{wt} cells. Figure is modified according to (Brandl et al. 2012; Wagner et al. 2015).

1.4 Epithelial-mesenchymal transition

During the reversible cellular program of EMT, the transitioning cells abandon their cell-cell and cell-matrix interactions, lose their apical-basal polarity, reorganize their cytoskeleton and initiate a new transcriptional program that impels them to adopt mesenchymal cell fate (Lamouille et al. 2014). The process of EMT involves a series of dynamic transitional states between the epithelial and mesenchymal phenotype. It can thus be rather seen as a continuous spectrum of slight, reversible changes occurring in the cellular phenotype than a black-and-white decision between epithelial and mesenchymal phenotype (Nieto et al. 2016; Dongre and Weinberg 2018). The reverse process of EMT, the mesenchymal-epithelial transition (MET) is contrarily associated with a loss of migratory freedom and a regain of apical-basal polarization in subjected cells (Nieto et al. 2016). Cellular EMT is essential during tissue development in embryogenesis, during wound healing in response to injuries, and during cellular transformation in neoplastic cells (Dongre and Weinberg 2018). Especially during tumor progression, EMT conveys a multitude of traits specifically associated with dismal, high-grade malignancy (Dongre and Weinberg 2018). These include tumor-initiating abilities, increased motility, the capacity to disseminate, and an augmented resistance to cell death programs elicited by commonly applied chemotherapeutics (Dongre and Weinberg 2018). Additionally, it has been demonstrated that ongoing EMT can generate cells that demonstrate stem cell properties and as a result obtain essential survival characteristics for dissemination and metastasis alongside, such as apoptosis resistance, transient quiescence, and the ability of self-renewal (Mani et al. 2008; Morel et al. 2008; Brabletz 2012). EMT initiation in cancer cells (type III EMT) is most often conferred by signals derived from the tumor-associated stroma that trigger intracellular signaling pathways, which in turn eventually result in the induction of expression of EMT associated TFs (Dongre and Weinberg 2018). Extracellular signals that intracellularly activate EMT-TFs include fibroblast growth factors (FGF), hepatocyte growth factor (HGF), platelet-derived growth factor (PDGF), cyclooxygenase 2 (COX2), estrogens, hypoxia, bile acids, nicotine, ultraviolet (UV) radiation, integrins, Wnt, transforming growth factor β (TGF-β), interleukin-6 (IL6), sonic hedgehog (Shh), bone morphogenetic protein (BMP), stem cell factor (SCF), and epidermal growth factor (EGF) (Thiery et al. 2009). Upon induction, EMT-specific TFs orchestrate the expression and activation of further key players of the EMT program (Dongre and Weinberg 2018). The classic, core EMT TFs are Snail Family Transcriptional Repressor 1 (SNAI1; or SNAIL), Snail Family Transcriptional Repressor 2 (SNAI2; or SLUG), Twist Family BHLH Transcription Factor 1 (TWIST1), Twist Family BHLH Transcription Factor 2 (TWIST2), Zinc Finger E-Box Binding Homeobox 1 (ZEB1), and Zinc finger E-box-binding homeobox 2 (ZEB2). On the one hand, these EMT-TFs govern their respective expression and on the other hand, they coordinate, in different combinations, the enhanced expression of hundreds of mesenchymal genes as well as the concurrent downregulation of epithelial genes (Peinado et al. 2007; Craene and Berx 2013; Dongre and Weinberg 2018). Owing to the high complexity and seemingly cancer cell type specific consequences of this TF signaling, the ensuing mechanisms are rarely exhaustively elucidated. Nevertheless, it is for instance described that SNAI1 suppresses the cell adhesion molecule E-cadherin in epithelial cells by recruitment of a repressive complex to the respective gene promoter (Batlle et al. 2000; Cano et al. 2000). Furthermore, in epithelial cells, SNAI1 enhances the expression of matrix-metalloproteinases (MMPs), which degrade a wide variety of extracellular matrix proteins and are thus actively involved in tissue remodeling during EMT (Jorda et al. 2005). ZEB1 suppresses E-Cadherin expression and concomitantly enhances expression of the mesenchymal structural protein vimentin (Sanchez-Tillo et al. 2010). TWIST1 activation by different stimuli such as hypoxia related HIF-1α results in the repression of E-cadherin while concurrently enhancing N-cadherin expression (Lamouille et al. 2014). Interestingly, ZEB1 expression is enhanced by SNAI1 activation in a TWIST1-dependent manner, as SNAI1 can directly target and activate the *ZEB1* gene (Dave et al. 2011). These are just a limited number of examples for reported EMT-TF regulated gene expression. A comprehensive review and overview of further EMT-TF functions and the plethora of their direct targets genes is given in (Lamouille et al. 2014) and (Craene and Berx 2013). Multiple studies showed that abrogation of the expression of a single EMT-TF can suffice to partly or completely prevent EMT potentially due to the loss of antiapoptotic signaling or the reduction of stem cell properties (Craene and Berx 2013). Moreover, growing evidence suggests that the cellular EMT program is additionally governed and convoluted by regulatory layers of small non-coding RNAs, the mechanism of alternative pre-mRNA splicing, and PTMs (Craene and Berx 2013). Collectedly, the analysis of these multiplex signaling pathways has led to the identification of a collection of biomarkers that serve to reliably identify EMT progression *in vitro* and *in vivo* (Zeisberg and Neilson 2009). For type III EMT in cancer cells, biomarkers include changes in cell surface markers (e.g. E-cadherin, ZO-1, integrins, OB-cadherin), cytoskeletal markers (e.g. cytokeratin, FSP1, β-catenin), extracellular matrix proteins (e.g. collagens, laminin1), EMT-TFs (e.g. SNAI1/SNAI2, TWIST1/2, ZEB1/2, LEF-1), and microRNAs (miR-21) (Zeisberg and Neilson 2009).

1.4.1 Influence of HDACs and HDACi on EMT

Prior to the implication of non-coding RNAs, alternative splicing mechanisms, and PTMs in regulatory pathways of EMT, the six central TFs SNAI1/2, TWIST1/2, and ZEB1/2 were described as key regulators of EMT signaling. One of the main reasons for the central standing of these EMT-TFs might be their functional interplay with diverse epigenetic modifiers that ensures the regulatory induction of significant large-scale alterations of gene expression (Craene and Berx 2013). This EMT-TF-associated epigenetic reprogramming during EMT includes DNA methyltransferases (DNMT1), histone demethylases (LSD1) and methyltransferases (EZH2, SUZ12, SUV39H1), chromatin remodelers (BRG1), Polycomb group proteins (BMI1), and most interestingly also the class I HDACs HDAC1, HDAC2, and HDAC3 as well as sirtuin 1 (SIRT1) (Craene and Berx 2013). SNAI1 does for instance mediate the introduction of repressive histone modifications at the Cadherin 1 (*CDH1*) promotor (coding for E-cadherin) through association with HDAC1 and HDAC2 (Peinado et al. 2004). In addition, in EMT under hypoxic conditions, HDAC3 is induced by HIF-1α and subsequently recruited to the promotors of *CDH1* and plakoglobin to repress gene expression corporately with SNAI1 (Wu et al. 2011). Apart from that, HDAC3 also interacts with hypoxia-induced WD repeat-containing protein 5 (WDR5) and its associated histone methyltransferase complex to enhance histone methylation in the promoters of genes encoding for the mesenchymal marker proteins N-cadherin and vimentin to enhance their respective expression (Wu et al. 2011). Ultimately, the NAD^+-dependent deacetylase SIRT1 cooperates with the EMT-TF ZEB1 to deacetylate histones in the *CDH1* promotor and reduce binding of RNA polymerase II (Byles et al. 2012). Given these intricate interactions between histone deacetylases and key EMT-TFs, it is unsurprising that diverse publications report a crucial regulation of EMT signaling in response to the inhibition of HDACs by various HDACi. However, the existing data are ambiguous as the various reports state, partially in direct contradiction, that HDACi either promote or abrogate EMT progression. For instance, in triple-negative breast carcinoma, the pan-HDACi LBH589 reduces ZEB1 and ZEB2 expression (Rhodes et al. 2014). Furthermore, it has been shown that HDAC2 activity is specifically necessary for tumor growth and metastasis of breast cancer cells, as expression of ZEB1 and ZEB2 is downregulated by the microRNA miR-200, whose expression is in turn negatively controlled by proline, glutamic acid and leucine rich protein 1 (PELP1) in a HDAC2-dependent manner (Roy et al. 2014). Fittingly, LBH589, VPA, and MS-275 treatment abrogates metastatic behavior of breast cancer cells (Göttlicher et al. 2001; Blaheta et al. 2005; Srivastava et al. 2010; Rhodes et al. 2014; Schech et al. 2015). In addition, class I HDAC inhibition by mocetinostat, MS-275, and the benzamide derivative CI994 is sufficient to partially revert EMT and restore E-cadherin expression in ovarian, pancreatic, and bladder cancer cells (Tang et al. 2016). A long non-coding RNA (*GAS5-AS1*), that represses the expression of mesenchymal marker proteins and EMT-TFs and thereby reduces cell migration, is induced by pan-HDACi treatment (LBH589, SAHA) in non-small-cell lung cancer (NSCLC) cells (Wu et al. 2016b). In lung cancer cells, the HDACi trichostatin A (TSA) antagonizes E-cadherin suppression that is mediated by the joined activity of the Groucho transcriptional corepressor TLE1 and HDAC1 (Yao et al. 2014). EMT and stem cell characteristics of castration-resistant prostate cancer cells are impaired by treatment with LBH589 (Ruscetti et al. 2016). Likely, mocetinostat downregulates ZEB1 by restoring miR-203 expression and thus induces drug sensitivity while reducing stem cell characteristics in pancreatic cancer cells (Meidhof et al. 2015). In sharp contrast to these data that clearly position HDACi as a treatment opportunity to reduce EMT and metastasis formation in multiple cancer types, others report EMT promoting effects mediated by HDACi treatment. For instance, HDACi treatment is described to result in the induction of specific morphologic changes in various cancer cell types, which include the loss of cell-cell interactions and apical-basal polarity and which were thus attributed to the general evolution of a mesenchymal phenotype (Hoshikawa et al. 1994b; Byler et al. 2012; Kong et al. 2012; Jeon et al. 2013; Cabanel et al. 2015; Ma et al. 2015; Wang et al. 2016; Wang et al. 2018). In addition, activity of the estrogen ligated ERα-HDAC1 corepressor complex inhibits the promotor of SNAI2, increases E-cadherin expression, and reduces migratory properties of breast cancer cell lines (Ye et al. 2010). Furthermore, treatment with the HDACi SAHA negatively regulates E-cadherin and positively regulates N-cadherin, vimentin, and fibronectin expression dependent on HDAC8 and downregulation of the transcription factor FOXA1 in triple negative breast cancer patients (Wu et al. 2016a). The HDACi SAHA and sodium butyrate (NaB) were shown to trigger a fibroblast-related morphology, the upregulation of SNAI1 and vimentin as well as the downregulation of E-cadherin in epithelial head and neck, liver, and colon cancer cell lines. These effects were primarily conveyed due to the modulation of PTMs in SNAI1 in response to HDACi treatment (Jiang et al. 2013). Finally, the HDACi TSA induces morphologic changes, vimentin expression, and invasiveness in head and neck cancer cells while paradoxically downregulating clonogenic sphere formation and reducing the number of cancer stem cells (Giudice et al. 2013). In conclusion, these overall contradictory findings regarding the general and specific effects of HDACi on EMT progression indicate a cancer cell type specific or even cell line dependent regulation of EMT and are a sign of the high degree of intricacy of the associated, incompletely elucidated signaling pathways.

1.5 Damage mechanisms of applied toxic stimuli

1.5.1 Damage mechanisms of fluoropyrimidines

Fluoropyrimidines are categorized as antimetabolite drugs. They exert their cytotoxic effects by impeding essential metabolic processes through inhibition of enzyme activity and by distorting regular DNA and RNA function through incorporation into these macromolecules. Wide-spread chemotherapeutic application of the most prominent fluoropyrimidine 5-FU is based on an observation that was made in the 1950s by Rutman and colleagues. They found that rat hepatomas employed the C^{14}-labeled pyrimidine base uracil more readily for nucleic acid biosynthesis than cells of normal tissue and thereby identified uracil metabolism as potential drug target (Rutman et al. 1954; Longley et al. 2003). Shortly thereafter, 5-FU was synthesized and introduced in the clinics (Duschinsky et al. 1957; Heidelberger et al. 1957). It remained to this date a mainstay in the standard treatment of colorectal, breast, and aerodigestive cancers (Longley et al. 2003). Additionally, a carbamate of 5-FU, N4-pentyloxycarbonyl-5'-deoxy-5-fluorocytidine or capecitabine, is administered routinely as 5-FU prodrug. Apart from its oral applicability, capecitabine displays heightened presence in tumor tissue as its metabolic activation relays on the conversion by cytidine deaminase and thymidine phosphorylase (TP), which are predominantly active in tumor tissue (Malet-Martino et al. 2002). It has been shown that the hepatic dihydropyrimidine dehydrogenase (DPD) rapidly eliminates over 80% of intravenously administered and capecitabine-derived 5-FU by reduction to dihydrofluorouracil (DHFU) (Malet-Martino et al. 2002; Longley et al. 2003). DHFU is further processed to fluoroureidopropanic acid and fluoro-β-alanine and urinary excreted (Heggie et al. 1987).

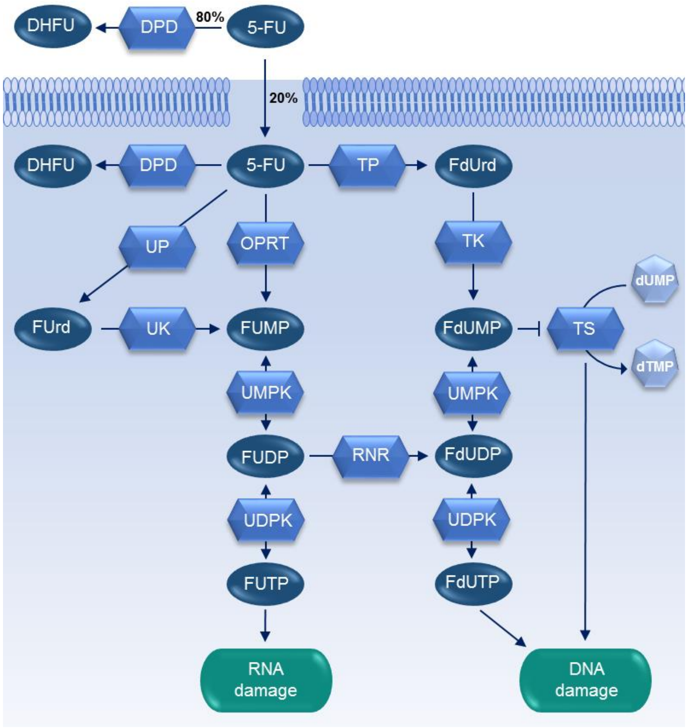

Figure 6: Metabolism of 5-fluorouracil. Over 80% of administered 5-FU is deactivated in the liver by dihydropyrimidine dehydrogenase (DPD) to dihyrofluorouracil (DHFU). Subsequently, around 20% of 5-FU is intracellularly converted to active metabolites. Specific description of the respective metabolic pathways is provided within the text. Enzymes: orotate phosphoribosyltransferase (OPRT), uridine phosphorylase (UP), uridine kinase (UK), uridine monophosphate kinase (UMPK), uridine diphosphate kinase (UDPK), thymidine phosphorylase (TP), thymidine kinase (TK), ribonucleotide reductase (RNR), thymidylate synthase (TS). Metabolites: fluorouridine (FUrd), fluorouridine monophosphate (FUMP), fluorouridine diphosphate (FUDP), fluorouridine triphosphate (FUTP), fluorodeoxyuridine (FdUrd), fluorodeoxyuridine monophosphate (FdUMP), fluorodeoxyuridine diphosphate (FdUDP), fluorodeoxyuridine triphosphate (FdUTP), deoxyuridine monophosphate (dUMP), deoxythymidine monophosphate (dTMP). Modified according to (Longley et al. 2003).

Intracellular, anabolic activation of 5-FU is divided in various parallel reactions (**Figure 6**). 5-FU can, on the one hand, be directly converted to fluorouridine monophosphate (FUMP) through the action of orotate phosphoribosyltransferase (OPRT) and its cofactor phosphoribosyl pyrophosphate (PRPP). On the other hand, FUMP can be indirectly generated via a first conversion to fluorouridine (FUrd) by uridine phosphorylase (UP) and a sequential phosphorylation by uridine kinase (UK). Downstream, FUMP is phosphorylated to fluorouridine diphosphate (FUDP) by uridine monophosphate kinase (UMPK), which can then be either phosphorylated to fluorouridine triphosphate (FUTP) by uridine diphosphate kinase (UDPK) or dehydroxylated to fluorodeoxyuridine diphosphate (FdUDP) by ribonucleotide reductases (RNR). The active metabolite FUTP is extensively integrated into cellular RNA as a substitute for uridine triphosphate (UTP) and hampers RNA function on multiple levels by disturbance of ribosomal RNA (rRNA) maturation, post-transcriptional modification of transfer RNAs (tRNAs), pre-mRNA splicing, pseudouridine generation and polyadenylation of mRNA (Longley et al. 2003). Furthermore, FdUDP can either be phosphorylated to fluorodeoxyuridine triphosphate (FdUTP) by a UDPK or dephosphorylated to fluorodeoxyuridine monophosphate (FdUMP) by UMPK. FdUTP represents a substrate for DNA polymerases and can thus be incorporated into DNA as a substitute of deoxythymidine triphosphate (dTTP). Moreover, the metabolite FdUMP is an inhibitor of the crucial enzyme thymidylate synthase (TS) through formation of a stable ternary complex TS* with TS and its cofactor and methyl donor 5,10-methylenetetrahydrofolate (CH_2THF) (**Figure 7B**). Free TS catalyzes the reductive methylation of deoxyuridine monophosphate (dUMP) to deoxythymidine monophosphate (dTMP) and thereby exclusively provides *de novo* synthesized thymidylate for DNA synthesis (**Figure 7A**).

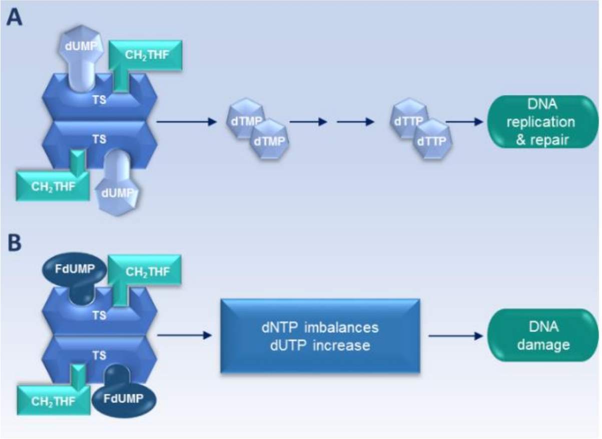

Figure 7: Thymidylate synthase inhibition by 5-fluorouracil. (**A**) TS catalyzes the reductive methylation of dUMP to dTMP in the presence of 5,10-methylene tetrahydrofolate (CH_2THF) as methyl donor. (**B**) FdUMP binds TS and blocks dUMP binding and conversion to dTMP. Consequently, deoxynucleosidtriphosphate (dNTP) imbalances and increased concentration of deoxyuridine triphosphate (dUTP) result in DNA damage. For specific descpriptions see text. Modified according to (Longley et al. 2003).

The TS inhibitor FdUMP is additionally derived by a secondary pathway through the phosphorylation of 5-FU by TP and subsequent phosphorylation of the resulting fluorodeoxyuridine (FdUrd) by thymidine kinase (TK). As a result of TS inhibition, dTMP and its downstream derivative dTTP are depleted. dTTP integration into DNA by DNA polymerases is abolished. Furthermore, reduction of dTTP concentration results in an imbalance of the overall deoxyribonucleotide pool as dTTP, deoxyadenosine triphosphate (dATP), deoxyguanosine triphosphate (dGTP), and deoxycytidine triphosphate (dCTP) abundance is crucially regulated by feedback mechanisms (Longley et al. 2003). Moreover, absent conversion of dUMP to dTMP ultimately results in the upregulation of nuclear deoxyuridine triphosphate (dUTP) concentration. Consequently, dUTP as well as dFUTP are increasingly misincorporated into DNA and subsequently trigger DNA damage recognition and associated repair mechanisms. As dUTP and dFUTP represent inappropriate bases in DNA molecules, they are readily recognized and excised by MMR and base excision repair (BER) pathways to prevent cytotoxic damage. However, as DNA resynthesis is required after effective base excision, repair mechanisms are unsuccessful because repetitive misincorporations are predestined in the presence of high dUTP and dFUTP and low dTTP concentrations (Longley et al. 2003; Wyatt and Wilson 2009). Such futile cycling of the repair machinery for misincorporated bases results in unrepaired intermediates that summon further mechanisms like homologous recombination (HR) repair to cope with the DNA damage (Wyatt and Wilson 2009). In summary, 5-FU exerts its cytotoxic effects through three metabolites that interfere with a plethora of central cellular mechanisms as a result of efficient RNA integration (FUTP), DNA integration (FdUTP), and TS inhibition (FdUMP). To further enhance this cellular toxicity, 5-FU has been combined with different compounds that modulate 5-FU degradation and TS inhibition. For instance, as described in **1.1.2**, 5-FU is combined with 5′-formyltetrahydrofolate (Leucovorin) to increase cellular tetrahydrofolate concentration and consequently improve TS inhibition (Longley et al. 2003). Furthermore, inhibition of DPD to reduce catabolic elimination of 5-FU is accomplished through combinatorial treatment with uracil and eniluracil (Longley et al. 2003).

1.5.2 Damage mechanisms of chloroethylating agents

Chloroethylating agents belong to the chemical group of nitrosoureas and are thus also termed chloroethyl nitrosoureas (CNU). Due to their capability to cross the blood-brain barrier, they are widely applied in the treatment of brain tumors and malignant melanomas (Nikolova et al. 2017b). CNUs are decomposed under physiological conditions to chloroethyl diazohydroxide and organic isocyanate (**Figure 8A**). Subsequent elimination of molecular nitrogen and hydroxide generates a reactive chloroethyl carbonium ion (**Figure 8A**). This chloroethyl carbonium ion alkylates guanine at the N7-, and the O^6-position to form N7-chloroethylguanine and O^6-chloroethylguanine (O^6-ClEtG) (**Figure 8B**). Intramolecular rearrangement of the unstable O^6-ClEtG yields the intermediate N1-O^6-ethanoguanine (**Figure 8B**). N1-O^6-ethanoguanine covalently binds to a cytosine in the complementary DNA strand and consequently generates a stable N1-guanine-N3-cytosine interstrand crosslink (ICL) (**Figure 8C**) (Nikolova et al. 2017b). Although O^6-ClEtG and the subsequently formed ICLs only represent a minority of all adducts formed upon CNU treatment, cytotoxicity is clearly associated with the extent of ICL formation (Wiencke and Wiemels 1995). Studies estimate that as few as 20 to 40 ICLs can be lethal for mammalian cells (Lawley and Phillips 1996). Toxicity of ICLs is based on the blockage of strand separation during replication and transcription and subsequent activation of DNA damage response and cell death pathways (Nikolova et al. 2017a). Around nine different CNUs are currently applied in clinical routine or in clinical trials (Zhao et al. 2014). Chemical composition of these agents was modified by the addition of varying residues at the N3 atom of the nitrosourea basic structure to enhance antineoplastic ability or to lower general toxicity (Zhao et al. 2014). Chemical composition of the three classic and most frequently used CNUs nimustine (ACNU), carmustine (BCNU), and lomustine (CCNU) is shown in **Figure 8D**.

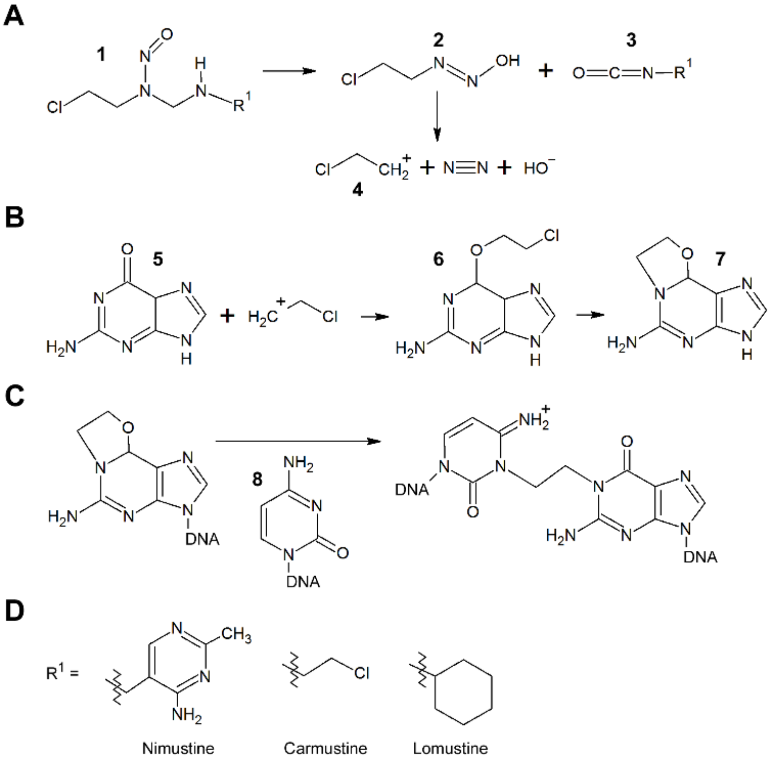

Figure 8: Nitrosourea induced chloroethylation of guanine and ICL formation. (A) Generation of the reactive carbonium ion. (**1**) chloroethyl nitrosoureas, (**2**) chloroethyl diazohydroxide, (**3**) organic isocyanate, (**4**) chloroethyl carbonium ion. (B) Guanine adduct formation. (**5**) guanine, (**6**) O^6-chloroethylguanine, (**7**) N1, O^6-ethanoguanine. (C) ICL formation. (**8**) cytosine. (D) Chemical nature of the R1 residue defines the different clinically applied chloroethyl nitrosoureas nimustine (ACNU), carmustine (BCNU), and lomustine (CCNU). Specific description of the reaction mechanisms is provided within the text.

ICL formation can be abrogated through direct repair of O^6-ClEtG adducts by the suicide repair enzyme O^6-methylguanine-DNA methyltransferase (MGMT) (Robins et al. 1983). MGMT directly transfers the added alkyl group to its hydrophobic pocket and thereby restores unmodified guanine. This repair pathway is stochiometric and results in the inactivation and proteasomal degradation of MGMT. Hence, basal MGMT expression and synthesis rate crucially define the sensitivity of tumor cells for CNU treatment. To circumvent this resistance mechanism, MGMT activity can be abrogated by the addition of suitable pseudosubstrates like *O*^{6}-benzylguanine (O^{6}BG) that exhaust cellular MGMT stock (Nikolova et al. 2017b). Should this primary O^6-ClEtG adduct not be removed by MGMT, the resulting ICL stalls DNA strand separation during transcription and replication and results in a complex sequence of repair mechanisms that may additionally generate toxic repair intermediates such as double strand breaks (DSBs). These mechanisms include Fanconi anemia (FA) proteins, nucleotide expression repair (NER), translesion synthesis (TLS), and HR repair (Nikolova et al. 2017a).

1.5.3 Damage mechanisms of ionizing radiation

During clinical ionizing radiation (IR) therapy and under experimental, laboratory conditions mainly one subtype of IR, the highly energetic γ-radiation, is applied. γ-radiation is electromagnetic radiation that consists of uncharged photons that are generated during radioactive decay of for instance ^{60}Co or ^{137}Cs (Council 2006). The induced energy dose of IR is measured using the unit Gray (Gy) with 1 Gy equaling the energy of 1 Joule/kg. Cellular damage and toxicity upon IR can be categorized into direct and indirect effects. Indirect damage is mainly mediated through the radiolysis of intracellular water molecules that leads to an extensive generation of highly reactive, free radical species. These free radicals induce oxidative, cellular damage through the reaction with DNA, proteins and lipids (Azzam et al. 2012). Furthermore, IR damages cellular DNA through direct collision and subsequent ionization as well as the breakage of the DNA-sugar-phosphate backbone. In summary, a dose of 1 Gy IR is sufficient to induce around 850 pyrimidine and 450 purine base lesions, 1.000 DNA single strand breaks (SSB), and 20 – 40 DNA DSB in a single mammalian cell (Lomax et al. 2013). Against a background of around 50.000 DNA lesions that are daily induced by reactive oxygen species (ROS) in a single cell, these numbers seem minor (Swenberg et al. 2011). However, due to their concurrent induction, these IR-mediated DNA lesions do have toxic, if not lethal, cellular effects. Herein, induction of DSBs entails the highest toxicity when compared to other induced lesions such as 8-oxoguanine, thymineglycol, and SSBs (Ward 1988; Lomax et al. 2013). To cope with this damage, the DNA damage response and cell cycle checkpoints are activated, DNA lesions are recognized and, dependent on their nature, either repaired by non-homologous end joining (NHEJ), HR, or BER (Lomax et al. 2013). Dependent on the extent of DNA damage, the cell either efficiently repairs the lesions or, if the damage exceeds repair capacity, triggers cell death programs. However, upon defects in crucial repair pathways, insufficient damage repair might furthermore provoke mutations and carcinogenesis (Jackson and Bartek 2009; Lomax et al. 2013).

1.6 DNA damage response and repair pathways

Damage to cellular DNA can be elicited by a broad variety of endogenous and exogenous noxae. Endogenous DNA damaging agents mainly constitute ROS, that are naturally generated in metabolically active cells and induce oxidative DNA damage such as hydroxylation of DNA bases, fragmentation of purine structure, DNA adduct formation with peroxidized lipids, and SSB formation in the DNA backbone (Chatterjee and Walker 2017). Further sources of endogenous DNA damage include base substitutions, single base insertions, and deletion errors that occur in the course of erroneous DNA replication through low fidelity replicative DNA polymerases (Chatterjee and Walker 2017). Finally, spontaneously occurring base deamination predominantly in single-stranded DNA (ssDNA) regions during active transcription, replication, and recombination as well as the formation of AP sites through spontaneous hydrolyzation of the DNA sugar phosphate backbone and the undesirable methylation of DNA bases through for instance the metabolic methyl donor s-adenosylmethionine (SAM) pose further mechanisms for the generation of potentially mutagenic, endogenous DNA damaging lesions (Chatterjee and Walker 2017). Exogenous DNA damage can either be provoked through ionizing (IR) or UV radiation or result from the exposure to a wide variety of chemical agents. DNA damage by IR can be summarized to base on a combination of the effects of a massive generation of ROS and the direct consequences of energy transfer to the chemical structure of DNA and has been extensively described in **1.5.3**. UV radiation, on the other hand, primary damages DNA by introducing bulky lesions in the form of covalently linked pyrimidines dimers (Chatterjee and Walker 2017). DNA damaging chemical agents with various mechanisms of action are widely applied in chemotherapy to exploit repair and cell cycle checkpoint deficiencies in fast growing tumor cells. These include alkylating agents that either introduce base alkylations or produce interstrand, intrastrand, or DNA protein crosslinks depending on their chemical nature (for chloroethylating agents see **1.5.2**). Diverse platinum drugs such as cisplatin, carboplatin, or oxaliplatin do induce monofunctional DNA adducts and cause DNA crosslinks similar to alkylating agents. Antimetabolites such as 5-FU do misincorporate into DNA and RNA and deprive the dNTP pool (see **1.5.1**). Topoisomerase inhibitors such as camptothecin and etoposide trap topoisomerase enzymes in complex with DNA and result in DNA SSBs and DSBs (Swift and Golsteyn 2014). This plethora of distinctively shaped DNA damage is repaired lesion-specific by five leading DNA repair pathways: BER, nucleotide excision repair (NER), HR, NHEJ, and MMR. These repair pathways are active throughout different phases of the cell cycle and are specialized to repair various but defined DNA damaging lesions (Roos et al. 2015). Selected base lesions such as O^6-methylguanine can additionally be repaired through direct chemical reversal by specifically equipped enzymes such as MGMT (Christmann et al. 2011). Should there exist no direct repair pathway for these simple base lesions, then they are repaired by

BER (Roos et al. 2015). Furthermore, repair of lesions such as ICL might depend on the orchestrated interplay of different repair pathways (see **1.6.4**) (Nikolova et al. 2017a). In general, base mismatches due to for instance deaminations or replication errors are repaired by MMR, whereas bulky DNA adducts such as cisplatin monoadducts or UV-induced pyrimidine dimers are subjected to NER (Roos et al. 2015). Highly cytotoxic DSBs, induced by IR or resulting from collapsed replication forks, are either repaired by NHEJ in G0/G1-phase or by HR in late S- and G2-phase in the presence of a homologous DNA template for high-fidelity repair (see **1.6.3**) (Chatterjee and Walker 2017). Throughout these repair mechanisms, DNA damage recognition and repair pathways are closely intertwined with pathways governing the induction of apoptosis, necrosis, senescence, and autophagy and jointly dictate cell death and survival decisions in response to DNA damage during tumorigenesis or genotoxic tumor therapy (Roos et al. 2015). Under optimal conditions this specialized network ensures that genomic instability is limited, cytotoxicity of unrepaired damage is mitigated, and neoplastic cell-killing is elevated to benefit survival of the entire organism. As DNA damage effects discussed during this work are mainly related to base mismatches, ICLs, DSBs, and base modifications, solely the key factors of the associated pathways of ICL repair, BER, NHEJ, and HR are described in further detail in the following. Closer description of the pathway of MMR is obviated as all relevant CRC cell lines in this work displayed deficiencies in the expression of central MMR proteins and were thus MMR-incompetent.

1.6.1 DNA damage recognition

Upon genotoxic stress, the resulting DNA damaging lesions are initially detected by the three central phosphoinositide 3-kinase (PI3K)-related kinases (PIKKs) Ataxia telangiectasia mutated (ATM), Ataxia telangiectasia- and Rad3-related (ATR), and DNA-dependent protein kinase (DNA-PK) (Blackford and Jackson 2017). To stably recruit to DNA damage sites, each kinase is dependent on a specific protein co-factor with a common C-terminal PIKK binding motif. ATM needs Nijmegen breakage syndrome 1 (NBS1), ATR needs ATR interacting protein (ATRIP), and DNA-PK needs Ku80 to successfully forward downstream signaling pathways that promote DNA repair induction, cell cycle arrest, transcriptional regulation, and cell death pathways (Blackford and Jackson 2017). Inactive, dimerized ATM is activated upon binding to NBS1, which is located in the MRE11-RAD50-NBS1 (MRN) complex at DSBs. Mechanistically, ATM activation is achieved through autophosphorylation at its serine residue 1981 (Ser1981) and subsequent monomerization (Awasthi et al. 2015). ATR is recruited via its binding partner ATRIP to extended sections of replication protein A (RPA)-coated ssDNA and its subsequent activation is associated with enhanced phosphorylation at its threonine residue 1989 (Thr1989) (Cimprich and Cortez 2008; Nam et al. 2011). These RPA-coated ssDNA segments may stem from resected DSBs or from helicase-polymerase uncoupling at stalled replication forks

(Blackford and Jackson 2017). On the other hand, DNA-PK primarily acts as a sensor of DSBs as is activated upon recruitment to DSB-bound Ku80 (Blackford and Jackson 2017). Hence, all three PIKKs are thought to be activated upon slightly divergent DNA lesions and to consequently promote the specific induction of different DNA repair pathways. However, in truth, ATM-, ATR-, and DNA-PK-dependent signaling pathways are intertwined, leading to a broad range of functional cross-talk between PIKKs (Blackford and Jackson 2017). For instance, ATM-dependent DNA-end resection of DSB in S- and G2/M-phase to promote HR additionally provides RPA-coated ssDNA as signal for ATR activation (Blackford and Jackson 2017). Moreover, ATM, ATR, and DNA-PK are able to phosphorylate each other and thereby modulate their respective activity (Stiff et al. 2006; Blackford and Jackson 2017; Zhou et al. 2017). Following this PIKK activation, DSBs and stalled replication forks are marked for subsequent localization of the respective repair machinery through a predominantly ATM- or ATR-mediated phosphorylation of the histone variant H2AX at serine residue 139 (γH2AX) (Burma et al. 2001; Ward and Chen 2001; Fernandez-Capetillo et al. 2004). γH2AX formation is observed in a megabase range adjoining both sides of the DSB and serves as a beacon to facilitate repair complex formation through enhancement of local repair factor concentration (Rogakou et al. 1998; Rogakou et al. 1999). In addition, activated ATM and ATR crucially induce phosphorylation of checkpoint kinase 1 (CHK1) and checkpoint kinase 2 (CHK2) which trigger DNA damage-dependent cell cycle arrest at specific cell cycle checkpoints (G1-S transition or G2-M transition) as a result of subsequent phosphorylation and degradation of cell division cycle phosphatase 25 (cdc25) (Mailand et al. 2000) or phosphorylation of p53 at serine 15 and successive induction of the CDK inhibitor p21 (Jabbur et al. 2000; Cazzalini et al. 2010). In summary, PIKKs do thus not only serve as primary sensors of DNA damage lesions but do furthermore stall cell cycle progression to allow sufficient time for DNA repair by lesions specific pathways and repair machineries.

1.6.2 Base excision repair

BER serves to repair base lesions that do not significantly distort the helical structure of DNA and are thus not recognized as bulky adducts by NER. In general, repair substrates for BER include oxidized, alkylated, and deaminated bases as well as AP sites and SSBs (Chatterjee and Walker 2017). Initial damage recognition and base removal by BER is conferred by specialized DNA glycosylases through hydrolysis of the *N*-glycosidic bond that anchored the damaged base to the DNA-sugar-phosphate backbone. Mammalian cells express 11 different glycosylases that can be subgrouped according to their enzymatic activity. Monofunctional, type I glycosylases like uracil *N*-glycosylase (UNG), MutY glycosylase homologue (MUTYH), single-strand-specific monofunctional uracil glycosylase 1 (SMUG), 3-alkyladenine DNA glycosylase (AAG), methyl-CpG binding domain protein (MBD4), and TDG solely possess glycosylase activity whereas bifunctional, type II glycosylases like 8-oxoguanine DNA glycosylase (OGG1), endonuclease III-like 1 (NTHL1), and endonuclease VIII-like 1, -2, and -3 (NEIL1, -2, -3) additionally display β-lyase activity (Bosshard et al. 2012). Accordingly, upon hydrolysis by monofunctional DNA glycosylases, an apurinic/apyrimidinic site (AP) site is generated in the DNA backbone that is subsequently processed through cleavage by apurinic/apyrimidinic endonuclease 1 (APE1) to generate a single nucleotide gap displaying a 3'-hydroxyl (OH) and a 5'-deoxyribose phosphate (5'-dRP) residue. The resulting strand break is filled by DNA polymerase (Pol) β by insertion of the first nucleotide to the 3' end of the lesion. Additional intrinsic 5'-dRP lyase activity of Polβ permits excision of the 5'-dRP residue and initiation of the short patch BER pathway (Christmann et al. 2003). In contrast, bifunctional glycosylases not only cleave the *N*-glycosidic bond, but additionally cleave the phosphodiester backbone neighboring the succeeding AP site. This β-elimination results in a single nucleotide gap that is either flanked by a 3' sugar phosphate (3'-ddR5P) and a 5'-phosphate residue that is further processed by APE1 or, in case of cleavage by NEIL1, -2, -3, by a 3'- and 5'-phosphate that is further processed by polynucleotide kinase (PNK). APE1 and PNK activity both yield a 3'-OH terminus that allows for insertion of the first nucleotide by Polβ (Bosshard et al. 2012).

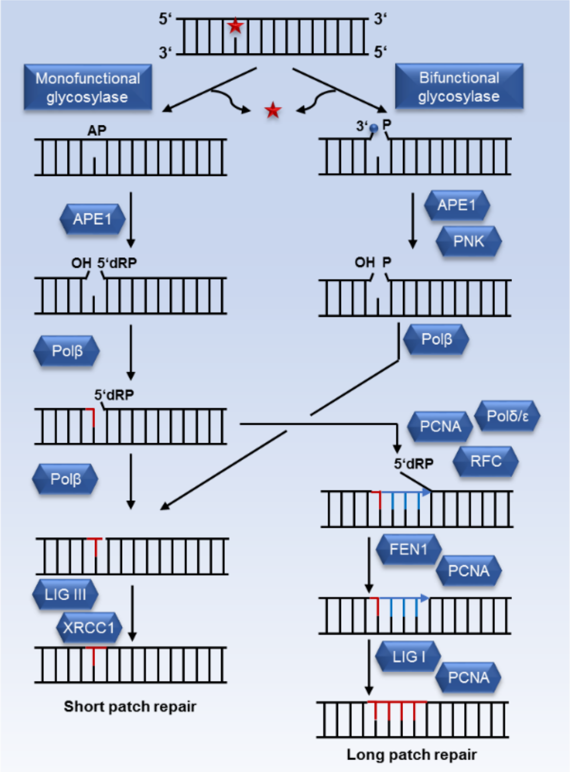

Figure 9: Base excision repair pathway. Base excision repair pathway can either be initiated by monofunctional or bifunctional DNA-glycosylases and can either be completed through the short patch or the long patch repair mechanism with the nature of the primary DNA damaging lesion being the main determinant of pathway choice. Further description is given in the text. Figure modified according to (Christmann et al. 2003; Bosshard et al. 2012).

Finally, both pathways, independent of mono- or bifunctional glycosylase activity, enable the sealing of the resulting single-nucleotide gap by a complex of X-ray repair cross-complementing protein 1 (XRCC1) and DNA ligase 3 (LIG III) via the short patch BER pathway (Christmann et al. 2003). On the other hand, for instance in cases of oxidized or reduced AP sites, excision of the 5'-dRP residues by lyase activity of Polβ is prevented and Polβ dissociates from the damaged DNA for further processing of the lesion by long patch repair. In these cases, displacement of the downstream strand and DNA synthesis are accomplished by the joint activity of Polδ, Polε, proliferating cell nuclear antigen (PCNA), and replication factor C (RFC). The generated 5'-flap can be recognized by flap endonuclease 1 (FEN1), whose cleavage activity yields a lesion that is finally religated by DNA ligase 1 (LIG I) (Christmann et al. 2003; Bosshard et al. 2012). Hence, short patch and long patch BER owe their respective names to the fact that in short patch repair a single nucleotide is replaced whereas in long patch repair 2-12 nucleotides are resynthesized.

1.6.3 DNA double-strand break repair

Double strand breaks in DNA are highly damaging lesions, that efficiently elicit cell death responses if they remain unrepaired or advance genomic instability in case of repair failure. In contrast to most other lesions, DSBs physically disrupt the linear structure of the chromosome and result in the loss of all upstream genetic material if repair is absent or failing prior to the next cell division (Deriano and Roth 2013). Against the background of an estimated ratio of one spontaneously arising DSB per cell cycle per 10^8 base pairs, a scale that equates the average number of base pairs of a human chromosome, and given the fact that unresolved DSB are at the heart of various disease mechanisms, effective repair mechanisms for this toxic lesion constitute a prerequisite for cell survival (Vilenchik and Knudson 2003; Jackson and Bartek 2009). In mammalian cells, two major repair routes for DNA double strand breaks exist. The predominant pathway in mammalian cells is NHEJ which occurs cell cycle-independent in dividing and non-dividing cells, as it does not require a homologous DNA template for repair. In contrast, DSB repair by HR only takes place during S- or G2/M-phase of the cell cycle as it is dependent on a homologous DNA strand for high fidelity, template-based DNA resynthesis (Chatterjee and Walker 2017). Pathway choice between both repair mechanisms is not yet fully elucidated but is thought to be controlled by multiple regulatory layers (Chapman et al. 2012). Among others, the two tumor suppressors p53-binding protein 1 (53BP1) and breast cancer 1 (BRCA1) are described as crucial determinants of pathway choice. 53BP1 binding to dimethyl-histone H3 (H3K79me2) at DSB sites prevents HR as it restrains the necessary, initial nucleolytic DNA end resection of DSBs and thus promotes NHEJ (Chapman et al. 2012). On the other hand, BRCA1 is thought to antagonize 53BP1 mediated HR-suppression during S- and G2-phase by potentially promoting chromatin interaction of the central HR endonuclease

CtBP-interacting protein (CtIP) and as a result contributes to a 53BP1- and BRCA1-governed HR-NHEJ equilibrium (Chapman et al. 2012). Further hypotheses include specific chromatin conformations or meiotic recombination 11 (MRE11) nuclease activity, and thus the MRN complex, as determinants of pathway choice (Chapman et al. 2012). In general, the underlying hypothesis for all these considerations is that NHEJ presents the less favorable pathway for DSB repair due to its enhanced error susceptibility and that increased HR rates result in augmented genomic stability. However, this general principle has recently been under discussion and a new model proposes that both DSB repair pathways encompass multiple underlying mechanisms with varying levels of error rate and associated mutagenic potential (Guirouilh-Barbat et al. 2014; Rodgers and McVey 2016). The mechanistic details of DSB repair, the determinants of pathway choice between HR and NHEJ, as well as the implications of DSB repair for genomic change and instability are thus still up for scientific debate.

1.6.3.1 Homologous recombination

Initial recognition of the DSB during HR is conferred by the MRN complex that is composed of the MRE11, RAD50, and NBS1 proteins. Subsequently, combined exonuclease activity of MRE11 and CtIP confers 5’-3’ nucleolytic resection of the DSB, which yields 3’ ssDNA overhangs (Sartori et al. 2007). Long-range resection is further forwarded by recruitment and activity of exonuclease 1 (EXO1) (Eid et al. 2010; Symington 2014). The resulting ssDNA is coated and stabilized through binding of RPA, which additionally leads to a full checkpoint activation via ATRIP and ATR activation (Iyama and Wilson 2013). Concurrent RAD52 localization and BRCA2 activity subsequently trigger the replacement of RPA by RAD51 and stimulate the formation of helical RAD51 nucleofilaments surrounding the single stranded DNA strands (Iyama and Wilson 2013). Finally, RAD51-coated ssDNA can efficiently invade a homologous strand of a neighboring duplex DNA helix. Following strand invasion, strand displacement at the undamaged helix and DNA synthesis by polymerase η (POLη) results in the creation of a displacement loop (D-loop) structure. Ongoing strand synthesis by POLη and polymerase δ (POLδ) and ligation of the two interacting DNAs promotes, according to the double strand break repair (DSBR) model, the formation of a complex DNA structure, the so-called Holiday-junction (or double Holiday junction) (Sebesta et al. 2011; Wyatt and West 2014). In eukaryotes, the helicase and topoisomerase activity of the BLM-TOPOIII-RMI1/2 complex primarily conveys the dissolution of the two junctions, resulting in exclusively non-crossover products (Wyatt and West 2014).

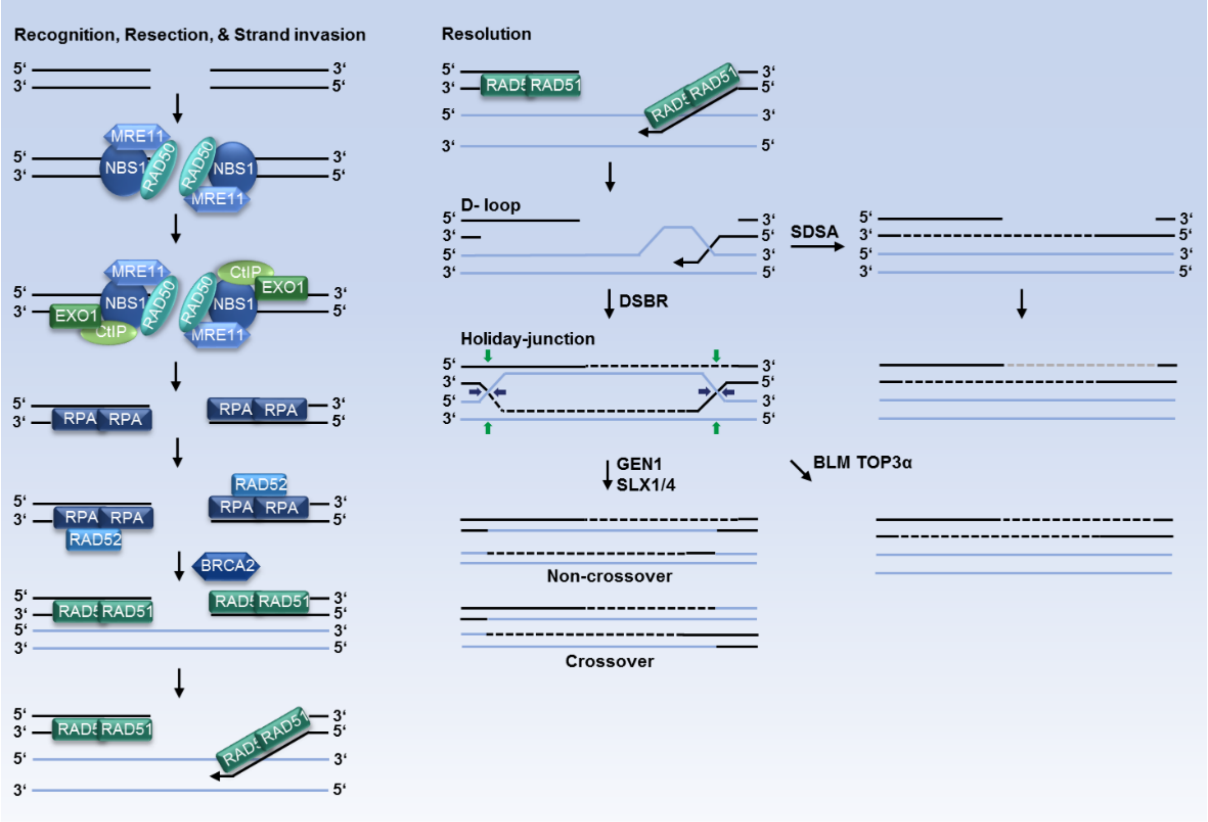

Figure 10: Homologous recombination repair pathway. Figure depicts crucial regulators and mechanistic sequence of recognition and resection of DSB lesions as well as subsequent homologous strand invasion. Furthermore, resolution of succeeding holiday-junctions by double strand break repair (DSBR), formation of crossover and non-crossover products, as well as the alternative synthesis-dependent strand annealing (SDSA) pathway are shown in the right panel. Further description is given in the text. Figure modified according to (Christmann et al. 2003; Iyama and Wilson 2013).

On the other hand, resolution of the Holiday-junction can be achieved by endonuclease-mediated cleavage. For this purpose, GEN1 and SLX1/4 nucleases cleave at the indicated arrows to generate either non-crossover (cleavage at blue arrows) or crossover (cleavage at blue arrows on one side and green arrows on the other side) products (Iyama and Wilson 2013). Formation of these crossover products provides the cell with the means of genomic rearrangements that might either be warranted for instance in immunologic V(D)J or class switch recombination or highly unwarranted like for instance in cases of genetic instability-related tumorigenesis (Guirouilh-Barbat et al. 2014). In addition to DSBR, the alternative model of synthesis-dependent strand annealing (SDSA) completes DSB repair by generation of non-crossover products without encountering Holiday-junction formation. Herein, the extended D-loop is reversed by dissociation of the invading, newly synthesized strand and annealing of the 3’ end to the respective, resected DSB end (Iyama and Wilson 2013).

1.6.3.2 Non-homologous end joining

Binding of the highly abundant KU heterodimer, consisting of KU70 (also XRCC6) and KU80 (also XRCC5), to the broken DNA ends at both sites of the DSB initiates NHEJ (Yang et al.

2016). KU thereby recognizes different end structures such as blunt ends, 5' or 3' overhangs, and covalently sealed hairpins and serves as a scaffold for the further repair protein localization (Deriano and Roth 2013). Following KU:DNA complex formation, DNA-PK is activated and binds the KU heterodimer through interaction with KU80 at both sides of the DSB (Yang et al. 2016). The majority of DSBs possess two DNA ends that are unsuitable for direct ligation as a result of diverse chemical modifications or mismatching overhangs. Consequently, end resection and modification by a varying combination of specialized enzymes is necessary to successfully seal the lesion (Chang et al. 2017). End resection is mediated through exo- or endonuclease activity to generate small domains of microhomology (≤ 4 nucleotides) between the strands to expedite subsequent end joining (Chang et al. 2017). The predominant endonuclease for this task at 3' and 5' overhangs is Artemis which is activated by and colocalizes to DNA-PK. Dependent on the modification and subsequent complexity of DNA ends further nucleases might contribute to NHEJ such as aprataxin (APTX), and aprataxin-and-polynucleotide kinase-like factor (APLF), or Werner syndrome protein (WRN) (Deriano and Roth 2013). Furthermore, modification by polynucleotide kinase/phosphatase (PNKP) is described to accomplish the correction of the chemical end groups of DSBs for subsequent DNA ligation by phosphorylation of 5'-OH termini and dephosphorylation of 3'-phosphate (Chappell et al. 2002). Another modification of DNA ends prior to ligation is mediated by tyrosyl DNA phosphodiesterase 1 (TDP1), which specifically cleaves 3′-phosphoglycolates that evolve at up to 10% of 3'ends of DSBs in response to IR (Chang et al. 2017). Subsequent DNA synthesis to extend DNA ends and fill the gap at or near DSB sites during NHEJ is carried out by three members of the POLX family of polymerases: POLλ, POLμ, and terminal deoxynucleotidyl transferase (TdT) (Deriano and Roth 2013). These polymerases share a N-terminal BRCT domain that is essential for their binding to the KU heterodimer (Chang et al. 2017). It is worth mentioning, that TdT is solely expressed in early B lymphocytes and T lymphocytes undergoing V(D)J recombination whereas POLλ and POLμ are ubiquitously expressed (Deriano and Roth 2013; Chang et al. 2017). Successful end processing and DNA synthesis allow for the final ligation of the DSB by DNA ligase 4 (LIG IV) that is embedded in the core XRCC4-XLF-LIG IV ligase complex (Yang et al. 2016). Cross-complementing protein 4 (XRCC4) and XRCC4-like factor (XLF) form long and supercoiled helical nucleofilaments that stabilize the aligned pair of DNA ends to allow effective ligation by LIG IV (Yang et al. 2016). Paralog of XRCC4 and XLF (PAXX) serves as additional structural subunit of this ligation complex and binds to the KU:DNA complex (Yang et al. 2016).

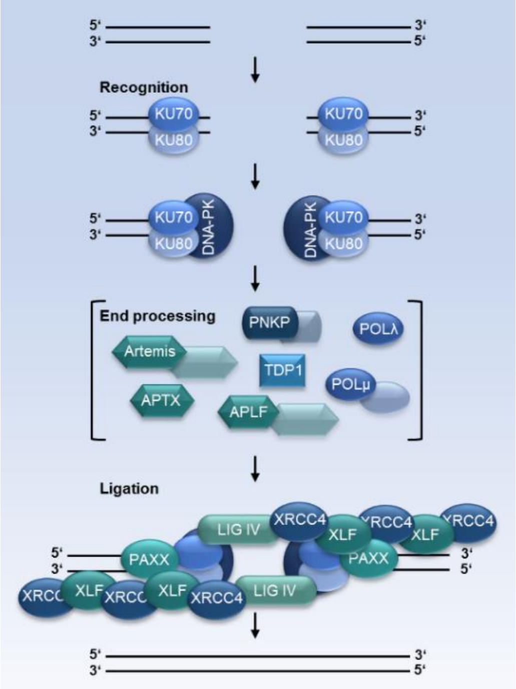

Figure 11: Classic non-homologous end joining pathway. Figure depicts crucial regulators and mechanistic sequence of recognition, end processing and ligation of DSB lesions by NHEJ. Further description is given in the text. Figure modified according to (Yang et al. 2016) and (Chang et al. 2017).

1.6.4 Interstrand crosslink repair

DNA crosslinks that covalently join the complementary strands of the DNA double helix restrict DNA function by physically blocking the progression of DNA and RNA polymerases at transcription and replication forks. Unrepaired or incorrectly repaired ICLs thus highly efficiently trigger cell death reactions or promote mutagenesis and genomic instability, respectively. Several different chemical agents are categorized as potent ICL inducers such as psoralens, mitomycin C, platinum compounds, nitrogen mustards, and nitrosoureas (Dronkert and Kanaar 2001). ICL inducers are widely applied in chemotherapy as their cytotoxic effects especially affect rapidly dividing cell populations like tumor cells. Apart from direct repair mechanisms prior to ICL formation such as alkylating adduct elimination by MGMT (see **1.5.2**), ICLs are primarily repaired by a complex sequence of various interacting repair machineries that includes the FA pathway, the NER machinery, polymerases of TLS, and the HR repair pathway (Nikolova et al. 2017a). Initial recognition of the polymerase blocking ICL and stabilization of the stalled fork is conveyed by the FA core complex, which is constituted of the eight FA proteins FANCA/B/C/E/F/G/L/M and which recruits the heterodimer of FANCI and FANCD2 to the lesion. Subsequently, FANCI and FANCD2 are ubiquitylated by the joint activity of the FANCL E3 ubiquitin ligase and the E2 conjugating enzyme UBE2T (Longerich et al. 2014). The FANC core complex and ubiquitinylated FANCD2 serve as a platform for the localization of NER nucleases and furthermore coordinate the final recombinatorial repair and translesion synthesis of the arising lesions (Nikolova et al. 2017b). Following the recognition by FA proteins, the ICL is uncoupled through consecutive 3’- and 5’-cleavage at the leading strand by the endonucleases XPG (or alternatively FAN1) and XPF:ERCC1. This unhooking of the ICL generates a one-ended DSB at the leading strand and gaps in the lagging strand that are filled by TLS polymerases (POLζ, κ, η, ι, ν), which possess the ability to bypass the hanging adduct. Further nucleolytic NER steps most probably excise the ICL, while HR machinery processes the one-ended DSB by end resection analogous to **1.6.3.1**. Finally, the modified DSB end is coated by RAD51 nucleoprotein filaments, due to the joint activity of BRCA2 and several RAD51 paralogues such as XRCC2, XRCC3, and RAD51B/C/D (Nikolova et al. 2017b). Repair of the one-ended DSB is accomplished comparably to the mechanism of HR described for common DSBs (see **1.6.3.1**) and conferred by the invasion of RAD51-coated ssDNA into the restored homologous strand. This HR sub pathway for one-ended DSBs is called break-induced replication (BIR) and results preferably in the reestablishment of a functional, unidirectional replication fork and DNA resynthesis by POLδ (Chapman et al. 2012; Malkova and Ira 2013). However, BIR is associated with an enhanced mutagenesis rate compared to ordinary S-phase replication and results in various types of chromosomal rearrangements such as template switching, translocations, and half-crossovers (Malkova and Ira 2013). This phenomenon is most likely caused by ineffective resolution of the Holiday-junction and subsequent DNA synthesis via D-loop migration, which prevents effective correction of replication errors due to quick dissociation of the newly synthesized strand from its template (Malkova and Ira 2013). In sum, the complex interplay of the involved repair sub pathways as well as the dependence on error-prone mechanisms like TLS and BIR renders ICL repair an intrinsically challenging cellular process. Hence, even successful ICL repair is associated with a high risk of mutagenic events. This explains long-term and secondary complications in patients treated with e.g. psoralen or alkylating agents (Shen and Li 2010).

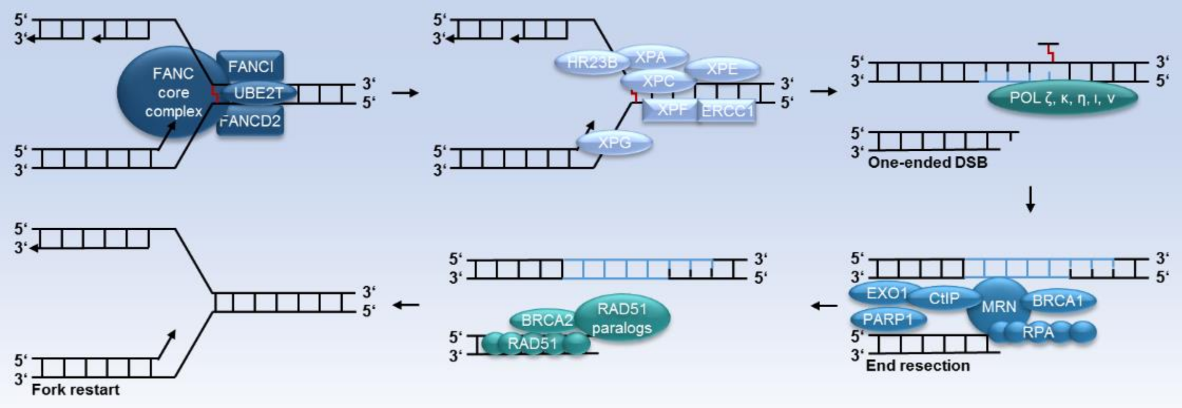

Figure 12: Interstrand crosslink repair pathway. A complex interplay of distinct repair pathways assures successful ICL repair. Recognition of ICLs at stalled replication forks is mediated by FA proteins. Endonuclease activity of the NER complex generates one-ended DSBs at one strand while allowing unhooking of the ICL and DNA resynthesis by DNA translesion polymerases at the complementary strand. The one-ended double strand break is recognized and processed by the HR repair machinery. Finally, effective DSB end resection and

subsequent RAD51 coating of the broken end results in fork restart and resumption of DNA replication. Further details are given in the text. Figure modified according to (Nikolova et al. 2017a).

1.6.5 Chromatin structure and DNA repair

In eukaryotic cells, DNA is organized and compacted in nucleosomes through tightly packaging around an octamer of the core histones H2A, H2B, H3, and H4. The complex macromolecular structure in which these nucleosomes are subsequently assembled is called chromatin. However, DNA accessibility is nonetheless dynamically regulated by specialized protein complexes (chromatin remodeling complexes) and intricate signaling pathways that, inter alia, prompt reversible changes in the epigenetic code of DNA and modulate posttranslational histone modifications. Flexible DNA condensation and decondensation is essential for key DNA functions in replication, transcription, and DNA repair (Biterge and Schneider 2014). One approach to shape DNA for repair is to alter functional properties of histones by PTM. Enhanced accessibility of DNA for repair is for instance conveyed by the augmented PTM of histones with acetyl residues that results in diminished interaction between histones and the negatively charged DNA phosphate backbone (Hong et al. 1993; Glozak and Seto 2007). Additionally, phosphorylation of the histone variant H2AX by the checkpoint kinases ATR and ATM has a major impact on DNA damage response as it serves as a platform for the localization of further repair factors (Biterge and Schneider 2014). Furthermore, posttranslational histone modifications govern pathway choice in DNA double strand break repair with acetylated histone H4K16 and monoubiquitinylated histone H2BK120 mediating HR but consecutive ubiquitylation of histone H2BK120, histone H1, and histone H2AK13/K15 directing for NHEJ (Hauer and Gasser 2017). Moreover, methylation of histone H3K36 is associated with open chromatin structure and HR-mediated repair of DSBs while methylation of histone H4K20 (H4K20me2) promotes NHEJ (Hauer and Gasser 2017). Alongside these regulatory mechanisms mediated by PTM of histones, DNA accessibility and repair are in addition controlled by adenosine triphosphate (ATP)-dependent chromatin remodelers, that enzymatically modulate the position, disassembly, and assembly of histones and histone variants and thereby crucially affect the maintenance of genomic stability (Papamichos-Chronakis and Peterson 2012). It has been shown that chromatin organization in cancer cells is the major determinant of regional DNA mutation rate with more than 55% of the disparities in single nucleotide variation density being associated with changes in histone modifications that are typical for inaccessible, heterochromatin-like regions (Schuster-Böckler and Lehner 2012). A likely explanation for this finding represents the indicated theory that heterochromatic DNA regions are less open for DNA repair machineries. Accordingly, is has been demonstrated that MMR repair efficiency is enhanced in euchromatic regions, which suppresses the accumulation of mutations in these regions (Supek and Lehner 2015). On the one hand, chromatin compaction thus generally affects DNA repair efficiency while, on the other hand, specific components of the chromatin remodeling machinery additionally possess explicit roles in various DNA repair pathways. Currently, four separate families of chromatin remodelers are described that commonly use ATP-dependent hydrolysis to modify histone-DNA interactions and thus share an analogous ATPase domain: the SWI/SNF family, the ISWI family, the CHD family, and the INO80 family (Clapier and Cairns 2009). These chromatin remodeling enzymes form complexes that are constituted of a varying number of heterogenous subunits built around one or more catalytically active central helicase with ATPase function. Whereas SWI/SNF complexes are constituted of as many as 8 to 14 subunits, ISWI remodeling complexes contain 2 to 4 subunits, CHD complexes 1 to 10 subunits, and INO80 complexes over 10 subunits (Clapier and Cairns 2009). Functionally, the INO80 complex is recruited to DSBs, colocalizes with phosphorylated H2A, and is necessary for 5’-3’-end resection of DSBs in yeast to allow HR repair (Clapier and Cairns 2009). In contrast, the SWR1 complex, who is also part of the INO80 family, is required for Ku80 loading and NHEJ execution (Clapier and Cairns 2009). The conserved ATPase subunits of ISWI complexes, SMARCA5 and SMARCA1, have been implicated in the enabling of PTM of histones prior to effective DSB repair factor recruitment for HR and NHEJ as well as in the detection and repair of photolesions by transcription coupled NER (Aydin et al. 2014). Alike INO80, the SWI/SNF complex is essential for DSB end processing prior to homologous strand invasion (Clapier and Cairns 2009). In mammals, the SWI/SNF complex BAF with its central helicase subunit BRG1 is recruited to γH2AX at DSB sites (Park et al. 2006). Strikingly, γH2A formation in the absence of BRG1 does neither persist nor spread normally in a megabase range around the DSB, which indicates that chromatin remodeling activity of the complex is necessary for the accessibility of neighboring nucleosomes (Park et al. 2006; Lee et al. 2010a). Notably, a crucial role in DSB end processing by EXO1 prior to HR mediated repair as well as an impact on γH2AX formation has also been assigned to the yeast ATPase Fun30 and its human orthologue SWI/SNF-related matrix-associated actin-dependent regulator of chromatin subfamily A containing DEAD/H box 1 (SMARCAD1) (Costelloe et al. 2012; Chakraborty et al. 2018). Interestingly, all SWI/SNF ATPases as well as several components of chromatin remodeling complexes of other families are defined through the expression of a BRD that specifically binds heterochromatin associated, acetylated lysine residues (Clapier and Cairns 2009; Chiu et al. 2017). It is thus of no surprise that these BRD containing readers of the acetyl-code interact in close proximity with the writers (HATs) and erasers (HDACs) of this code to collectively modify chromatin structure and DNA damage signaling and repair. For example, histone acetylation by the HATs CBP (KAT3A) and p300 (KAT3B) (for SMARCA2 ATPase) or GCN5 (KAT2A) (for SMARCA4 ATPase) was shown to be essential for SWI/SNF mediated chromatin remodeling around DSBs and subsequent potential recruitment of the KU heterodimer for NHEJ repair (Ogiwara et al. 2011; Rother and van Attikum 2017). Furthermore, close interaction between HDACs and chromatin remodelers of the CHD family is given in the NuRD complex which contains either CHD3 or CHD4 ATPase as well as HDAC1 or HDAC2. The NuRD complex maintains a higher-order chromatin structure that is essential for DSB repair and additionally controls G1/S-arrest by modification of p53 acetylation (Price and D'Andrea 2013). The helicase SMARCAD1 has been demonstrated to directly associate with HDAC1/HDAC2 and further factors to regulate histone modification throughout the cell cycle and to ensure heterochromatin maintenance and faithful chromosome segregation in mitosis (Rowbotham et al. 2011). Despite the not fully elucidated explicit intricacies, ongoing research and accumulating evidence demonstrate the importance of this functional acetylation signaling network between readers, writers, and erasers of the acetyl-code (Chiu et al. 2017). For instance, large scale proteomic studies unveiled the substantial extent of changes in protein acetylation that govern DNA damage response within the complexity of chromatin architecture (Choudhary et al. 2009; Elia et al. 2015; Chiu et al. 2017). The elucidation of additional interactions, modifications, and signaling pathways among histone modifiers and chromatin remodelers will serve to unveil the complexity of this additional, chromatin-dependent, regulatory layer of DNA damage repair.

2 Aims and Objective

Enhanced expression of HDACs is a crucial hallmark of numerous hematologic and solid tumors and associated with a deregulation of the homeostasis of posttranslational protein acetylation (Li and Seto 2016). Reverting this excessive HDAC activity by therapeutic treatment with small molecules that specifically target and inhibit selective classes of HDACs is a promising clinical strategy and has been shown to result in favorable results in selected, mostly hematologic, carcinomas such as cutaneous and peripheral T cell lymphoma and multiple myeloma (Ceccacci and Minucci 2016; Li and Seto 2016). At present, HDACi gain further impact in solid tumor therapy as they have been shown to improve treatment outcomes of ICI by enhancing tumor antigen presentation and T-cell-mediated tumor lysis (Suzuki et al. 2010; Woods et al. 2013; Kim et al. 2014; Woods et al. 2015; de Charette et al. 2016; Gameiro et al. 2016; Terranova-Barberio et al. 2017; Booth et al. 2018; Briere et al. 2018). However, not least due to the multitude of molecular targets affected by drugs that disturb PTM, the intricate signaling pathways elicited by HDACi remain insufficiently elucidated. Thus, this work aimed at deciphering the role of class I HDACs and their specific inhibitors in key cellular signaling networks in particularly kidney- and colon-derived cancer cell lines.

Renal carcinoma

In RCC cells, it is still a matter of debate in the literature whether HDACi predominantly evoke cytotoxic effects or rather facilitate metastatic spread by induction of EMT (see **1.4.1**). This ambiguity provoked the following questions that were examined and subsequently answered in the first part of this work.

- How do HDACi affect global protein expression and signaling pathways in RCC cells?
- Does HDACi treatment evoke EMT signaling and functional cellular transition in RCC cells?
- How do HDACi affect cell growth, survival, and autophagy of RCC cells?
- Can the observed effects in RCC cell lines be transferred to primary RCC cells?
- Can the observed HDACi effects be attributed to the inhibition of specific HDACs?
- Does the RCC cell line Renca harbor mutations in p53?

Colorectal carcinoma

Our group previously reported that the specific sumoylation of HDAC2 affects p53- and NF-κB-dependent gene expression in CRC cells (Brandl et al. 2012; Wagner et al. 2015). Proceeding studies were intended to elucidate if these regulatory mechanisms have implications for the chemosensitivity of CRC cells and were predominantly oriented at the following questions:

- How does HDAC2 sumoylation affect cellular sensitivity towards 5-FU and other chemotherapeutic agents?
- Are potential differences in cellular sensitivity based on the modification of p53 by HDAC2?
- How does HDAC2 sumoylation affect global protein expression?
- Do further changes in basal protein expression in response to the abrogation of HDAC2 sumoylation account for cellular sensitivity and DNA repair capacity?
- Do HDACi cause effects that are comparable to those seen in response to the loss of HDAC2 sumoylation?

3 Material and Methods

3.1 Material

3.1.1 Equipment

Equipment	**Manufacturer**
[137Cs]-Source Gammacell Irradiator 2000	Mølsgaard Medical, DK
Autoclave 5075 ELV	Tuttnauer Europe B.V., Breda, NL
Balance PJ precisa junior 500	Precisa Gravimetrics AG, Switzerland
Benchtop centrifuge 5417 C	Eppendorf AG, Hamburg, DE
Cell counter TC20TM	BioRad, Hercules, CA, USA
ColorView SoftImagingSystem	Olympus Soft Imaging Solutions, Münster, DE
Electronic repeating pipette, HandyStep®	Brand, Wertheim, DE
FACS Canto II	BD Biosciences, Heidelberg, DE
FiveEasy™ pH bench meter FE20	Mettler Toledo, OH, USA
Freezer -20°C	Liebherr, CH
Heracell™ 150i CO_2 incubator	Thermo Fisher Scientific, MA, USA
Hereaus Labofuge 400R	Thermo Fisher Scientific, MA, USA
Hereaus Megafuge 16	Thermo Fisher Scientific, MA, USA
Infrared imaging system Odyssey 9120	LI-COR, Bad Homburg, DE
LaminAir® HB 2472 workbench	Heraeus Instruments, Hanau, DE
Laser Scanning Microscope LSM 710	Carl Zeiss GmbH, Oberkochen, DE
Megafuge 16	Thermo Fisher Scientific, MA, USA
Micoscope Axiovert 35	Carl Zeiss GmbH, Oberkochen, DE
Microcentrifuge Micro Star 17R	VWR, PA, USA
Microplate Reader Sunrise™	Tecan Trading AG, CH
Microstar 17R centrifuge	VWR, PA, USA
Neubauer counting chamber	Marienfeld-Superior, Lauda-Königshofen, DE
Olympus BX50 equipped with a ColorView camera	Olympus, Münster, DE
Orbital shaker Certomat R	B.Braun, Melsungen, DE
Pipet-Lite™ XLS™, varied sizes	VWR, PA, USA
Pipettboy Ranin Pipet-X	Mettler Toledo, OH, USA
Pipette controller, PIPETBOY acu	VWR, PA, USA
PowerPac™ HC High-Current Power Supply	Bio-Rad, Hercules, CA, USA
Primovert microscope	Carl Zeiss GmbH, Oberkochen, DE
Rocking platform	VWR, PA, USA
Rolator RM5 CAT	M. Zipperer GmbH, Ballrechten-Dottingen, DE
Sartorius precision balance basic	Sartorius, Göttingen, DE
SDS-PAGE chamber TransBlot Cell	Bio-Rad, Hercules, CA, USA
Thermomixer 5436	Eppendorf AG, Hamburg, DE
UP200Ht Ultrasonic Homogenizer	Hielscher Ultrasonic GmbH, Teltow, DE
V.I.P. ® Series -86°C Ultra Low Freezer	Sanyo, Osaka, JP
Vortex-genie 2	Scientific Industries, NY, USA

3.1.2 Consumables

Consumables	Manufacturer
0.5, 1.5, 2 ml tubes	Eppendorf AG, Hamburg, DE
15, 50 ml tubes	Greiner Bio-One, Frickenhausen, DE
5, 10, 25 ml plastic pipettes	Greiner Bio-One, Frickenhausen, DE
6, 10 cm cell culture dishes	Greiner Bio-One, Frickenhausen, DE
6,12, 24, 96 well plates	Greiner Bio-One, Frickenhausen, DE
Cell culture flasks	Greiner Bio-One, Frickenhausen, DE
Cover slips 20x20mm	Carl Roth, Karlsruhe, DE
Cover slips Comet assay 24x60 mm	Carl Roth, Karlsruhe, DE
Cryogenic tubes	Greiner Bio-One, Frickenhausen, DE
FACS-tubes	Sarstedt, Nümbrecht, DE
Frosted microscope slides 76x26 mm	Diagonal, Münster, DE
Nitrocellulose membrane Amersham protran 0.2µM	A. Hartenstein GmbH, Würzburg, DE
Pipette tips	Greiner Bio-One, Frickenhausen, DE
Whatman paper, grade 703	VWR, PA, USA

3.1.3 Software

Software	Developers
Adobe Photoshop	Adobe Systems, München, DE
BD FACSDiva^{TM} Version 6	BD Biosciences, Heidelberg, DE
Cell^A Imaging Software	Olympus Soft Imaging Solutions, Münster, DE
ChemSketch	ACD/Labs, Toronto, CA
Comet IV software	Perceptive Instruments Ltd., Bury St Edmunds, GB
EndNote Version X6	Thomas Reuters, NY, USA
Flowing Software Version 2.5.1	Turku Centre for Biotechnology, University of Turku, FI
GraphPad Prism Version 6	GraphPad Software, CA, USA
Graph Pad Prism Version 7	GraphPad Software, CA, USA
Image Studio Lite 5.2	LI-COR, NE, USA
ImageJ 1.51j8	U.S. National Institute of Health, MD, USA
Magellan^{TM}	Tecan Trading AG, CH
MS Office 365	Microsoft, Unterschleißheim, DE
Odyssey Version 3.0	LI-COR, NE, USA
ZEISS ZEN Imaging Software 2.1	Carl Zeiss GmbH, Oberkochen, DE
ZEISS LSM Image Browser Version 4.2	Carl Zeiss GmbH, Oberkochen, DE
TScratch Version 1.0	CSElab, ETH Zurich, CH

3.1.4 Chemicals

Compound	Manufacturer
40% Acrylamide/bisacrylamide 37.5:1	Carl Roth, Karlsruhe, DE
Acetone	Thermo Fisher Scientific, MA, USA
Agarose standard	Carl Roth, Karlsruhe, DE
Ammonium persulfate (APS)	Carl Roth, Karlsruhe, DE

Annexin-V FITC	BD Biosciences, NJ, USA
Bovine serum albumin (BSA) Fraction V	Carl Roth, Karlsruhe, DE
$CaCl_2$	Merck, NJ, USA
Coomassie Brilliant Blue G-250	Merck, NJ, USA
Crystal violet	Merck, NJ, USA
CytoID Kit	Enzo Biochem, NY, USA
DAPI	Roche, Basel, CH
Dimethyl sulfoxide (DMSO)	Sigma-Aldrich, MO, USA
Dithiothreitol (DTT)	Carl Roth, Karlsruhe, DE
Dulbecco’s Modified Eagle’s Medium	Sigma-Aldrich, MO, USA
Ethanol (EtOH)	Carl Roth, Karlsruhe, DE
Ethylenediaminetetraacetic acid (EDTA)	Applichem, Darmstadt, DE
G418, Geneticin	Sigma-Aldrich, MO, USA
Gibco Fetal calf serum (FCS)	Thermo Fisher Scientific, MA, USA
Gibco OptiMEM	Thermo Fisher Scientific, MA, USA
Gibco Penicillin/streptomycin	Thermo Fisher Scientific, MA, USA
Giemsa solution	Carl Roth, Karlsruhe, DE
Glycerol	Sigma-Aldrich, MO, USA
Glycine	Carl Roth, Karlsruhe, DE
Hydrochloric acid (HCl)	Carl Roth, Karlsruhe, DE
Hydroxyethyl piperazineethanesulfonic acid (HEPES)	Carl Roth, Karlsruhe, DE
Isopropanol (2-Propanol)	Carl Roth, Karlsruhe, DE
Lipofectamine® RNAiMAX	Invitrogen, CA, USA
Methanol (MeOH)	Carl Roth, Karlsruhe, DE
NaCl	Sigma-Aldrich, MO, USA
NewBlot™ Nitro Stripping Buffer, 5x	LI-COR, NE, USA
Nonfat dry milk powder	Carl Roth, Karlsruhe, DE
Normal goat serum	Life Technologies, CA, USA
NP-40	Fluka Analytical, Seelze, DE
PageRuler$^{\mathrm{TM}}$ prestained protein ladder	Thermo Fisher Scientific, MA, USA
Paraformaldehyde (PFA)	Carl Roth, Karlsruhe, DE
Phosphatase inhibitor cocktail 2	Sigma-Aldrich, MO, USA
Phosphate-buffered saline (PBS)	Merck, NJ, USA
Phosphoric acid (85% (*w/v*) in H_2O)	Carl Roth, Karlsruhe, DE
Propidium iodide (PI)	Sigma-Aldrich, MO, USA
protease inhibitor (cOmplete tablets, Mini, EDTA-free, EASY*pack)*	Roche, Basel, CH
Puromycin	InvivoGen, CA, USA
RNAse A	Carl Roth, Karlsruhe, DE
RPMI 1640	Sigma-Aldrich, MO, USA
Serva blue G	Serva Electrophoresis, Heidelberg, DE
Sodium dodecyl sulfate (SDS)	Carl Roth, Karlsruhe, DE
tBOOH	Sigma-Aldrich, MO, USA
Tetramethylethylenediamine (TEMED)	Carl Roth, Karlsruhe, DE
TO-PRO-3	Life Technologies, CA, USA
Tris base	Carl Roth, Karlsruhe, DE
Triton X-100	Sigma-Aldrich, MO, USA

Trypan blue	Sigma-Aldrich, MO, USA
Trypsin EDTA	Merck, NJ, USA
Tween20	Carl Roth, Karlsruhe, DE
Vectashield®	Vector Laboratories, CA, USA
WST1	Roche, Basel, CH

3.1.5 Inhibitory, cytostatic and genotoxic drugs

Compound	Manufacturer
5-Fluorouracil	Sigma-Aldrich, MO, USA
Doxorubicin	MedacPharma, Wedel, DE
Entinostat	Selleck Chemicals, TX, USA
Fluorodeoxyuridine	Cayman Chemical, MI, USA
Fluorouridine	Sigma-Aldrich, MO, USA
Hydroxyurea	Sigma-Aldrich, MO, USA
Nimustine	Sigma-Aldrich, MO, USA
O^6-benzylguanine	Sigma-Aldrich, MO, USA
Olaparib	Selleck Chemicals, TX, USA
Oxaliplatin	Selleck Chemicals, TX, USA
Uridine	Carl Roth, Karlsruhe, DE
Valproic acid	Sigma-Aldrich, MO, USA
Z-VAD-FMK	Bachem, Bubendorf, CH

3.1.6 Antibodies

Primary antibody	Origin	Dilution	ref. number	Manufacturer
anti-53BP1	Mouse	1:1000	MAB3802	Merck Millipore, MA, USA
anti-acHistone H3	Rabbit	1:1000	06-599	Merck Millipore, MA, USA
anti-acHistone H4	Mouse	1:2500	1:5000	(Göttlicher et al. 2001)
anti-acH2AX (K5)	Rabbit	1:1000	ab129217	Abcam, Cambridge, UK
anti-βActin	Mouse	1:50000	sc47778	Santa Cruz Biotechnology, Heidelberg, DE
anti-ATM	Rabbit	1:1000	ab32420	Abcam, Cambridge, UK
anti-ATR	Rabbit	1:1000	CS2790	Cell Signaling Techn., MA, USA
anti-BAX	Rabbit	1:1000	ab32503	Abcam, Cambridge, UK
anti-βCatenin	Mouse	1:5000	BD610154	BD Biosciences, NJ, USA
anti-Beclin1	Rabbit	1:1000	CS438	Cell Signaling Techn., MA, USA
anti-BRG1	Mouse	1:1000	sc17796	Santa Cruz Biotechnology, Heidelberg, DE
anti-BRM	Rabbit	1:1000	ab15597	Abcam, Cambridge, UK
anti-Caspase 3	Mouse	1:1000	sc7272	Santa Cruz Biotechnology, Heidelberg, DE
anti-Caspase 6	Rabbit	1:500	CS9762	Cell Signaling Techn., MA, USA
anti-Caspase 9	Mouse	1:1000	CS9508	Cell Signaling Techn., MA, USA
anti-CHK1	Mouse	1:1000	CS2360	Cell Signaling Techn., MA, USA
anti-CHK2	Rabbit	1:1000	CS2662	Cell Signaling Techn., MA, USA
anti-cleaved Caspase 3	Rabbit	1:500	CS9661	Cell Signaling Techn., MA, USA
anti-DDB2	Rabbit	1:1000	ab77765	Abcam, Cambridge, UK
anti-ECadherin	Rabbit	1:1000	CS3195	Cell Signaling Techn., MA, USA

anti-GAPDH	Mouse	1:500	sc137179	Santa Cruz Biotechnology, Heidelberg, DE
anti-γH2AX	Rabbit	1:1000	sc101696	Santa Cruz Biotechnology, Heidelberg, DE
anti-γH2AX	Mouse	1:1000	05-636	Merck Millipore, MA, USA
anti-H2AX	Rabbit	1:1000	07-6271	Merck Millipore, MA, USA
anti-HDAC1	Mouse	1:1000	ab46985	Abcam, Cambridge, UK
anti-HDAC2	Mouse	1:1000	sc9959	Santa Cruz Biotechnology, Heidelberg, DE
anti-HDAC2	Rabbit	1:1000	sc7899	Santa Cruz Biotechnology, Heidelberg, DE
anti-HDAC3	Rabbit	1:5000	ab32369	Abcam, Cambridge, UK
anti-HDAC3	Rabbit	1:1000	ab16047	Abcam, Cambridge, UK
anti-HSP90	Mouse	1:1000	AdiSPA830	Enzo Life Sciences, NY, USA
anti-LC3B	Rabbit	1:1000	CS3868	Cell Signaling Techn., MA, USA
anti-mSin3a	Rabbit	1:20000	sc994	Santa Cruz Biotechnology, Heidelberg, DE
anti-NCadherin	Mouse	1:1000	BD610921	BD Biosciences, NJ, USA
anti-NCadherin	Mouse	1:500	33-3900	Thermo Fisher Scientific, MA, USA
anti-p21	Rabbit	1:1000	ab109520	Abcam, Cambridge, UK
anti-p21	Mouse	1:1000	sc6246	Santa Cruz Biotechnology, Heidelberg, DE
anti-p53	Mouse	1:5000	sc81168	Santa Cruz Biotechnology, Heidelberg, DE
anti-pATM (S1981)	Rabbit	1:750	ab81292	Abcam, Cambridge, UK
anti-pATR (T1989)	Rabbit	1:1000	GTX4703	GeneTex, CA, USA
anti-pCHK1 (S317)	Rabbit	1:1000	CS2344	Cell Signaling Techn., MA, USA
anti-pCHK2 (T68)	Rabbit	1:500	CS2661	Cell Signaling Techn., MA, USA
anti-PDGFRβ	Rabbit	1:250	sc432	Santa Cruz Biotechnology, Heidelberg, DE
anti-PIG3	Rabbit	1:1000	ab96819	Abcam, Cambridge, UK
anti-pp53 (S15)	Rabbit	1:1000	CS9284	Cell Signaling Techn., MA, USA
anti-SMARCAD1	Rabbit	1:500	CS12458	Cell Signaling Techn., MA, USA
anti-Survivin	Rabbit	1:5000	NB500-201	Novus Biologicals, CO, USA
anti-TS	Rabbit	1:1000	CS0945	Cell Signaling Techn., MA, USA
anti-V5	Mouse	1:200	sc271944	Santa Cruz Biotechnology, Heidelberg, DE
anti-Vimentin	Mouse	1:1000	MS-129-P	Thermo Fisher Scientific, MA, USA

Secondary antibody	**Origin**	**ref. number**	**Manufacturer**
IRDye® 680RD anti-Mouse IgG	Goat	925-68070	LI-COR, NE, USA
IRDye® 680RD anti-Rabbit IgG	Goat	925-68071	LI-COR, NE, USA
IRDye® 800CW anti-Mouse IgG	Goat	925-32210	LI-COR, NE, USA
IRDye® 800CW anti-Rabbit IgG	Goat	925-32211	LI-COR, NE, USA
Alexa Fluor® 488 F(ab’2) anti-Mouse IgG (H+L)	Goat	A11017	Life Technologies, CA, USA
Alexa Fluor® 488 F(ab’2) anti-Rabbit IgG (H+L)	Goat	A11070	Life Technologies, CA, USA
Cy3 anti-Rabbit IgG (H+L)	Goat	111-165-144	Dianova, Hamburg, DE

3.1.7 siRNAs

Name	**ref. number**	**Supplier**
control siRNA-A	sc37007	Santa Cruz Biotechnology, Heidelberg, DE
control siRNA-B	sc44230	Santa Cruz Biotechnology, Heidelberg, DE
control siRNA-C	sc44231	Santa Cruz Biotechnology, Heidelberg, DE

BRG1 siRNA (h)	sc29827	Santa Cruz Biotechnology, Heidelberg, DE
HDAC1 siRNA (m)	sc29344	Santa Cruz Biotechnology, Heidelberg, DE
HDAC1 siRNA (h)	sc29343	Santa Cruz Biotechnology, Heidelberg, DE
HDAC2 siRNA (m)	sc29346	Santa Cruz Biotechnology, Heidelberg, DE
HDAC2 siRNA (h)	sc29345	Santa Cruz Biotechnology, Heidelberg, DE
SMARCAD1 siRNA (h)	L-013801-00-0005	Dharmacon, CO, USA

3.1.8 Buffers and solutions

Buffer	**Preparation**
Cell lysate preparation	
NETN lysis buffer	10 mM Tris-HCl pH 8.0 100 mM NaCl 10% glycerol 1 mM EDTA 0.5% NP-40 in ddH_2O stored at 4 °C protease inhibitor (cOmplete Mini) – added: stable for 1 week 1/1000 phosphatase inhibitor (cocktail 2) – added fresh
NuPAGE LDS (1x)	1/4 NuPAGE LDS sample buffer (4x) 1/10 1M DTT ad ddH_2O
1 M DTT	154.25 mg DTT ad 1 ml ddH_2O
Sample buffer (6x)	375 mM Tris-HCl pH 6.8 12% SDS (*w/v*) 30% glycerol 500 mM dithiothreitol (DTT) spatula tip bromophenol blue in ddH_2O
Bradford assay	
Bradford reagent	50 mg Brilliant Blue G-250 50 ml phosphoric acid 25 ml EtOH ad 500 ml ddH_2O filtrate and storage at 4 °C in the dark
SDS polyacrylamide-gel electrophoresis	
5 x Lämmli buffer	30 g (0.25 M) Tris 144 g (1.92 M) glycine ad 1000 ml ddH_2O
1x SDS-PAGE running buffer	200 ml 5 x Lämmli buffer 10 ml 10% SDS ad 1000 ml ddH_2O
10% APS	1 g ammoniumpersulfate ad 10 ml ddH_2O Aliquots: storage at -20 °C
10% SDS	10 g SDS (sodium dodecyl sulfate) ad 100 ml ddH_2O
Western Blot	
1x Transfer buffer	100 ml 5 x Lämmli buffer 200 ml ethanol ad 1000 ml ddH_2O
Tris buffered saline (TBS; 10x)	0.2 M Tris-HCl pH 7.6 1.4 M NaCl

	in ddH$_2$O
TBS + Tween-20 (TBST)	1/10 TBS (10x) 0.05% Tween-20 in ddH$_2$O
COMET assay	
Lysis buffer	2.5 M NaCl 100 mM EDTA 10 mM Tris in ddH$_2$O stored at 4 °C 1% Triton X-100 – added fresh
Alkaline electrophoresis buffer	300 mM NaOH 1 mM EDTA in ddH$_2$O prior to use: ensure pH > 13
Neutralization buffer	0.4 M tris pH7.5 in ddH$_2$O
Colony formation	
Giemsa stain	1.25% Giemsa solution 0.125% crystal violet (*w/v*) in ddH$_2$O

3.2 Methods

3.2.1 Cell culture

All cell culture work was carried out in sterile conditions using a clean bench with laminar air flow. All cell lines were cultured in the appropriate cell culture medium ( ) supplemented with 10% fetal calf serum (FCS) under humidified, 5% CO$_2$ atmosphere at 37 °C. Adherent cell lines were passaged, with respect to the proliferation characteristics of the individual cell line, 2-3 times a week in a ratio of 1:5 - 1:20 by removal of residual cell culture medium, washing with phosphate buffered saline (PBS), detachment with trypsin/EDTA (0.5 g/l), resuspension in cell culture medium and centrifugation (5 min, 1300 rpm). The resulting cell pellet was resuspended in a defined volume of cell culture medium and the appropriate proportion of cell suspension was reseeded in a cell culture flask with fresh cell culture medium. For long term cryopreservation, exponentially growing cells were detached likewise and the resulting cell pellet was resuspended in FCS supplemented with 10% dimethylsulfoxide (DMSO) and 0.5 – 1 ml aliquots thereof were transferred immediately to a -80 °C deep freezer prior to long term storage in liquid nitrogen. Cryopreserved cells were thawed at 37 °C in a water bath and added to a cell culture flask containing 5 ml cell culture medium. After 24 h, cell culture medium was exchanged and cells were allowed to recover for 7 days to ensure stable growth conditions and cell properties for subsequent experimental procedures. Cell lines were cultured for a maximum of 3 - 4 months before being replaced by a new cryopreserved aliquot.

Table 2: Cell lines used in this work.

Cell line	Medium	Supplement	Source / Reference
Colorectal cancer cell lines			
RKO-ATCC	DMEM	10% FCS	DSMZ Braunschweig, Dr. M. Zörnig, GSH Frankfurt/Main, (Krämer et al. 2008a)
RKO-ES	DMEM	10% FCS	Prof. M. Esteller, Barcelona, Spain, (Ropero et al. 2006)
RKO HDAC2^{wt}	DMEM	10% FCS, 0.8 mg/ml G418	Dr. A. Brandl, CMB, FSU Jena, (Brandl et al. 2012)
RKO HDAC2^{K462R}	DMEM	10% FCS, 0.8 mg/ml G418	Dr. A. Brandl, CMB, FSU Jena, (Brandl et al. 2012)
HCT116	DMEM	10% FCS	ATCC
HROC 24	DMEM	10% FCS	Dr. M. Linnebacher, University Medicine Rostock
HROC 113	DMEM	10% FCS	Dr. M. Linnebacher, University Medicine Rostock
HROC 50	DMEM	10% FCS	Dr. M. Linnebacher, University Medicine Rostock
Renal cancer lines			
Renca	RPMI	10% FCS	(Maurer-Gebhard et al. 1999)
Mz-ccRCC1	RPMI	10% FCS	Prof. W. Brenner, University Medical Center Mainz
Mz-ccRCC2	RPMI	10% FCS	Prof. W. Brenner, University Medical Center Mainz

3.2.2 Treatment of cells with cytostatic and inhibitory drugs

To ensure complete cell adherence to cell culture dishes, seeding of cells was carried out 24 h prior to treatment. Cell density was adjusted for each cell line to ensure exponential cell growth throughout the entire experiment. A summary of all applied treatments and the respective stock and working solutions of all substances is given in **Table 3**. Treatment was performed through direct addition of working solution to the culture medium. Working solutions were prepared freshly for each experiment by addition of the respective volume of stock solution to PBS. For HU, VPA, and thymidine, the working solution was prepared freshly for each experiment through solvation of a defined quantity of powdered substance in the appropriate volume of PBS (cell culture medium for thymidine). Pretreatment with *O*^{6}BG was carried out 1 h prior to the addition of the alkylating agent ACNU to deplete the repair enzyme MGMT.

Table 3: Compounds used in this work.

Compound	Stock solution	Working solution
5-Fluorouracil	385 mM in DMSO (-80 °C)	1 mM
Doxorubicin	3.45 mM in DMSO (-80 °C)	100 µM
Entinostat	5 mM in DMSO (-80 °C)	500 µM
Fluorodeoxyuridine	40 mM in DMSO (-80 °C)	400 µM

Fluorouridine	10 mM in PBS (-20 °C)	1 mM
Hydroxyurea	powder (4 °C)	100 mM
Nimustine	10 mM in H_2O (-80 °C)	10 mM, 1mM
O^6-benzylguanine	10 mM in DMSO (-80 °C)	10 mM
Olaparib	20 mM in DMSO (-80 °C)	2 mM
Oxaliplatin	10 mM in DMSO (-80 °C)	1 mM
Uridine	100 mM in PBS (-20 °C)	100 mM, 1 mM
Valproic acid	powder (4 °C)	100 mM
Z-VAD-FMK	20 mM in DMSO (-80 °C)	20 mM

3.2.3 γ-irradiation of cells

Cells were irradiated using a ^{137}Cs radiation source (Gammacell 2000). To achieve a dose equivalent of 6 Gy, cells were irradiated for 126 s. Corresponding control cells were kept under equivalent conditions during the irradiation procedure.

3.2.4 Protein extraction, SDS-PAGE, and Western Blot

3.2.4.1 Cell lysate preparation

For whole cell lysate preparation, all following steps were carried out on ice to slow down the activity of proteases and phosphatases. The supernatant of the cell culture dish or well plate containing the treated cells was collected (unless stated otherwise) and the remaining adherent cells were washed with PBS to remove residual culture medium. The PBS fraction was collected and added to the collected supernatant. Adherent cells were detached using trypsin/EDTA (0.5 g/l) for 5 min before cell culture medium was added and cells were removed from the plate through resuspension. Cell suspension was added to the hitherto collected supernatant and PBS fraction. The plate was rinsed with PBS to ensure complete cell yield. The collected cell suspension was centrifuged (5 min, 317x g), the resulting cell pellet was washed with PBS, and transferred to 1.5 ml tubes. Centrifugation (5 min, 17,000 x g, 4 °C) yielded a cell pellet which was resuspended in lysis buffer. Dependent on the cell line, the pellet size, or the analyzed proteins, different lysis buffer systems were applied, or dried cell pellets were stored at -20 °C prior to lysis.

Cell lysates using NETN lysis buffer

Predominantly, cells were lysed for 30 min on ice using NETN lysis buffer freshly supplemented with protease inhibitor (cOmplete Mini) and 1:1000 phosphatase inhibitor cocktail 2 (**3.1.8**). Lysis solution was sonicated (10 pulses, amplitude 40%, 0.1 s pulse duration) to ensure complete lysis and centrifuged (15 min, 17,000 x g, 4 °C) to remove debris. Supernatant was stored as whole cell lysate at -80 °C. Protein concentration of NETN lysates was determined using Bradford assay.

Cell lysates using NuPAGE LDS buffer

Alternatively, cell lysates were prepared using NuPAGE LDS (4x) sample buffer (ThermoFisher Scientific) to determine protein expression of untreated cell cultures (e.g. to confirm knockdown following siRNA transfection), to determine BRG1 expression in Western Blot, or prior to global protein analysis via mass spectrometry. 1 ml NuPAGE lysis buffer (1x) was freshly prepared using 0.25 ml NuPAGE LDS (4x) sample buffer, 0.1 ml 1M DTT, and 0.65 ml ddH_2O. Cell pellets were resuspended in preheated (70 °C) NuPAGE lysis buffer (1x) and lysates were boiled for 10 min at 70 °C to ensure protein denaturation prior to sonification (10 pulses, amplitude 40%, 0.1 s pulse duration). NuPAGE lysates were stored at -20 °C.

3.2.4.2 Determination of protein concentration

The Bradford method was used as a photometric assay to allow quantitative determination of protein concentration in NETN lysates. It is based on the principle that the dye Coomassie Brilliant Blue G-250 shifts its absorbance from 470 nm to 595 nm after binding to protein sidechains under acidic conditions (Bradford 1976). Briefly, a calibration curve with 1 – 5 µg BSA as reference protein was pipetted into a 96-well plate in technical duplicates. 10 µl of a 1:10 solution of each NETN lysate in ddH_2O were loaded onto the plate and 200 µl Bradford reagent were added to each well containing calibration or sample solution. The absorbance of each well at 595 nm was determined following 5 min incubation time in the dark. As the measured absorbance is proportional to the protein concentration in each solution, sample protein concentration can be calculated in relation to the reference protein concentration.

3.2.4.3 SDS Polyacrylamide-Gel electrophoresis (SDS-PAGE)

For denaturation of proteins in NETN lysates, the volume of each lysate containing the desired amount of total protein (usually 20 – 40 µg / lane) was adjusted to a common total volume / lane for each gel by addition of ddH_2O. To each sample a fifth of this common total volume was subsequently added as sample buffer (6x) (e.g. 10 µl lysate in ddH_2O + 2 µl sample buffer (6x)). Lysates were heated for 5 min at 95 °C. NuPAGE lysates were loaded directly onto the gel. PageRuler^{TM} prestained protein ladder (Thermo Scientific) was loaded in one lane per gel to validate protein size. With respect to the molecular weight of the proteins of interest different compositions of the separation gels were used as described in **Table 4**. Run of SDS-PAGE was carried out in SDS-running buffer (**3.1.8**).

Whilst samples were concentrated inside the stacking gel, a constant voltage of 95 V was applied. During the run in the separation gel, voltage was increased over time in steps of 10 V to a final voltage of 125 V.

Table 4: Composition of SDS Polyacrylamide gels.

Components	Stacking gel (2x)	Separation gel			
		7.5%	10%	12.5%	10%
ddH_2O	4.4 ml	6.5 ml	5.7 ml	5.1 ml	4.3 ml
1.5 M Tris (pH 8.8)	-	3 ml	3 ml	3 ml	3 ml
1 M Tris (pH 6.8)	0.76 ml	-	-	-	-
10% SDS	60 µl	60 µl	60 µl	60 µl	60 µl
acrylamide	0.76 ml	2.3 ml	3.0 ml	3.6 ml	4.5 ml
10% APS	60 µl	60 µl	60 µl	60 µl	60 µl
TEMED	6 µl	6 µl	6 µl	6 µl	6 µl

3.2.4.4 Western Blot analysis

Following SDS-PAGE separation protein transfer onto nitrocellulose membrane was carried out in Transfer buffer (**3.1.8**) at a current of 175 mA / gel for 2 h at RT using the Mini Trans-Blot® Cell system equipped with cool pads. After transfer, the membrane was rinsed with Tris buffered saline containing 0.05% Tween-20 (TBST). Non-specific antibody binding was blocked by incubation of the membrane in 5% non-fat dry milk powder in TBST for 1 h. Primary antibodies (**3.1.6**) were diluted in 5% BSA or 2% non-fat dry milk powder in TBST according to manufacturer's specifications and incubated with the membrane over night at 4 °C. Following three washing steps with TBST for 5 min each, the suitable secondary antibody (**3.1.6**) was diluted 1: 10,000 in TBST and incubated with the membrane at RT for 2 h in the dark. The membrane was washed thrice with TBST for 5 min prior to detection of fluorescence signal with the LI-COR® Odyssey system. Relative protein expression was determined as signal intensity by densitometric analysis using Image Studio Lite Software (LI-COR).

3.2.5 Flow cytometry analyses

3.2.5.1 Analysis of cell cycle distribution and cell death by Propidium iodide staining

The fluorescent dye propidium iodide (PI) penetrates ethanol-fixed cells through perforated cell membranes and intercalates into cellular DNA. The resulting fluorescence signal intensity for each cell is proportional to its DNA content. Thus, the signal intensity of PI fluorescence of cells in G2-cell cycle phase (4n) is twofold higher than the signal intensity in cells with diploid DNA content (2n) in G1-cell cycle phase. Cells with intermediate fluorescence signal intensity can be allocated as dividing and replicating cells in S-phase with intermediate DNA content. Cells undergoing cell death programs loose DNA content through DNA fragmentation and show lower PI fluorescence signal intensity than G1-phase cells and are therefore termed as SubG1 cells. Analysis of a representative cell population thus results in a statistic distribution of PI fluorescence intensity that can be interpreted as the percental distribution of cell cycle phases in this cell population. **Figure S 7** shows representative gating (as dot plots) and cell cycle distribution (as histogram) for an exemplary cell population. Debris was excluded through gating of cells in the forward (FSC) and sideward (SSC) scatter and cell duplets were excluded through gating of cells in depending on the PI fluorescence signal width (PI(FL-3)-W) and area (PI(FL-3)-A). For determination of cell death and cell cycle distribution, adherent cells were harvested through detachment with trypsin/EDTA (see **3.2.4.1**) and the resulting collected cell solution was centrifuged (5 min, 317x g). The cell pellet was resuspended in 1 ml PBS to remove remaining cell culture medium. Anew centrifugation (5 min, 317x g) led to a cell pellet that was resuspended in 100 µl PBS. Fixation was carried out by addition of 2 ml ice-cold (-20 °C) 80% EtOH under constant vortexing and subsequent storage at -20 °C (min. 1 h, max. 1 week). Prior to measurement, samples were centrifuged (5 min, 317x g), resuspended in 334 µl RNAse A in PBS (final concentration of RNAse A for each sample: 20 µg/ml) and incubated for 1 h at RT. Samples were incubated for 10 min on ice following addition of 164 µl PI staining solution (final concentration of PI for each sample: 16.5 µg/ml), measured with the FACSCanto Flow Cytometer (BD Biosciences) and analyzed using FACSDiva^{TM} Software (BD Biosciences) or Flowing Freeware (Turku Centre for Biotechnology).

3.2.5.2 Autophagy detection by Cyto-ID staining

Autophagy was measured using the CYTO-ID® Autophagy Detection Kit (ENZO Life Sciences). CYTO-ID® stains accumulated autophagic vacuoles. Cell pellets were obtained and washed with 1 ml PBS as in **3.2.5.1**. Centrifugation (5 min, 317x g) yielded a cell pellet that was resuspended in 0.25 ml phenol red-free cell culture medium supplemented with 5% FCS. 1 µl CYTO-ID dye was diluted in 1 ml phenol red-free cell culture medium supplemented with 5% FCS and 250 µl of this dilution were added to each sample. Following resuspension, samples were incubated for 30 min at 37 °C in the dark. Anew centrifugation (5 min, 317x g) led to a cell pellet that was washed with 1 ml PBS and centrifuged (5 min, 317x g). The pellet was resuspended in 1 ml PBS and transferred to FACS tubes on ice prior to measurement at a FACSCanto Flow Cytometer (BD Biosciences). Data was analyzed using FACSDiva^{TM} Software (BD Biosciences). **Figure S 9** shows exemplary histograms obtained by this measurement.

3.2.6 Quantitative polymerase chain reaction (qPCR)

Renca cells were treated with HDACi as indicated, harvested, lysed and denatured with 1x sample buffer and stored at RT. Analysis by qPCR was kindly performed by [redacted] at LMU Munich, who is hereby gratefully acknowledged. In brief, total RNA was isolated by RNeasy kit (Qiagen), and qPCR was performed using the StepOnePlus real-time PCR device (Applied Biosystems). In a final volume of 20 µl, Power SybrGreen Master-Mix (Applied Biosystems), 20 ng cDNA, and 100 nM of forward and reverse primers were prepared. Experiments were performed in technical and biological triplicates and $\Delta\Delta C_t$ method was applied for analysis with β-actin as housekeeping control. Primer efficiencies were controlled using 10^(-1/slope). For detailed description of primer sequences see (Kiweler et al. 2018).

3.2.7 Immunofluorescence

3.2.7.1 Preparation of coverslips

20 x 20 mm coverslips were soaked in diethylether for 20 min and rinsed in a series of 100% ethanol, 70% ethanol and ddH_2O. Coverslips were subsequently washed in 1 M HCl on a shaker for 20 min, rinsed in ddH_2O and stored in 70% EtOH at 4 °C until usage.

3.2.7.2 Immunofluorescence staining

β-Catenin immunofluorescence in RCC cells

Cells were seeded on pretreated coverslips (**3.2.7.1**) in 6-well plates. After 24h treatment, cell culture medium was removed. Adherent cells were gently rinsed thrice with 2 ml PBS, fixed with acetone at -20°C for 2 min and air-dried. Non-specific antibody binding was blocked by incubation with 10% NGS in PBS/0.25% Triton-X-100 for 1 h at RT. Blocking solution was removed and coverslips were incubated with primary antibody solution (anti-βcatenin (BD610154) 1:200 in 10% NGS in PBS/0.25% Triton-X-100) at 4 °C overnight. Coverslips were washed thrice with PBS for 5 min and incubated with the appropriate AF488 coupled secondary antibody in solution (**3.1.6**, 1:400 in PBS/0.3% Triton-X-100) for 1 h at RT in the dark. Coverslips were washed thrice with PBS and stained with TO-PRO®-3 solution (100 µM stock diluted 1:100 in PBS) for 15 min at RT. Coverslips were rinsed with PBS, mounted with Vecatshield H-100 (Vector Laboratories), sealed with nail polish, and stored at 4 °C in the dark.

HDAC2 immunofluorescence in CRC cells

Cells were grown on coverslips for 24 h. Coverslips were washed twice with PBS. Cells were fixed with -20°C methanol:acetone (7:3) for 8 min. Coverslips were washed thrice with PBS prior to incubation with blocking solution (5% BSA, 0.3% Triton X-100 in PBS) for 1h at RT. Cells were incubated with HDAC2 primary antibody (sc9959) diluted 1:400 in PBS/1% BSA/0.3% Triton X-100 overnight at 4°C. Coverslips were washed three times with PBS and incubated with the appropriate AF488-conjugated secondary antibody (diluted 1:400 in PBS/0.3% Triton X-100) for 3 h at RT. Following three washing steps with PBS, the nuclear staining was performed for 15 min at RT using TO-PRO-3 (1 µM in PBS). Slides were mounted with Vectashield® (Vector Labs) and sealed with nail polish.

γH2AX and 53BP1 immunofluorescence in CRC cells

Cells (transfected or non-transfected) were seeded and grown on coverslips for 24 h before initiation of treatment as indicated. Following treatment period, cells washed twice with PBS and fixed with -20°C methanol:acetone (7:3) for 8 min. Coverslips were washed thrice with PBS and blocked with 5% BSA in PBS/0.3%Trition X100 for 1 h at RT. Coverslips were incubated overnight at 4°C with primary antibody against γH2AX (sc101696) and 53BP1

(MAB3802), each diluted 1:500 in PBS/1% BSA/0.3% Triton X-100. Coverslips were washed thrice with PBS and incubated with the appropriate secondary antibodies for 3 h at RT. For this purpose, Cy3-conjugated goat anti-rabbit was diluted 1:600 and AF488-conjugated goat anti-mouse was diluted 1:300 in PBS/0.3% Triton-X-100. Slides were washed thrice with PBS and stained with TO-PRO-3 (1 µM in PBS) for 15 min at RT. Slides were mounted with Vectashield® (Vector Labs) and sealed with nail polish.

Image capturing and analysis

Image capturing was attained via confocal microscopy using a Zeiss Axio Observer.Z1 microscope equipped with a LSM710 laser-scanning unit (Zeiss). Mean fluorescence intensity was quantified using ImageJ software. Quantification of protein foci was accomplished using ImageJ and the Foci Counter Macro provided by the Bioimaging Center of the University of Konstanz. ZEISS LSM Image Browser was used for image presentation and scale bar addition.

3.2.8 Single cell gel electrophoresis (SCGE)

SCGE, also known as COMET assay, allows for the detection and quantification of DNA damage on single cell level. Cells are embedded into agarose and lysed under alkaline conditions to ensure separation of both DNA strands and to allow detection of DNA double and single strand breaks. Submission of samples to electrophoresis leads to a migration of negatively charged DNA towards the anode. PI-stained migrated DNA fragments appear as a comet complete with head and tail, whose dimensions (e.g. tail length, head intensity, tail intensity) can be quantified and are proportional to the extent of broken DNA strands in the individual cell. In contrast to DNA fragments resulting from strand breaks, spacious genomic DNA is not submitted to movement in the electric current. In this work, the COMET assay was additionally modified to detect DNA ICLs that were formed upon treatment with the alkylating agent ACNU. For this reason, all samples were submitted to IR (**3.2.3**) prior to assay execution to induce DNA strand breaks and DNA fragmentation. The extent of crosslinked DNA can then be quantified because crosslinking in ACNU-pretreated, irradiated samples reduces DNA mobility and comet size compared to solely irradiated controls.

Slides were washed with EtOH and heated over a Bunsen burner. Slides were coated with 1% agarose (normal melting point) on one side and allowed to air dry. Cells were harvested after treatment with ACNU using a reduced trypsin concentration (0.005 g/l). Following resuspension in PBS, the cell number for each sample was determined using the automatic cell counter. The cell suspension of each sample was split equally into two parts permitting the irradiation (6 Gy) of one half of the sample, while the other half was kept as unirradiated control. Samples were immediately stored on ice to prevent DNA repair processes and all subsequent steps were carried out in the dark. 120 µl of each sample (2 x 10^4 cells/120 µl in PBS) were mixed with 120 µl low melting-point (LMP) agarose (1% in PBS, 37 °C). 120 µl of this LMP solution were spread onto the agarose-coated glass slides, covered, and solidified on ice. Coverslips were gently removed and slides were incubated in lysis buffer (**3.1.8**) for 1 h at 4 °C. Slides were transferred into the electrophoresis chamber and submerged in alkaline electrophoresis buffer (**3.1.8**) for 20 min at 4 °C to unwind DNA. Electrophoresis was performed for 20 min at 0.74 V/cm and 300 mA. Slides were washed thrice with neutralization buffer for 5 min prior to fixation in 100% ethanol at 4 °C for 20 min. Slides were air-dried, stored at 4 °C, and stained with 45 µl PI (50 µg/ml) for detection. Samples were analyzed by fluorescence microscopy using an Olympus BX50 microscope equipped with a ColorView camera. At least 50-100 cells were scored per sample using Comet IV software. Damage was measured as tail intensity in %, which is comprised of the sum of all measured pixel intensity values of the comet tail relative to total fluorescence intensity of DNA.

Tail intensity (%) = [total intensity (tail DNA) / total intensity (cellular DNA)] x 100

3.2.9 Determination of cell number and growth curves

Cells were seeded at a defined cell density to ensure exponential growth throughout the experiment. At the indicated timepoints cells were harvested through detachment with trypsin/EDTA (see **3.2.4.1**). Cell number was determined by counting in a Neubauer chamber. To determine viable cell number, dead cells were excluded by trypan blue. For this purpose, the cell suspension in PBS was diluted 1:1 with 0.4% (w/v) trypan blue in PBS. Cells that were stained blue were excluded. Growth curves were displayed using GraphPad Prism. Growth equations and doubling time were determined through nonlinear fitting of the given growth curve in Graph Pad Prism 6. Graph Pad Prism’s nonlinear regression dialog offers an equation model for exponential growth to permit curve fitting assuming a constant doubling time.

3.2.10 Documentation of cell morphology

Images of cellular morphology were captured using phase-change light microscopy. Observation and image acquisition were accomplished with a magnification of 100x using an AxioVert 35 microscope (Carl Zeiss), a digital Olympus color view soft imaging camera, and Olympus Cell^A 2.7 software. Cells were seeded at defined cell densities, to ensure exponential cell growth during the experiment, and treated 24 h post seeding. At least 10 images of each sample were taken for the indicated timepoints and treatment conditions. Representative pictures are shown.

3.2.11 Transient siRNA mediated knockdown

Cells were transfected with siRNA directed against targeted gene products (**0**) to achieve a temporary gene knockdown. Lipofectamine RNAiMAX reagent (Invitrogen) was used for transfection. Cells were transfected at a cell density of 60 – 80% with a ratio of 1.5:1

lipofectamine:siRNA in serum-free OptiMEM according to supplier’s protocol. 1 h prior to transfection, cell culture medium was exchanged to penicillin/streptomycin-free cell culture medium to minimize the toxicity of the transfection. 24 h post transfection, cells were reseeded and split 1:6 to 1:8 depending on the desired treatment time, analysis method, and required sample number. Treatment was carried out 48 h post transfection and 24 h after reseeding. Efficient knockdown was confirmed and quantified via Western Blot. Cells were transfected in parallel with the corresponding amount of non-targeting control siRNA.

Table 5: Amount of siRNA used for transient transfection. Values apply for transfection in 6-well plates in 2 ml cell culture medium; for siRNA specification see 0.

siRNA	amount
BRG1 siRNA	100 pmol
HDAC1 siRNA	20 pmol
HDAC2 siRNA	40 pmol
SMARCAD1 siRNA	25 pmol

3.2.12 Colony formation

24 h after seeding, Renca cells were treated as indicated. Subsequent to a 24 h treatment period, cells in the supernatant were collected, transferred to a new dish, and cultivated for 8 days. Cell culture medium was removed and plates were washed with 1 ml PBS. Cells were fixed by addition of 2 ml 100% MeOH and 20 min incubation at -20 °C. The fixative was discarded and plates were air-dried. Cells on culture plates were stained with 1 ml Giemsa stain (**3.1.8**) for 15 min at RT. Stain was removed, plates were gently rinsed with ddH$_2$O, and air-dried. Quantification of cell colonies was achieved through manual counting under a phase-change light microscope.

3.2.13 Proteome analysis

3.2.13.1 Sample analysis via mass spectrometry

Cells were treated as indicated and harvested as cell pellets through detachment with trypsin/EDTA as described in **3.2.4.1**. Cells were lysed and denatured in NuPAGE® LDS lysing buffer as described in **3.2.4.1**. Samples were analyzed by mass spectrometry at the IMB Proteomics Core Facility in Mainz by the lab of [redacted], who is hereby gratefully acknowledged. Briefly, the proteins were in-gel digested with mass spectrometry grade trypsin (Sigma-Aldrich) and purified using StageTip (Dejung et al. 2016). The resulting data was analyzed with Maxquant v1.5.2.8 using label-free quantitation (LFQ) and the ENSEMBL GRCm38 peptide database. The output data was further refined using custom R scripts. Specific protein expression data as log2 of LFQ intensity is further depicted in heatmaps that were generated using GraphPad Prism 7 software.

3.2.13.2 Pathway enrichment analysis for proteome analysis of Renca cells

In general, GO term analysis offers the possibility to assess the biological relevance of extensive proteomic or genomic data sets. Using a defined set of genes or proteins, that is significantly regulated under defined conditions, enrichment analysis will provide GO terms that are over- or under-represented under these conditions (Ashburner et al. 2000; Falcon and Gentleman 2007). Pathway enrichment analysis was conducted with Gene Ontology terms (www.geneontology.org) associated with the murine proteins by [redacted] at the IMB Proteomics Core Facility in Mainz, who is hereby gratefully acknowledged. Preceding statistical analysis using R software version 3.2 and unpaired t-test (two conditions) or one-way ANOVA (multiple conditions) resulted in the employed set of significantly regulated proteins. The background set was considered to be composed of all proteins successfully quantified in the experiment (5812 proteins). For each set of significantly regulated proteins, 3 hypergeometric tests (for biological processes, for molecular functions, and for cellular components) were executed using the R package “GOstats” to determine if the GO terms that were associated with significantly changing genes were over-represented over the background (Falcon and Gentleman 2007). For each protein listed, the Entrez gene ID was obtained using the annotation R package “BiomaRt”.

3.2.14 Scratch wound healing assay

During a typical scratch wound healing assay, an artificial gap in a cell monolayer is created through mechanical scratching and the closing of this gap, either by cellular migration or proliferation, can be monitored and quantified at regular intervals. Renca cells were seeded in 24 well-plates in triplicates at a defined cell density to ensure confluence 24 h after seeding. Pre-treatment with HDACi as indicated was performed for 14 h prior to scratch application to each well. Two perpendicular scratches forming a cross were applied to the cell monolayer in each well by gentle manual scraping with a 200 µl pipette tip. Cell culture medium was discarded and the wells were washed gently with 1 ml PBS. Fresh cell culture medium with a lower percentage of serum supplementation (5% FCS instead of 10% FCS) was added to minimize proliferation effects during the experiment. HDACi treatment was repeated to ensure continuous HDAC inhibition. Images of the samples in triplicates were taken at intervals of 2 h starting with the timepoint t=0 immediately after scratch application and medium change. To reduce variability in results, plates were marked so that images of approximately the same spot were taken over time. Image capturing was performed using the AxioVert 35 microscope (Carl Zeiss) equipped with a digital Olympus color view soft imaging camera and Olympus Cell^A 2.7 software. Open image area was quantified using the TScratch software Version 1.0 provided as freeware by the CSElab of the ETH Zurich (Gebäck et al. 2009).

4 Results

4.1 Effects of HDAC inhibition in renal carcinoma cells

4.1.1 Class I HDACi induce histone hyperacetylation, affect class I HDAC expression, and cell morphology

As previously reported, the hyperacetylation of histones H3 and H4 is a characteristic indication for class I HDAC inhibition (Beyer et al. 2017). To confirm that the HDAC inhibitors VPA and MS-275 are effective in Renca cells, the accumulation of acetylated forms of histone H3 and histone H4 was determined in whole cell lysates. Treatments were done with various doses of the HDACi for 24 h and 48 h (**Figure 13**). Treatment with all HDACi concentrations led to a clear induction of histone H3 acetylation at both timepoints. Hyperacetylation of histone H4 was observed for all applied treatment conditions except for treatment with 0.5 mM VPA. Overall, the observed levels of histone H3 and histone H4 hyperacetylation remained either stable or increased from 24 h to 48 h treatment time.

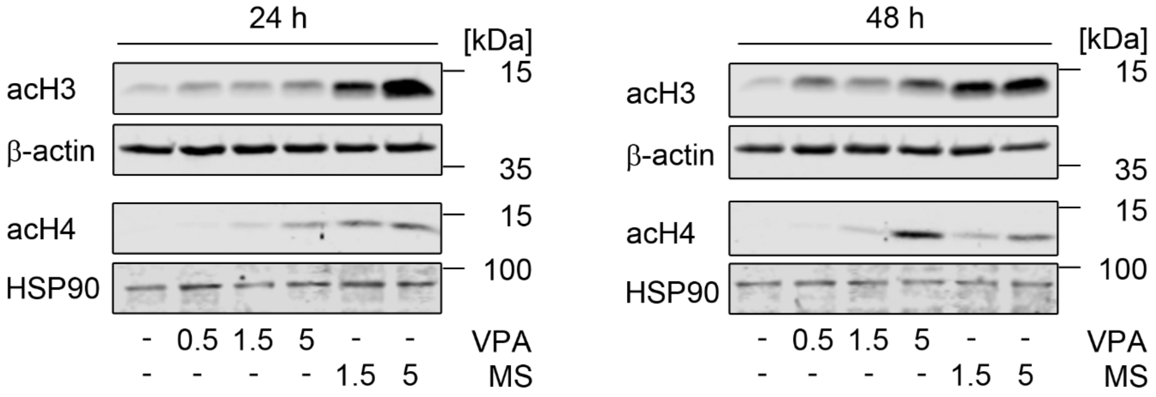

Figure 13: Class I HDAC inhibition induces histone hyperacetylation in Renca. Cells were treated with the indicated concentrations of VPA (mM) and MS-275 (µM) for 24 h and 48 h. Induction of the acetylation of the histones H3 and H4 was determined by Western Blot. HSP90 and β-actin served as loading controls.

It has previously been described for murine teratocarcinoma and human embryonic kidney cells that VPA not only selectivly inhibits the catalytic activity of class I HDACs, but additionally reduces HDAC2 expression through induction of its proteasomal degradation (Krämer et al. 2003). Having shown that the chosen HDACi treatment conditions effectivly induce histone hyperacetylation in Renca cells, changes in HDAC1, -2, and -3 expression were analyzed by Western Blot (**Figure 14**). Treatment with different concentrations of VPA for 24 h did not alter the expression levels of either of the three detected HDACs, whereas sustained treatment for 48 h with 5 mM VPA resulted in a reduction of HDAC2 expression and additionally attenuated the expression of HDAC1 and HDAC3. In contrast, treatment with MS-275 led to a transient induction of HDAC1 and HDAC2 expression levels after 24 h. Following 48 h treatment with the higher concentration of 5 µM MS-275 HDAC1, -2, and -3 levels slightly decreased compared to untreated control cells. While a reduction of HDAC2 expression by VPA but not by MS-275 has been reported in several cell types and tissues (Wagner et al. 2014), previous data also suggested that certain cell types retain stable HDAC2 levels in the prescence of VPA (Krämer et al. 2008b).

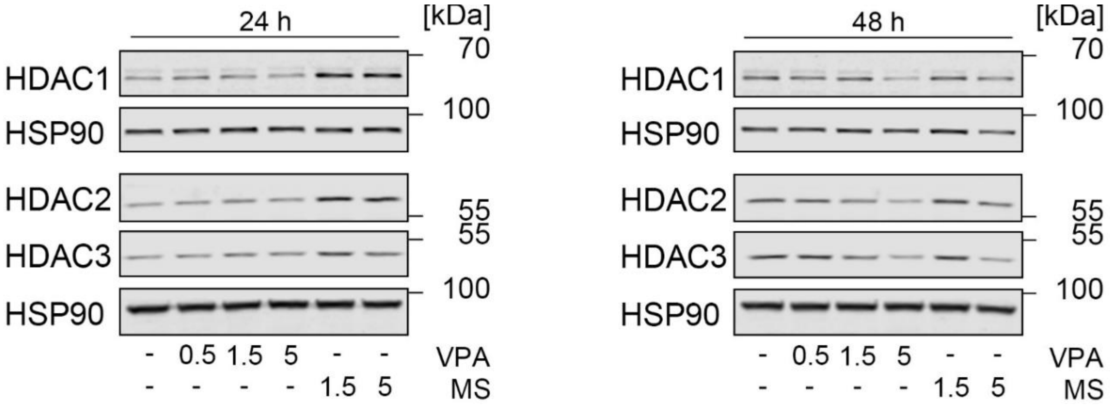

Figure 14: Class I HDAC expression in Renca in response to HDACi treatment. Cells were treated with the indicated concentrations of VPA (mM) and MS-275 (µM) for 24 h and 48 h. The expression of HDAC1, -2, and -3 was determined by Western Blot. HSP90 served as loading control.

To obtain a global overview of protein expression in response to HDACi treatment, Renca cells were treated for 24 h and 48 h with 1.5 µM and 5 µM MS-275 and submitted to global proteome analysis via label-free mass spectrometry. Therewith the basal as well as the dose- and treatment time-dependent expression levels of > 5000 proteins were determined (see section **3.2.13.1** and (Kiweler et al. 2018)). Hierarchical clustering analysis of significantly different expressed proteins is shown to demonstrate the multitude of proteins whose expression was influenced by MS-275 treatment (**Figure 15**). Only few clusters of proteins with a prominently increased or decreased expression were found in response to a 24 h treatment with 1.5 µM MS-275 (**Figure 15**). Changes in protein expression at 24 h were more notably induced with the higher MS-275 concentration of 5 µM (**Figure 15**). The most widespread changes in protein expression were obtained after prolonged treatment with either concentration. At least five clusters were discernable through significant expression changes after 48 h treatment (**Figure 15**). These data indicate, that the majority of changes in protein expression in response to MS-275 treatment occurred between 24 h and 48 h post treatment. Detailed examination of the mass spectrometric protein expression analysis supported the Western blot data that are presented in **Figure 13** and **Figure 14**. HDAC1, HDAC2, and HDAC3 protein expression did not change distinguishably in response to MS-275 treatment (**Figure 14**). Interestingly, the expression of HDAC6 increased up to 2-fold in MS-275-treated cells (**Figure S 1**). The measurement of the expression level of diverse other regulators of histone acetylation by mass spectrometry analysis allowed the further visualization of overall changes in histone acetylation. For instance, the expression levels of proteins that are directly or indirectly responsible for the acetylation of histone H3 (e.g. BRD7, BRD1) and histone H4 (e.g. HAT1, KAT7, KAT8) were altered considerably (**Figure S 1**). Furthermore, expression levels of BRD2, BRD3, and BRD4, which bind acetylated histones, were increased in response to MS-275 treatment (**Figure S 1**). Such alterations might sustain the hyperacetylation seen with HDACi.

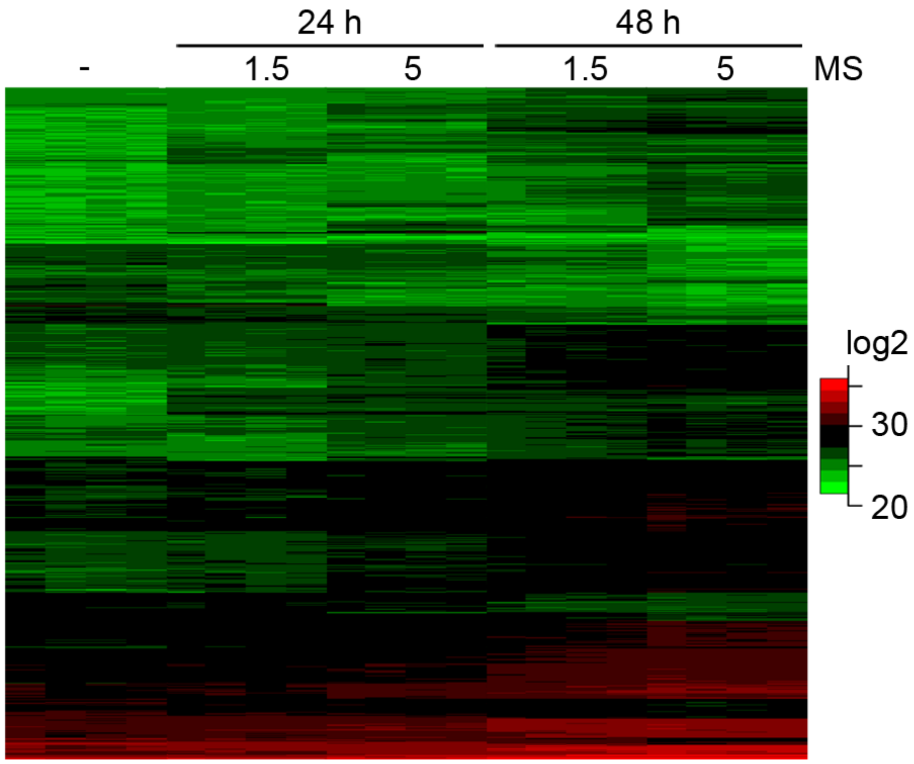

Figure 15: Heatmap of significantly different expressed proteins in MS-275-treated Renca. Hierarchical cluster analysis of protein expression following all applied treatment conditions (0 µM, 1.5 µM, and 5 µM MS-275 for 24 – 48h). The significant set of proteins considered for analysis was obtained through one-way ANOVA analysis by selecting those proteins that were significantly regulated in at least four of the total ten comparisons. Protein expression levels are depicted as log2 values of signal intensity obtained via mass spectrometry. Each row represents the expression levels of one protein under all applied treatment conditions. Statistical analysis and hierarchical clustering were kindly performed by [redacted] IMB Mainz. Complete dataset is published and can be accessed in (Kiweler et al. 2018).

Succeeding microscopical observation of Renca cells revealed that HDACi treatment induced characteristic alterations in cell morphology (**Figure 16**) that had previously been described in diverse cell types in response to various HDACi (Hoshikawa et al. 1994a; Byler et al. 2012; Kong et al. 2012; Jeon et al. 2013; Jiang et al. 2013; Cabanel et al. 2015; Ma et al. 2015; Wang et al. 2016; Wang et al. 2018). Whereas untreated Renca cells grew in distinct and clearly separated islands, HDACi-treated Renca cells grew in a scattered pattern with visible interspace between individual cells. Moreover, HDACi led to distinct alterations of overall cell shape. The cobblestone-like cell body of untreated Renca cells elongated and transformed in response to treatment to resemble a star-like outer cell contour.

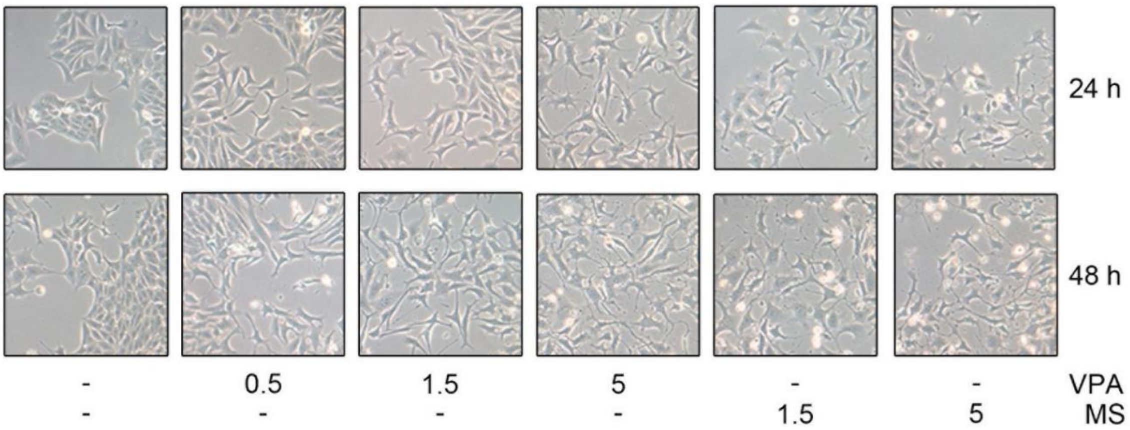

Figure 16: Class I HDACi induces morphological alterations in Renca. Cells were treated with the indicated concentrations of VPA (mM) and MS-275 (µM) for 24 h and 48 h. Cell morphology was documented with phase-change light microscopy. Images are representative for four independent experiments. Shown are sections of **Figure S 2**.

The observed morphological changes were already visible at 24 h with higher concentrations of VPA and with both concentrations of MS-275 but were most eminent following 48 h treatment in response to either HDACi (**Figure 16**). In summary, VPA and MS-275 are effective HDACi in Renca cells. The expression of HDAC1-3 was reduced after 48 h treatment at high HDACi concentrations. Strikingly, Renca cell morphology was highly affected by treatment with VPA and MS-275, indicating an impact of HDACi on substantial cellular processes.

4.1.2 Global proteome analysis to determine significantly regulated signaling pathways in response to HDACi treatment

The protein expression data resulting from proteome analysis via mass spectrometry was further submitted to computational analysis for identification of enriched gene ontology (GO) terms in response to MS-275 treatment (see section **3.2.13.2**). During this analysis, significantly regulated signaling pathways were determined on the one hand by direct comparison of all significantly regulated proteins in the samples using one-way ANOVA testing (multiple conditions; **Figure 17**). On the other hand, regulated signaling pathways were determined based on significantly altered protein expression in response to each treatment condition in direct comparison to untreated cells that were used as control group. The t-test was used for statistical analysis between the two conditions (**Figure 18** for 48 h 5 µM MS-275).

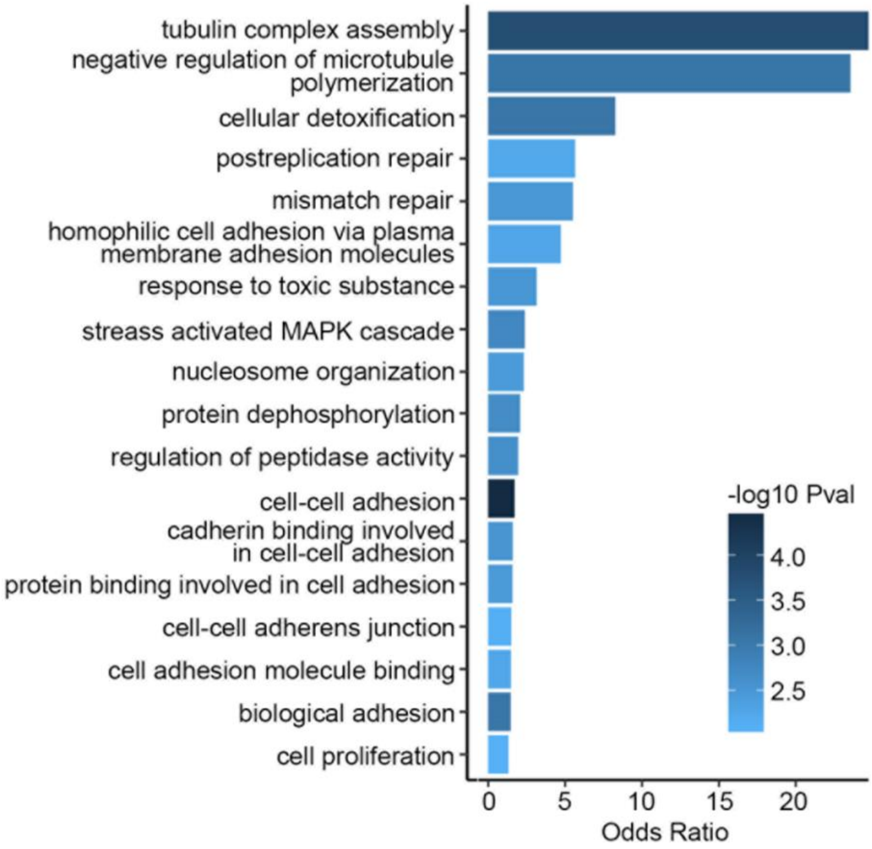

Figure 17: GO-term enrichment in response to all applied treatment conditions. GO-term enrichment following all applied treatment conditions (0 µM, 1.5 µM, and 5 µM MS-275 for 24 – 48h). The significant set of proteins considered for analysis was obtained through one-way ANOVA analysis by selecting those proteins that were significantly regulated in at least four of the total ten comparisons. Statistical analysis was kindly performed by [redacted] IMB Mainz. Complete list of all enriched GO-terms is shown in **Table S 1**.

The depicted signaling pathways are a selection of the complete GO-term analysis, which is shown in **Table S 1** and **Table S 2**. The pathways were chosen based on their relevance for the topics discussed in this work as well as the extent (-log 10 p-Value) and robustness (Odds ratio) of their regulation. The two analyses demonstrate that MS-275 treatment influences a large number of cancer-relevant signaling pathways and biological processes. Prominent alterations occurred for instance in pathways that regulate structural properties of Renca cells such as tubulin complex assembly, microtubule polymerization, and various forms of cellular adhesion. HDACi treatment also led to significant changes in epigenetic signaling pathways such as histone acetylation, DNA methylation, and nucleotide- and protein-phosphorylation. Furthermore, GO-terms with relevance for DNA repair signaling such as post replication repair and mismatch repair as well as ATP-dependent chromatin remodeling were significantly enriched. Both analyses showed the enrichment of several GO-terms that reveal HDACi-induced alterations of cell growth, cell death signaling, growth factor responses, and chromatin regulation. The morphological changes that are induced by HDACi treatment in Renca cells (**Figure 16**) resemble morphological changes described for epithelial cells undergoing EMT

(Zeisberg and Neilson 2009). However, no GO-terms connected to EMT signaling were found (**Figure 17**, **Figure 18**).

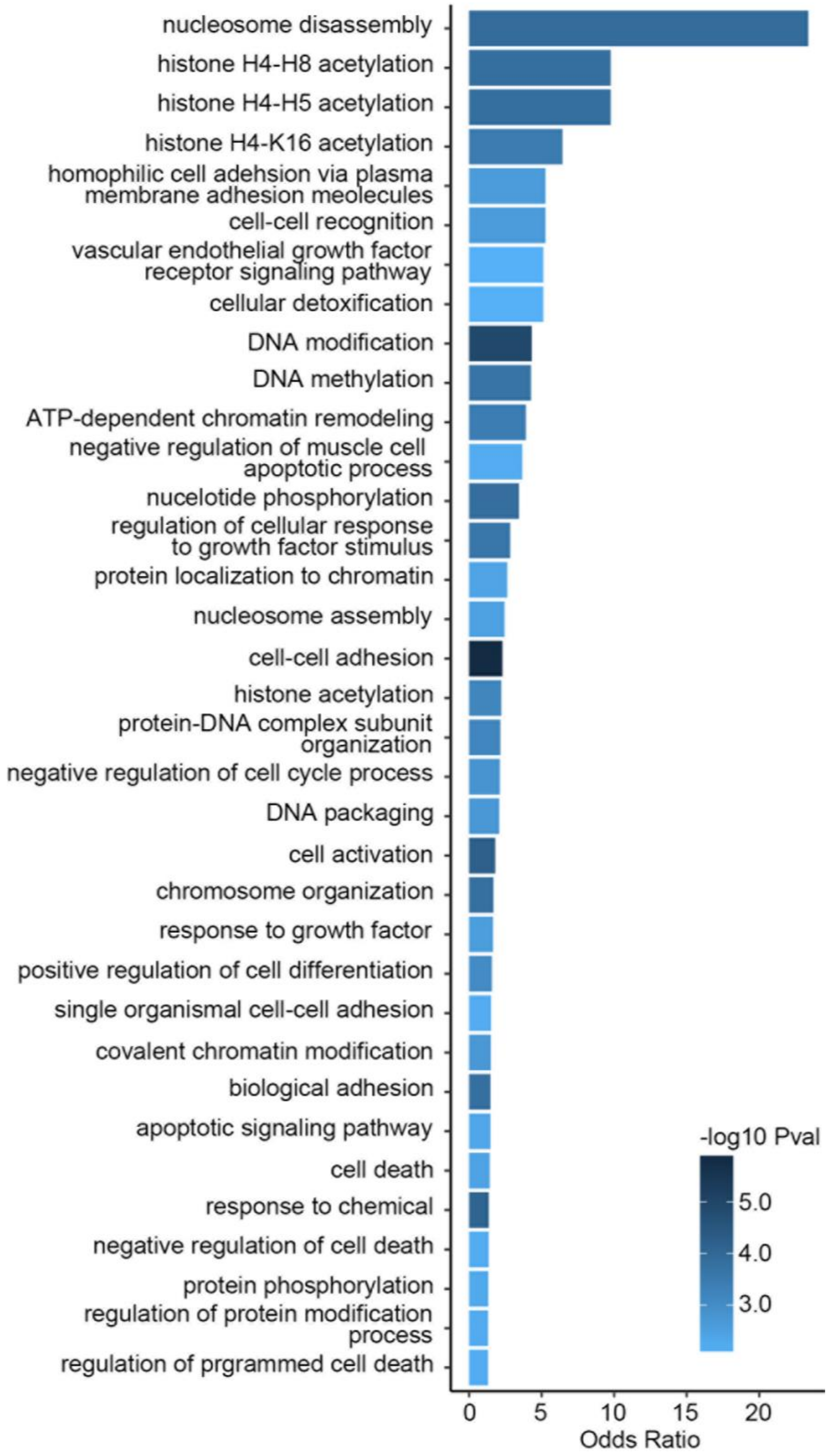

Figure 18: GO-term enrichment in response to 48 h 5 µM MS-275. The significant set of proteins that was considered for the analysis was obtained through unpaired Students t-test analysis by selecting those proteins that were significantly regulated in samples treated with 5 µM MS-275 for 48 h. Statistical analysis was kindly performed by [redacted] IMB Mainz. Complete list of all enriched GO-terms is shown in **Table S 2**.

In summary, mass spectrometric analysis of protein expression in Renca cells and subsequent GO-term enrichment analysis revealed a multitude of differently regulated cellular signaling pathways in response to HDACi treatment. These include central regulatory pathways of cell fate, such as cell growth, cell death, cell adhesion, cytoskeleton assembly, DNA damage repair, and epigenetic DNA modification. GO-term analysis thus served efficiently as a global survey of changed protein expression and cellular signaling in class I HDACi-treated Renca.

4.1.3 HDACi treatment does not affect EMT signaling

Although the proteomics analyses did not indicate a general and effective execution of EMT signaling pathways, the expression levels of a few individual EMT signature proteins in renal carcinoma cells such as E-cadherin (*Cdh1*), β-catenin *(Ctnnb1*), ZEB1 (*Zeb1*), and platelet derived growth factor receptor β (PDGFR-β, *Pdgfrb*) were downregulated (**Figure S 3**). To confirm that the observed morphological changes (**Figure 16**) were no indication for cellular transition, the mRNA expression levels of the characteristic EMT TFs SNAI1 (*Snai1*), SNAI2 (*Snai2*), TWIST1, -2 (*Twist1, -2*) and ZEB1, -2 (*Zeb1, -2*) were determined via qPCR analysis.

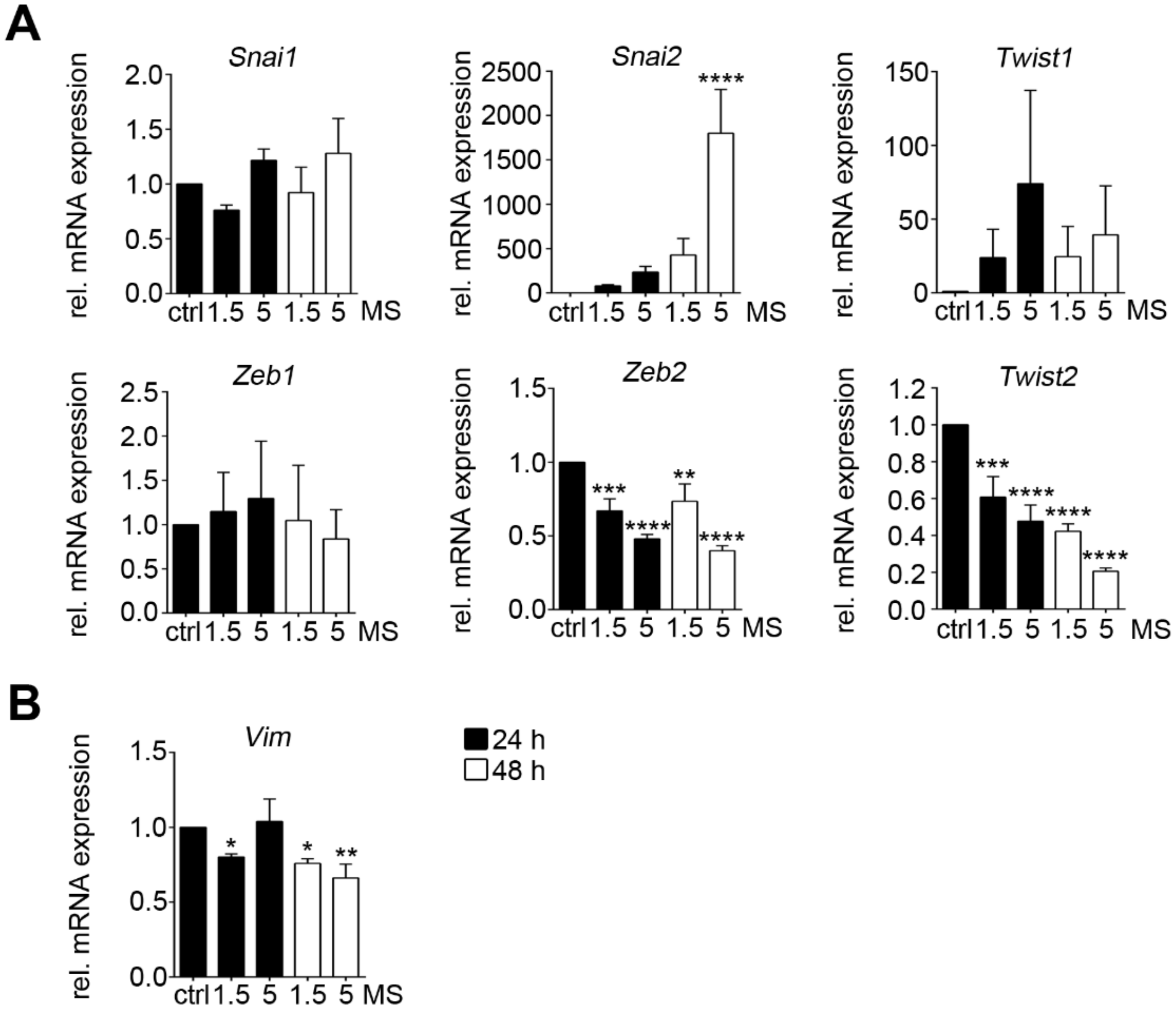

Figure 19: EMT transcription factor and Vimentin mRNA expression in response to HDACi treatment. Cells were treated with 1.5 µM and 5 µM MS-275 for 24 h and 48 h. (**A**) Independent triplicates were analyzed for quantitative mRNA expression of EMT transcription factor genes by qPCR analysis. (**B**) Independent triplicates were analyzed for quantitative mRNA expression of Vimentin gene by qPCR analysis. qPCR analysis was kindly

performed by [redacted] LMU Munich. Graphs show mean ± SD (n=3; one-way ANOVA; Dunnett multiple comparison test; ***P*<0.01, ****P*<0.001, *****P*<0.0001).

Twist1 mRNA was found to be insignificantly upregulated and *Twist2* mRNA was paradoxically downregulated following MS-275 treatment (**Figure 19A**). *Snai1* mRNA expression was not altered in response to MS-275 treatment and *Snai2* mRNA expression was strongly upregulated following treatment with 5 µM MS-275 for 48 h (**Figure 19A**). Albeit *Zeb1* and *Zeb2* are verified target genes of SNAI1 and SNAI2 (Lamouille et al. 2014) and should therefore be upregulated in response to enlarged SNAI2 expression, *Zeb1* mRNA levels did not alter and *Zeb2* mRNA was even downregulated following treatment with 1.5 µM and 5 µM MS-275 for 24 – 48h (**Figure 19A**). Hence, effective SNAI1/SNAI2-dependent gene expression seems to be impaired in Renca cells in response to MS-275 treatment. Furthermore, mRNA expression of the mesenchymal maker and filament protein Vimentin (*Vim*) was diminished in MS-275-treated cells (**Figure 19B**). This is consistent with its attenuated protein expression in mass spectrometry analysis (**Figure S 3**) after 48 h treatment. Another marker protein for mesenchymal cells is the cell-cell adhesion protein N-cadherin. Elevated expression of N-cadherin indicates for EMT signaling in metastasizing cancer cells (Zeisberg and Neilson 2009). Strikingly, Western Blot analysis showed no expression of N-cadherin in untreated and HDACi-treated Renca cells (**Figure S 4**). PC3 cells (a cell line derived from bone metastasis of prostatic adenocarcinoma), that were analyzed in parallel as positive control for their metastatic origin, showed characteristic expression of N-cadherin, thereby verifying the specificity of the N-cadherin antibody. The expression of E-cadherin, as marker protein for epithelial cells, was found to be diminished in Western blot analysis (**Figure 20**). Quantification of E-cadherin signal intensity confirmed, that this reduction of E-cadherin protein was significant after 24 h treatment in four of five treatment conditions and in all treatment conditions after 48 h. At the same time, mRNA expression of E-cadherin (*Cdh1*) was not altered after 24 h with both concentrations of MS-275 (**Figure S 5**). 48 h treatment with 5 µM MS-275 led to a loss of *Cdh1* mRNA transcription (**Figure S 5**).

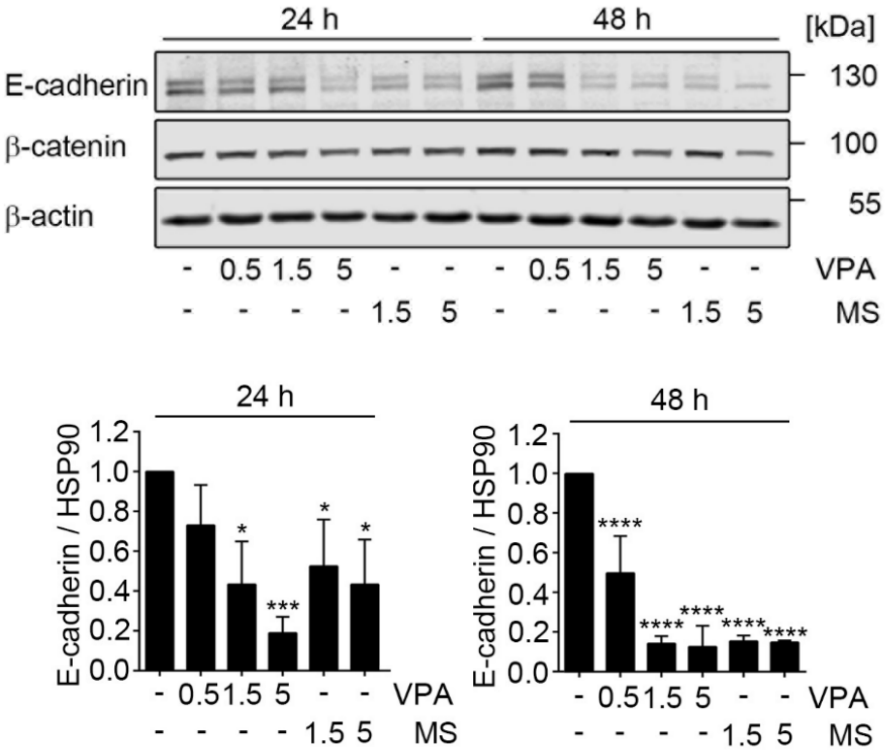

Figure 20: E-Cadherin and β-catenin expression in HDACi-treated Renca. Cells were treated with the indicated concentrations of VPA (mM) and MS-275 (µM) for 24 – 48h and analyzed for E-cadherin and β-catenin expression in Western blot. β-actin served as loading control. Quantification of E-cadherin expression was achieved by densitometric analysis of E-cadherin signal intensities and normalization to respective loading control signal intensities. Graphs depict relative levels of E-cadherin expression as mean ± SD (n=3; one-way ANOVA; Dunnett multiple comparison test; *P<0.05, ***P<0.001, ****P<0.0001).

A loss of E-cadherin expression could cause a liberation of its binding partner β-catenin out of the adherens junction complex at cell-cell junctions in epithelial tissue. This could initiate β-catenin translocation to the nucleus, which is considered to be one of the first steps of EMT (Conacci-Sorrell et al. 2002; Bienz 2005; Zeisberg and Neilson 2009). In HDACi-treated Renca cells, β-catenin protein expression was slightly diminished after 48 h (**Figure 20**). This loss of β-catenin protein (encoded by the *Ctnnb1* gene) could also be confirmed with mass spectrometry analysis of global protein expression (**Figure S 3**). In addition to expression levels, intracellular β-catenin localization was studied by confocal microscopy. In untreated Renca cells, β-catenin localization was restricted to the cytoplasm, with a partially higher fluorescence intensity detectable at the inner cell membrane (**Figure 21**). As shown with phase-change light microscopy in **Figure 16**, morphology of Renca cells was visibly altered in response to VPA and MS-275 treatment (**Figure 21**). Although HDACi treatment resulted in a more evenly cytoplasmic staining, indicating a loss of membrane bound β-catenin in response to E-cadherin downregulation, there was no nuclear β-catenin translocation visible in VPA- and MS-275-treated cells (**Figure 21**). Quantification of β-catenin signal intensity in ToPro3-stained nuclei confirmed that the overall nuclear β-catenin fluorescence intensity did not significantly increase in response to HDACi treatment (**Figure 21**).

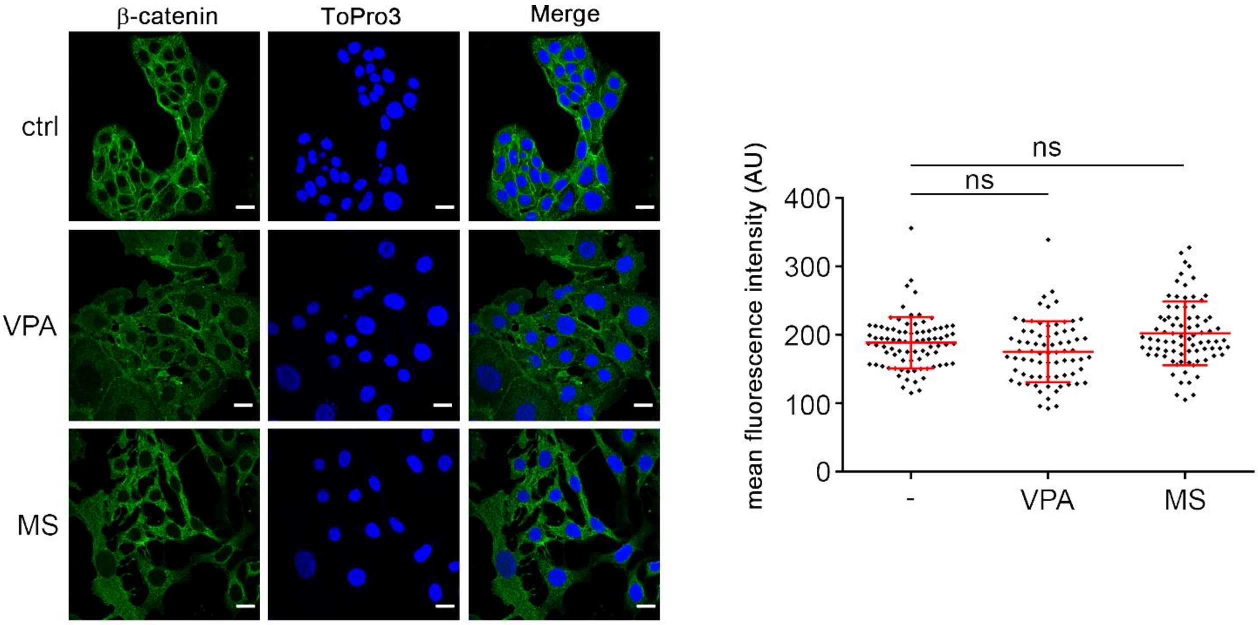

Figure 21: Immunofluorescence analysis of β-catenin localization in Renca in response to HDACi treatment. Cells were treated with 1.5 mM VPA and 1.5 µM MS-275 for 24 h. Cell nuclei were stained with ToPro3. Chosen pictures are representative images of three independent experiments. Scale bar corresponds to 20 µm. Immunofluorescent staining was kindly performed by [redacted] Nuclear β-catenin signal was quantified as mean fluorescence intensity of AF488 in arbitrary units (AU) in ToPro3 stained nuclei. Each dot represents the fluorescence intensity of a single nucleus. 74 - 83 cells were counted for each treatment condition. Graph shows mean ± SD (one-way ANOVA; Tukey's multiple comparison test; ns = no significant differences).

Since an increased cellular migration is a hallmark of cells undergoing EMT, our collaboration partners [redacted] (Clinic of Obstetrics and Women's Health, University Medical Center Mainz) determined the migratory potential of Renca cells by performing a chemotactic migration assay using a Boyden chamber. The assay showed that 1.5 mM and 5 mM VPA as well as 1.5 µM and 5 µM MS-275 treatment for 24 h did significantly reduced the number of migrated Renca cells compared to control (Kiweler et al. 2018).

To further strengthen this finding, migratory behavior of Renca cells in response to HDACi treatment was additionally determined with Scratch assay. Whereas the Boyden chamber assay quantifies migration of cells in solution, the Scratch assay is performed with adherent cells. Cell culture plates containing HDACi-pretreated triplicates of Renca cells were mechanically scratched to receive a straight cell free area on each plate (see **3.2.14**). Cellular migration towards this scratch was then monitored via image capturing using phase-change light microscopy at different time points post-scratching. Exemplary images for the timepoints t = 0 h and t = +10 h are shown in **Figure S 6**. Quantification of open image area showed that there was no significant difference of wound healing capacity in response to HDACi treatment as the open image area of all samples declined equally over time (**Figure 22**).

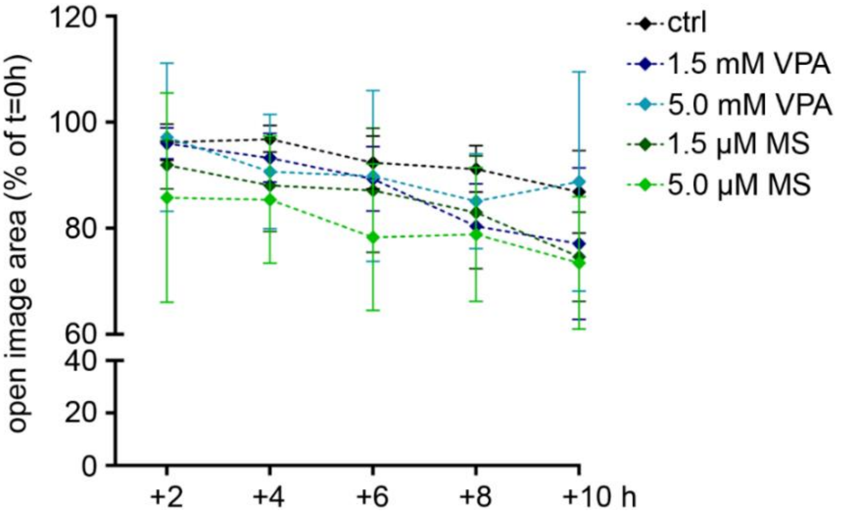

Figure 22: Quantification of Scratch assay in HDACi-treated Renca. Cells were pretreated for 14 h with the indicated concentrations of VPA and MS-275. Cells were submitted to Scratch assay at t = 0h and images of cells were taken every 2 h. Open image area of all samples in triplicates was quantified using TScratch software. Graph shows mean ± SD (n=2, triplicates). Exemplary images for t = 0h and t = +10h are shown in **Figure S 6**.

Alongside TF-dependent changes of gene expression, advantageous growth factor signaling is required to gain effective EMT execution. For human RCC, signaling via PDGFRβ has been shown to be a major driver of cell growth and pulmonal metastasis formation (Xu et al. 2005). Mass spectrometric analysis hinted at a downregulation of PDGFRβ expression (**Figure S 3**). This finding was confirmed by Western blot analysis (**Figure 23**). Quantification of PDGFRβ signal intensities showed that expression of the receptor was significantly reduced with 1.5 mM and 5 mM VPA as well as with 1.5 µM and 5 µM MS-275 after 48 h treatment (**Figure 23**).

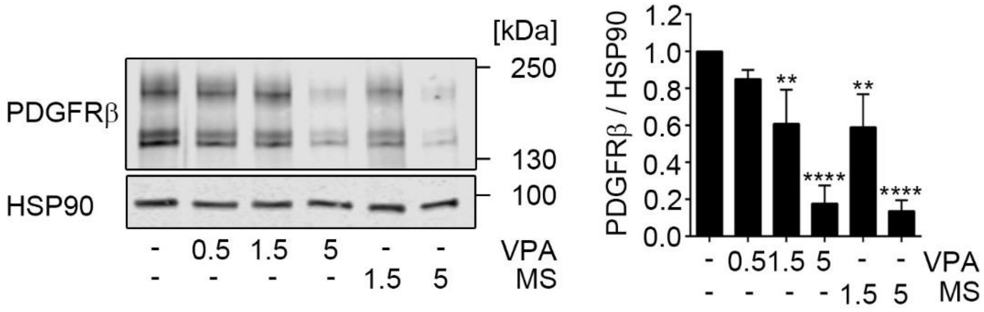

Figure 23: PDGFRβ expression in HDACi-treated Renca. Cells were treated with the indicated concentrations of VPA (mM) and MS-275 (µM) for 48h and analyzed for PDGFRβ expression in Western blot. HSP90 served as loading control. Quantification of PDGFRβ expression was achieved by densitometric analysis of PDGFRβ signal intensities and normalization to respective loading control signal intensities. Graph depicts relative levels of PDGFRβ expression as mean ± SD (n=3; one-way ANOVA; Dunnett multiple comparison test; ***P*<0.01, *****P*<0.0001).

In summary, HDACi treatment did not lead to effective EMT execution in Rena cells. Analysis of the mRNA expression of the major EMT TFs did not hint to an effective induction of subsequent EMT signaling pathways (**Figure 19A**). Although the central epithelial marker E-cadherin was downregulated in response to HDACi treatment, there was no upregulation of the central mesenchymal marker proteins Vimentin and N-cadherin (**Figure 19B**, **Figure 20**,

Figure S 4). Effective downstream signaling of E-cadherin loss in terms of β-catenin liberation and nuclear translocation was not detectable (**Figure 21**). Furthermore, neither Boyden chamber nor Scratch assay provided any indication for an enhancement of the migratory potential of HDACi-treated Renca cells (**Figure 22**) (Kiweler et al. 2018). Finally, the expression of PDGFRβ, a central driver of renal metastasis, was shown to be significantly downregulated (**Figure 23**).

4.1.4 HDAC class I inhibition impedes growth and survival of Renca cells

Mass spectrometric analysis of global protein expression showed that HDAC inhibition by MS-275 alters global cell death signaling pathways (**Figure 17**, **Figure 18**) as well as the individual expression levels of characteristic regulator proteins of apoptotic signaling (**Figure 24**). Modulated factors include the antiapoptotic protein Survivin (encoded by the *Birc5* gene) and the apoptosis executers APAF-1 (*Apaf1*), Caspase 3 (*Casp3*), and Caspase 6 (*Casp6*). There was also an upregulation of different MAP kinases detectable. The apoptotic regulator BAX (*Bax*) was not affected, whereas the expression of other BCL-2 family members (*Bak1*, *Bid*, and *Bad*) was slightly regulated.

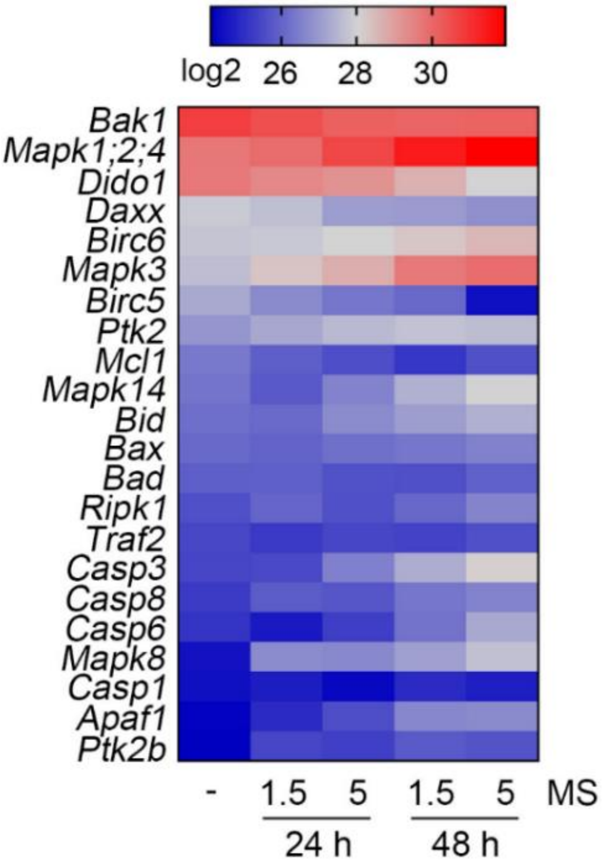

Figure 24: Heatmap of protein expression of cell death regulators. Cells were treated with the indicated concentrations of MS-275 (µM) for 24–48 h. Four independent replicates were analyzed for global protein expression by LFQ via mass spectrometry. Heatmap lists changes in LFQ expression levels of the indicated proteins with implication in cell death signaling.

To confirm apoptosis execution in Renca cells in response to HDACi treatment, the expression levels and cleavage fragments of members of the apoptotic caspase cascade were detected by Western blot analysis (**Figure 25**). The initiator caspase Caspase 9 was cleaved in all HDACi-treated samples after 24 h, with a second cleavage fragment being detectable at higher concentrations of HDACi after 48 h treatment (**Figure 25**). The basal levels of the executioner caspase Caspase 6 were confirmed to be upregulated in response to 5 mM VPA and 5 µM MS-275 at 48 h (**Figure 25**). A second executioner caspase Caspase 3 was found to be cleaved with higher HDACi concentrations at 24 h and with all HDACi concentrations, except for 0.5 mM VPA, at 48 h (**Figure 25**). In parallel, the expression of the antiapoptotic protein Survivin was reduced after 48 h VPA and MS-275 treatment (**Figure 25**). These data confirm the mass spectrometry results (**Figure 24**).

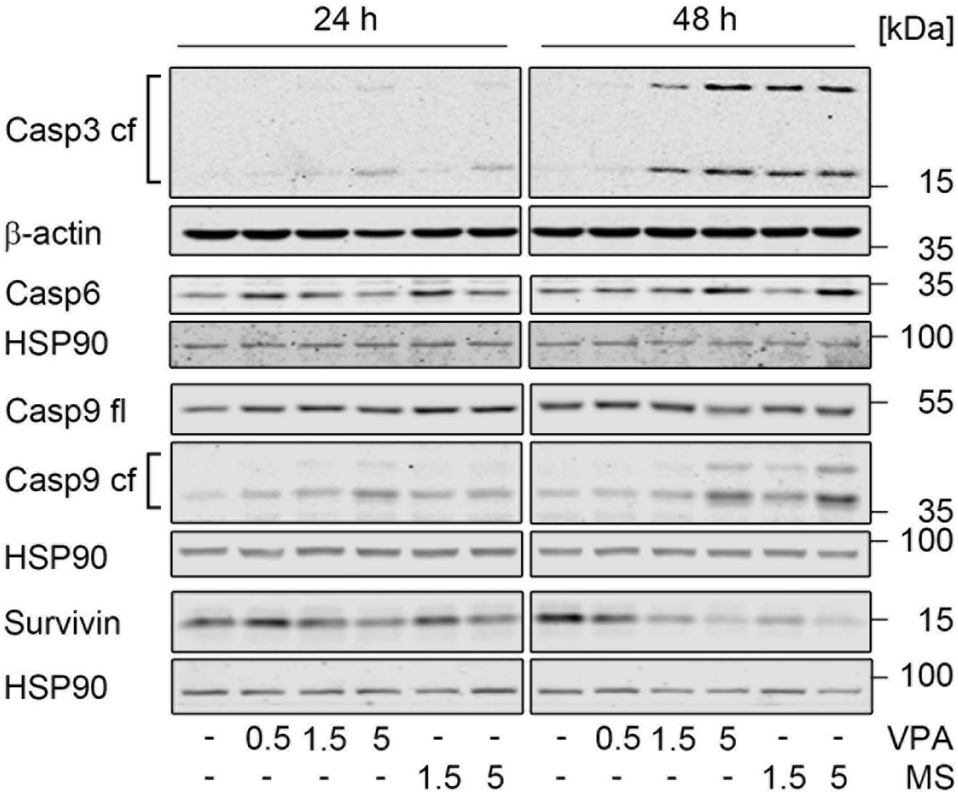

Figure 25: Caspase cleavage and Survivin expression in HDACi-treated Renca. Cells were treated with indicated concentrations of VPA (mM) and MS-275 (µM) for 24 – 48 h. Expression levels of the indicated proteins were determined by Western blot analysis. HSP90 and β-actin served as loading control.

Subsequent to analysis of the apoptotic signaling cascade, the extent of cell death was measured by flow cytometry. Nuclear DNA of HDACi-treated Renca cells was stained with PI to receive a quantitative predication of the percentage of cells in all different cell cycle phases. In this analysis, dead cells (subG1 fraction) are defined as all cells harboring fragmented DNA (DNA content below 2*n*). The percentage of the subG1 fraction was already increased significantly after 24 h treatments with 5 mM VPA and 5 µM MS-275 (**Figure 26**). 48 h post treatment, the percentage of dead cells increased further to about 35% for these two concentrations of VPA and MS-275 (**Figure 26**). In addition, cell death was triggered significantly in response to 1.5 µM MS-275 after 48 h. 0.5 to 1.5 mM VPA did not lead to a significant increase in cell death. However, there was a trend to an elevated percentage of subG1 fraction with 1.5 mM VPA at 48 h (**Figure 26**). Strikingly, the extent of cell death correlates with the intensity of the observed morphological alterations of Renca cells in response to HDACi treatment (**Figure 16**).

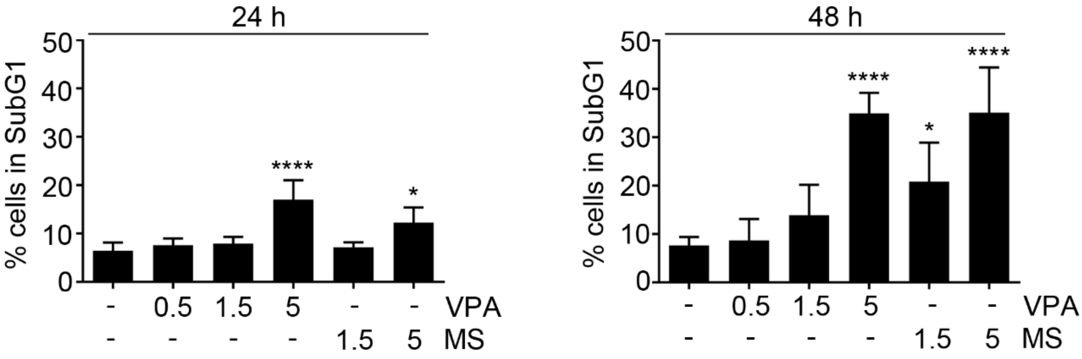

Figure 26: Cell death induction in HDACi-treated Renca. Cells were treated with the indicated concentrations of VPA (mM) and MS-275 (µM) for 24 h and 48 h. Cell death was determined by flow cytometry analysis of fixed and PI-stained cells as fraction of cells with fragmented DNA (subG1 fraction). Graph shows mean ± SD (n=4; one-way ANOVA; Dunnett's multiple comparison test; *P<0.05, ****P<0.0001).

Detection of DNA single and double stand breaks in Renca cells was achieved with the alkaline COMET assay. Distinct increase in tail intensity of was observed with 5 µM MS-275 after 24 h and with 1.5 µM and 5 µM MS-275 after 48 h treatment as strand breaks were induced around 6- to 9-fold in response to treatment (**Figure 27**). The observed DNA damage induction generally correlated with cell death induction and thus represents DNA SSBs and DSBs that are formed in cells entering apoptosis. Hence, the detected strand breaks are likely a direct consequence of cell death and additionally confirm apoptosis induction in MS-275-treated Renca cells.

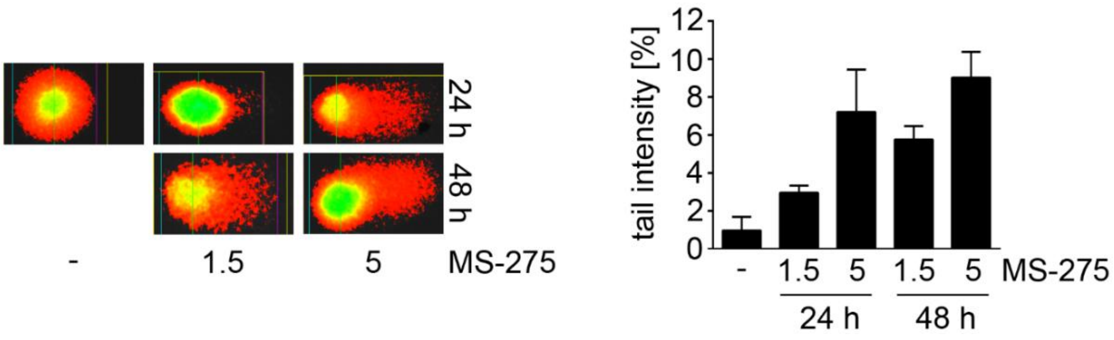

Figure 27: Alkaline COMET-Assay of HDACi-treated Renca. Cells were treated with the indicated concentrations of MS-275 for 24 h and 48 h. Tail intensity of the individual experiments was quantified. Graph shows mean ± SD (n=2). Analysis of HDACi-treated cells via COMET assay was kindly performed by [redacted] University Medical Center Mainz.

Induction of DNA damage in terms of DNA strand break formation was further confirmed through analysis of phosphorylation of the histone H2AX (γH2AX) in HDACi-treated Renca cells via Western blot. γH2AX formation was clearly enhanced with all applied HDACi concentrations at 24 h as well as at 48 h after treatment (**Figure 28**). The observed γH2AX induction generally correlated with cell death in response to treatment (**Figure 26, Figure 28**). Curiously, similar extent of cell death induction, for instance after 48 h treatment with 5 mM VPA and 5 µM MS-275, was associated with a stronger γH2AX induction in VPA-treated samples than in MS-275-treated samples (**Figure 26, Figure 28**). These data suggest that the accumulation of γH2AX in VPA-treated cells is not merely a consequence of apoptosis.

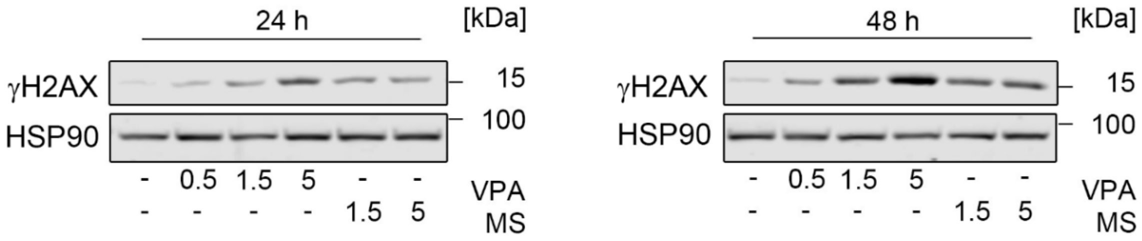

Figure 28: Phosphorylation of histone H2AX in HDACi-treated Renca. Cells were treated with the indicated concentrations of VPA (mM) and MS-275 (µM) for 24 h and 48 h. Phosphorylation of histone H2AX was analyzed by Western blot analysis. HSP90 served as loading control.

To further clarify the effects of HDACi treatment in Renca cells, the cell cycle distribution of the surviving cells following treatment was analyzed. For this purpose, the shown subG1 fraction was mathematically omitted after the measurement and the cell cycle was calculated to consist solely of cells with a DNA content of 2*n* (G1-phase), 2-4*n* (S-phase), and 4*n* (G2/M-phase). The analysis showed that at 24 h post treatment, cell cycle distribution was significantly altered with 5 mM VPA and 1.5 µM and 5 µM MS-275 (**Figure 29, Figure S 8**). The percentage of cells in S-phase was significantly reduced in response to these three treatment conditions (**Figure S 8**). Moreover, 5 mM VPA as well as 5 µM MS-275 did significantly reduce the percentage of cells in G2-phase as well as increase the percentage of cells in G1-phase (**Figure S 8**). Following 48 h treatment, the significant reduction of cells in in G2-phase and the significant induction of cells in G1-phase in response to 5 mM VPA and 5 µM MS-275 were sustained (**Figure S 8**). However, there were no longer significant changes in S-phase proportion detectable at 48 h (**Figure S 8**).

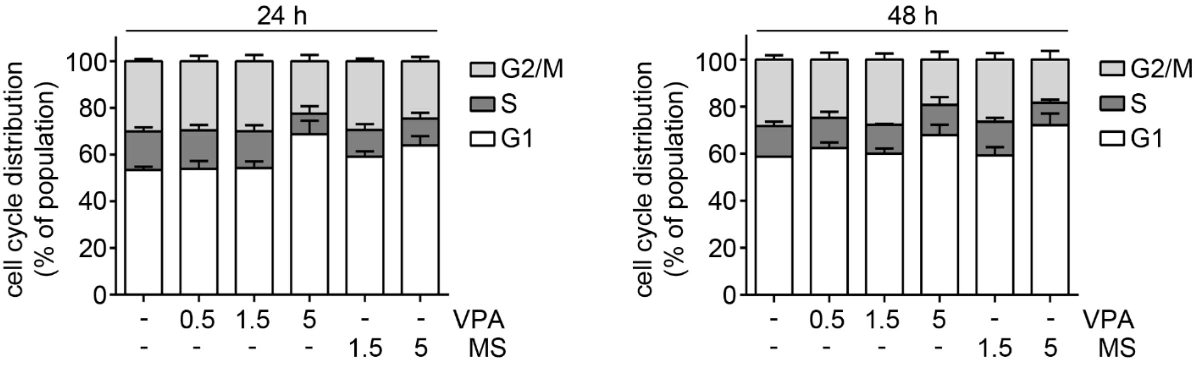

Figure 29: Cell cycle distribution of HDACi-treated Renca. Renca cells were treated with the indicated concentrations of VPA (mM) and MS-275 (µM) for 24 h and 48 h. Cell cycle distribution was determined by flow cytometry analysis of fixed and PI-stained cells. Cells with fractionated DNA (subG1 fraction) were excluded to receive the cell cycle distribution of the viable cell population. Graph shows mean ± SD (n=4). For statistical analysis of individual cell cycle phases see **Figure S 8**.

As cell cycle changes often imply variations in cell growth and proliferation, the number of viable cells in response to HDACi treatment at 24 h was determined. This early timepoint was chosen to ensure that a reduction in the number of viable cells was not primarily due to the execution of cell death (**Figure 26**) and could therefore be accounted as proliferation effect. The analysis showed that the viable cell number was reduced significantly with 1.5 mM and 5 mM VPA as well as with 1.5 µM and 5 µM MS-275 in comparison to untreated controls (**Figure 30**).

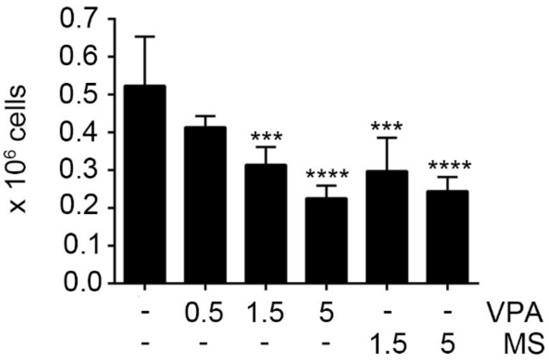

Figure 30: Viable Renca cell number in response to HDACi treatment. Cells were treated with the indicated concentrations of VPA (mM) and MS-275 (µM) for 24 h. Dead cells were excluded through trypan blue staining and viable cell population was counted in a Neubauer chamber. Graph depicts mean ± SD (n=5; one-way ANOVA; Dunnett's multiple comparisons test; ***P<0.001, ****P<0.0001).

As apparent in **Figure 16**, the visible number of cells in suspension was increased in response to HDACi treatment. To resolve whether these detached Renca cells are dead or viable and proliferative, meaning conceivably able to relocate and adhere at distant sites in *in vivo* experiments, supernatant cells were collected and reseeded in new plates in fresh growth medium. The colony formation ability was significantly reduced in all HDACi-treated samples compared to controls (**Figure 31**), even though the initial number of detached cells in untreated controls was visibly lower (**Figure 16**). There were no colonies detectable in response to treatment with 5 mM VPA and 5 µM MS-275 (**Figure 31**). Phase-change light microscopy following treatment with 0.5 mM VPA, 1.5 mM VPA, and 1.5 µM MS-275 showed furthermore that the resulting colonies displayed a reduced number of cells per colony compared to control (data not shown). These results indicate, that detached cells in HDACi-treated samples were genuinely apoptotic and did not represent a cell population that gained increased metastatic potential through activation of EMT signaling.

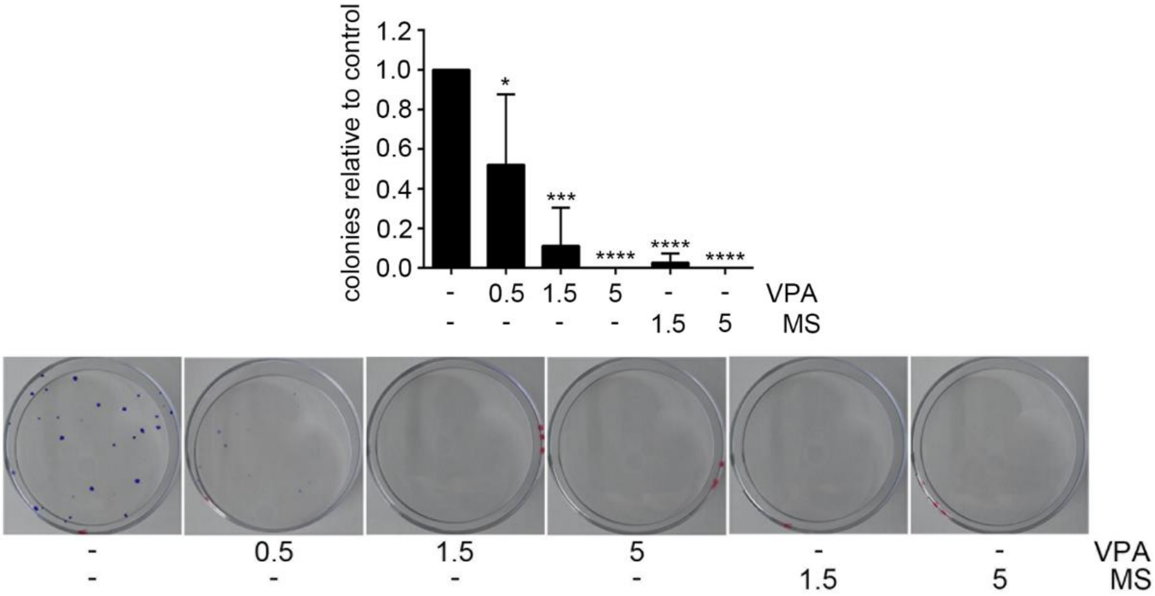

Figure 31: Cell colony formation of supernatant Renca cells in response to HDACi. Cells were treated with the indicated concentrations of VPA (mM) and MS-275 (µM) for 24 h. Cells in supernatant were collected, transferred to new dishes and cultivated for 8 days. Subsequently, adherent cells were fixed and stained with Giemsa-stain. Quantification of cell colonies was accomplished optically via phase-change light microscopy. Graph shows mean ± SD (n=3; one-way ANOVA; Dunnett's multiple comparison test; *P<0.05, ***P<0.001, ****P<0.0001).

To furthermore analyze, how Renca cells are affected by HDACi treatment in an *in vivo* setting, our collaboration partner [redacted] at the Georg-Speyer-Haus/Institute for Tumor Biology and Experimental Therapy in Frankfurt am Main employed a Renca^{lacZ} xenotransplantation model (Maurer-Gebhard et al. 1999; Kiweler et al. 2018). Renca^{lacZ} cells were injected into the tail vein of BALB/c mice and allowed to grow for eleven days. HDACi treatment was carried out from day eleven to day thirty-nine and mice were treated with 400 mg/kg VPA i.p. or PBS as vehicle control twice daily. Renca^{lacZ} cells efficiently formed pulmonary colonies, that could be stained due to expression of the *lacZ* transgene. Quantification showed that treatment with VPA led to a significant reduction of quantity and size of Renca cell colonies that seeded into the lungs (Kiweler et al. 2018). These data verify that an inhibition of class I HDACs effectively impairs tumor growth *in vivo*. In summary, these data demonstrate that class I HDAC inhibition effectively induces apoptotic signaling pathways in Renca cells. Moreover, cell cycle distribution was affected and cell growth was reduced *in vitro* and *in vivo*. The finding that HDACi-treated cells in the supernatants were not able to reseed and to effectively form secondary colonies further proves that apoptotic cell death and growth inhibition are predominate HDACi effects. Taken together, these analyses confirm the findings that we obtained with the global protein expression and subsequent GO-term analysis. They additionally indicate proliferative effects, cell death induction, and changes in cellular adhesion and cytoskeleton assembly as key cellular response to HDACi (**Figure 17, Figure 18**).

4.1.5 Assessment of autophagy in Renca cells in response to HDACi treatment

As HDACi have been shown to induce autophagy as survival mechanism in several cellular systems (Zhang et al. 2015; Göder et al. 2017; Mrakovcic et al. 2017), flow cytometric analysis to assess mean fluorescence intensity of the autophagic vesicle marker CYTO-ID® in Renca cells was conducted (**Figure 32A, Figure S 9**). A 24-h treatment with HDACi did not change the mean fluorescence intensity of CYTO-ID®, indicating that no differences of the autophagic flux occurred at early timepoints. However, a 48 h treatment with 5 mM VPA, 1.5 µM MS-275, and 5 µM MS-275 led to an increase of around 1.5- to 2-fold in CYTO-ID® mean fluorescence (**Figure 32A**). The respective histograms in **Figure S 9** visualize this effect by revealing a shift of the fluorescence spectra to higher CYTO-ID® signal intensities. This effect is most prominent for samples that were treated for 48 h with 5 mM VPA and 5 µM MS-275 (**Figure 32A**). The nominal values of mean CYTO-ID® fluorescence signal intensity in 48 h treated samples are shown in **Figure S 10**.

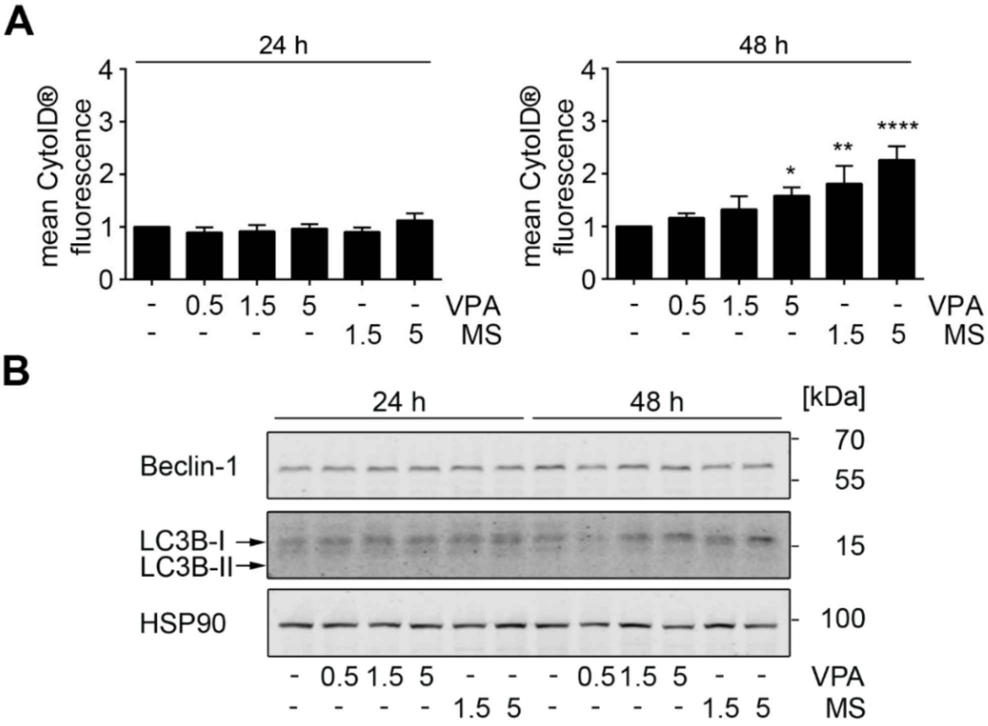

Figure 32: Autophagy in HDACi-treated Renca. (A) Cells were treated with the indicated concentrations of VPA (mM) and MS-275 (µM). Autophagy was determined by flowcytometry detection of mean fluorescence of CYTO-ID® stained cells. Graph depicts mean ± SD (n=4; one-way ANOVA; Dunnett's multiple comparison test; *P<0.05, **P<0.001, ****P<0.0001). Values were normalized to untreated samples. (B) Cells were treated with the indicated concentrations of VPA (mM) and MS-275 (µM). Beclin-1 and LC3B expression was determined by Western blot;

HSP90, loading control. Quantification of protein expression of Western blot analyses (n=3) is shown in Fehler! Verweisquelle konnte nicht gefunden werden.

To further examine autophagy induction upon higher concentrations of VPA and MS-275, the expression levels of two crucial autophagic marker proteins were analyzed by Western blot (**Figure 32B**). Beclin-1 is a central autophagic protein, that is involved in the maturation process of phagosomes to autophagosomes and its mRNA and protein levels are upregulated in the course of autophagy (Kang et al. 2011). In HDACi-treated Renca cells, Beclin-1 protein expression did not change significantly in response to treatment (**Figure 32B**, **Figure S 11A**). Furthermore, the analysis of LC3B isoforms showed that only LC3B-I was expressed in untreated and HDACi-treated Renca cells (**Figure 32**). As LC3B-I is modified upon autophagic signaling by conjugation to a PE moiety to generate LC3B-II and to be inserted in the membranes of autophagosomes, the sole expression of LC3B-I further disfavors ongoing autophagic processes (Tanida et al. 2004). Due to potential differences in hydrophobicity, autophagy-related LC3B-II would be expected to migrate faster in SDS-page than LC3B-I and thus form a subjacent band (Mizushima and Yoshimori 2007). Moreover, LC3B-I expression did not change significantly in response to HDACi treatment (**Figure S 11B**).

On the one hand, measurement of CYTO-ID® signal intensities indicated an induction of autophagy with higher VPA and MS-275 concentrations at 48 h. On the other hand, neither Beclin-1 nor LC3B expression favored ongoing autophagic processes. This discrepancy raises further questions that are commented on in the discussion.

4.1.6 HDAC class I inhibiton induces apoptosis and restrains growth of human primary RCC cells

To assess the transferability of the observed HDACi responses in murine renal carcinoma cells to human RCC, the effects of HDACi in the primary human clear cell renal carcinoma cells Mz-ccRCC1 and Mz-ccRCC2 were analyzed. Mz-ccRCC1 cells were treated with 1.5 mM and 5 mM VPA as well as 1.5 µM and 5 µM MS-275 for 48 h and analyzed for histone hyperacetylation to ensure effective HDAC inhibition. Except for 1.5 mM VPA, all treatment conditions led to an observable increase in histone H3 and H4 acetylation on Western blot (**Figure 33A**). In comparison, in Mz-ccRCC2 cells, hyperacetylation of histone H3 and H4 by MS-275 was more pronounced, while VPA induced hyperacetylation was nearly undetectable (**Figure S 12**). Furthermore, cleavage of caspase 3 and caspase 9 was detectable in Mz-ccRCC1 cells that were treated with 5 mM VPA and 5 µM MS-275 (**Figure 33B**). In comparison to Renca cells, Mz-ccRCC1 showed a slowed proliferation rate. Therefore, analysis timepoints and treatment duration for the different assays were extended by 24h.

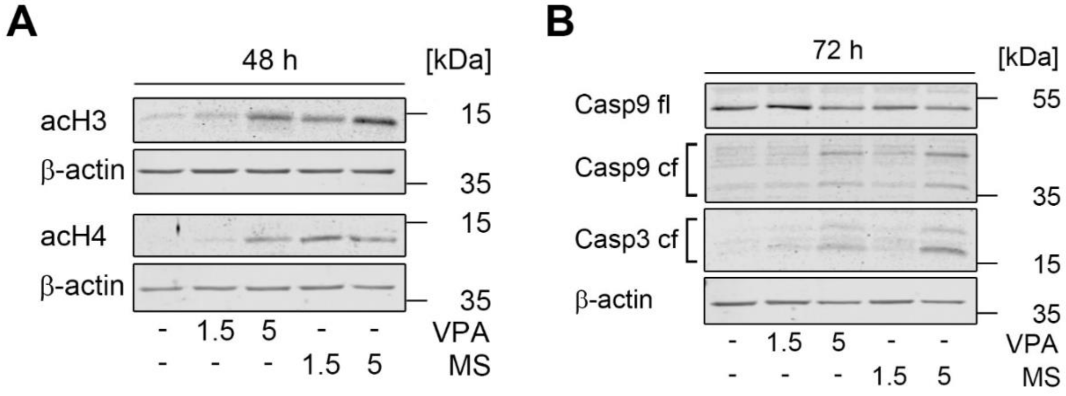

Figure 33: HDAC class I inhibition induces histone hyperacetylation and caspase cleavage in MZ-ccRCC1. (**A**) Cells were treated with the indicated concentrations of VPA (mM) and MS-275 (µM) for 48 h. Hyperacetylation of the histones H3 and H4 was analyzed in Western blot. β-actin serves as loading control. (**B**) Cells were treated with the indicated concentrations of VPA (mM) and MS-275 (µM) for 72 h. Expression and cleavage of the indicated proteins was analyzed by Western blot. β-actin serves as loading control.

Cell death induction in Mz-ccRCC1 cells was measured at 48 h and 72 h post treatment. At 48h, no applied HDACi concentration did result in a significant increase in the percentage of dead cells (**Figure 34**). Following 72 h treatment, doses of 5 mM VPA and 1.5 µM and 5 µM MS-275 led to a significant increase in the proportion of dead cells compared to controls (**Figure 34**). The extent of cell death in Mz-ccRCC1 cell cultures in response to 5 mM VPA and 1.5 µM MS-275 was comparable to that observed in Renca cells (**Figure 26**), with around 35% and 20% respectively. However, treatment with 5 µM MS-275 had a stronger effect on Mz-ccRCC1 cells than on Renca cells, with an increase of cell death to over 50% (**Figure 26**, **Figure 34**). Treatment with 1.5 mM VPA led to a slight, insignificant induction of cell death after 72 h (**Figure 34**). Cell death in response to HDACi was furthermore measured in a second human primary renal carcinoma line Mz-ccRCC2 (**Figure S 13**).

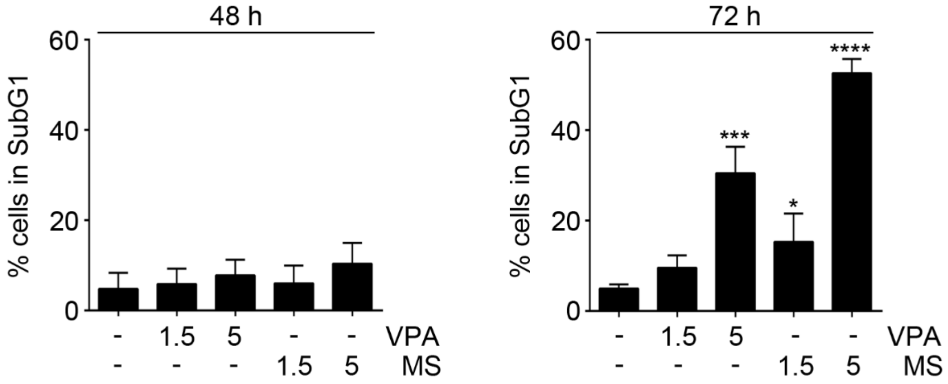

Figure 34: Cell death induction in HDACi-treated MZ-ccRCC1. Cells were treated with the indicated concentrations of VPA (mM) and MS-275 (µM) for 48 h and 72 h. Cell death induction was analyzed by flow cytometric analysis of fixed and PI-stained cells as fraction of cells with fragmented DNA (subG1 fraction). Graph shows mean ± SD (n=3; one-way ANOVA; Dunnett's multiple comparison test; **P*<0.05, ****P*<0.001 *****P*<0.0001).

Herein, significant cell death induction occurred already after 24 h treatment with 5 mM VPA and 5 µM MS-275 (**Figure S 13**). Following 48 h treatment with 5 mM VPA, the percentage of dead cells rose to around 30%, which is comparable to the extent of cell death observed in Renca and Mz-ccRCC1 cells (**Figure 26**, **Figure 34**). As in the other two cell lines, treatment with 1.5 mM VPA for longer time periods led to an insignificantly enhanced percentage of Mz-ccRCC2 cells in subG1 fraction. Remarkably, Mz-ccRCC2 cells showed the highest sensitivity of all three cell lines towards MS-275. After 48 h treatment, the percentage of dead cells rose to about 30% upon a treatment with 1.5 µM and about 75% with 5 µM MS-275.

Subsequently, cell cycle distribution for both primary human renal carcinoma lines was determined by mathematically omitting the percentage of dead cells. Mz-ccRCC1 showed the most prominent changes in cell cycle distribution after 48 h HDACi treatment (**Figure 35**, **Figure S 14**). The percentage of Mz-ccRCC1 cells in G1-phase increased significantly following treatment with 1.5 µM and 5 µM MS-275 (**Figure S 14**). Treatment with 5 mM VPA had the same effect, but the observed trend was not significant (**Figure S 14**). Furthermore, HDACi-treated Mz-ccRCC1 cells showed a significant loss of cells in S-phase, which was most prominent for MS-275-treated cells, but also pronounced after treatment with 5 mM VPA (**Figure S 14**). There were no significant changes regarding the percentage of cells in G2-phase observable after 48 h treatment with either HDACi (**Figure S 14**). After 72 h treatment, only samples with high cell death induction showed visible changes in cell cycle distribution, with the effects observed with 5 mM VPA and 5 µM MS-275 being largely different (**Figure 35**, **Figure S 14**). Whereas Mz-ccRCC1 cells that were treated with 5 µM MS-275 sustained a trend to an elevated percentage of cells in G1-phase at 72 h, 5 mM VPA treatment tends to result in a decreased proportion of G1-phase cells (**Figure S 14**). Furthermore, the percentage of cells in G2-phase was significantly elevated following treatment with 5 mM VPA, whereas it was significantly decreased following 5 µM MS-275 (**Figure S 14**). The only common feature for both treatments was a trend of increased proportion of cells in S-phase (**Figure S 14**).

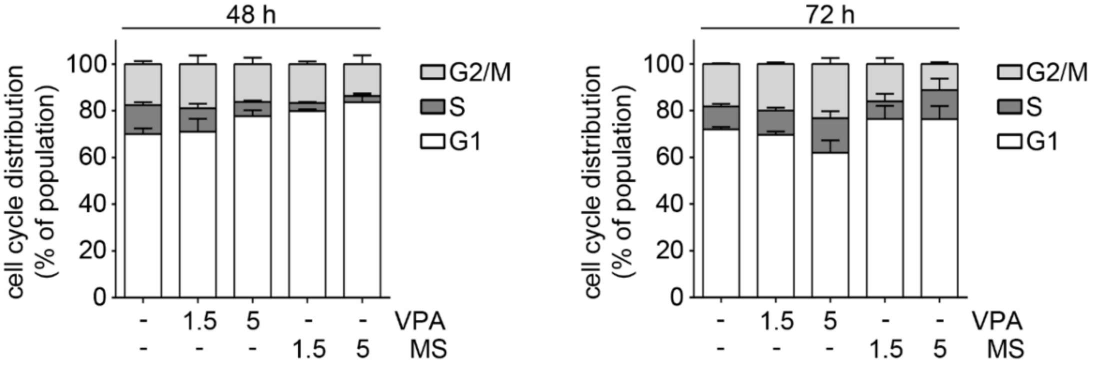

Figure 35: Cell cycle distribution of HDACi-treated MZ-ccRCC1. Cells were treated with the indicated concentrations of VPA (mM) and MS-275 (µM) for 48 h and 24 h. Cell cycle distribution was determined by flow cytometry analysis of fixed and PI-stained cells. Cells with fractionated DNA (subG1 fraction) were excluded to obtain cell cycle distribution of the viable cell population. Graph shows mean ± SD (n=3). For statistical analysis of individual cell cycle phases see **Figure S 14**.

Cell cycle analysis in the second primary human renal carcinoma line Mz-ccRCC2 revealed significant changes in cell cycle distribution after 24 h as well as after 48 h (**Figure S 15**). Notably, 1.5 mM VPA, a dose that had no significant effect on cell death induction in these cells (**Figure S 13**), led to remarkably different changes in cell cycle profile at 24 h than observed in any of the other two analyzed cell lines under any HDACi treatment condition (**Figure S 15**). Treatment with 1.5 mM VPA led to a significantly reduced percentage of cells in G1-phase and alongside significantly induced the number of cells in S- and G2-phase of the cell cycle. It is further noteworthy, that at 48 h, after another 24 h treatment, there were no longer any deviations in cell cycle distribution detectable for Mz-ccRCC2 cells treated with 1.5 mM VPA compared to control cells (**Figure S 15**). As observed in Renca cells and Mz-ccRCC1 cells, HDACi concentrations that did induce cell death at later timepoints, promoted characteristic changes in cell cycle profile at earlier time-points. For example, MS-275 treatment led to an increased percentage of cells in G1-phase and a reduced percentage of cells in S-phase at 24 h treatment (**Figure S 15**). On the other hand, the trend to a higher percentage of cells in G1-phase was only sustained at 48 h in cells treated with 5 µM MS-275. In contrast, treatment with 5 mM VPA and 1.5 µM MS-275 reduced the number of cells in G1-phase after 48 h (**Figure S 15**). There were no visible changes in the percentage of cells in S-phase at 48 h. Strikingly, at 48 h the G2 population was significantly increased following treatment with 5 mM VPA and 1.5 µM MS-275 (**Figure S 15**), comparable to the increase observed in Mz-ccRCC1 cells with 5 mM VPA after 72 h (**Figure S 14**). On the other hand, a trend for a lower percentage of S-phase cells was measurable in response to 48 h treatment with the higher dose of 5 µM MS-275 (**Figure S 15**). Despite the varying HDACi-induced cell cycle alterations, there were nevertheless common changes observable in all three cell lines such as an increase of G1-phase percentage ahead of apoptotic cell death induction. This indicates, that a common consequence of HDACi treatment is lethal cell death execution.

Furthermore, treatment of Mz-ccRCC1 cells with HDACi resulted in a significant loss of viable cells (**Figure 36**). As this effect occurred after 48 h treatment, i.e. in the absence of significant cell death induction (**Figure 34**, **Figure 36**), it implicates an influence of HDACi treatment on cell growth due to the observed changes in cell cycle distribution (**Figure 35**). The growth arrest compared to control was even more pronounced after 72 h treatment, with the viable cell number of untreated cells doubling from 48 h to 72 h, but no increase of total cell number observable in any HDACi-treated sample (**Figure 36**). In contrast, in HDACi-treated Mz-ccRCC2 cells, a reduction of cell number was solely observed at 48 h treatment in samples that simultaneously displayed cell death induction (**Figure S 13**, **Figure S 16**). There was no decrease in the number of viable Mz-ccRCC2 cells detectable after 24 h treatment, although at least MS-275-treated samples showed an increase of G1-phase and a decrease of S-phase percentage at this timepoint (**Figure S 15**, **Figure S 16**).

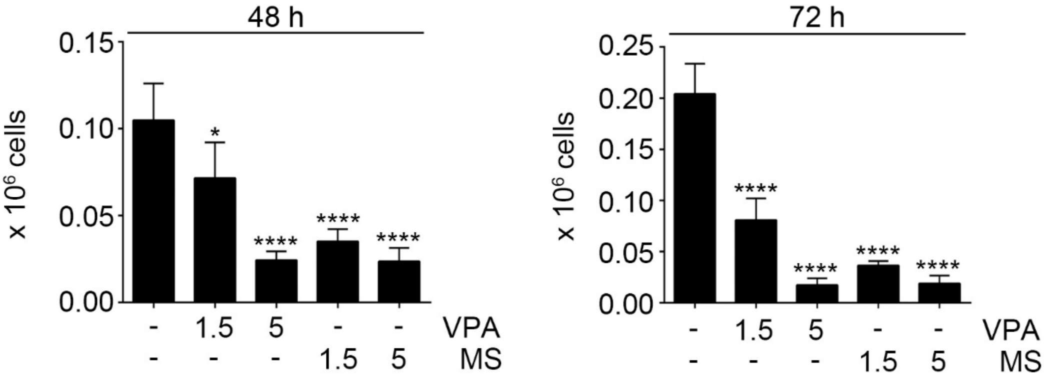

Figure 36: Viable MZ-ccRCC1 cell number in response to HDACi treatment. Cells were treated with the indicated concentrations of VPA (mM) and MS-275 (µM) for 48 h and 72 h. Dead cells were excluded by trypan blue staining and viable cell population was counted in a Neubauer chamber. Graph depicts mean ± SD (n=4; one-way ANOVA; Dunnett's multiple comparisons test; **P*<0.05, *****P*<0.0001).

Next, E-cadherin expression in response to treatment with both HDACi was analyzed. In contrast to Renca cells, Western blot analysis showed that Mz-ccRCC1 cells accumulated E-cadherin (**Figure 37**). This increase in protein expression was significant for all applied HDACi concentrations at 48 h and quantification showed that it reached around 4- to 6-fold of control level (**Figure 37**). 72 h post treatment, E-cadherin levels declined in all apoptotic samples (5 mM VPA; 1.5 µM and 5 µM MS-275), with E-cadherin expression in 5 mM VPA and 5 µM MS-275-treated samples almost reverting to control level (**Figure 34, Figure 37**). In Mz-ccRCC2 cells, MS-275 induced an upregulation of E-cadherin expression after 24 h and 48 h, whereas untreated and VPA-treated cells displayed no expression of E-cadherin in Western blot (**Figure S 17**).

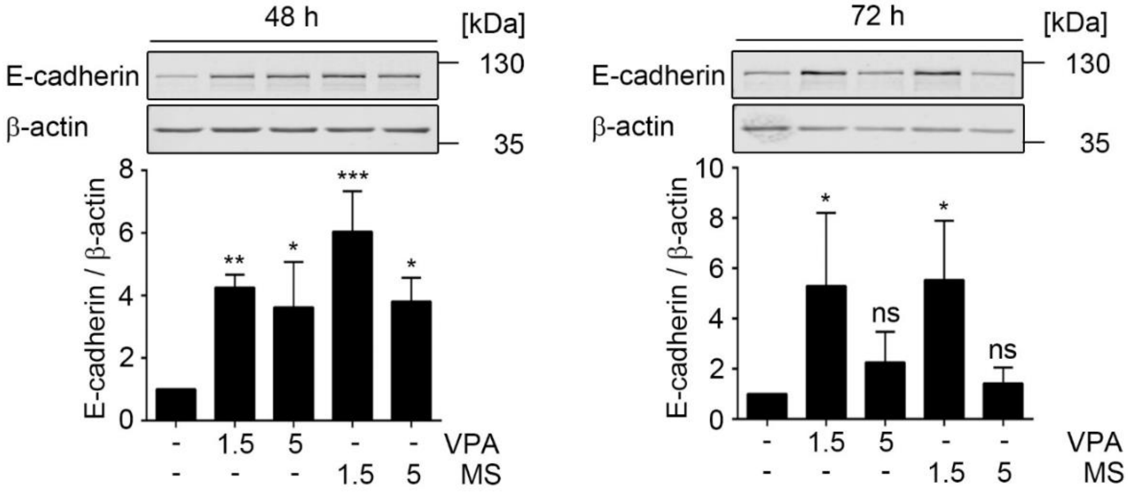

Figure 37: E-Cadherin expression in HDACi-treated MZ-ccRCC1. Cells were treated with the indicated concentrations of VPA (mM) and MS-275 (µM) for 48 – 72h and analyzed for E-cadherin expression in Western blot. β-actin served as loading control. Quantification was achieved by densitometric analysis of signal intensities and normalization to respective loading control signal intensities. Graphs depict relative levels of E-cadherin expression as mean ± SD (n=3; one-way ANOVA; Dunnett multiple comparison test; **P*<0.05, ***P*<0.01, ****P*<0.001).

In summary, these data confirm that the observed HDACi effects in Renca cells were transferable to two different primary human clear cell renal carcinoma cells, Mz-ccRCC1 and Mz-ccRCC2. For instance, in both analyzed cell lines, cell death induction in response to HDACi treatment was observable. Moreover, HDACi treatment resulted in significant changes in cell cycle distribution which led to a cell death-independent decrease of the viable cell number in Mz-ccRCC1 cells. Although there were divergent changes in cell cycle distribution and E-cadherin expression in the three cell lines in response to HDACi, cell death induction was commonly observed.

4.1.7 HDAC1 and HDAC2 as mechanistic targets of HDACi

As both HDACi VPA and MS-275 are potent inhibitors of class I HDACs, and especially effective against HDAC1 and HDAC2, targeted siRNA mediated knockdown of both deacetylases was performed to analyze if the observed HDACi effects can be specifically ascribed to a loss of HDAC1 and HDAC2 function. Transfection was conducted in Renca cells as described in **3.2.11**. Initially, transfection efficiency was determined by quantification of the residual protein expression with Western blot analysis (**Figure 38**). Individual and combined knockdown of HDAC1 and HDAC2 expression was successfully accomplished (**Figure 38A**).

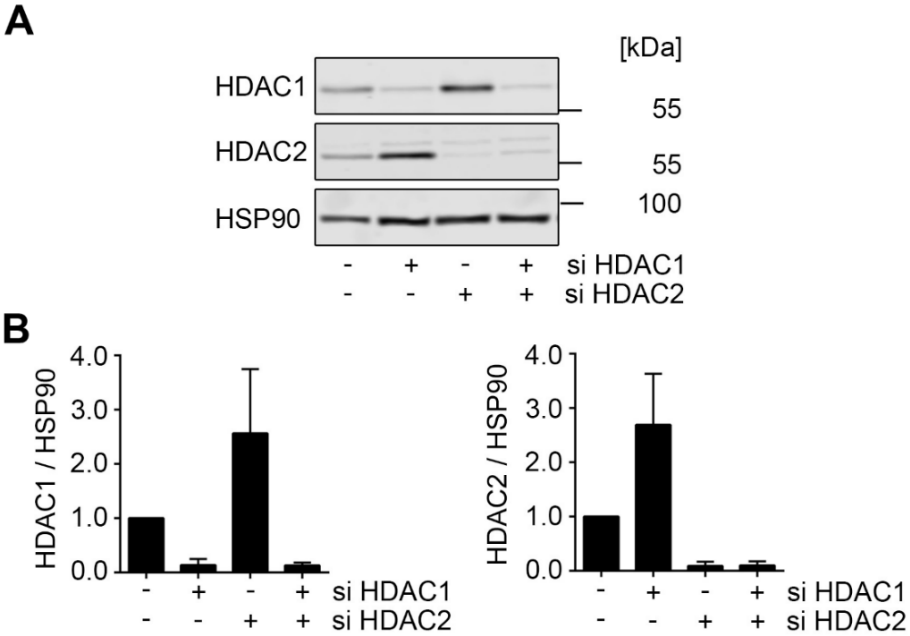

Figure 38: Transfection of Renca with siRNA against HDAC1 and HDAC2. (**A**) Cells were transfected with siRNA directed against the mRNA of *Hdac1* and *Hdac2* and analyzed for the indicated protein expression on Western blot. HSP90 served as loading control. (**B**) Quantification of transfection efficiency was obtained by densitometric analysis of HDAC1 and HDAC2 signal intensities on Western blot. Signals were normalized to the respective loading control. Graph depicts mean ± SD (n=3).

Quantification of the respective signal intensities showed a reduction of HDAC1 and HDAC2 protein expression to around 10% of control level in response to siRNA application (**Figure**

38B). Notably, HDAC1 and HDAC2 were upregulated to around 3-fold of control level in the single knockdown to compensate for the loss of the respective other HDAC (**Figure 38B**). This finding is consistent with the described homology of both enzymes and their resulting partial functional redundancy (Jurkin et al. 2011). Renca cells transfected with a combination of the two siRNAs directed against the mRNA of *Hdac1* and *Hdac2* showed characteristic morphologic changes that resembled the morphologic changes induced by HDACi treatment (**Figure 16**, **Figure 39**). Distinctive knockdown of either HDAC led to the advent of dispersed cells with altered morphological features. This effect was less extensive as it was in response to the combined reduction of HDAC1 and HDAC2 (**Figure 39**, **Figure S 18**).

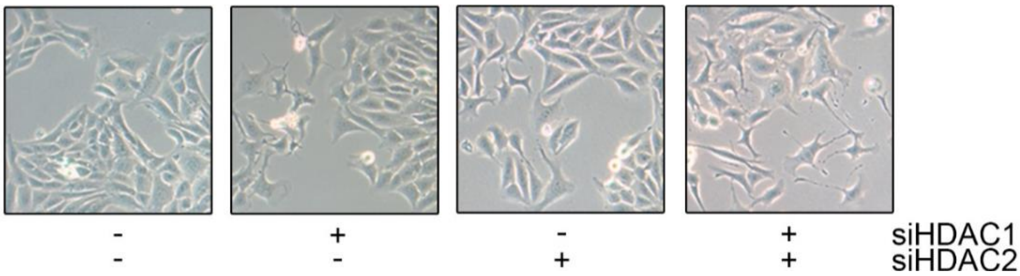

Figure 39: Morphological alterations in Renca upon HDAC1 and HDAC2 knockdown. Cells were transfected with siRNA as indicated and images were taken 72 h post transfection. Cell morphology was documented with phase-change light microscopy. Images are representative for n=3. Shown are sections of **Figure S 18**.

Congruent with the effects of HDACi treatment in Renca cells, combined transfection with both siRNAs did lead to a cleavage of caspase 3, indicating induction of apoptotic signaling in cells lacking HDAC1 and HDAC2 expression (**Figure 40A**). Furthermore, combinatorial knockdown of both HDACs effectively reduced the number of viable Renca cells significantly (**Figure 40B**).

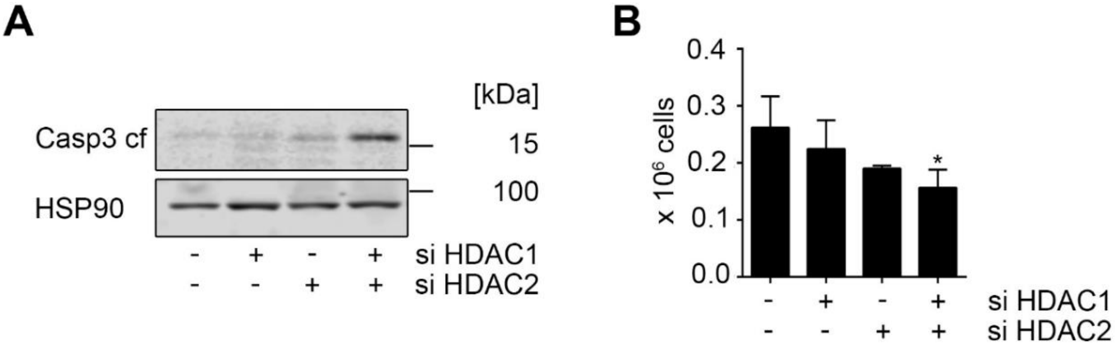

Figure 40: Caspase 3 cleavage and reduction of viable cell number upon HDAC1 and HDAC2 knockdown. Cells were transfected with siRNA as indicated. (**A**) Transfected cells were analyzed for the abundance of cleaved caspase 3 72 h post transfection by Western blot. HSP90 served as loading control. (**B**) Cells were harvested 48 h post transfection and stained with trypan blue. Viable cells were counted in a Neubauer chamber. Graph depicts mean ± SD (n=3; one-way ANOVA; Dunnett’s multiple comparisons test; *P<0.05).

As consistently demonstrated for HDACi-treated Renca cells, a loss of HDAC class I function, more precisely HDAC1 and HDAC2 function, reduced the protein expression of E-cadherin (**Figure 20**, **Figure 41**). Quantification of Western blot signal intensity confirms that the individual loss of either HDAC1 or HDAC2 is sufficient to significantly reduce E-cadherin expression (**Figure 41**). This effect is even more pronounced upon the loss of the expression of both HDAC proteins. In these samples, E-cadherin expression is reduced significantly to around 25% (**Figure 41**).

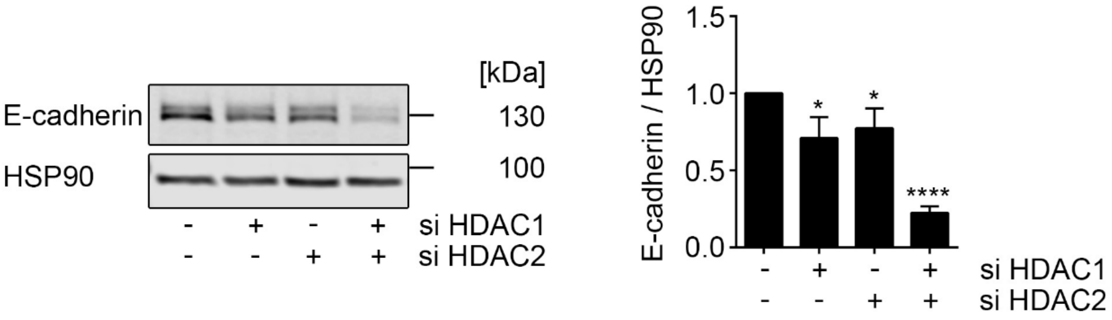

Figure 41: E-cadherin expression in Renca upon HDAC1 and HDAC2 knockdown. Cells were transfected as indicated and analyzed for E-cadherin expression by Western blot. HSP90 served as loading control. Densitometric analysis of signal intensities was performed and signal intensities were normalized to the respective loading controls. Graph displays mean ± SD (n=3; one-way ANOVA; Dunnett's multiple comparisons test; *$P<0.05$, ****$P<0.0001$).

As shown, HDACi treatment in Renca cells reduces the expression of the growth factor receptor PDGFRβ, whose associated signal pathways are considered to play a major role in RCC metastasis formation (**Figure 23**). Analysis of PDGFRβ expression in response to knockdown of HDAC1 and HDAC2 protein expression, confirmed that a specific loss of expression of one or both of these two HDACs efficiently reduces the receptor expression (**Figure 42**).

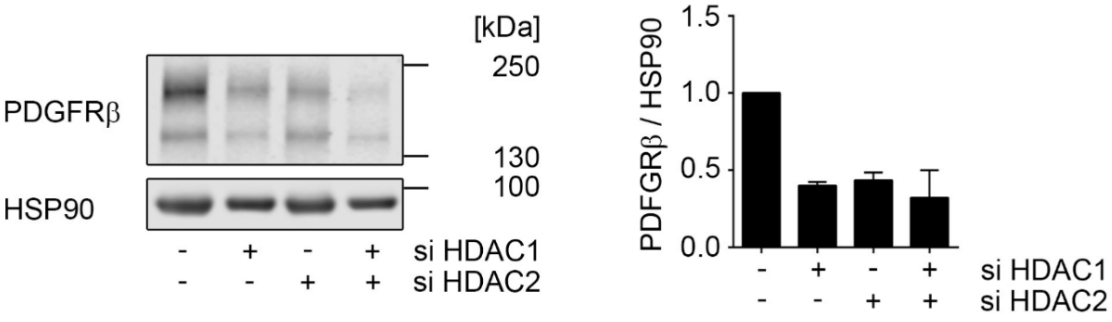

Figure 42: PDGFRβ expression in Renca upon knockdown of HDAC1 and HDAC2. Cells were transfected with siRNA as indicated. PDGFRβ expression was analyzed by Western blot. HSP90 served as loading control. Quantification of signal intensities was accomplished by densitometric analysis and subsequent normalization to the respective loading controls. Graph displays mean ± SD (n=2).

In summary, these data gained with HDAC1 and HDAC2 knockdown experiments prove that the observed effects of class I HDAC inhibition in Renca cells are a direct result of the specific loss of HDAC1 and/or HDAC2 function. Whereas loss of E-cadherin and PDGFRβ expression is already induced as a consequence of single loss of HDAC1 or HDAC2 function, cell death induction, cell growth inhibition, and full induction of morphological changes are dependent on the mutual loss of function of both HDACs.

4.1.8 Elucidation of the p53 status of Renca cells

Considering the relevance of the p53 mutation status for the general reactions of cancer cells towards chemotherapeutic drugs (Muller and Vousden 2013; Hientz et al. 2016), it is of interest to obtain basic knowledge on the p53 expression and potential p53 mutations in Renca cells. Major databases for the identification of cell lines and catalogues of known mutations in cancer were searched for entries concerning the p53 status of the Renca cell line, but none of these data base searches led to any favorable results. Considered databases were, among others, the International Agency for Research on Cancer TP53 Database (IARC, http://p53.iarc.fr/), the Catalogue Of Somatic Mutations In Cancer (COSMIC, https://cancer.sanger.ac.uk/cosmic) the Cancer Cell Line Encyclopedia (CCLE, https://portals.broadinstitute.org/ccle), the American Type Culture Collection (ATCC, https://www.atcc.org), and the TP53 website cell line compendium (https://p53.fr). In general, *TP53* mutation rates of common renal carcinoma are exceptionally low in comparison to other cancer types with 2.5% for renal papillary-cell carcinoma and 2.4% renal clear-cell carcinoma (Wang and Sun 2017). To nevertheless gain further insight into the mutation status of p53 in Renca cells, p53 expression of Renca cells was compared to p53 expression in the murine pancreatic primary tumor cell line PPT-5436. This cell line is especially suited for comparison, as it is a PDAC cell line with a genetically defined p53 mutation status. It harbors the point mutation $p53^{R172H}$ that corresponds to the human $p53^{R175H}$ hotspot mutation (Schneider et al. 2010; Conradt et al. 2013). p53 protein expression in PPT-5436 cells was about 6-fold higher than p53 expression in Renca cells (**Figure 43**). As the majority of mutations in p53 are missense mutations, they lead to the expression a full-length modified p53 protein with a prolonged half-life (Strano et al. 2007; Freed-Pastor and Prives 2012). In contrast, wild-type p53 is a short-lived protein under unstressed conditions, rendering the minor expression of p53 in Renca cells an indication for wild-type p53 (Strano et al. 2007; Freed-Pastor and Prives 2012; Conradt et al. 2013). The different migration behavior of p53 in Renca and PPT-5436 cells additionally suggests the presence of wild-type and mutant p53, respectively.

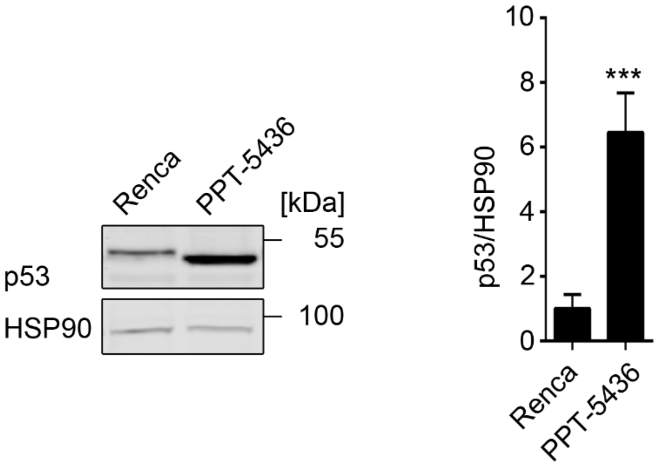

Figure 43: p53 expression in Renca and PPT-5436. Untreated Renca and PPT-5436 cells were analyzed for p53 expression on Western blot. HSP90 served as loading control. Quantification of signal intensities was accomplished by densitometric analysis and subsequent normalization to the respective loading controls. Graph displays mean ± SD (n=4; two-tailed unpaired student's t-test, ***P>0.001).

Accumulation of p53 in response to genotoxic stress indicates wild-type p53 (Schneider et al. 2010). Therefore, the p53 response in Renca cells to a stress stimulus, in this case doxorubicin treatment, was analyzed. Western blot analysis and subsequent quantification of signal intensities revealed that total p53 protein expression as well as expression of its target protein BAX were upregulated in response to doxorubicin (**Figure 44**). The increase in BAX protein levels indicates wild-type p53 expression in Renca cells as it implies characteristic wild-type p53-dependent activation of a pro-apoptotic target gene in response to replication stress and DNA damage.

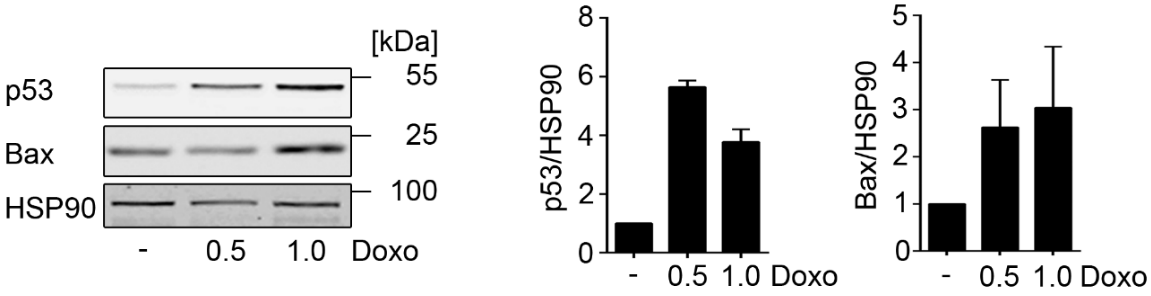

Figure 44: p53 and BAX expression in Renca in response to doxorubicin treatment. Cells were treated with the indicated concentrations of doxorubicin for 16 h. p53 and BAX expression was analyzed by Western blot. HSP90 served as loading control. Quantification of signal intensities was accomplished by densitometric analysis and normalization to the respective loading controls. Graph displays mean ± SD (n=2).

4.2 HDAC2 expression in colorectal cancer cells and the effects of HDAC2 sumoylation and HDAC inhibition

4.2.1 Heterogenous HDAC2 expression in colorectal cancer cells

The human RKO and HCT116 cell lines were analyzed for HDAC2 expression by immunofluorescence staining. In addition, various recently established human primary cancer cell lines (HROC24, HROC113, and HROC50 (Linnebacher et al. 2010; Maletzki et al. 2012)) were analyzed for HDAC2 expression. RKO, HCT116, and HROC24 cells displayed heterogenous expression of HDAC2 (**Figure 45**). The frequency of HDAC2 loss in these three cell lines was rated as RKO > HROC24 > HCT116. RKO cells displayed the highest percentage of HDAC2 negative cells and HCT116 cells displayed solely the two depicted HDAC2 negative cells in all three independent experiments (**Figure 45**). Immunofluorescence staining of HROC113 and HROC50 yielded no HDAC2 negative cells.

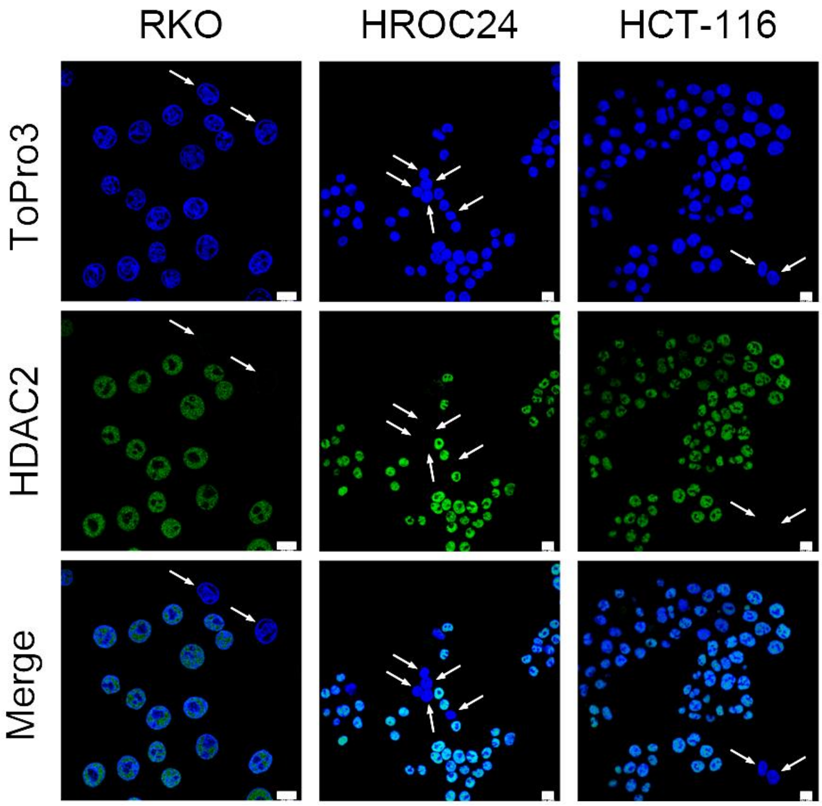

Figure 45: Heterogenous HDAC2 expression in CRC cells. Untreated RKO, HCT116, and HROC24 cells were submitted to immunofluorescence analysis and stained with HDAC2 primary antibody. Graph shows representative pictures of at least three independent experiments. Scale bar represents 10 µm. Arrows indicate cells that stain negative for HDAC2.

These data show that HDAC2 expression in MSI cell lines is frequently lost in individual cells, giving rise to the formation of heterogenous CRC subpopulations. Such findings demonstrate the importance of further investigations concerning HDAC2 function and activity in CRC.

4.2.2 Characterization of the RKO HDAC2^{wt} and RKO HDAC2^{K462R} cell lines

RKO cells stably expressing HDAC2^{wt} and HDAC2^{K462R} were established and described (Brandl et al. 2012). Recombinant wild-type HDAC2 in HDAC^{wt} expressing cells can be posttranslationally modified through sumoylation at its lysine residue K462. In contrast, this sumoylation is prevented in cells that recombinantly express mutant HDAC2^{K462R}. Loss of HDAC2 sumoylation impairs interaction of HDAC2 and p53 and subsequently modifies p53- and NFκB-dependent gene expression (for further details see **1.3.2**). Protein expression analyses via Western blot were conducted regularly to ensure that cells were genuinely as characterized by (Brandl et al. 2012).

Initially, stable expression of HDAC2^{wt} and HDAC2^{K462R} was verified by detection of the V5 tag attached to the recombinant HDAC2 proteins in both cell lines using a V5 specific primary antibody in Western blot analysis. The analysis confirmed V5 tag expression and thus recombinant HDAC2 expression in both RKO cell lines (**Figure 46A**). In comparison, endogenous HDAC2 expression is shown in K562 cells (**Figure 46A**). The presence of the V5 tag on the recombinant HDAC2^{wt} and HDAC2^{K462R} proteins prohibits their detection with the applied HDAC2 antibody as the position of the V5 tag masks the HDAC2 epitope. Thus, only application of V5 and HDAC2 antibody in parallel in Western blot analysis of RKO cells and K562 cells expressing endogenous HDAC2, results in the successful detection of all three different HDAC2 proteins. The analysis revealed that addition of the V5 tag (~ 8 kDa) led to a slower migration of the recombinant HDAC2 proteins in comparison to endogenous HDAC2 in K562 cells and reflects their slightly enhanced molecular weight (**Figure 46A**). RKO HDAC2^{wt} and RKO HDAC2^{K462R} were described to display different p53-dependent protein expression profiles under unstimulated conditions (Brandl et al. 2012). Indeed, RKO HDAC2^{K462R} showed a decreased expression of p53 total protein and an increased expression of its target proteins BAX and p21 when compared to HDAC2^{wt} expressing RKO cells (**Figure 46B**).

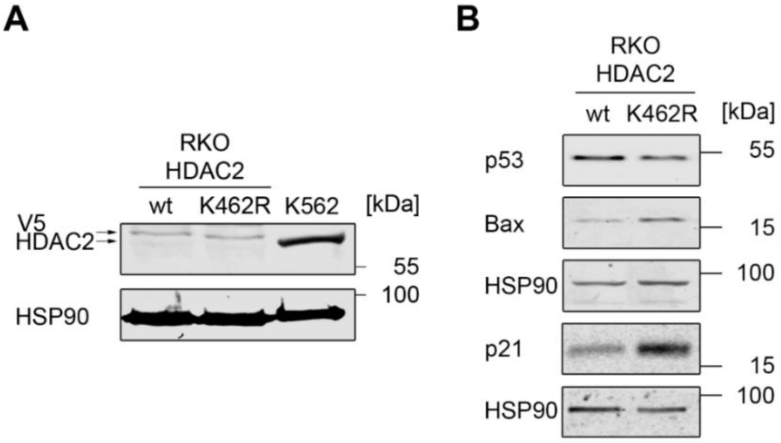

Figure 46: Characteristic protein expression in RKO HDAC2^{wt}-V5 and RKO HDAC2^{K462R}-V5. (**A**) Expression of V5-tagged HDAC2^{wt} and HDAC2^{K462R} in RKO ES cells was determined by Western blot analysis. In comparison,

application of HDAC2 primary antibody confirmed HDAC2 expression in K562 cells, that served as control. HSP90 served as loading control.

To ensure equivalent culture and treatment conditions in all subsequent experiments, growth curves were determined for RKO HDAC2^{wt} and RKO HDAC2^{K462R} cells. No induction of cell growth was detectable for 24 h post seeding. This indicates an initial growth phase comparable to the lag phase known in bacterial cell growth kinetics, in which cells primarily adhere and adapt to the growth conditions prior to the initiation of exponential cell growth (**Figure 47A**). At 48 h and 72 h post seeding, cell number for both cell lines doubled with a 4-fold increase in the seeded cell number at 48 h and 8- to 9-fold at 72 h (**Figure 47A**).

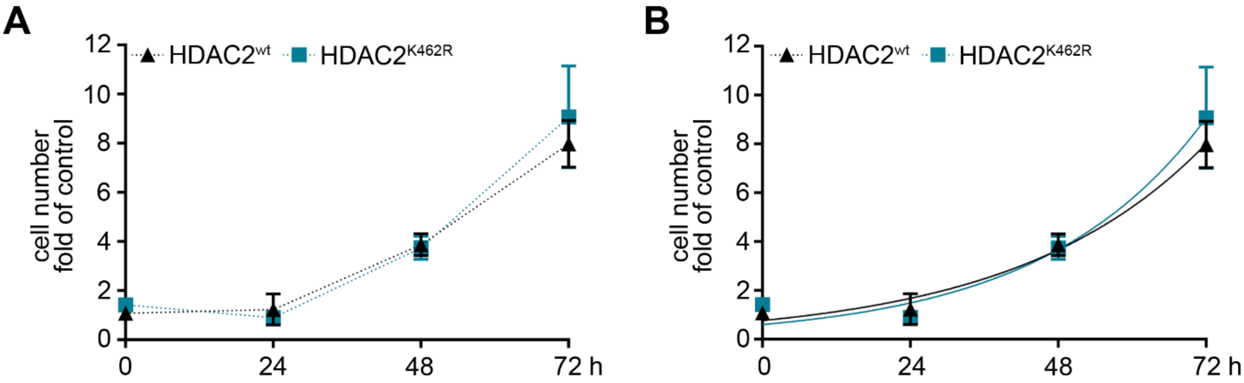

Figure 47: Cell growth of RKO HDAC2^{wt} and RKO HDAC2^{K462R}. (**A**) Cells were seeded at equal density and viable cell number was determined every 24 h for 72 h. Graph shows mean ± SD (n=3). (**B**) Calculated exponential growth curves through nonlinear fit of (**A**). Parameters of nonlinear fit and derived growth equations are shown in **Table 5**.

Growth equations were determined by nonlinear fitting of the given growth curve to determine doubling time. Resulting growth equations for RKO HDAC2^{wt} and RKO HDAC2^{K462R} cell growth are given in **Table 6**. Calculated doubling time in RKO HDAC2^{K462R} was shorter with 18.44 h compared to 21.3 h in RKO HDAC2^{wt} (**Table 6**). However, this might be a result of the observed higher standard deviation at 72 h in RKO HDAC2^{K462R} cells (**Figure 47**).

Table 6: Cell growth equations of RKO HDAC2^{wt} and RKO HDAC2^{K462R} cells. Parameters were derived by nonlinear fit of growth curves using GraphPad Prism software.

	RKO HDAC2^{wt}	**RKO HDAC2^{K462R}**
Growth Equation	$y = 0.7687*e^{0.3255x}$	$y = 0.6046*e^{0.03760x}$
Parameters ± SD	$y_0 = 0.7687 \pm 0.1596$	$y_0 = 0.6046 \pm 0.2342$
	$k = 0.03255 \pm 0.003092$	$k = 0.03760 \pm 0.005672$
Doubling Time	21.3 17.58-27.02 (95% CI)	18.44 13.80-27.77 (95% CI)

These results confirm that the stable expression of HDAC2^{wt} and HDAC2^{K462R} cells led to characteristic changes in p53 and p53 target gene expression (Brandl et al. 2012), without largely affecting the growth properties of RKO cells.

4.2.3 Sensitivity of RKO HDAC2^{wt} and RKO HDAC2^{K462R} to treatment with various chemotherapeutics

Standard treatment schemes for colorectal cancer generally include the administration of fluoropyrimidines (see **1.1.2**). Interestingly, RKO cells expressing the sumoylation-deficient HDAC2^{K462R} were significantly more sensitive to increasing concentrations of 5-FU (incorporated into DNA and RNA, see **1.5.1** (Longley et al. 2003)) than RKO cells expressing wild-type HDAC2 (**Figure 48A**). Curiously, such differential effects were not visible with the 5-FU metabolite FdUrd (incorporated into DNA, see **1.5.1** (Longley et al. 2003)) (**Figure 48B**).

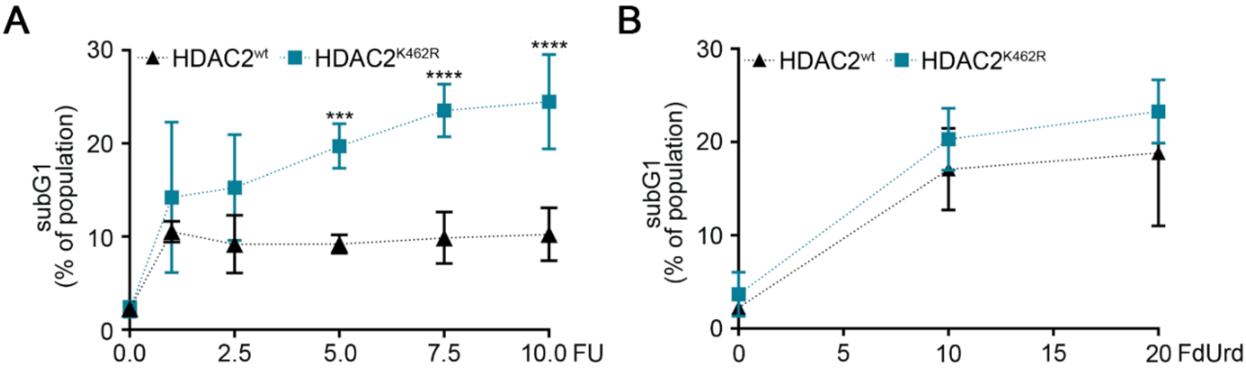

Figure 48: Cell death induction in RKO HDAC2^{wt} and RKO HDAC2^{K462R} in response to 5-FU and FdUrd. Cell death induction was measured by flow cytometry analysis of fixed and PI-stained cells as induction of the fraction of cells with fragmented DNA (subG1 fraction). (**A**) Cells were treated with the indicated concentrations of 5-FU (µM) for 48 h. Graph shows mean ± SD (n=5; two-way ANOVA; Sidak's multiple comparisons test; ***$P<0.001$, ****$P<0.0001$). (**B**) Cells were treated with the indicated concentrations of FdUrd (µM) for 48 h. Graph shows mean ± SD (n=5; two-way ANOVA; Sidak's multiple comparisons test; no significant differences).

Strikingly, although RKO HDAC2^{wt} and RKO HDAC2^{K462R} cells displayed significantly different sensitivities towards 5-FU treatment, there were no significant changes in cell cycle distribution of viable cells detectable after 48 h treatment with any applied concentration of 5-FU (**Figure 48A**, **Figure S 19A**). However, when cell cycle distribution of RKO HDAC2^{wt} and RKO HDAC2^{K462R} cells in response to equivalent 5-FU concentrations was compared, there was a tendency towards enhanced G2/M-phase and reduced G1-phase percentage in sumoylation-deficient cells detectable (**Figure S 19A**). This clearly discernable but insignificant effect indicates a slightly divergent cell cycle regulation in RKO HDAC2^{wt} and RKO HDAC2^{K462R} cells in response to 5-FU that might be related to the different expression levels of the cell cycle regulator p21 in these cell lines (**Figure 46B**). In addition, this trend coincided with enhanced cell death in RKO HDAC2^{K462R} following 5, 7.5, and 10 µM 5-FU. In response to treatment with two different concentrations of FdUrd, there was a significant increase of S-phase and a significant decrease of G2-phase percentage in viable cells (**Figure S 19B**). In contrast to 5-FU, FdUrd induced cell cycle changes whose extent was equivalent in RKO HDAC2^{wt} and RKO HDAC2^{K462R} cells (**Figure S 19B**).

As described in **1.5.1**, the treatment with 5-FU leads to multiple types of toxic cell damage due to its integration into DNA and RNA. To understand which of these damage mechanisms of 5-FU were affected differently in RKO HDAC2^{wt} and RKO HDAC2^{K462R} cells, and were therefore causal for the observed difference in sensitivity, additional chemotherapeutics with varying mechanisms of action were applied in the two cell lines.

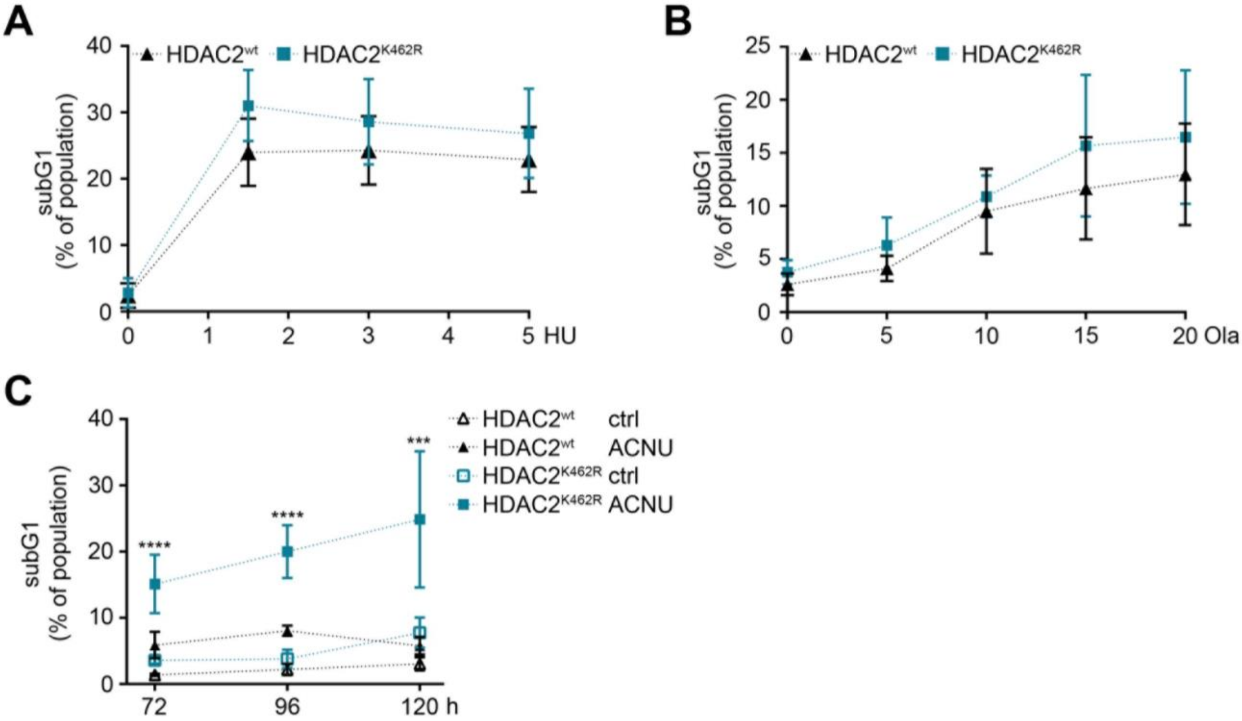

Figure 49: Cell death induction in RKO HDAC2^{wt} and RKO HDAC2^{K462R} in response to HU, olaparib, and ACNU. Cell death induction was measured by flow cytometry analysis of fixed and PI-stained cells as induction of the fraction of cells with fragmented DNA (subG1 fraction). (**A**) Cells were treated with the indicated concentrations of HU (mM) for 48 h. Graph shows mean ± SD (n=10; two-way ANOVA; Sidak's multiple comparisons test; no significant differences). (**B**) Cells were treated with the indicated concentrations of olaparib (µM) for 48 h. Graph shows mean ± SD (n=4; two-way ANOVA; Sidak's multiple comparisons test; no significant differences). (**C**) Cells were treated with 5 µM ACNU for the indicated period. Graph shows mean ± SD (n=4-5; for differences between ACNU-treated HDAC2^{wt} and HDAC2^{K462R}: two-way ANOVA; Sidak's multiple comparisons test; ****P*<0.001, *****P*<0.0001).

Hydroxyurea (HU) is classified as an antimetabolite anticancer drug like 5-FU, and inhibits ribonucleotide reductase and disrupts DNA replication by inhibition of dNTP production (Dobbelstein and Sørensen 2015). Regardless of this similarity, there were no differences in cell death induction in RKO HDAC2^{wt} and RKO HDAC2^{K462R} cells in response to HU (**Figure 49A**). Treatment with HU for 48 h led to a reduction of cells in G2-phase, but this effect was only significant in RKO HDAC2^{wt} cells treated with higher concentrations of HU (**Figure S 20A**). Furthermore, treatment with HU led to an overall increase of S-phase percentage, but this effect was only significant with 1.5 mM HU in RKO HDAC2^{wt} cells (**Figure S 20A**). Furthermore, both cell lines responded with similar cell death induction to the poly ADP ribose polymerase (PARP)-inhibitor olaparib (**Figure 49B**). This finding rules out that loss of HDAC2 sumoylation leads to a DNA repair deficiency that can be exploited for synthetic lethality. Olaparib treatment for 48 h induced a general reduction of cells in G1-phase while increasing the number of cells in G2-phase (**Figure S 20B**). This effect was comparable in RKO HDAC2^{wt} and RKO HDAC2^{K462R} cells (**Figure S 20B**).

The alkylating and ICL inducing agent ACNU ultimately induces cell death through inhibition of DNA double strand separation during replication and subsequent DSB formation (Nikolova et al. 2017a; Nikolova et al. 2017b) (see **1.5.2**). RKO HDAC2^{K462R} cells were significantly more sensitive to ACNU treatment than RKO HDAC2^{wt} cells (**Figure 49C**). Whereas 5-FU and HU induced cytotoxicity at 48 h post treatment (**Figure 49A**, **B**), cell death induction in response to ACNU occurred at later time points (**Figure 49C**). This delay is primarily due to the complex mechanism of crosslink formation (**1.5.2**) that has been described to initially result in a prolonged cell cycle arrest which finally culminates in ICL-associated lethal DNA damage (Nikolova et al. 2012). Concordantly, 24 h ACNU treatment led to a substantial arrest of RKO HDAC2^{wt} and RKO HDAC2^{K462R} cells in G2/M-phase (**Figure S 21A**), which was resolved after 48 h (**Figure S 21B**). Concurrently, at 48 h, cell death induction was only mildly induced in RKO HDAC2^{K462R} cells (**Figure S 21C**). ACNU treatment for 72, 96, and 120 h did not induce striking differences in cell cycle distribution aside from a reduction of cells in G1-phase after 120 h treatment in RKO HDAC2^{K462R} cells (**Figure S 20C**). However, this effect could be based on an increase of G1-phase population in untreated RKO HDAC2^{K462R} cells at this timepoint, which in turn could be the first sign of increased cell density in these untreated samples (**Figure S 20C**). Additionally, after 120 h ACNU, RKO HDAC2^{K462R} cells displayed a tendency for enhanced G2/M-phase and reduced G1-phase percentage compared to RKO HDAC2^{wt} cells (**Figure S 20C**). This effect was comparable to the observed trend in cell cycle distribution noticed after higher concentrations of 5-FU (**Figure S 19**). Furthermore, ICL formation in response to ACNU treatment was detected by modified alkaline COMET assay. COMET tail intensity declined in both cell lines significantly following 24 h ACNU treatment to around 93% (RKO HDAC2^{wt}) and 91% (RKO HDAC2^{K462R}) of the mean tail intensity in the respective control cells (**Figure S 22**). This indicates that the initial formation of ICLs was comparable for RKO HDAC2^{wt} and RKO HDAC2^{K462R} cells. Thus, the divergent sensitivity towards ACNU in these two cell lines more likely stems from an unequal repair capacity for putative RNA damage as well as ICLs and subsequent DSBs.

In summary, only treatment with 5-FU and ACNU evoked a divergent induction of cell death in the compared cell lines, with RKO HDAC2^{K462R} cells being more sensitive.

4.2.4 p53-dependent gene expression in RKO HDAC2^{wt} and RKO HDAC2^{K462R} in response to 5-FU, FdUrd, and HU treatment

As shown in **4.2.2** and by (Brandl et al. 2012), p53-dependent gene expression differed in untreated RKO HDAC2^{wt} and RKO HDAC2^{K462R} cells. To determine whether these changes in basal protein expression contribute to the observed sensitization to 5-FU treatment in RKO HDAC2^{K462R} cells (**Figure 48A**), p53 expression in response to 5-FU, FdUrd, and HU treatment was analyzed by Western blot (**Figure 50**). The induction of p53 total protein expression mediated by 5-FU, FdUrd, and HU was comparable in both cell lines (**Figure 50A, B**). However, due to the enhanced basal p53 expression in RKO HDAC2^{wt}, the absolute p53 expression in response to treatment was slightly higher in this cell line (**Figure 50A**, **B**).

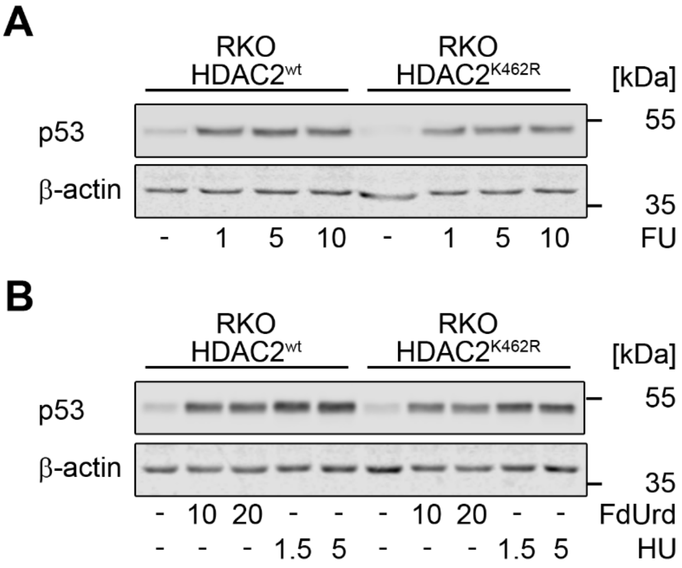

Figure 50: Induction of p53 expression in 5-FU-, FdUrd-, and HU-treated RKO HDAC2^{wt} and RKO HDAC2^{K462R}. (**A**) Cells were treated with the indicated concentrations of 5-FU (µM) for 48 h. (**B**) Cells were treated with the indicated concentrations of FdUrd (µM) and HU (mM). Expression of p53 was analyzed by Western blot. β-actin served as loading control.

This upregulation of p53 as well as its subsequent target gene activation is initiated by DNA damage signaling that leads to the phosphorylation of p53 at serine 15 (Ser15) and thereby inhibits interaction of p53 with its negative regulator HDM2 (Shieh et al. 1997; Canman et al. 1998). No apparent differences in drug-induced p53 (Ser15) phosphorylation were detectable in the two cell lines in response to 5-FU (**Figure 51A**). Likewise, p53 phosphorylation did not differ for both cell lines in response to HU treatment (**Figure 51B**).

Furthermore, expression of the quinone oxidoreductase PIG3, which is another transcriptional target of p53, was determined in response to 5-FU and HU treatment. PIG3 is important for p53 stability and upregulation in response to DNA damage and has a role in early DNA damage response. Moreover, PIG3 colocalizes with γH2AX and 53BP1 to sites of DNA damage (Lee et al. 2010b; Jin et al. 2017). As expected, accumulation and phosphorylation of p53 induced

PIG3 expression in response to 5-FU and HU treatment (**Figure 51A**, **B**). This PIG3 upregulation was comparable in RKO HDAC2^{wt} and RKO HDAC2^{K462R} (**Figure 51A**, **B**).

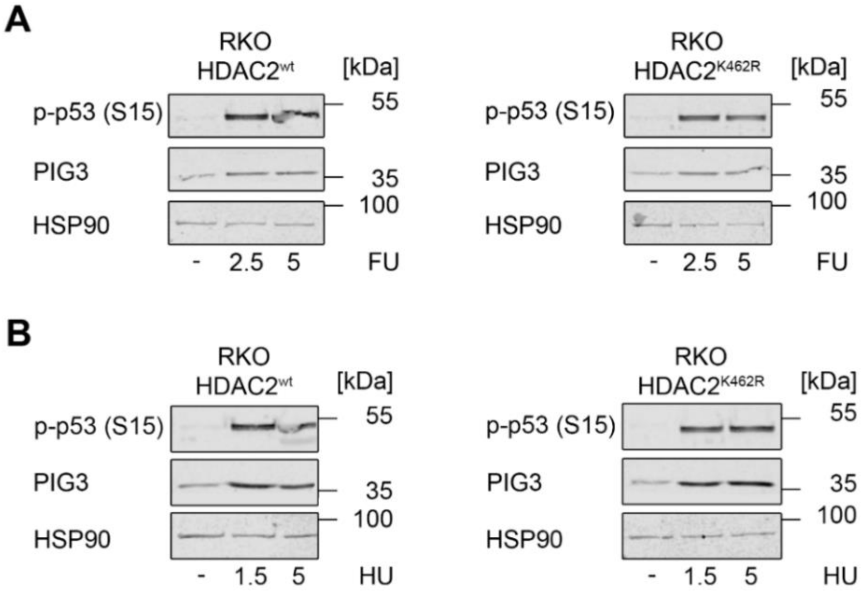

Figure 51: Induction of p53 (Ser15) phosphorylation and PIG3 expression in 5-FU- and HU-treated RKO HDAC2^{wt} and RKO HDAC2^{K462R}. (**A**) Cells were treated with the indicated concentrations of 5-FU (µM) for 48 h. Phosphorylation of p53 at Ser15 and expression levels of PIG3 was analyzed by Western blot. HSP90 served as loading control. (**B**) Cells were treated with the indicated concentrations of HU (mM) for 48 h. Phosphorylation of p53 at Ser15 and expression levels of PIG3 was analyzed by Western blot. HSP90 served as loading control.

In contrast, induction of the p53 target protein p21 in response to 5-FU seemed to be more prominent in RKO cells expressing HDAC2^{K462R} (**Figure 52A**, **B**). However, quantification of signal intensities showed that this effect was a result of the enhanced p21 basal expression in RKO HDAC2^{K462R} cells (**Figure 46B**, **Figure 52**, **Figure S 23**). When the different basal p21 expression levels were considered, p21 fold-induction compared to control was equivalent in both cell lines at all time points (**Figure S 23**). Thus, a similar degree of upregulation of the cell cycle regulator p21 occurred in both cell lines in response to 5-FU treatment. In contrast, FdUrd treatment did not result in a visible upregulation of p21 (**Figure 52**).

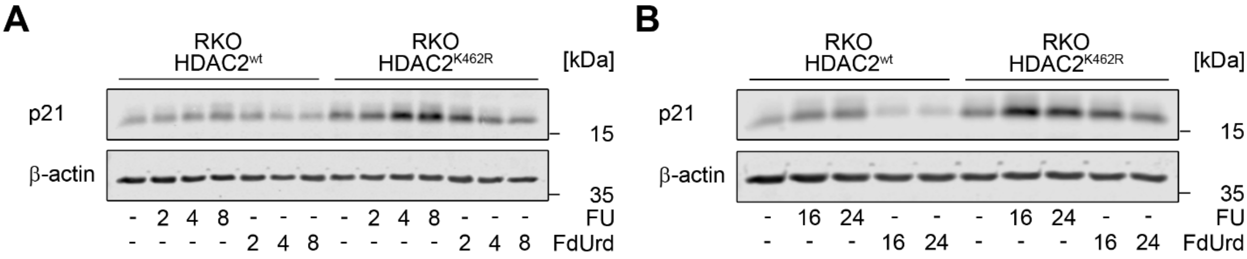

Figure 52: Induction of p21 expression in 5-FU- and FdUrd-treated RKO HDAC2^{wt} and RKO HDAC2^{K462R}. (**A**) Cells were treated with 10 µM 5-FU and 20 µM FdUrd for 2 h, 4 h, and 8 h and analyzed for p53 and p21 expression by Western blot. β-actin served as loading control. (**B**) Cells were treated with 10 µM 5-FU and 20 µM FdUrd for 16 h and 24 h and analyzed for p53 and p21 expression by Western blot. β-actin served as loading control.

These data hint to an equivalent p53 activation in RKO HDAC2^{wt} and RKO HDAC2^{K462R} cells. This finding cannot offer an explanation for the observed differences in cell death induction in response to 5-FU.

4.2.5 Thymidylate synthase inhibition in 5-FU-treated RKO HDAC2^{wt} and RKO HDAC2^{K462R}

As described in **1.5.1**, one of the central toxic mechanisms of 5-FU is the inhibition of TS. To determine whether sensitization of HDAC2^{K462R} expressing RKO cells was associated with differences in TS inhibition, expression of active TS and the inactive FdUMP-CH$_2$THF-TS complex (TS*) was determined by Western blot (**Figure 53**). Quantification of free and complexed TS was feasible because TS* displays reduced mobility on SDS-PAGE compared to free TS. However, there was no different TS inhibition detectable for HDAC2^{wt} and HDAC2^{K462R} expressing RKO cells in short-term (**Figure 53A**) or long-term (**Figure 53B**) treated samples. These data indicate that the extent of TS* complex formation and the ensuing DNA damage through TS inhibition-mediated dTTP depletion is comparable in both cell lines and thus independent of HDAC2 sumoylation.

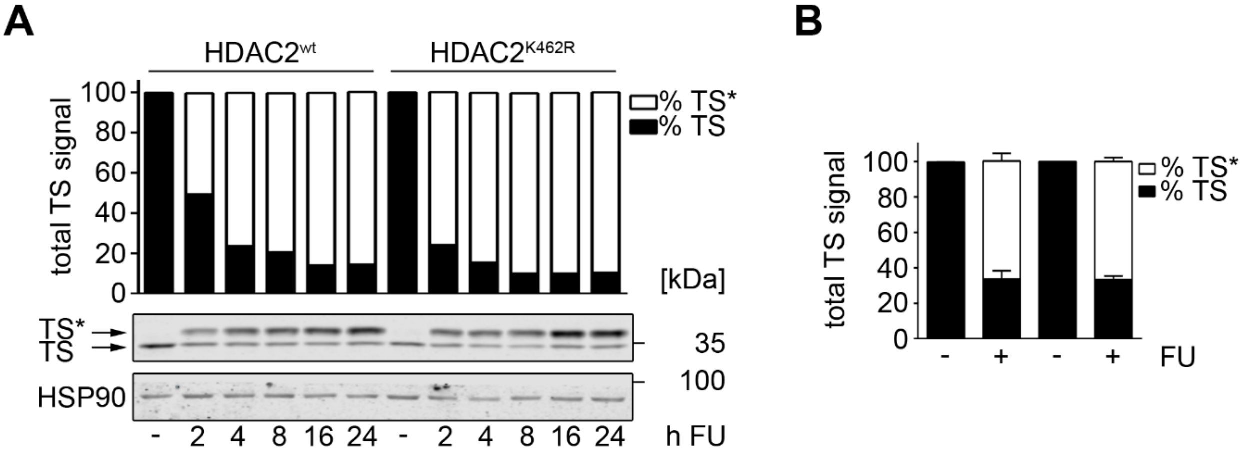

Figure 53: Thymidylate synthase inhibition in RKO HDAC2^{wt} and RKO HDAC2^{K462R} treated with 5-FU. Cells were treated with 10 µM 5-FU for 2, 4, 8, 16, and 24 h (**A**) or 48 h (**B**). Expression of free thymidylate synthase protein (TS) and the FdUMP-CH$_2$THF-TS complex (TS*) was determined by Western blot. HSP90 served as loading control. Quantification was performed by measuring signal intensities of both TS bands and normalization to the respective loading control. (**B**) shows mean ±SD (n=2).

4.2.6 Global protein expression analysis in RKO HDAC2^{wt} and RKO HDAC2^{K462R}

Divergent sensitivity of sumoylation-deficient RKO cells might stem from differences in basal protein expression in both cell lines. In an attempt to uncover differently expressed proteins in RKO HDAC2^{wt} and RKO HDAC2^{K462R} cells, a mass spectrometric analysis of global protein expression was performed. Using this approach, the expression levels of 5901 different proteins were measured in both cell lines and depicted in a scatter plot as log2 values of label free quantification (LFQ) (**Figure 54**). The blue diagonal in this scatter plot indicates equal expression levels in RKO HDAC2^{wt} and RKO HDAC2^{K462R} cells, while the two red lines define a threshold for the identification of significantly differentially expressed proteins. Each detected protein is symbolized by an individual dot and differently expressed proteins are colored in red. Thus, the analysis revealed that 54 proteins are variably expressed in untreated RKO HDAC2^{wt} and RKO HDAC2^{K462R} cells. 17 of these proteins are lower expressed and 37 are higher expressed in RKO HDAC2^{K462R} cells in comparison to RKO HDAC2^{wt} cells.

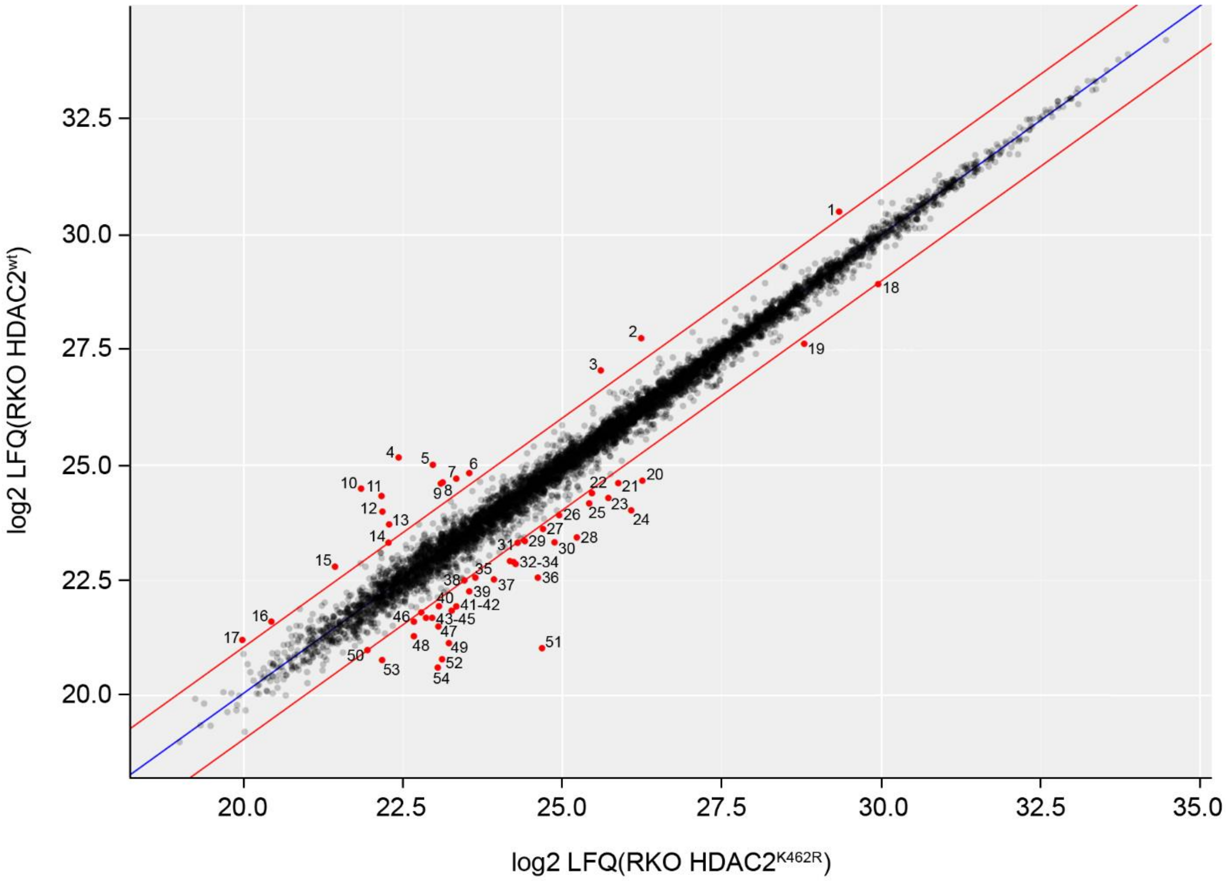

Figure 54: Mass spectrometric analysis of protein expression in RKO HDAC2^{wt} and RKO HDAC2^{K462R}. Four independent replicates of RKO HDAC2^{wt} and RKO HDAC2^{K462R} cells were analyzed for global protein expression by LFQ via mass spectrometry. Graph shows differences in LFQ protein expression levels. Each dot represents an individual protein and differently expressed proteins are colored in red and serially numbered. Annotation is provided in **Figure 55**.

Detailed expression values for all differently regulated proteins are listed in the heatmaps in **Figure 55**. As values are given in a log2 scale, a difference of 1 unit depicts a doubling of protein expression. Knowing that RKO HDAC2^{wt} and RKO HDAC2^{K462R} differ in their p53 expression and their p53-dependent gene expression, the differently expressed proteins in our analysis were initially screened for their dependence on p53 as a transcription factor. All identified 54 differently expressed proteins were for this purpose compared to a list of p53-activated target genes that was compiled by (Fischer 2017). In this analysis, Fischer compared 16 different high-throughput data sets derived from genome-wide analyses aimed at identifying

53 target genes and conclusively listed 116 genes that were found in at least 6 out of 16 datasets. Two proteins that were found in 16 out of 16 datasets were also the only 53 target proteins to be differently regulated in our analysis: the cell cycle regulator p21 (*CDKN1A*; nr. 32) and the ribonucleotide reductase p53R2 (*RRM2B*; nr. 24) were upregulated roughly 2-fold in RKO cells expressing HDAC2^{K462R} (**Figure 55**). The remaining 52 differently expressed proteins are not known as p53 target genes. This indicates further changes in gene expression that are associated with HDAC2^{K462} sumoylation and independent of p53 activity.

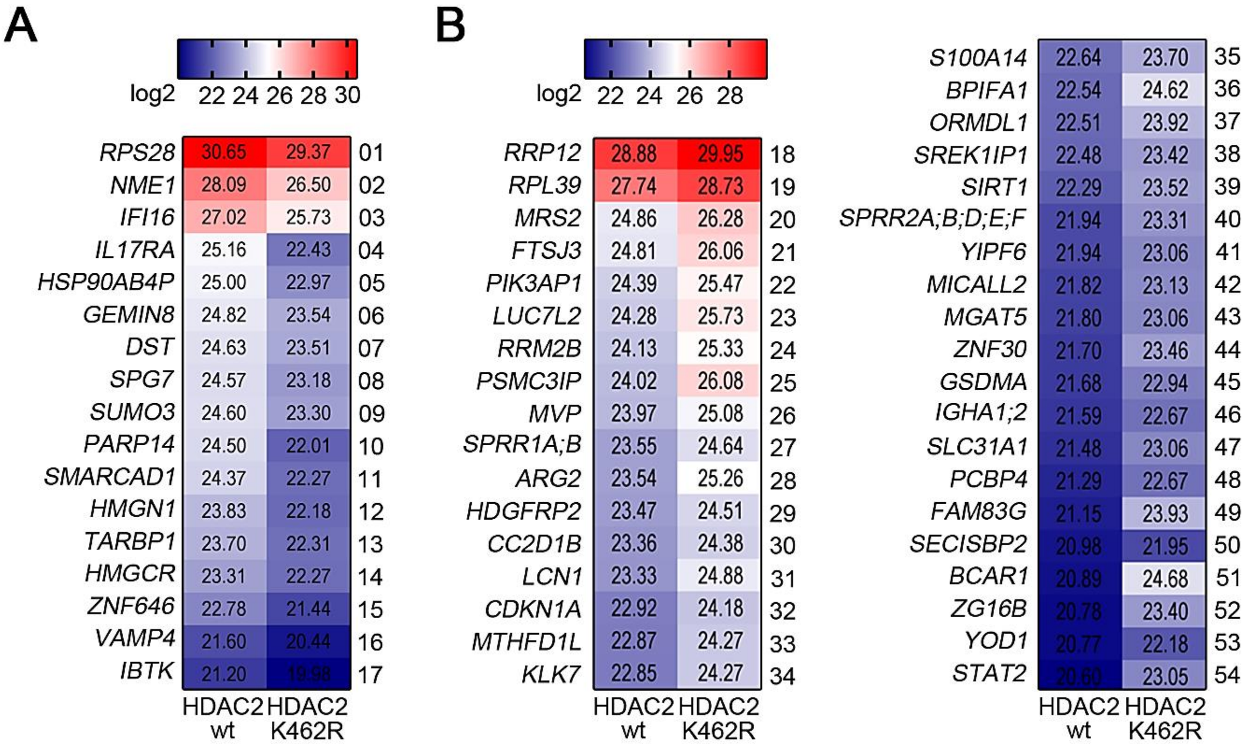

A

	HDAC2 wt	HDAC2 K462R	
RPS28	30.65	29.37	01
NME1	28.09	26.50	02
IFI16	27.02	25.73	03
IL17RA	25.16	22.43	04
HSP90AB4P	25.00	22.97	05
GEMIN8	24.82	23.54	06
DST	24.63	23.51	07
SPG7	24.57	23.18	08
SUMO3	24.60	23.30	09
PARP14	24.50	22.01	10
SMARCAD1	24.37	22.27	11
HMGN1	23.83	22.18	12
TARBP1	23.70	22.31	13
HMGCR	23.31	22.27	14
ZNF646	22.78	21.44	15
VAMP4	21.60	20.44	16
IBTK	21.20	19.98	17

B

	HDAC2 wt	HDAC2 K462R	
RRP12	28.88	29.95	18
RPL39	27.74	28.73	19
MRS2	24.86	26.28	20
FTSJ3	24.81	26.06	21
PIK3AP1	24.39	25.47	22
LUC7L2	24.28	25.73	23
RRM2B	24.13	25.33	24
PSMC3IP	24.02	26.08	25
MVP	23.97	25.08	26
SPRR1A;B	23.55	24.64	27
ARG2	23.54	25.26	28
HDGFRP2	23.47	24.51	29
CC2D1B	23.36	24.38	30
LCN1	23.33	24.88	31
CDKN1A	22.92	24.18	32
MTHFD1L	22.87	24.27	33
KLK7	22.85	24.27	34

	HDAC2 wt	HDAC2 K462R	
S100A14	22.64	23.70	35
BPIFA1	22.54	24.62	36
ORMDL1	22.51	23.92	37
SREK1IP1	22.48	23.42	38
SIRT1	22.29	23.52	39
SPRR2A;B;D;E;F	21.94	23.31	40
YIPF6	21.94	23.06	41
MICALL2	21.82	23.13	42
MGAT5	21.80	23.06	43
ZNF30	21.70	23.46	44
GSDMA	21.68	22.94	45
IGHA1;2	21.59	22.67	46
SLC31A1	21.48	23.06	47
PCBP4	21.29	22.67	48
FAM83G	21.15	23.93	49
SECISBP2	20.98	21.95	50
BCAR1	20.89	24.68	51
ZG16B	20.78	23.40	52
YOD1	20.77	22.18	53
STAT2	20.60	23.05	54

Figure 55: Heatmap of protein expression in RKO HDAC2^{wt} and RKO HDAC2^{K462R} determined by mass spectrometric analysis. Four independent replicates of RKO HDAC2^{wt} and RKO HDAC2^{K462R} cells were analyzed for global protein expression by LFQ via mass spectrometry. Heatmaps show differences in LFQ expression levels of the indicated proteins as log2 values. Numbers refer to the numbered dots in **Figure 54**. (**A**) shows proteins whose expression is downregulated in RKO HDAC2^{K462R} and (**B**) shows proteins whose expression is upregulated in RKO HDAC2^{K462R} in comparison to RKO HDAC2^{wt}.

Specific candidate proteins were evaluated and selected within this list with regard to their potential functional relevance for 5-FU-related repair mechanisms and toxicity. Like p53R2, the kinase NME1 (*NME1*; nr. 02) has implications in 5-FU metabolism and was found to be regulated in dependence of HDAC2 sumoylation (**Figure 55A**). In consideration of the fact that 5-FU toxicity might be linked to its RNA-damaging effects, it is noteworthy, that the expression of three proteins with functions in ribosome biogenesis was affected by HDAC2-sumoylation: the ribosomal proteins RPS28 (*RPS28*; nr. 01) and RPL39 (*RPL39*; nr. 19) and the regulator of ribosomal assembly RRP12 (*RRP12*; nr. 18) (**Figure 55**). Furthermore, three proteins with known implications in DNA damage repair were differentially expressed in RKO HDAC2^{wt} and RKO HDAC2^{K462R} cells: SIRT1 (*SIRT1*; nr. 39) is upregulated 2-fold, HMGN1 (*HMGN1*; nr. 12) is downregulated 2-fold, and SMARCAD1 (*SMARCAD1*; nr. 11) is downregulated 4-fold in HDAC2^{K462R}-expressing cells (**Figure 55**). The distinct functions and the possible implications of the regulation of each of these selected proteins is going to be outlined in detail in the discussion of this work (**5.2.6**).

In summary, around 0.9% of the detected proteins were found to be differently expressed in untreated RKO HDAC2^{wt} and RKO HDAC2^{K462R} cells. Out of these 54 candidate proteins the expression of two factors was known to be dependent on p53. This finding indicates that an influence on p53 activity is not the only consequence of HDAC2^{K462} sumoylation. In light of the importance of chromatin regulators such as SMARCAD1 in DNA repair and the fact that its expression was most prominently regulated in dependence of HDAC2-sumoylation, subsequent studies were focused on its possible role in 5-FU-mediated toxicity.

4.2.7 Expression of chromatin remodeling complex helicases in RKO HDAC2^{wt} and RKO HDAC2^{K462R}

Furthermore, the list of 54 differently expressed proteins in mass spectrometry was evaluated with regard to the molecular functions of each protein. SMARCAD1 is an ATPase of the SNF2 family and this class of helicases are known core subunits of chromatin remodeling complexes that are implicated in different DNA damage repair pathways and play essential roles in chromatin organization and DSB repair (Adra et al. 2000; Brownlee et al. 2015; Rother and van Attikum 2017). Considering that the sensitivity of RKO HDAC2^{K462R} cells to 5-FU and ACNU might be caused by a DNA damage repair deficiency, the more than 4-fold decrease in the expression of the DNA helicase SMARCAD1 (*SMARCAD1*, nr. 11) is noteworthy (**Figure 55**). The mass spectrometric result was confirmed by Western blot (**Figure 56A**). Concurrent analysis of the p53 target proteins DDB2 and p21 confirmed that recombinant HDAC2^{wt} and HDAC2^{K462R} expression affected p53 target gene expression as expected in these samples (**Figure 56**). Quantification of SMARCAD1 expression in multiple independent Western blot analyses showed that expression in RKO HDAC2^{K462R} cells was reduced to around 15% of the expression of SMARCAD1 in RKO HDAC2^{wt} cells (**Figure 56B**).

As expression of the DNA helicase SMARCAD1 was shown to be reduced in HDAC2^{K462R} expressing RKO cells, expression levels of further, central chromatin remodeling-associated DNA helicases were also accessed by Western blot analysis. The two ATP-dependent helicases BRG1 (*SMARCA4*) and BRM (*SMARCA2*) are central catalytic subunits of the crucial mammalian chromatin remodeling complexes BAF and PBAF which are widely implicated in the regulation of embryonic development, chromosomal stability, DNA repair, and general tumor biology (Reisman et al. 2009; Hodges et al. 2016) (see **1.6.5**).

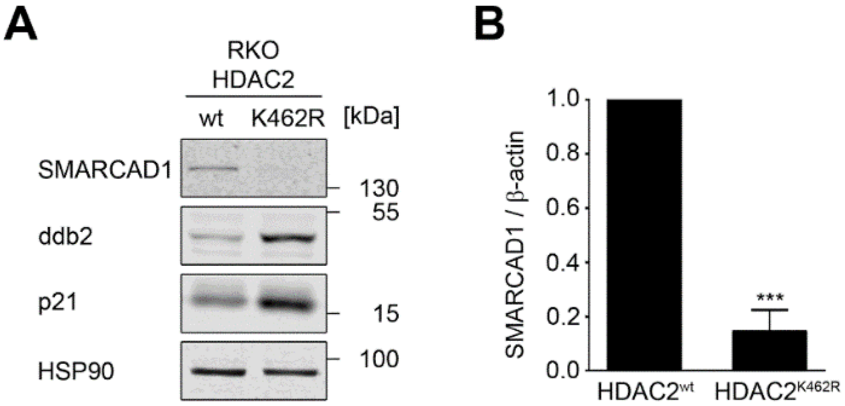

Figure 56: SMARCAD1 expression in RKO HDAC2^{wt} and RKO HDAC2^{K462R}. (**A**) Expression of the indicated proteins was analyzed in untreated cells. HSP90 served as loading control. (**B**) Quantification of SMARCAD1 expression was achieved by densitometric analysis of SMARCAD1 signal intensity and normalization to the respective loading control signal intensity. Graph shows mean ± SD (n=4; two-tailed paired student's t-test, ***P>0.001).

BRG1 was not found in mass spectrometric analysis (**Figure 54**), but its expression was significantly reduced to around 20% in HDAC2^{K462R} expressing RKO cells in Western blot (**Figure 57**). Concurrent detection of p53 shows that HDAC2^{wt} and HDAC2^{K462R} affected p53 expression in these samples as expected (**Figure 57A**). As BRG1, BRM protein was not found using mass spectrometry. In contrast to BRG1, BRM was expressed equally in RKO HDAC2^{wt} and RKO HDAC2^{K462R} cells (**Figure S 24**). Thus, the focus of further investigations lay on BRG1 and SMARCAD1 expression.

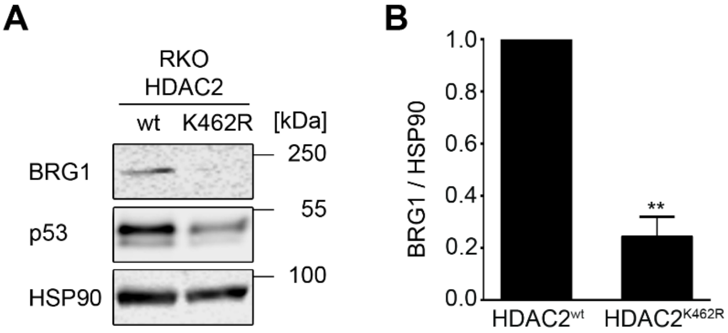

Figure 57: BRG1 expression in RKO HDAC2^{wt} and RKO HDAC2^{K462R}. (**A**) Expression of the indicated proteins was analyzed in untreated cells. HSP90 served as loading control. (**B**) Quantification of BRG1 expression was achieved by densitometric analysis of BRG1 signal intensity and normalization to the respective loading control signal intensity. Graph shows mean ± SD (n=3; two-tailed paired student's t-test, ***P>0.01).

Lysates of MS-275-treated HDAC2 positive tumor cell lines were analyzed to determine if class I HDAC inhibition did result in the same reduction of SMARCAD1 and BRG1 expression that was observed in RKO HDAC2^{K462R} (**Figure 56**, **Figure 57**, **Figure 58**). In the human chronic myeloid cell line K562, treatment with 5 µM MS-275 resulted in an 87% reduction of SMARCAD1 expression (**Figure 58A**). Furthermore, the human colon carcinoma cell line HCT116 as well as the human pancreatic tumor cell line MiaPaca showed a 50% reduction in

SMARCAD1 expression in response to MS-275 treatment (**Figure 58B, C**). SMARCAD1 expression in HDAC2 wild-type RKO cells was decreased to 30% by MS-275 (**Figure 58D**). Furthermore, BRG1 expression was reduced to less than 10% in RKO and HCT116 cells as a result of MS-275 treatment (**Figure 58E, F**). Following HDAC2 knockdown in RKO HDAC2^{wt} by siRNA transfection, a reduced expression of SMARCAD1 was detectable (**Figure S 25**).

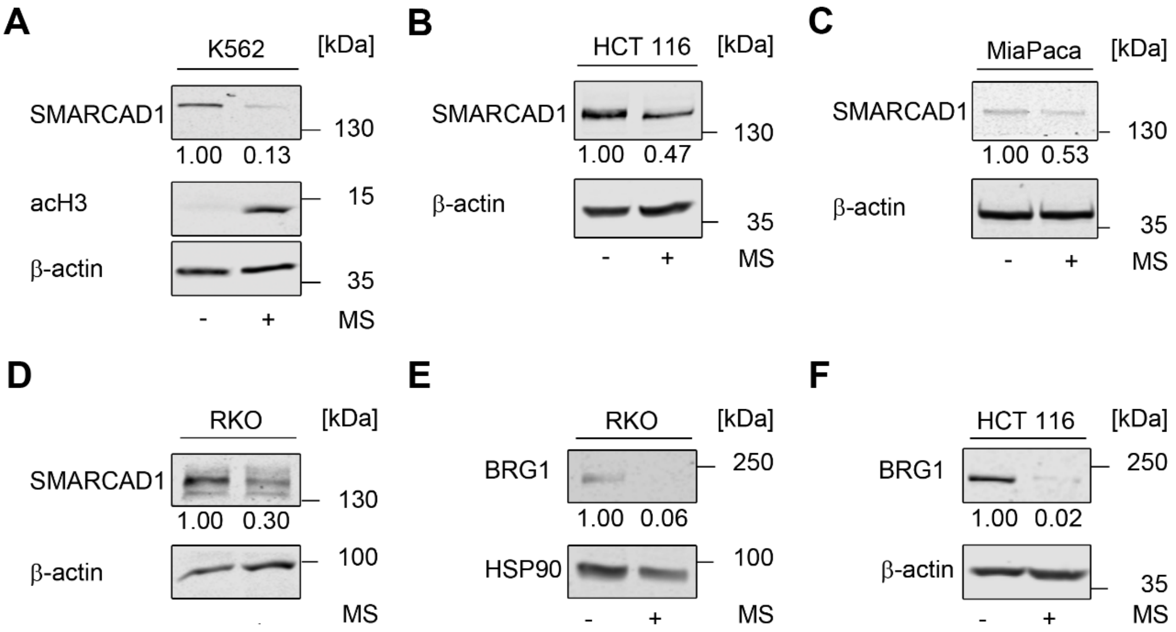

Figure 58: SMARCAD1 and BRG1 expression in selected MS-275-treated cell lines. (**A**) K562 cells were treated with 5 µM MS-275 for 48 h. SMARCAD1 expression and histone H3 acetylation was determined by Western blot analysis. β-actin served as loading control. (**B**) HCT116 cells were treated with 2 µM MS-275 for 24 h. SMARCAD1 expression was determined by Western blot analysis. β-actin served as loading control. (**C**) MiaPaca cells were treated with 2 µM MS-275 for 24 h. SMARCAD1 expression was determined by Western blot analysis. β-actin served as loading control. K652 and MiaPaca lysates for (**A**) and (**C**) were kindly provided by [redacted] and HCT116 lysates for (**B**) were kindly provided by [redacted] (**D**) RKO cells were treated with 2 µM MS-275 for 48 h. SMARCAD1 expression was determined by Western blot analysis. β-actin served as loading control. (**E**) RKO cells were treated with 2 µM MS-275 for 72 h. BRG1 expression was determined by Western blot analysis. HSP90 served as loading control. (**F**) HCT116 cells were treated with 2 µM MS-275 for 96 h. BRG1 expression was determined by Western blot analysis. β-actin served as loading control.

In summary, these data demonstrate the close relationship between the sumoylation and activity of HDAC2 and the expression of SMARCAD1 and BRG1.

4.2.8 DNA damage response in 5-FU-treated RKO HDAC2^{wt} and RKO HDAC2^{K462R}

In light of the finding that the DNA helicases SMARCAD1 and BRG1 were differentially expressed in dependence of HDAC sumoylation, DNA damage signaling in response to 5-FU was analyzed in closer detail. Early DNA damage response signaling pathways are critically orchestrated by the kinases ATM and ATR (see **1.6.1**) (Roos and Kaina 2013). Phosphorylation of ATM at Ser1981 and phosphorylation of ATR at Thr1989 was induced in RKO HDAC2^{wt} and RKO HDAC2^{K462R} cells after treatment with different concentrations of 5-

FU (**Figure 59**). Phosphorylation of ATM was more prominent than ATR phosphorylation in both cell lines (**Figure 59**). There was no difference in the extent of induced ATM nor ATR phosphorylation between the two cell lines (**Figure 59**). Phosphorylation of CHK1 and CHK2, which are both direct downstream targets of ATM and ATR in DNA damage signaling (Roos and Kaina 2013), was induced equally in RKO HDAC2^{wt} and in RKO HDAC2^{K462R} cells in response to 5-FU treatment (**Figure 59**).

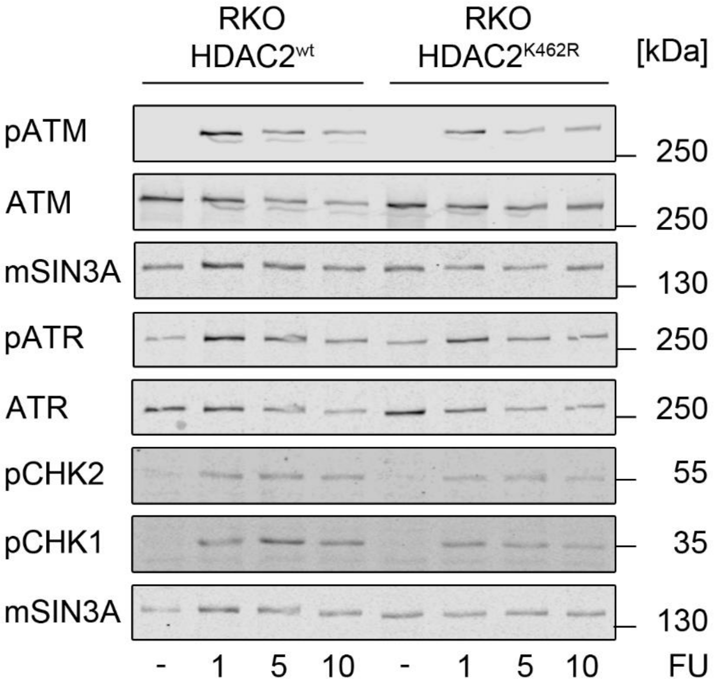

Figure 59: DNA damage signaling in 5-FU-treated RKO HDAC2^{wt} and RKO HDAC2^{K462R}. Cells were treated with the indicated concentrations of 5-FU (µM) for 48 h. Expression and phosphorylation of the indicated proteins was analyzed by Western blot. mSin3a served as loading control.

Furthermore, phosphorylation of ATM and ATR was uniformly induced in response to FdUrd and HU treatment in RKO HDAC2^{wt} and RKO HDAC2^{K462R} cells (**Figure 60**). FdUrd and HU treatment led to increased phosphorylation of CHK1 and CHK2 at comparable levels in both cell lines (**Figure 60**). Phosphorylation of ATM and CHK1 were additionally analyzed at earlier timepoints (16 h and 24 h) in 5-FU- and FdUrd-treated RKO HDAC2^{wt} and RKO HDAC2^{K462R} cells. FdUrd induced higher phosphorylation of ATM and CHK1 than 5-FU did at equal timepoints (**Figure 61**). Phosphorylation of CHK1 was especially high in response FdUrd at both time points (**Figure 61**). However, there was no significant difference in the extent of phosphorylation of ATM or CHK1 between RKO HDAC2^{wt} and RKO HDAC2^{K462R} cells with either treatment (**Figure 61**).

In summary, these data indicate that initial ATM- and ATR-dependent DNA damage signaling and the phosphorylation of ATM and ATR target proteins CHK1 and CHK2 was independent of HDAC2 sumoylation.

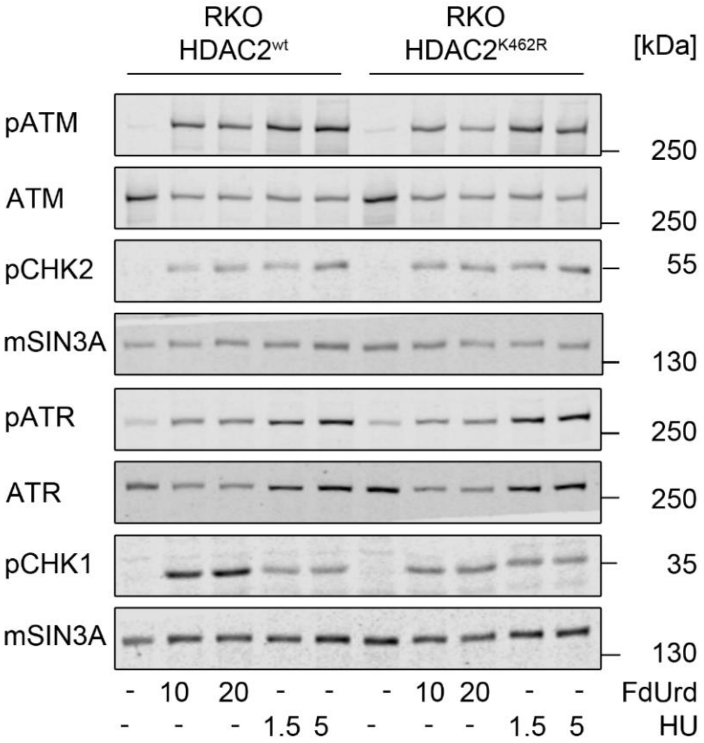

Figure 60: DNA damage signaling in FdUrd- and HU-treated RKO HDAC2^{wt} and RKO HDAC2^{K462R}. Cells were treated with the indicated concentrations of FdUrd (µM) and HU (mM) for 48 h. Expression and phosphorylation of the indicated proteins was determined by Western blot. mSin3a served as loading control.

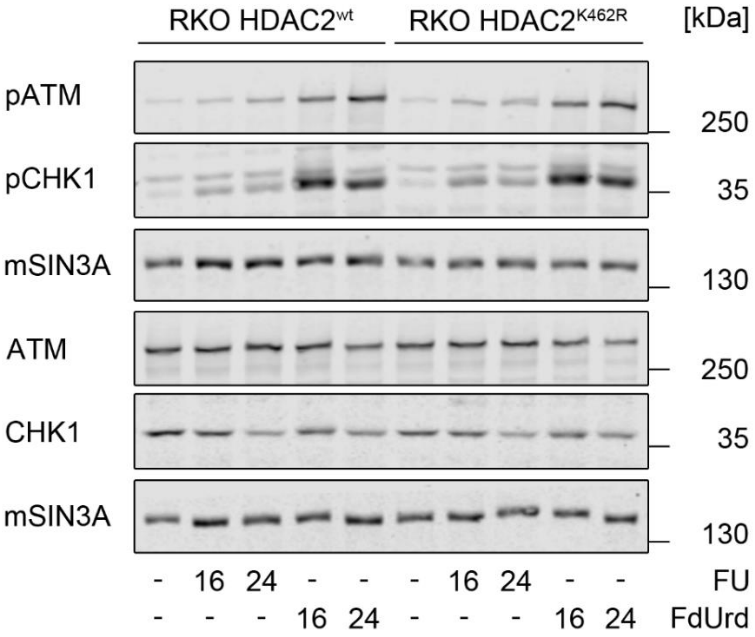

Figure 61: DNA damage signaling in 5-FU- and FdUrd-treated RKO HDAC2^{wt} and RKO HDAC2^{K462R}. Cells were treated with 10 µM 5-FU and 20 µM FdUrd for 16 h and 24 h. Expression and phosphorylation of the indicated proteins was analyzed by Western blot. mSin3a served as loading control.

4.2.9 Effect of HDAC2^{K462R} expression on γH2AX formation

The phosphorylation of H2AX at Ser-139 plays a central role in DNA repair mechanisms, as the resulting phosphorylated H2AX (γH2AX) triggers the accumulation of a plethora of different DSB repair and DNA damage signaling molecules in discrete foci (see **1.6.1**; (Fernandez-Capetillo et al. 2004)). The formation of these approximately 2 Mbp domains of γH2AX is acknowledged as genuine and quantitative marker for DSB induction and repair (Rogakou et al. 1998; Rothkamm and Löbrich 2003). Chromatin remodeling complexes and especially their core helicase subunits like BRG1 and SMARCAD1 have been implicated in DNA repair processes (see **1.6.5**). It has been shown that they contribute to effective DSB repair by stimulating the phosphorylation of histone H2AX and thereby enabling repair and preventing apoptosis in response to DNA damage induction (Kwon et al. 2015; Chakraborty et al. 2018). Noteworthy, loss of H2AX phosphorylation observed in cells lacking the expression of chromatin remodeling complex helicases does not lead to changes in the expression and activation of ATM, ATR, and DNA-PK (Kwon et al. 2015), which corresponds to the unchanged expression and activation of these PIKKs and their target proteins CHK1 and CHK2 seen in **4.2.6**. Phosphorylation of H2AX in response to 5-FU treatment was therefore more closely determined in RKO HDAC2^{wt} and RKO HDAC2^{K462R} cells. Western blot analyses showed that γH2AX formation in RKO HDAC2^{K462R} was impaired in response to 5-FU when compared with equally treated RKO HDAC2^{wt} cells (**Figure 62A**). This effect was consistent when samples of both cell lines were blotted on the same membrane (**Figure S 26**).

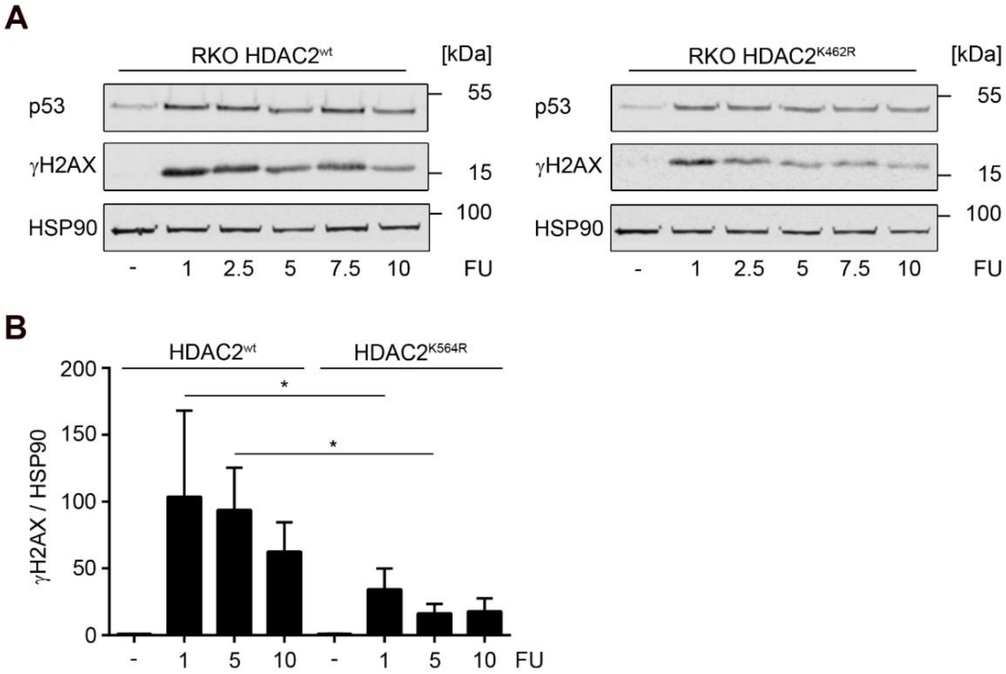

Figure 62: Phosphorylation of histone H2AX in 5-FU-treated RKO HDAC2^{wt} and RKO HDAC2^{K462R}. (**A**) Cells were treated with the indicated concentrations of 5-FU (µM) for 48 h. p53 expression and histone H2AX phosphorylation were analyzed by Western blot. HSP90 served as loading control. (**B**) Quantification of H2AX phosphorylation was achieved by densitometric analysis of γH2AX signal intensity and normalization to the

respective loading control signal intensity. Graph shows mean ± SD (n=3-4; one-way ANOVA; Tukey's multiple comparisons test; *$P<0.05$). Divergent regulation of H2AX phosphorylation in both cell lines is likewise detectable when respective samples for both cell lines are blotted on the same membrane (see **Figure S 26** for example).

Quantification of H2AX phosphorylation confirmed that the extent of γH2AX formation in response to multiple 5-FU concentrations was significantly lower in RKO HDAC2^{K462R} cells than in RKO HDAC2^{wt} cells (**Figure 62B**). Furthermore, phosphorylation of histone H2AX was determined in response to treatment with FdUrd and HU. The reduced extent of γH2AX formation in FdUrd-treated RKO HDAC2^{K462R} was distinct and the same effect was present in HU-treated RKO HDAC2^{K462R} cells (**Figure 63**).

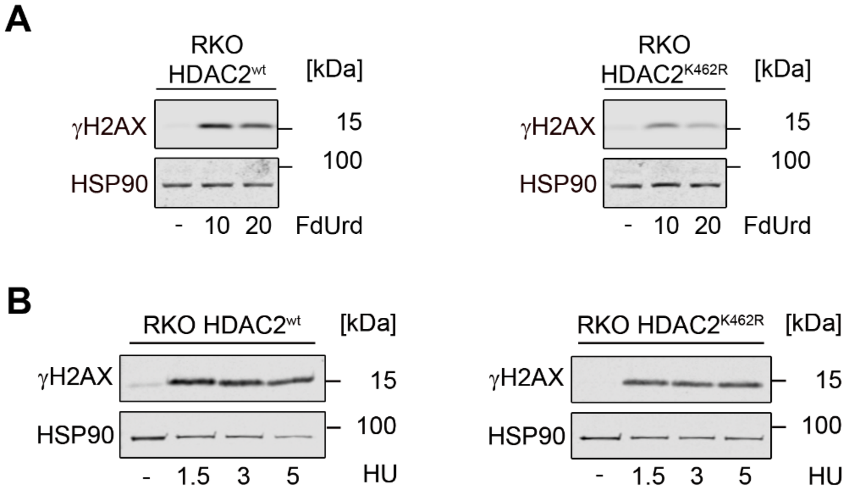

Figure 63: Phosphorylation of histone H2AX in FdUrd- and HU-treated RKO HDAC2^{wt} and RKO HDAC2^{K462R}. (**A**) Cells were treated with the indicated concentrations of FdUrd (µM) for 48 h. Histone H2AX phosphorylation was analyzed by Western blot. HSP90 served as loading control. (**B**) Cells were treated with the indicated concentrations of HU (mM) for 48 h. p53 expression and histone H2AX phosphorylation was analyzed by Western blot. HSP90 served as loading control. Divergent regulation of H2AX phosphorylation in response to FdUrd in both cell lines is likewise detectable when respective samples for both cell lines are blotted on the same membrane (see **Figure S 26** for example).

Noteworthy, the observed difference in H2AX phosphorylation in response to 5-FU and FdUrd treatment in RKO HDAC2^{wt} and RKO HDAC2^{K462R} cells was persistent in the presence of the apoptosis inhibitor Z-VAD-FMK (**Figure 64**).

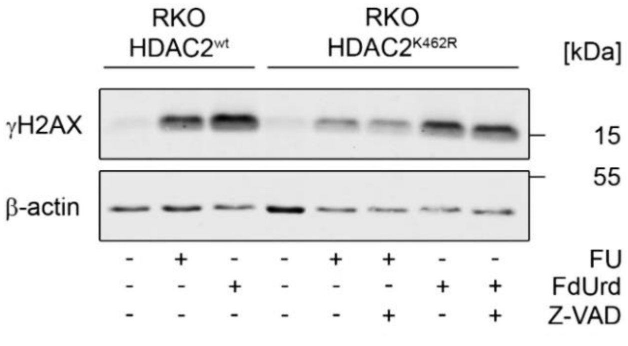

Figure 64: Phosphorylation of histone H2AX in 5-FU, FdUrd, and Z-VAD-treated RKO HDAC2^{wt} and RKO HDAC2^{K462R}. Cells were treated as indicated with 5 µM FU, 10 µM FdUrd, and 30 µM Z-VAD for 48 h. Phosphorylation of histone H2AX was determined by Western blot analysis. β-actin served as loading control.

Unfortunately, γH2AX formation in response to 5-FU treatment at earlier timepoints was not profound enough to be reliably detectable in Western blot analysis (**Figure S 27**).

In summary, these results indicate that H2AX phosphorylation in response to DNA damage is differentially regulated in RKO cells in dependence of HDAC2 sumoylation. This finding supports previously published data on the impact of chromatin remodelers on γH2AX formation (Park et al. 2006; Kwon et al. 2015).

4.2.10 Immunofluorescence analysis of H2AX phosphorylation and 53BP1 foci in dependence of SMARCAD1, HDAC2, and BRG1 expression

Immunofluorescence analysis was used to gain further insight into the significance of SMARCAD1 and BRG1 helicase expression for DNA damage recognition by γH2AX.

For this purpose, RKO HDAC2^{wt} cells were transfected with siRNA directed against SMARCAD1 and BRG1 to mimic the loss of expression of these helicases that was observed in RKO HDAC2^{K462R} cells (**Figure 56**, **Figure 57**). Following transfection, RKO HDAC2^{wt} cells were challenged with 5-FU for 6 h and 24 h and γH2AX fluorescence was assessed by confocal microscopy. In contrast to data in the literature that specifically links the loss of chromatin complex activity to defects in H2AX phosphorylation (Park et al. 2006; Lee et al. 2010a; Kwon et al. 2015), there were no striking optical disparities detectable in γH2AX immunofluorescence in response to 5-FU (**Figure 65A**, **Figure S 28**). Quantification of mean fluorescence intensity of γH2AX signal confirmed that H2AX phosphorylation was equal in RKO HDAC2^{wt} and RKO HDAC2^{K462R} cells after 6 h and 24 h 5-FU treatment (**Figure 65B**). These data indicate that sole loss of BRG1 and SMARCAD1 expression in RKO HDAC2^{wt} cells was not sufficient to induce differences in γH2AX formation in response to 5-FU treatment (**Figure 65**). As quantification γH2AX fluorescence in this experiment was complicated by the absence of the formation of distinct of 5-FU-mediated γH2AX repair foci in most cells (**Figure 65**, **Figure S 28**), IR was exploited as a substitute for 5-FU in the subsequent immunofluorescence analyses. IR is an explicit inducer of DSBs and a frequently used stimulus to study γH2AX foci formation (Vignard et al. 2013).

Thus, RKO HDAC2^{wt} and RKO HDAC2^{K462R} were irradiated and confocal microscopy was used to determine mean γH2AX intensity and the quantity of γH2AX and tumor suppressor 53BP1 repair foci. Both cell lines showed equal mean γH2AX fluorescence intensities, indicating similar H2AX phosphorylation 1 h post irradiation with 6 Gy (Figure 66**A, B, Figure S 29**). In accordance, subsequent quantification of γH2AX foci displayed no difference of H2AX phosphorylation in RKO HDAC2^{wt} and RKO HDAC2^{K462R} cells (**Figure S 30**).

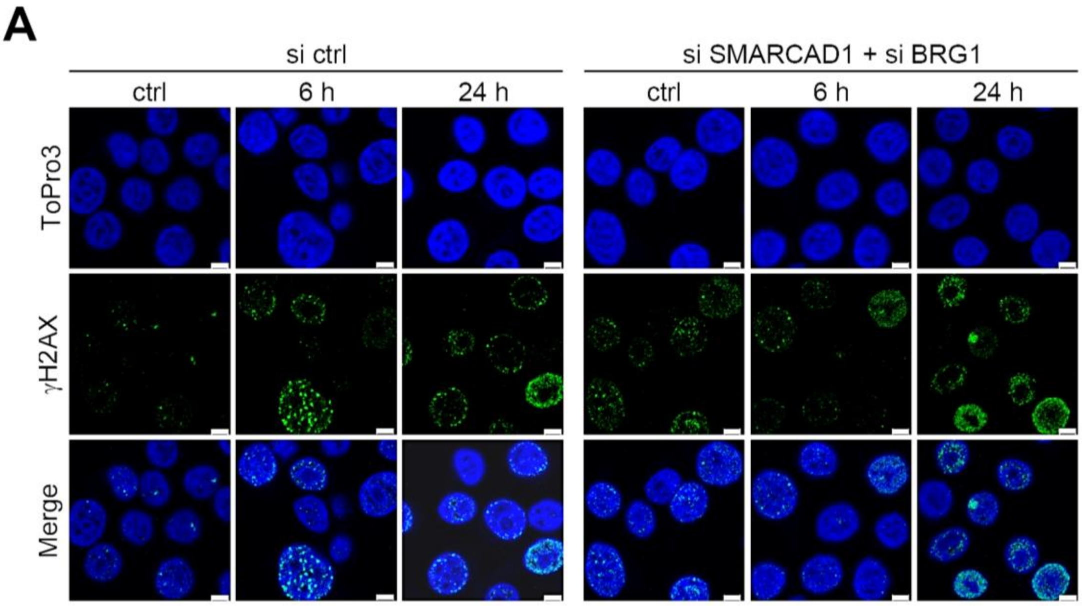

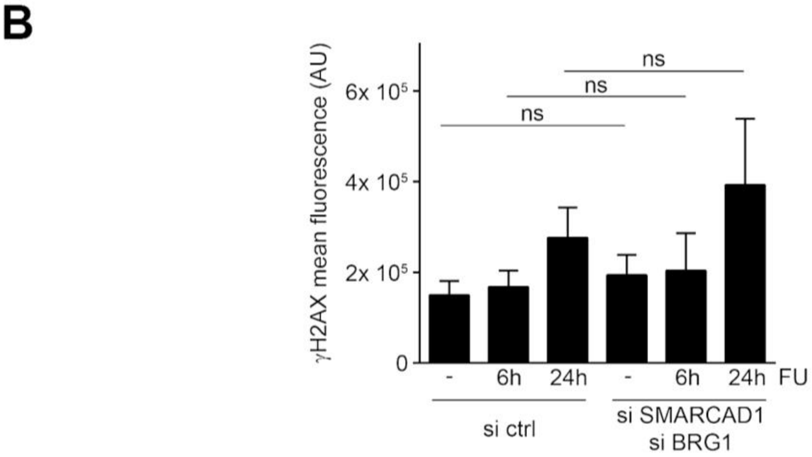

Figure 65: 5-FU induced γH2AX formation in SMARCAD1- and BRG1-depleted RKO HDAC2^{wt}. Cells were transfected with siRNA directed against SMARCAD1 and BRG1 and subsequently treated with 10 µM 5-FU for 6 h and 24 h prior to fixation and staining with γH2AX primary antibody and immunofluorescence analysis. (**A**) Representative immunofluorescence images of all samples. Scale bar represents 5 µm. Images are representative sections of images in **Figure S 28**. (**B**) Mean fluorescence of γH2AX was determined in arbitrary units (AU) using Image J. 134 - 427 cells were counted per sample. Graph shows mean ± SD (n=3; one-way ANOVA; Tukey's multiple comparisons test; no significant difference).

Analysis of 53BP1 could serve to discriminate DSB-associated γH2AX foci from DSB-independent γH2AX staining for example at ssDNA regions during replicative stress, as 53BP1 solely accumulates at DSBs at replication sites (Vignard et al. 2013). Furthermore, loss of BRG1 activity has previously been described to result in an amelioration of 53BP1 recruitment to DSB sites downstream of γH2AX formation (Park et al. 2006; Kwon et al. 2015). Indeed, analysis revealed that 53BP1 foci formation and localization to DNA damage sites was slightly but significantly diminished in HDAC2^{K462R} expressing RKO cells post irradiation (Figure 66**C**). This finding indicates differences in DNA damage recognition and repair in RKO HDAC2^{wt} and RKO HDAC2^{K462R} cells at this time point post irradiation.

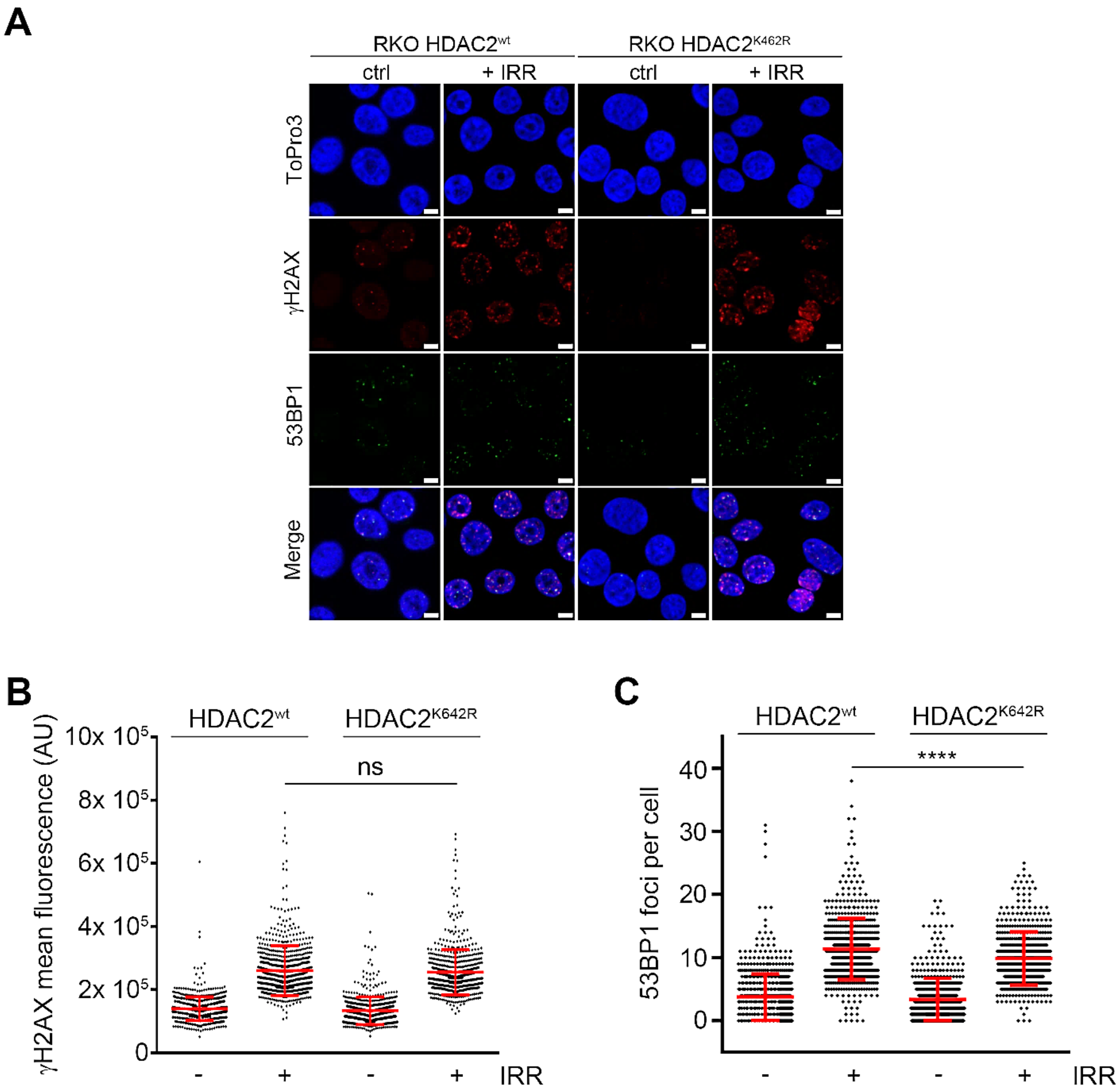

Figure 66: γH2AX and 53BP1 foci formation in response to irradiation in RKO HDAC2^{wt} and RKO HDAC2^{K462R}. Cells were irradiated with 6 Gy and incubated for 1 h prior to fixation and staining with γH2AX and 53BP1 primary antibodies. (**A**) Representative immunofluorescence images of all samples. Scale bar represents 5 µm. Images are representative sections of images in **Figure S 29**. (**B**) Mean fluorescence of γH2AX was determined in arbitrary units (AU). Each dot represents the fluorescence intensity of a single cell. 116 - 240 cells were counted per sample. Graph shows mean ± SD (n=4; one-way ANOVA; Tukey's multiple comparisons test; no significant difference). (**C**) Number of 53BP1 foci per cell was determined using Image J. Each dot represents the amount of foci measured in a single cell. 112 - 212 cells were counted per sample (n=4; one-way ANOVA; Tukey's multiple comparisons test; *****P*<0.0001).

As an additional experiment, RKO HDAC2^{wt} cells, that were transfected with siRNA directed against BRG1 and SMARCAD1, were irradiated likewise using IR as distinct DSB-inducing stimulus. Immunofluorescence analysis was applied to determine if this straightforward generation of DSBs would result in measurable changes in γH2AX and 53BP1 localization dependent on helicase expression. Phosphorylation of H2AX and formation of 53BP1 foci was visible in all irradiated samples (**Figure 67**, **Figure S 31A**). Colocalization of γH2AX and 53BP1 in irradiation-induced foci was obvious (**Figure 67**).

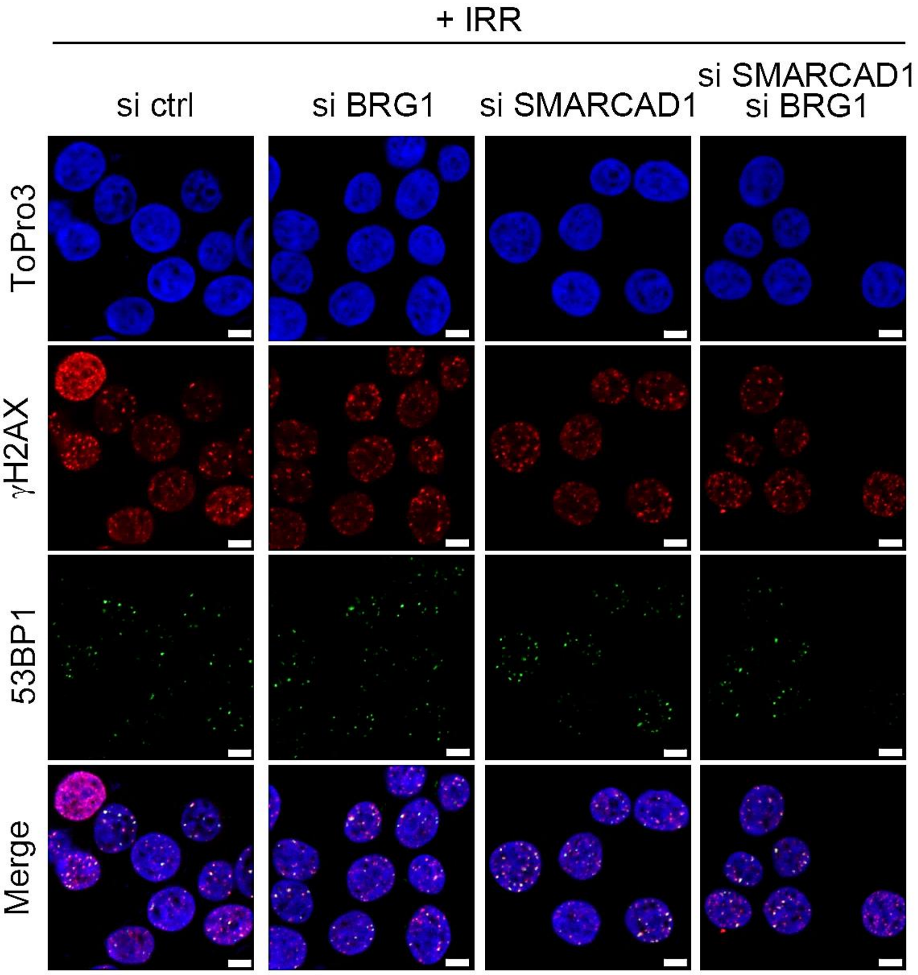

Figure 67: Ionizing radiation induced γH2AX and 53BP1 foci formation in BRG1-, SMARCAD1-, and HDAC2-depleted RKO HDAC2^{wt}. Cells were transfected with the indicated combinations of siRNA directed against BRG1, SMARCAD1, and HDAC2, subsequently irradiated with 6 Gy and incubated for 1 h prior to fixation and staining with γH2AX and 53BP1 primary antibody and immunofluorescence analysis. Scale bar represents 5 µm. Images are representative sections of images of all irradiated samples in **Figure S 31A**. Representative pictures of unirradiated controls are shown in **Figure S 31B**.

Quantification of γH2AX mean fluorescence and 53BP1 foci revealed differences between the various samples (**Figure 68**). Mean fluorescence intensity of γH2AX was slightly increased in RKO HDAC2^{wt} cells transfected with siBRG1 (**Figure 68A**). Single loss of SMARCAD1 had no impact on H2AX phosphorylation in response to irradiation (**Figure 68A**). Combined transfection with siRNA against BRG1 and SMARCAD1 reduced IR-induced H2AX phosphorylation (**Figure 68A**). Quantification of 53BP1 foci unfolded that individual loss of BRG1 or SMARCAD1 resulted in a decreased basal number of 53BP1 foci in untreated RKO HDAC2^{wt} cells (**Figure 68B**). This effect has to be taken into account as the reduction of SMARCAD1 expression also lessened the number of 53BP1 foci under irradiated conditions (**Figure 68B**). Moreover, the combined loss of BRG1 and SMARCAD1 expression significantly reduced the amount of 53BP1 foci in response to IR (**Figure 68B**).

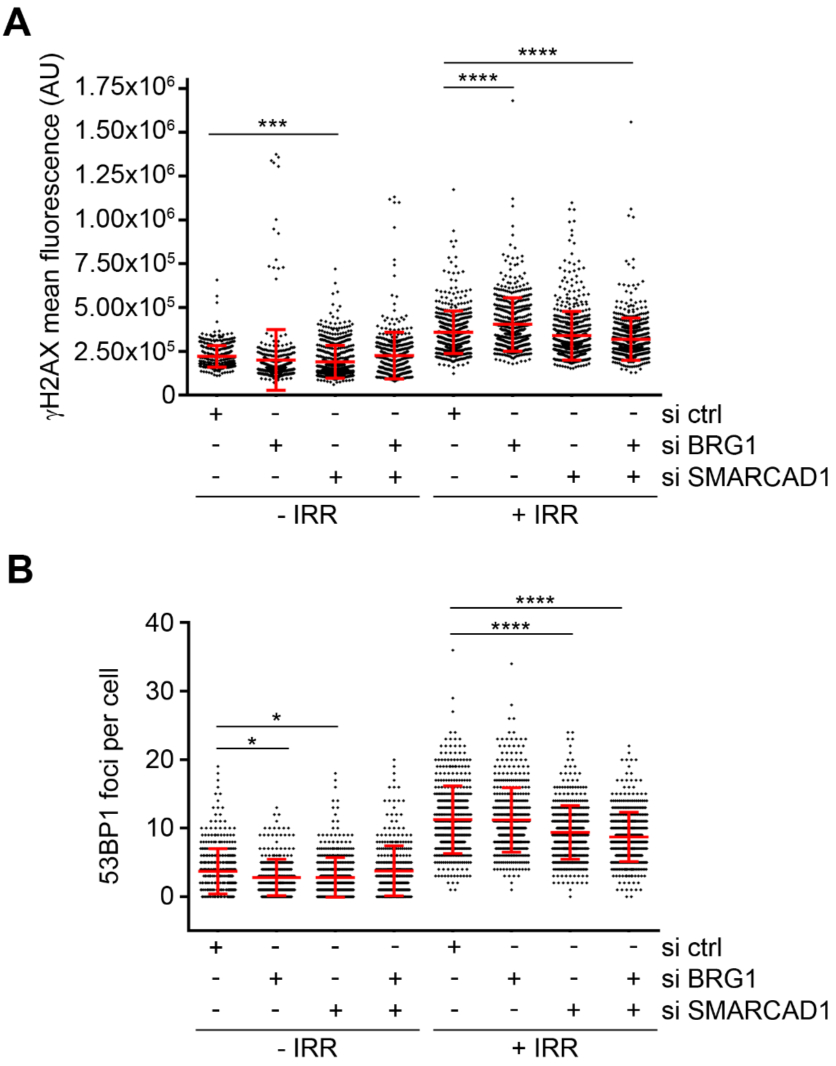

Figure 68: Quantification of ionizing radiation induced γH2AX and 53BP1 foci in BRG1-, SMARCAD1-, and HDAC2-depleted RKO HDAC2^{wt}. Cells were transfected with the indicated combinations of siRNA directed against BRG1, SMARCAD1, and HDAC2, subsequently irradiated with 6 Gy and incubated for 1 h prior to fixation and staining with γH2AX and 53BP1 primary antibody and immunofluorescence analysis. (**A**) Mean fluorescence of γH2AX was determined in arbitrary units (AU) using Image J. Each dot represents the fluorescence intensity of a single cell. 56 – 212 cells were counted per sample. Graph shows mean ± SD (n=3-4; one-way ANOVA; Tukey's multiple comparisons test; ***$P<0.001$; ****$P<0.0001$). (**B**) Number of 53BP1 foci per cell was determined using Image J. Each dot represents the amount of foci measured in a single cell. 40 - 180 cells were counted per sample (n=3-4; one-way ANOVA; Tukey's multiple comparisons test; *$P<0.05$; ****$P<0.0001$).

Given that the quantified changes in γH2AX formation and 53BP1 foci count were not extensive, the transfection efficiency for this experiment was determined by Western blot analysis of SMARCAD1 and BRG1 expression (**Figure S 32**). Quantification of the respective residual signal intensity revealed that the average expression of SMARCAD1 was reduced to only around 60% of the protein expression in mock transfected cells in response to either SMARCAD1 single knockdown or combined knockdown with BRG1 (**Figure S 32B**). BRG1 was reduced around 50% in response to single BRG1 knockdown but only around 25% in response to combined knockdown of BRG1 and SMARCAD1 (**Figure S 32A**). A reason for this less effective knockdown of BRG1 in combination with SMARCAD1 knockdown might be that SMARCAD1 single knockdown resulted in an upregulation of BRG1 expression to around three times the expression in mock transfected cells (**Figure S 32D**). In contrast to this, SMARCAD1 expression was slightly downregulated in RKO HDAC2^{wt} cells transfected with siRNA against BRG1 (**Figure S 32C**). Furthermore, neither BRG1 nor SMARCAD1 knockdown by siRNA in RKO HDAC2^{wt} cells was effective enough to mimic the loss of protein expression that was observed in RKO HDAC2^{K462R} cells (**Figure 56, Figure 57, Figure S 32**). These data indicate that the combined specific reduction of SMARCAD1 and BRG1 expression impairs the cellular response towards DNA damage by DSBs.

4.2.11 Effects of SMARCAD1, HDAC2, and BRG1 knockdown on cell death induction in HCT116, RKO, and RKO HDAC2^{wt}

Single loss of either BRG1 or SMARCAD1 has been described to be detrimental for cellular DNA damage recognition and thus to be critical for cellular sensitivity towards various DNA damaging stimuli (Park et al. 2006; Zhang et al. 2009; Lee et al. 2010a; Costelloe et al. 2012; Kothandapani et al. 2012; O'Donnell et al. 2012; Kwon et al. 2015; Qi et al. 2015; Smith-Roe et al. 2015; Chakraborty et al. 2018). To further explore whether the observed differences in DSB recognition that were triggered through the specific reduction in DNA helicase expression (**Figure 68**) result in the macroscopic sensitization of CRC cells towards 5-FU, HDAC2-proficient colorectal cancer cells were transfected with siRNA targeting SMARCAD1 and HDAC2. Western blot analysis confirmed the effective knockdown of SMARCAD1 and HDAC2 protein expression in HCT116 and RKO cells (**Figure 69**).

Transfection with siRNA directed against SMARCAD1 reduced its expression in HCT116 cells to around 10 – 20% and in RKO cells to around 50% of the SMARCAD1 level in mock transfected controls (**Figure 69**). HDAC2 transfection efficiency was heterogenous, ranging from a minor 25% reduction in siHDAC2 and siSMARCAD1 transfected RKO cells to complete abolishment of protein expression in equivalently transfected HCT116 cells (**Figure 69**). Concordant with Western blot analyses of RKO HDAC2^{wt} cells, isolated loss of HDAC2 protein led to a slight reduction of SMARCAD1 expression in both cell lines (**Figure 69**, **Figure S 25**).

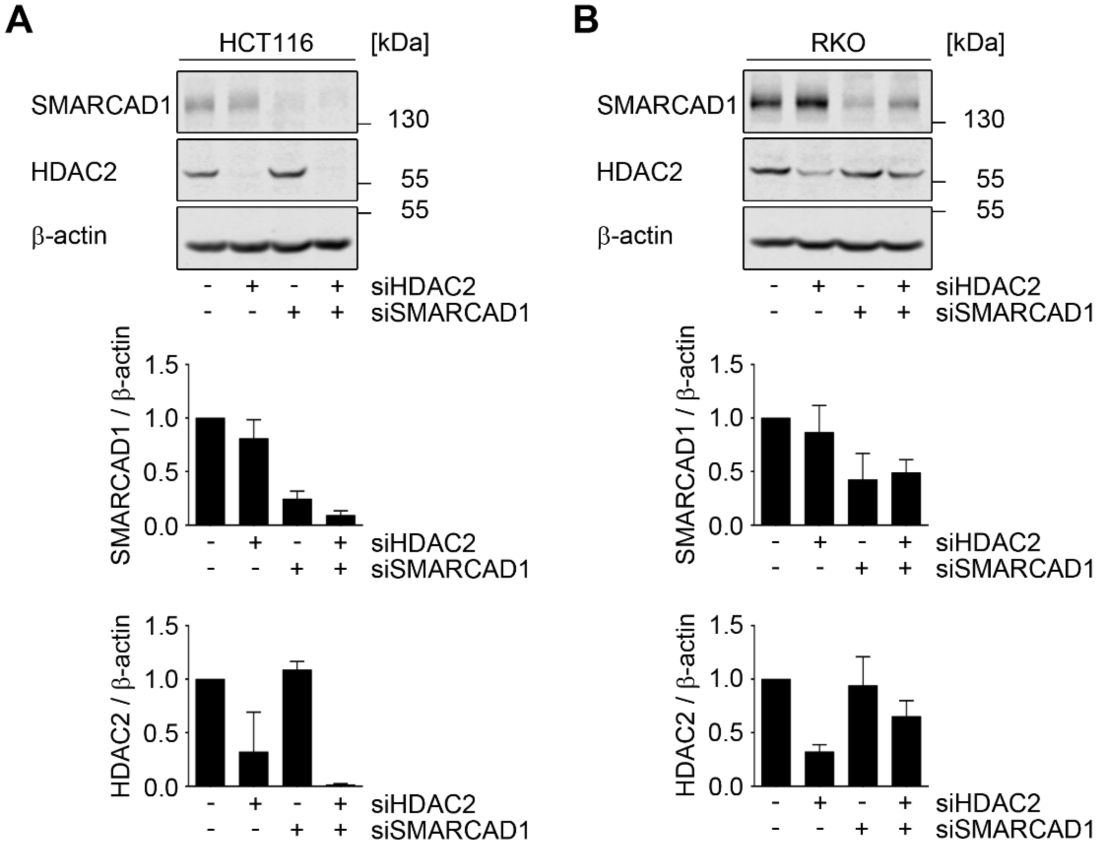

Figure 69: siRNA mediated knockdown of SMARCAD1 and HDAC2 in HCT116 and RKO. HCT116 (**A**) and RKO (**B**) cells were transfected with the indicated siRNAs to abrogate the indicated protein expression. Transfection efficiency after 96 h was determined by Western blot analysis of protein expression. Β-actin served as loading control. Quantification of SMARCAD1 and HDAC2 expression was achieved by densitometric analysis of fluorescence signal intensity and normalization to the respective loading control. Graph shows mean ± SD (n=3 for SMARCAD1; n=2 for HDAC2).

Transfected HCT116 and RKO cells were treated with 5-FU and FdUrd and analyzed for cell death induction. Neither transfection with siRNA directed against SMARCAD1 or HDAC2, nor a combination of both led to a significantly higher induction of cell death in response to treatment with 5-FU (**Figure 70**). Likewise, FdUrd toxicity was not affected by a reduction of HDAC2 and/or SMARCAD1 in either cell line (**Figure 70**).

Thus, the described effect of sensitization towards 5-FU-induced cell death in RKO HDAC2^{K462R} cells (**Figure 48A**) cannot be reproduced in HDAC2-proficient CRC cells through segregated elimination of HDAC2 activity and SMARCAD1 expression. This indicates that, in contrast to data in the literature (Costelloe et al. 2012; Chakraborty et al. 2018), single loss of SMARCAD1 expression is not sufficient to sensitize cells towards DNA damaging stimuli.

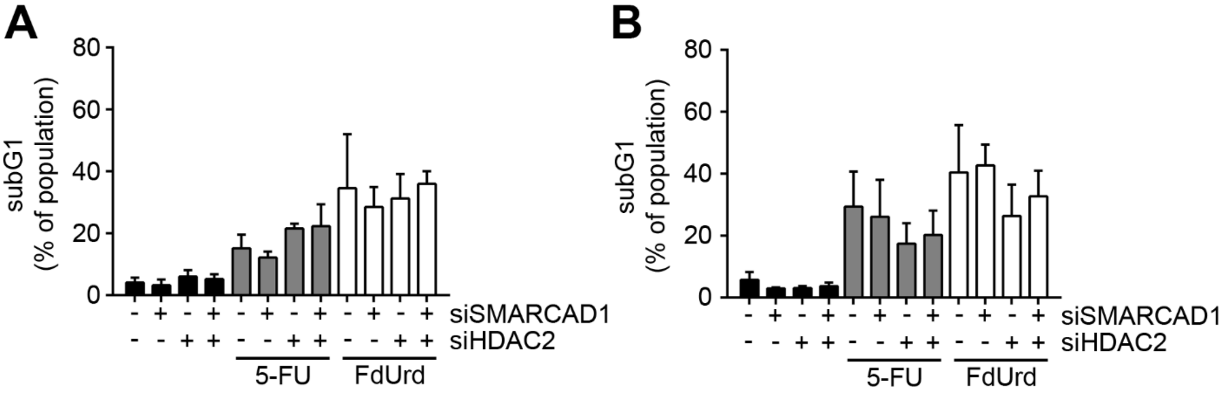

Figure 70: Effect of SMARCAD1 and HDAC2 knockdown on cell death induction in 5-FU- and FdUrd-treated HCT116 and RKO. (**A**) HCT116 cells and (**B**) RKO cells were transfected with siRNA directed against SMARCAD1 and/or HDAC2 and treated with 5 µM 5-FU and 2 µM FdUrd for 48 h. Graph shows mean ± SD (n=3; one-way ANOVA; Tukey's multiple comparisons test; no significant difference).

Likewise, RKO HDAC2^{wt} were depleted for SMARCAD1 and/or BRG1 expression and cell death induction was assessed in response to 5-FU (**Figure 71**). siRNA transfection successfully diminished SMARCAD1 and BRG1 expression (**Figure S 33**). Nevertheless, neither knockdown of BRG1 nor SMARCAD1 nor the combined knockdown of both helicases resulted in any change in 5-FU-induced cell death compared to mock transfected cells (**Figure 71**). Furthermore, siRNA-mediated reduction of the expression of SMARCAD1 and/or BRG1 did not alter cell death induction in response to treatment with FdUrd (**Figure S 34**).

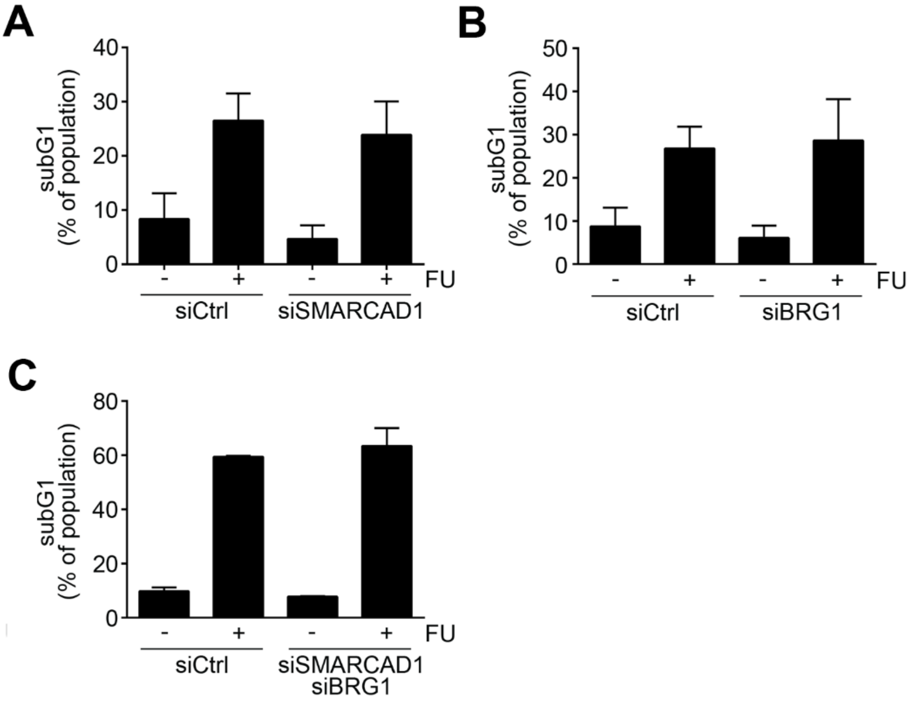

Figure 71: Effect of SMARCAD1 and BRG1 knockdown on cell death induction in 5-FU-treated RKO HDAC2^{wt}. (**A**) Cells were transfected with siRNA directed against SMARCAD1 and treated with 5 µM 5-FU for 48 h. Graph shows mean ± SD (n=4; one-way ANOVA; Tukey's multiple comparisons test; no significant difference). (**B**) Cells were transfected with siRNA directed against BRG1 and treated with 5 µM 5-FU for 48 h. Graph shows mean ± SD (n=4; one-way ANOVA; Tukey's multiple comparisons test; no significant difference). (**C**) Cells were transfected with siRNA directed against SMARCAD1 and BRG1 and treated with 5 µM 5-FU for 48 h. Graph shows

mean ± SD (n=2). Cell death was determined by flow cytometric analysis of fixed and PI-stained cells as fraction of cells with fragmented DNA.

In summary, these findings indicate, that the sole loss of HDAC2, SMARCAD1, and/or BRG1 expression is not sufficient to mimic the 5-FU-sensitive phenotype that has been observed in RKO HDAC2^{K462R} cells (**Figure 48A**).

4.2.12 HDACi and fluoropyrimidines: Combinatorial treatment as well as reversibility by Urd administration

HDAC2^{K462R} sensitized RKO cells towards 5-FU (**Figure 48A**). Furthermore, HDAC class I inhibition resulted in a decreased expression of the ATP-dependent helicases BRG1 and SMARCAD1 that was comparable to the loss of expression observed in RKO HDAC2^{K462R} cells (**Figure 56, Figure 57, Figure 58B, D-F**). RKO cells, that endogenously expressed wild-type HDAC2, were thus treated with the HDAC class I specific inhibitor MS-275 to evaluate if general loss of HDAC class I activity equally sensitizes cells towards treatment with fluoropyrimidines. 5-FU treatment led to a significant cell death induction of around 35 % and FdUrd treatment resulted in around 43 % cell death induction in RKO cells (**Figure 72A**). Combination of 5-FU with MS-275 led to cell death induction that was merely additive and not significant when compared to 5-FU single treated cells (**Figure 72A**). This contradicts data in the literature, that describe a sensitization towards 5-FU by HDACi (Flis et al. 2010; Noro et al. 2010; Okada et al. 2016; Huang et al. 2017). Comparative analyses show that the CRC cell line HCT116 is clearly sensitized towards 5-FU by MS-275 and synergistic cell death induction was apparent upon combinatorial treatment (**Figure S 35**). Unlike HCT116 cells, RKO cells were additionally not sensitized towards FdUrd by MS-275 as combinatorial treatment did not result in enhanced cell death induction in comparison to single treatment (**Figure 72A**, **Figure S 35**). RKO cells are thus not sensitized towards both fluoropyrimidines by HDAC class I inhibition, while MS-275 efficiently sensitized HCT116 cells towards 5-FU as well as FdUrd.

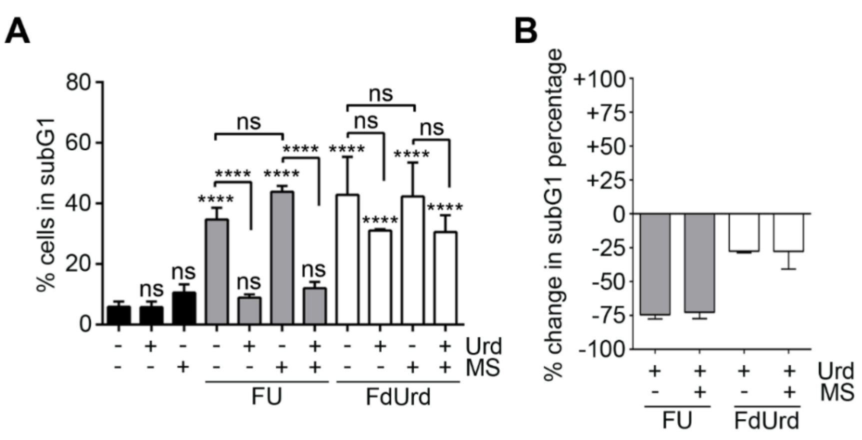

Figure 72: Cell death induction in RKO treated with MS-275, Urd, 5-FU, and FdUrd. (**A**) Cells were treated with 2 µM MS-275, 10 mM Urd, and 5 µM 5-FU for 48h. Cell death induction was determined by flow cytometric analysis of fixed, PI-stained samples. Graphs show mean ± SD (n=3-11; one-way ANOVA; Tukey's multiple comparisons

test; ns: no significant difference, ****$P<0.0001$). Significances positioned above each bar indicate significance compared to control samples. (**B**) Reversibility of cell death induction by Urd treatment is shown as mean ± SD (n=3-4).

Furthermore, it is still widely discussed whether 5-FU cytotoxicity is predominantly evoked by its damaging effects on RNA or DNA (see **1.5.1**). It has been shown that 5-FU incorporates into RNA at 3.000- to 15.000-fold higher levels than into DNA in HeLa and SW480 cells (Pettersen et al. 2011). The above finding that the loss of DNA helicase expression and the subsequent changes in the recognition of DNA DSBs were not sufficient to cause a sensitization of RKO HDAC2^{wt} cells to 5-FU (**Figure 71**) implies RNA-damage as a main trigger of 5-FU toxicity. Assessment of the reversibility of 5-FU effects through treatment with uridine (Urd) serves as a method to evaluate the significance of RNA-damage for the general cytotoxicity of 5-FU (Pettersen et al. 2011). Thus, RKO cells were additionally treated with suitable concentrations of the nucleotide Urd in combination with 5-FU and FdUrd (**Figure 72**). Prior to administration of Urd in these combinatorial treatment schemes, flow cytometric analyses were conducted and it was excluded that the applied Urd concentration affects cell cycle or cell death (**Figure S 36**). Noticeably, Urd supplementation lead to a pronounced reversion of 5-FU cytotoxicity (- 75%) in RKO cells (**Figure 72**). This effect was unaltered by additional HDAC inhibition (**Figure 72**). In contrast, FdUrd cytotoxicity in RKO cells was less affected by Urd administration (- 25%) (**Figure 72**).

Comparable reversibility of 5-FU toxicity by Urd (- 60%) was additionally observed in RKO HDAC2^{K462R} cells (**Figure 73**). FdUrd-mediated toxicity was not as reversible in these cells (-6%) (**Figure 73**). These findings indicate that overall 5-FU toxicity is caused to a significant proportion by RNA-damage, while 5-FdUrd toxicity can be predominantly ascribed to DNA damage. Thus 5-FU is not the appropriate stimulus to further study the discovered impairment of DNA damage response by reduced DNA helicase expression in HDAC2-sumoylation-deficient cells (see **4.2.7**, **4.2.9**, **4.2.10**).

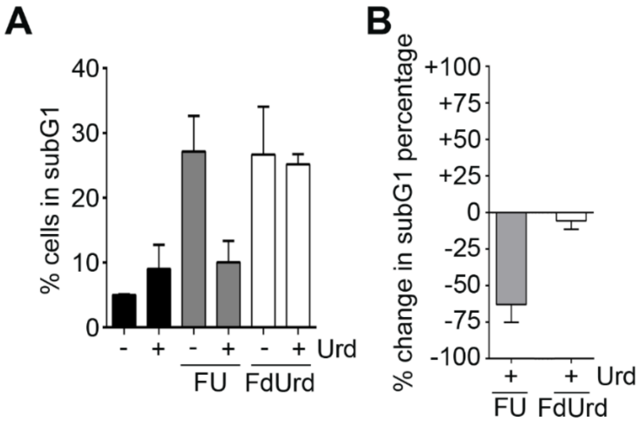

Figure 73: Cell death induction in RKO HDAC2^{K462R} treated with Urd, 5-FU, and FdUrd. (**A**) Cells were treated with 10 mM Urd, 1 µM 5-FU, and 10 µM FdUrd for 48h. Cell death induction was determined by flow cytometric analysis of fixed and PI stained samples. Graphs show mean ± SD (n=2). (**B**) Reversibility of cell death induction by Urd treatment is shown as mean ± SD (n=2).

As excessive Urd might revert TS inhibition and thereby reduce 5-FU-dependent DNA-damage via dTTP depletion, formation of TS* was assessed by Western blot (**Figure S 37**). Single treatment with 5-FU and FdUrd effectively inhibited TS through TS* complex formation in HCT116 and RKO cells (**Figure S 37**). Whereas TS inhibition by FdUrd was unaffected, TS inhibition by 5-FU was marginally reduced by Urd treatment (**Figure S 37**). In addition, a second 5-FU metabolite, FUrd, was included in the experiment. FUrd is primarily considered as a mimetic to simulate 5-FU mediated RNA-damage. However, Western blot analysis showed that FUrd could not be applied in further analyses as it inhibited TS as efficiently as 5-FU and FdUrd and was thus prone to display comparable DNA-damaging effects (**Figure S 37**). However, in contrast to 5-FU and FdUrd, FUrd-mediated TS inhibition was highly reversible by Urd (**Figure S 37**). The absence of such reversible effects of Urd on 5-FU- and FdUrd-mediated TS inhibition indicates stable dTTP depletion and associated DNA-damage induction in response to these two substances.

In summary, these findings indicate that cell death induction by 5-FU is likely eminently dependent on its RNA integration. However, constant and Urd-independent TS inhibition in 5-FU samples implies that non-toxic DNA damage is triggered by 5-FU concurrently. Nevertheless, the observed loss of DNA helicase expression and the subsequent changes in DNA damage repair might be neglectable for general 5-FU toxicity and did thus justifiably not suffice to sensitize RKO cells towards 5-FU in the analyses described above (**Figure 69**, **Figure 70**). Future experiments should thus consider applying other stimuli than 5-FU to analyze changes in DNA damage response upon loss of DNA helicase expression in HDAC2 sumoylation-deficient cells. Furthermore, as loss of HDAC2 sumoylation sensitizes RKO HDAC2^{K462R} cells to 5-FU mediated RNA damage, future experiments should include methods to quantify RNA damage and to assess the related signaling pathways.

5 Discussion

5.1 Effects of HDAC inhibition in renal carcinoma cells

Considering the poor prognosis of metastatic RCC and the new advent of clinical application of HDACi in combination with ICI in this tumor type (see **1.1.1**), it is of importance to further define molecular effects of HDACi in RCC and to especially address conflicting data in the literature regarding the influence of HDACi on EMT. The question whether and to what extent HDACi activate or deactivate EMT signaling pathways in cancer, and especially in RCC cells, is widely unknown as published data gathered in various cell systems shows widely ambiguous results (see **1.4**) (Kiweler et al. 2018). The following work in RCC cells was thus aimed to provide a comprehensive insight into HDACi elicited cellular responses and signaling mechanisms with special regard to potential implications of HDACi on EMT to not only ensure drug effectiveness but also drug safety. Here, I show that HDACi are promising agents that induce RCC apoptosis and a loss of protein expression that controls EMT.

5.1.1 Class I HDACi induce histone hyperacetylation, affect class I HDAC expression and cell morphology

VPA and MS-275 are specific inhibitors of the class I HDACs HDAC1-3 (Bradner et al. 2010). As the deacetylation of histones is a prominent function of these HDACs, increased acetylation of specific histones functions as a readout for efficient HDAC class I inhibition (Beyer et al. 2017). Determination of the hyperacetylation of histone H3 and histone H4 confirmed that treatment with the HDACi VPA and MS-275 was successful within the chosen timeframe and with the applied concentrations (**Figure 13**). It has previously been described in human erythroleukemia, human embryonic kidney carcinoma, and mouse teratocarcinoma cells that HDAC inhibition by VPA not only results in the restriction of HDAC1, 2, 3 activity but also reduces HDAC2 expression through modulation of its proteasomal degradation (Krämer et al. 2003) and thereby potentially intensifies the deficit of HDAC activity. In contrast, albeit this reduction of HDAC2 expression by VPA has been described in a variety of cell types and tissues (Wagner et al. 2014), others also found that specific cell types exhibit unaltered HDAC2 levels in response to VPA (Krämer et al. 2008b). However, in Renca cells, prolonged treatment with higher concentrations of either HDACi reduced the expression of HDAC1, 2, and 3 (**Figure 14**). Mass spectrometric protein expression analysis contrarily showed no significant changes in either HDAC class I expression (**Figure S 1**). On the other hand, the expression of a plethora of further epigenetic modulators with implications in histone and non-histone acetylation, such as lysine acetyltransferase (KAT) family members and further acetyl-lysine recognizing, BRD containing proteins, is affected by the loss of class I HDAC activity (**Figure S 1**). This illustrates the association of the expression of these proteins with HDAC1, 2, and 3 and implies potential compensatory feedback mechanisms upon MS-275 treatment. For instance, the mass spectrometric screen was effective to detect the expression levels of the three HAT proteins KAT7, KAT8, and HAT1 in Renca cells. Whereas KAT7 and KAT8 were downregulated, expression of HAT1 increased in a dose- and time-dependent manner (**Figure S 1**). While KAT7 (or HBO1) and KAT8 (or MOF) are expressed in the nucleus and implicated in histone acetylation, HAT1 is located in the cytoplasm and primarily acetylates non-histone proteins and free, freshly translated cytoplasmic histones. Such a divergent regulation of KATs implies that the equilibrium between protein acetylation and deacetylation is affected differently in response to HDACi in the cell’s nucleus and cytoplasm (Peserico and Simone 2011). Mass spectrometric analysis in Renca cells demonstrated the high extent of protein expression changes in response to HDAC class I inhibition (**Figure 15**). Herein, 48 h treatment resulted in the highest quantity of individual proteins whose expression was found to be significantly different compared to untreated control samples, confirming that prolonged hyperacetylation of histone and non-histone proteins has large-scale effects on global protein expression levels and thus on cellular signaling pathways in Renca cells (**Figure 15**). A prominent consequence of the massive HDACi-induced alterations in global protein expression was a marked change of the morphological phenotype of Renca cells in response to HDACi (**Figure 16**, **Figure S 2**). Comparable morphological alterations in response to treatment with HDACi have previously been described by others (Hoshikawa et al. 1994; Byler et al. 2012; Kong et al. 2012; Jeon et al. 2013; Jiang et al. 2013; Cabanel et al. 2015; Ma et al. 2015; Wang et al. 2016; Wang et al. 2018). Strikingly, the observed structural changes of cell shape, such a loss of cell polarity and development of a spindle-shaped cell body, have been associated with tumor progression as they may be potential indications for EMT (Zeisberg and Neilson 2009; Mikami et al. 2016; Nieto et al. 2016). EMT induction through HDACi would query the applicability of these drugs in clinical cancer treatment. However, morphological alterations alone are not sufficient to confirm cellular transformation. The results of further experiments, that were conducted to determine the impact of HDAC inhibition on EMT are going to be discussed in the following.

5.1.2 Global proteome analysis to determine significantly regulated signaling pathways in response to HDACi treatment

Additionally, the expression levels in MS-275-treated Renca cells, that were identified by mass spectrometric analysis for over 5,000 proteins, were employed to perform Gene Ontology (GO) term enrichment analysis to concisely determine how HDACi affect Renca cell fate on a comprehensive scale. In the presented analysis, the obtained GO terms correspond to specific biological processes. Prior to GO term enrichment analysis, the set of proteins to be analyzed was constructed by determination of significantly different expressed proteins through statistical analysis via one-way ANOVA (for comparison of all treatment conditions; **Figure 17**) or t-test (for comparison of untreated samples to 48 h 5 µM MS-275 treatment; **Figure 18**). The heatmap of general protein expression shown in **Figure 15** indicates that 48 h treatment with MS-275 profoundly elevated changes in protein expression when compared with 24 h treatment and would thus result in a broader subset of regulated proteins to be analyzed. Expectedly, the GO term analyses of the two differently shaped subsets of significantly regulated proteins yielded enrichment of distinct biological processes (**Figure 17, Figure 18, Table S 1, Table S 2**). The first GO term analysis, comparing all treatment conditions, predominantly yielded enrichment of GO terms that relate to cell structure and adhesion, indicating that signaling pathways and proteins related to these cellular processes were highly affected by HDACi over the entire treatment period (**Figure 17**, **Table S 1**). These GO term results correspond to the observed morphological features of Renca cells in response to HDACi treatment (**Figure 16**). Treatment with 5 µM MS-275 for 48 h and analysis of the resulting dataset of significantly regulated proteins yielded enrichment of GO terms associated with histone acetylation and protein and nucleotide phosphorylation (**Figure 18**). While this finding illustrates the consequences of HDAC inhibition for epigenetic signatures, the enrichment of several GO terms that are related to histone acetylation verifies the analysis. Apart from this, HDAC inhibition for 48 h critically impacted chromatin regulation, cell growth, growth factor responses, and apoptotic cell death (**Figure 18**). However, no enriched GO terms were found by these analyses that implied changes in any signaling pathways associated with EMT (**Table S 1, Table S 2**). In summary, HDACi treatment resulted in the enrichment of a plethora of GO terms related to key biological processes (**Table S 1**, **Table S 2**). On the one hand, these data underline the impact of HDACi via the disturbance of the equilibrium of protein acetylation and deacetylation. However, such complexity hampers the interpretation of data gathered by this analysis. As this analysis presents, to our knowledge, the first global compilation of protein expression and subsequent GO term enrichment analysis in HDACi-treated RCC cells, the acquired data may provide first hints to define areas of interest for future research projects. For instance, both GO term enrichment analyses yielded terms related to immune response and especially B and T cell response (**Table S 1**, **Table S 2**). Among others these involved the following: *immune response activating signal transduction* (GO:0002757), *B cell activation* (GO:0042113), *regulation of leukocyte activation / proliferation* (GO:0002694 / GO:0070663), *T cell receptor signaling pathway* (GO:0050852), *B cell homeostasis* (GO:0001782), *alpha-beta T cell differentiation* (GO:0046632), *lymphocyte proliferation* (GO:0046651), *leukocyte proliferation* (GO:0070661) and the general *positive regulation of immune systemic process* (GO:0002684). Thus, the global protein expression data gathered in this project might offer helpful additional insight into the molecular principles that underly the observed HDACi-induced sensitization to immunotherapy with ICIs (see **1.1.1**) and subsequently serve to further enhance clinical treatment efficiency. Furthermore, two of the most eminently enriched GO terms in the first GO term analysis were *tubulin complex assembly* (GO:0007021) and *negative regulation of microtubule polymerization* (GO:0031115) (**Figure 17**, **Table S 1**). Enrichment of these two terms implies crucial impacts of HDACi on cell division, cell structure, and intracellular transport mechanisms, since tubulin polymers are the main components of mitotic spindles and the cytoskeleton. Disturbance of tubulin and microtubule polymerization leads to cell death induction as a result of disturbed mitotic spindle formation, as has been shown in studies with the microtubule-destabilizing vinca alkaloids (Manchado et al. 2012). Immunofluorescence analysis of α- and β-tubulin in microtubule, γ-tubulin in centrosomes, and nuclear DNA separation in mitotic HDACi-treated Renca cells might allow the detection of abnormalities in mitotic spindle and cytoskeleton formation. Moreover, future analysis of the expression and HDAC-dependent regulation of tubulin cofactors (TBC), a group of proteins that ensure correct folding and dimerization of α- and β-tubulin prior to microtubule polymerization (Grynberg et al. 2003), might be of interest as the present proteome analysis indicated that TBCA, TBCB, TBCC, and TBCD were significantly overexpressed in response to MS-275 treatment (Kiweler et al. 2018). Notably, it has been shown that dysregulated expression of these various TBC impairs α- and β-tubulin homeostasis, microtubule dynamics, and has potentially lethal consequences through impairment of accurate mitosis (Radcliffe et al. 1999; Kortazar et al. 2007; Cunningham and Kahn 2008; Hage-Sleiman et al. 2010). Thus, suitable combinatorial treatment schemes of HDACi and tubulin targeting agents are going to be outlined in section **5.1.4** in the course of the discussion of cell death inducing properties of HDACi in Renca cells.

5.1.3 HDACi treatment does not trigger effective EMT signaling

Although the performed global protein expression and subsequent GO term enrichment analysis did not give apparent indications for a noticeable EMT regulation through HDAC inhibition, it nevertheless revealed expression changes of a few proteins with implications in EMT (**Figure S 3**). For instance, expression of the EMT TF ZEB1 and the epithelial marker proteins E-cadherin (*Cdh1*) and β-catenin (*Ctnnb1*) were repressed upon MS-275 treatment (**Figure S 3**). Whereas ZEB1 downregulation would contradict EMT signaling, downregulation of E-cadherin and β-catenin is suggestive for cellular transformation (Zeisberg and Neilson 2009). Furthermore, expression of Vimentin (*Vim*) was not affected and expression of the receptor *PDGFRβ* was diminished (**Figure S 3**). As vimentin is a mesenchymal marker protein (Zeisberg and Neilson 2009) and signaling through PDGFRβ is described to be a major driver of RCC growth and pulmonal metastasis formation (Xu et al. 2005), this further implies negative regulation of EMT. Given this antithetic EMT protein regulation and the observed morphological changes, additional experiments had to be conducted, to clarify the impact of HDACi treatment on cellular transformation in further detail. First, mRNA expression analysis of the six central EMT TFs SNAI1 (*Snai1*), SNAI2 (*Snai2*), TWIST1 (*Twist1*), TWIST2 (*Twist2*), ZEB1 (*Zeb1*), and ZEB2 (*Zeb2*) in MS-275-treated Renca cells showed that SNAI1, ZEB1, and TWIST1 mRNA was unaffected, ZEB2 and TWIST2 mRNA expression was reduced after 24 h and 48 h treatment and SNAI2 mRNA was upregulated after 48 h treatment (**Figure 19A**). As these TFs channel cells through transformation to the mesenchymal state by largely analogous gene expression programs and in strong dependence of their mutual activation for successful transformation (Peinado et al. 2007; Dave et al. 2011; Craene and Berx 2013; Lamouille et al. 2014), sole activation of just *Snai2* does not provide sufficient evidence for profound EMT activation as consequence of MS-275. Moreover, the two TFs SNAI1 and SNAI2 are reported enhancers of ZEB1 and ZEB2 expression (Lamouille et al. 2014). Thus, the lack of ZEB1/2 induction in response to SNAI2 upregulation suggests that SNAI2-dependent target gene expression is impaired. In addition, the absence of mesenchymal marker protein upregulation (N-cadherin, Vimentin) further disfavors effective EMT signaling and mesenchymal transition (**Figure 19B**, **Figure S 4**). Still, on the other hand, the epithelial marker protein E-cadherin and its corresponding *Cdh1* mRNA expression were downregulated significantly in HDACi-treated Renca cells (**Figure 20**, **Figure S 5**), which is regarded as a hallmark of mesenchymal transition in solid tumors (Zeisberg and Neilson 2009). Thus, overall analysis of EMT TFs and epithelial-mesenchymal marker protein expression delivered contradictory results. Hence, β-catenin expression and its liberation in response to E-cadherin degradation were analyzed and neither β-catenin expression nor its nuclear localization, that would indicate active Wnt signaling and EMT (Conacci-Sorrell et al. 2002; Bienz 2005), were enhanced by HDAC inhibition (**Figure 20**, **Figure 21**). Furthermore, two distinct assays indicated that migratory potential of Renca cells was not upregulated but downregulated or unaffected by HDACi treatment (**Figure 22**) (Kiweler et al. 2018). In summary, no functional consequences of potential EMT signaling through SNAI2 upregulation and E-cadherin downregulation were detectable. However, the observed inconsistency of EMT TF and epithelial-mesenchymal marker protein expression provides an explanation for the multitude of disputed data in the literature (see **1.4.1**), as it shows that the application of narrow and selected criterions to define EMT might result in the drawing of different absolute conclusions. Furthermore, the classic description of EMT as transformation from epithelial to mesenchymal state has changed and in doing so, gained complexity. As EMT is now considered to be a transitional, dynamic process with multiple more or less stable, intermediary states, it seems possible that cancer cells lose certain epithelial features and undergo partial EMT, but in the end never gain the full mesenchymal, metastatic phenotype for all intermediary stages are reversible (Nieto et al. 2016). Hence, we believe that, given the dynamic and multi-step nature of EMT (Nieto et al. 2016), reliable assessment of EMT inducing potential of therapeutic drugs can only be achieved by assessing a multitude of EMT biomarkers and combining those with reasonable experiments to assess functional outcome of these EMT signaling pathways. By examination of single, selected, or limited EMT biomarkers and by omission of functional analysis, one will be at risk to draw premature conclusions concerning a drug's EMT inducing potential. Collectively, the obtained comprehensive results of global protein expression, consequential EMT TF expression, and the analysis of functional outcome of EMT signaling indicate that HDAC inhibition does not trigger effective EMT in Renca cells. If morphological changes, SNAI2 upregulation, or E-cadherin reduction were indicators for progressing EMT in these cells, the concurrent failure of mesenchymal marker protein upregulation, the shortfall of β-catenin signaling induction, the absence of increase in migratory potential, and the downregulation of the metastatic driver PDGFRβ (**Figure 23**) illustrate that this signaling has no functional consequences and is ineffective to promote the full mesenchymal, metastatic RCC phenotype.

5.1.4 HDAC class I inhibition impedes growth and survival of Renca cells

The GO terms *cell death* and *regulation of programmed cell death* occurred as prominently regulated in Renca cells that were treated with MS-275 for 48 h (**Figure 18**). This implication of apoptotic cell death execution in response to HDAC inhibition was confirmed, when the significantly regulated proteins associated with these terms were analyzed. In particular, expression of members of the apoptotic signaling cascade (Caspase 3, Caspase 6, APAF1) was upregulated (**Figure 24**). Concurrently, expression of the crucial antiapoptotic signaling protein Survivin was downregulated (**Figure 24**). Caspase 3 and Caspase 9 cleavage as well as Caspase 6 upregulation and Survivin downregulation in response to MS-275 and VPA could be confirmed through Western blot analysis (**Figure 25**). Notably, Survivin expression has previously been associated with the restriction of apoptotic cell death, has implications in cell cycle regulation, and is correlated with metastatic spread and tumor invasiveness (Rauch et al. 2014). Additionally, prior to our report in RCC cells, others showed that HDACi reduce Survivin expression in prostate, colon, hepatocellular, melanoma, and breast cancer cells and thereby impact cell cycle distribution and cell death induction in these cell lines (Rauch et al. 2014). Cell death measurements, that were conducted based on these strong indications, affirmed that VPA and MS-275 treatment resulted in significant cell death in Renca cells after 24 h and 48 h treatment (**Figure 26**). As nuclear DNA is fragmented during apoptotic cell death, DNA single and double strand breaks in MS-275-treated Renca cells were detectable by alkaline COMET (**Figure 27**). However, correlation with the quantity of detected DNA fragmentation using flow cytometry was not optimal, as 24 h and 48 h treatment with 5 µM MS-275 yielded comparable tail intensity values albeit percentage of cells in subG1 fraction was different (**Figure 26, Figure 27**). This discrepancy reflects the reduced sensitivity of the COMET assay technique in comparison to flow cytometry-based assays. As the histone H2A variant H2AX is phosphorylated at Ser139 in response to DNA double strand break formation, Western blot analysis of the resulting γH2AX confirmed DNA double strand break formation in Renca cells in response to HDACi (**Figure 28**). Interestingly, the extent of γH2AX formation in relation to the induced cell death was notably higher in VPA- than in MS-275-treated cells (**Figure 26**, **Figure 28**). This finding indicates that VPA-induced H2AX phosphorylation is potentially non-exclusively provoked by apoptotic DNA fragmentation. However, whether the detected DNA breaks solely result from apoptosis or are furthermore consequences of specific, intrinsic DNA damaging mechanisms of HDACi, such as increased ROS production (Robert and Rassool 2012), and thus are not caused by but are in turn causal for apoptosis, remains to be determined in future studies. Several other mechanisms are conceivable that might underlie cell death induction by HDACi treatment and elucidation of these mechanisms offers areas of interest for future research projects. For instance, as discussed in **5.2.1**, disruption of tubulin and subsequent microtubule polymerization through dysregulation of TBC expression might provoke cell death due to mitotic failure. Interestingly, a substantial number of HDACi has been functionally associated with the deterioration of genomic stability through three distinct mechanisms: the regulation of ROS concentration, the control of DNA damage repair, and the induction of mitosis defects (Eot-Houllier et al. 2009). Further assessment and subsequent in-depth knowledge of the specific weighting of these mechanisms in individual cancer types might thus allow for the composition of individual combinatorial treatment schemes of HDACi with different specific chemotherapeutics that are especially beneficial under the given molecular background. For instance, as the observed morphological alterations and the results of the GO term enrichment analysis of global protein expression implied that tubulin and microtubule polymerization were especially affected by HDACi treatment in Renca cells, combinatorial treatment schemes with taxanes or vinca alkaloids might be specifically effective in RCC cells. Appropriately, several publications report synergistic effects of HDACi and the taxane paclitaxel in non-small cell lung, ovarian, and endometrial cancer and of HDACi and the vinca alkaloid vinorelbine in ovarian cancer (Dowdy et al. 2006; Cooper et al. 2007; Kakihana et al. 2009; Dietrich et al. 2010; Owonikoko et al. 2010; Zuco et al. 2011). Furthermore, the HDACi triggered cell death in Renca cells provides an explanation for the induced morphological alterations and the reduction of E-cadherin expression besides EMT induction, as caspases and γ-secretase have been found to cleave E-cadherin protein in apoptotic cells (Steinhusen et al. 2001; Keller and Nigam 2003; Yoo et al. 2012). Thus, future experiments with inhibitors of caspases (Z-VAD-FMK) and γ-secretase (DAPT) might be conducted to determine if co-treatment prevents E-cadherin cleavage and morphological changes in HDACi-treated Renca cells.

Subsequent analysis of cell cycle distribution revealed that S-phase and G2-phase percentage were significantly reduced 24 h post treatment while cells arrested in G1-phase of the cell cycle in response to higher concentrations of HDACi (**Figure 29**, **Figure S 8**). 24 h later, the arrest in G1-phase and the reduction of G2-phase were preserved, while S-phase percentage was generally reduced and thus no significant reduction compared to control was detectable (**Figure 29**, **Figure S 8**). Overall, these changes indicate that higher concentrations of VPA and MS-275 have profound and lasting influence on cell cycle distribution in Renca cells. Mechanistically, these cell cycle aberrations might be founded in the deregulation of crucial regulators of cell cycle. It has been shown that pan- and class-selective HDACi modulate p21, Rb, APAF1, BAX, BCL-2, Survivin, XIAP, CyclinA/B/D3, CDK1/2/4, and Aurora-A/-B in RCC cells (Kanao et al. 2008; Cha et al. 2009; Jones et al. 2009a; Mahalingam et al. 2010; Yamada et al. 2013; Juengel et al. 2014). Our proteomics approach can confirm the downregulation of Aurora-A and -B and Survivin as well as an upregulation of p21, Apaf-1, and CyclinD3 (Kiweler et al. 2018). In contrast to these reports, in Renca cells, CDK1/2/4 expression was up- and not downregulated and BAX expression was not affected by HDACi treatment (Kiweler et al. 2018). The expression levels of Rb, Bcl-2, XIAP, and CyclinA/B were not detected, most probably due to expression levels below the detection limit of the analysis. To fully elucidate the regulatory mechanisms that cause the cell cycle abrogation in HDACi-treated Renca cells, future experiments would be reasonable that monitor especially Cyclin and CDK levels in dependence of the individual cell cycle phases in synchronized cells. Congruent with the observed alterations in cell cycle distribution, doses of and above 1.5 mM VPA and 1.5 µM MS-275 led to a significant reduction of the number of viable Renca cells (**Figure 30**). As cell numbers were counted 24 h post treatment, the reduction of cell growth was mostly independent of cell death induction and could thus be accounted as proliferation effect (**Figure 26**, **Figure 30**). As, in the course of HDACi treatment, the visible number of suspended Renca cells increased (**Figure 16**), it was important to demonstrate that these cells did not represent a growing reservoir of transformed cells as a result of EMT progression, but rather detached from plates following apoptotic cell death (**Figure 26**). Hence, Renca cells were treated with HDACi and cells in suspension were reseeded to assess their colony formation ability. Resulting numbers of colonies were significantly lower in HDACi-treated samples compared to untreated control, although initial amount of detached cells was visibly higher in untreated controls (**Figure 16**, **Figure 31**). This straightforward experiment proved that there were no effective EMT signaling pathways initiated in HDACi-treated Renca cells, that facilitated seeding efficacy or enhanced metastatic potential and indicates that the detached cells populations were truly apoptotic. Most importantly, *in vivo* xenotransplantation experiments in BALB/c mice demonstrated that i.p. VPA treatment significantly reduced the quantity and size of pulmonary Renca cell colonies (Kiweler et al. 2018), indicating that HDACi treatment effectively impairs RCC tumor growth *in vivo*. Overall number of lung metastases in our study was significantly reduced ≥ 80% compared to vehicle treatment (Kiweler et al. 2018). This finding is of high interest, as lung metastasis formation alongside bone metastasis formation represents the typical clinical presentation and metastatic RCC is associated with poor prognosis (Agrawal et al. 2015; Chandrasekar et al. 2017). Moreover, apoptotic cell death induction might provide an explanation for the conflicting results in **5.1.3**, as caspase mediated cleavage of E-cadherin offers a suitable reason for its reduced expression and the observed morphological alterations. As our proteomic assay also revealed diminished expression levels of several integrins (e.g. Itgb1, Itgb5, Itga1) and β-catenin, a general proteolytic degradation of cell adhesion molecules as a result of cell death induction might be causal for morphologic alterations (Kiweler et al. 2018) (**Figure S 3**). In fact, previous reports have shown that VPA induced aberrations in integrin expression, intra- and extra-cellular localization, and contingent signaling mechanisms might have substantial impact on RCC proliferation *in vivo* (Jones et al. 2009b; Juengel et al. 2011) and thus offer an explanation for the VPA induced growth inhibition of Renca cells *in vivo* (Kiweler et al. 2018). Besides disturbance of integrin signaling, the HDACi induced loss of PDGFRβ expression *in vitro* might have detrimental consequences *in vivo* (**Figure 23**), as signaling via this specific tyrosine kinase receptor has been described to be pivotal for RCC growth and lung metastasis formation in orthotopic mouse models (Xu et al. 2005). Future experiments using the information obtained in our mass spectrometric proteome analysis, could thus be able to identify the specific changes in integrin and tyrosine kinase receptor expression using knockdown approaches that might be essential for the observed *in vitro* and *in vivo* growth inhibition. In summary, these data demonstrate that the predominant effects of HDAC class I inhibition in Renca cells *in vitro* and *in vivo* are the induction of growth arrest and subsequent apoptotic cell death. As *in vitro* and *in vivo* experiments gave no conclusive hint of induced migratory or metastatic potential, application of HDACi in RCC cells could present a safe and promising therapeutic option.

5.1.5 Assessment of autophagy in Renca cells response to HDACi treatment

The process of macroautophagy, that was assessed with the performed experiments in this work, is a catabolic process executed in healthy cells at basal level and serves to degrade and recycle non-functional, dysfunctional, or unnecessary proteins or organelles (Koeneke et al. 2015). In short, degradation of these defective cell components is achieved by engulfment of portions of the cytoplasm within double-membraned vesicles termed autophagosomes and subsequent fusion of these autophagosomes with acidic lysosomes to form autolysosomes in which the entrapped cytosolic components are finally degraded (Ravikumar et al. 2010). With regard to cancer initiation, autophagy has been described to display tumor suppressive as well as tumor promoting roles. On the one hand, autophagy is important to prevent chronic tissue damage and thus cancer initiation, on the other hand, cancer cells may upregulate autophagy as a survival mechanism to endure stressful metabolic conditions and acquire therapy resistance (White 2012). Diverse members of the HDAC family have been described to play roles in the regulation of autophagy and treatment with HDACi has accordingly been shown to influence autophagy in diverse tumor types (Koeneke et al. 2015). Remarkably, the existing data describing the aftermath of HDAC inhibition in various cancer cells is conflicting as some reports categorize HDACi as inhibitors of autophagy (El-Khoury et al. 2014; Stankov et al. 2014), while the majority conversely classifies HDACi as autophagy inducers (Shao et al. 2004; Carew et al. 2007; Martin et al. 2009; Li et al. 2010; Liu et al. 2010; Wei et al. 2010; Lopez et al. 2011; Francisco et al. 2012; Gammoh et al. 2012; Gandesiri et al. 2012; Lee et al. 2012; Rao et al. 2012; Bhalla et al. 2013; Dupere-Richer et al. 2013; Oehme et al. 2013; Torgersen et al. 2013; He et al. 2014; Zhang et al. 2015; Chiu et al. 2016; Gilardini Montani et al. 2017; Gao et al. 2018). Furthermore, among these publications, induced autophagy as consequence of HDACi treatment is not uniformly defined as cell survival mechanism but also as apoptosis enhancer (Shao et al. 2004; Liu et al. 2010; Wei et al. 2010; Lee et al. 2012; Chiu et al. 2016). Underlying explanations for this controversial autophagy regulation by HDACi might be that inhibitors of different subclasses of HDACs have varying influence on autophagy or that the tumor types studied exhibited different basal levels of autophagy depending on prevailing metabolic conditions and subsequent stress levels (Koeneke et al. 2015). Furthermore, time points of analysis and applied concentrations of HDACi might account for conflicting results (Koeneke et al. 2015). Nevertheless, given these complex and controversary influences and consequences of HDACi treatment on autophagy mechanisms in cancer cells, it was essential to ensure that MS-275 and VPA treatment did not promote autophagy as a potential survival mechanism in a subpopulation of Renca cells. Flowcytometric analysis of CYTO-ID® staining showed that prolonged treatment with MS-275 and VPA led to dose-dependent enhancement of mean fluorescence signal intensity of CYTO-ID® in Renca cells after 48 h (**Figure 32A, Figure S 9, Figure S 10**). In contrast to this, neither LC3B-II nor Beclin-1 protein levels were enhanced according to quantification of Western blot expression analysis (**Figure 32B**, **Figure S 11**). Beclin-1 and LC3B-II are acknowledged markers of early autophagy induction as Beclin-1 expression is accumulated during autophagosome formation (Kang et al. 2011) and LC3B-II is generated specifically upon autophagic signaling and integrated into autophagosomal membranes (Tanida et al. 2004), and thus their expression analysis is a reliable method for autophagy detection (Koeneke et al. 2015). Unfortunately, the exact mechanism of CYTO-ID® staining is unknown, as its distributor only describes it as cationic amphiphilic tracer dye, that effectively and predominantly labels autophagic compartments with reduced affinity for lysosomes (Guo et al. 2015). Nevertheless, several publications show that CYTO-ID® staining is effortlessly applicable for detection and quantification of marcroautophagy (Chan et al. 2012; Guo et al. 2015). However, the observed increase in CYTO-ID® mean fluorescence exclusively occurred in highly apoptotic samples (**Figure 26**, **Figure 32**) and might thus be based on increased autofluorescence in Renca cells in response to apoptosis induction at 48 h. Thus, future experiments should include unstained samples for each treatment condition to allow for normalization. Furthermore, as neither LC3B-II expression nor Beclin-1 expression confirmed the up to 2-fold induction of CYTO-ID® mean fluorescence intensity observed by flow cytometric analysis, further experimental setups might be needed to safeguard that HDACi-treated Renca cells do not induce autophagy. LC3B-II and CYTO-ID® staining could be likewise performed using confocal fluorescence microscopy to allow for higher resolution compared to Western blot and flow cytometry. In addition, experiments should be performed using an autophagy inducing stimulus as positive control. Unfortunately, previous trials to induce autophagy in Renca cells using rapamycin, irinotecan, or doxorubicin were not successful. Serum starvation might provide a suitable stimulus for future experiments. Moreover, combined application of chloroquine and HDACi might provide higher CYTO-ID® signals as well as higher levels of LC3B-II and Beclin-1 as a result of inhibition of the autophagic flux and thus enable reliable comparison of basal and potential, HDACi induced autophagy in Renca cells. As others have already shown (Carew et al. 2007; Li et al. 2010; Lopez et al. 2011; Rao et al. 2012; Bhalla et al. 2013; Dupere-Richer et al. 2013; Torgersen et al. 2013; El-Khoury et al. 2014; He et al. 2014; Stankov et al. 2014; Zhang et al. 2015), combinatorial treatment with chloroquine and HDACi and subsequent assessment of cell death induction, would moreover offer the possibility, to detect if autophagy induction through HDACi represents a survival or apoptosis inducing mechanism in Renca cells.

5.1.6 HDAC class I inhibiton induces apoptosis and restrains growth in human primary RCC cells

Thanks to a cooperation with the Department of Urology of the University Medical Center Mainz [redacted] it was possible to obtain patient-derived human primary clear cell renal carcinoma cells to additionally asses the transferability of the discussed HDACi mediated effects from murine to human background. Therefore, the two primary cell lines, Mz-ccRCC1 and Mz-ccRCC2, were analyzed to determine the general cytotoxicity and growth inhibitory effect of VPA and MS-275 in human RCC. VPA and MS-275 induced histone hyperacetylation differently in Mz-ccRCC1 and Mz-ccRCC2 cells (**Figure 33A**, **Figure S 12**). While MS-275 treatment led to a stable hyperacetylation of histone H3 and H4 in both cell lines, VPA mediated HDAC class I inhibition was low in Mz-ccRCC2 cells with scarcely detectable upregulation of histone hyperacetylation (**Figure 33A**, **Figure S 12**). This indicates, that higher VPA concentrations might be needed in certain human RCC cells to induce reliable histone hyperacetylation. Nevertheless, both primary cell lines exhibited significant cell death induction in response to VPA as well as MS-275 treatment (**Figure 34**, **Figure S 13**). Detection of caspase cleavage in Mz-ccRCC1 cells confirmed that cell death was caused by apoptotic signaling cascades comparable to HDACi induced cell death in Renca cells (**Figure 33B**). In general, proliferation of Mz-ccRCC1 was diminished in comparison to proliferation of Renca and Mz-ccRCC1 cells and thus endpoints of the diverse analyses were generally extended for 24 h to ensure equivalent cell cycle progression during treatment in all tested cell lines. Thus, whereas cell death induction in Mz-ccRCC2 cells was significant with the higher concentrations of VPA and MS-275 already after 24 h and even further pronounced after 48 h (**Figure S 13**), cell death in Mz-ccRCC1 cells was significantly induced as late as 72 h (**Figure 34**). Nevertheless, the extent of induced cell death in both human primary cell lines was comparable or higher than in Renca cells (**Figure 26**, **Figure 34**, **Figure S 13**). In general, in all three cell lines 1.5 mM VPA was not sufficient to induce the full apoptotic response whereas 5 mM VPA, 1.5 µM MS-275, and 5 µM MS-275 were effective (**Figure 26**, **Figure 34**, **Figure S 13**). In clinical studies, achievable blood concentrations of VPA range from around 0.4 mM to around 88 mM depending on dosage and drug application schedule (Münster et al. 2007; Forooghipour et al. 2009; Damegunta 2014) and are thus comparable to our applied concentrations. In contrast, measured MS-275 blood concentrations range from 0.01 µM to around 0.3 µM depending on dosage and drug application schedule (Ryan et al. 2005; Gojo et al. 2007; Gore et al. 2008; Pili et al. 2011; Connolly et al. 2017) and are thus substantially lower than the applied concentrations in this work. However, measurements of enhanced acetylation of histones in patients at these low concentrations of MS-275 prove that HDAC inhibition is effective (Ryan et al. 2005; Gojo et al. 2007; Gore et al. 2008) and thus *in vivo* mechanisms of MS-275 are relatable to our observed results with higher concentrations.

Treatment with VPA and MS-275 did induce cell cycle changes in Mz-ccRCC1 and Mz-ccRCC2 cells, that were in part comparable to those observed in HDACi-treated Renca cells (**Figure S 8**, **Figure S 14**, **Figure S 15**). For instance, MS-275 treatment led to an increase of cells in G1-phase and a decrease of cells in S-phase at early timepoints in both human cell lines (**Figure S 14**, **Figure S 15**), which indicates that MS-275 treatment induced a cell cycle block in both cell lines. VPA treatment, on the other hand, did show the same trend of enhancement in G1-phase and reduction in S-phase in Mz-ccRCC1 cells, but cell cycle changes in response to VPA treatment in Mz-ccRCC2 cells were entirely different (**Figure S 14**, **Figure S 15**). In this cell line, 1.5 mM VPA reduced the percentage in G1-phase while inducing S-phase percentage and thus nor G1-phase arrest was observable in response to VPA in Mz-ccRCC2 cells (**Figure S 15**). In accordance with these findings, viable cell number of Mz-ccRCC1 cells was reduced prior to cell death induction as a result of the induced G1-phase arrest (**Figure 34**, **Figure 36**, **Figure S 14**) but viable cell number of Mz-ccRCC2 cells was solely reduced under apoptotic conditions (**Figure S 13**, **Figure S 16**, **Figure S 15**). Thus, even in the absence of cell cycle blockage in G1-phase, viable cell number was reduced as a result of cell death induction and VPA and MS-275 were effective in both cell lines. Future experiments should be directed to determine the molecular differences of Mz-ccRCC1 and Mz-ccRCC2 cells that prevent cell cycle arrest in G1-phase in Mz-ccRCC2 cells in response to HDACi treatment. Moreover, analysis of E-cadherin expression in both human cell lines showed, that, in contrast to Renca cells, HDACi treatment provoked an upregulation of protein expression (**Figure 20**, **Figure 37**, **Figure S 17**). Noteworthy, in Mz-ccRCC1 cells, this upregulation was reversed as soon as significant cell death occurred (**Figure 37**). This finding indicates that HDAC inhibition may regulate E-cadherin expression in both directions and supports the hypothesis in **5.1.4** that E-cadherin downregulation is a direct consequence of the execution of cell death programs. In summary, these experiments in Mz-ccRCC1 and Mz-ccRCC2 cells demonstrate that human RCC cells are as vulnerable as the murine Renca cell line towards the inhibition of class I HDACs. However, they also highlight that unidentified molecular differences between these patient derived RCC cells influence the phenotypical consequences of HDACi treatment. Future global analysis of protein expression in these two human RCC lines in response to HDACi might be helpful to decipher which molecular alterations result in the dissimilar cell cycle distribution in HDACi-treated Mz-ccRCC1 and Mz-ccRCC2 cells. Nevertheless, as early cell cycle arrest was dispensable for subsequent cell death induction and the reduction of the viable cell number in Mz-ccRCC2 cells, class I specific HDACi have proven to be effective in killing patient derived RCC cells. Thus, application of VPA and MS-275 in combinatorial treatment schemes, as indicated above, seems to be a feasible and promising approach.

5.1.7 HDAC1 and HDAC2 as mechanistic targets of HDACi

As previously described MS-275 and VPA specifically target HDAC1, 2, and 3 (Bradner et al. 2010). To further identify the role of individual HDACs in this background, HDAC1 and HDAC2 expression levels were successfully knocked down (**Figure 38**). Knockdown of HDAC1 resulted in upregulation of HDAC2 and vice versa. This compensatory regulation has been described in various other reports and is thought to be enabled by regulatory feedback loops at a translational or posttranslational level (Jurkin et al. 2011). As HDAC1 and HDAC2 evolutionary derive from a gene duplication, and thus display high structural homology that encompasses 86% identity on the level of amino acids, functional redundancy of both proteins is a likely consequence (Jurkin et al. 2011). Thus, it must be expected that inhibition of the expression and activity of both HDACs is necessary in Renca cells to prevent compensatory mechanisms. Fittingly, individual loss of either HDAC1 or HDAC2 expression did not induce the same extent of morphological alterations that was observed upon combined knockdown (**Figure 39**). In general, these morphological alterations were comparable to the changes observed in response to HDACi treatment (**Figure 16**, **Figure 39**) and implied that specific loss of HDAC1 and HDAC2 expression was sufficient to induce the plethora of global effects observed in Renca cells in response to VPA and MS-275 treatment. Furthermore, combined knockdown of HDAC1 and HDAC2 induced caspase cleavage, reduced the viable cell number, and reduced the expression of E-cadherin and the metastatic driver PDGFRβ akin to HDACi treatment in Renca cells (**Figure 40**, **Figure 41**, **Figure 42**). All these parameters verify that particularly HDAC1 and HDAC2 activity is necessary for Renca cell proliferation and survival. Abrogation of their specific molecular function by VPA and MS-275 treatment is crucial for the described apoptotic phenotype. Critically, E-cadherin expression was similarly downregulated even in the absence of either HDAC1 or HDAC2 expression (**Figure 37**). This indicates that in this individual aspect HDAC1 and HDAC2 do not fully compensate for each other's loss of function and implies independent HDAC1 and HDAC2 controlled regulatory mechanisms of E-cadherin expression. Reasons for this non-redundant HDAC1 and HDAC2 function might include specific recruitment of HDAC1 and HDAC2 to different TF complexes or separate roles for HDAC1 and HDAC2 in the regulation of E-cadherin protein stability. Albeit the majority of studies reported compensatory regulation and function of HDAC1 and HDAC2, there have previously also been isolated reports of specific HDAC1 and HDAC functions other than the here described E-cadherin regulation (Jurkin et al. 2011). In summary, the results of the conducted knockdown experiments suggest that specifically inhibition of HDAC1 and HDAC2 attenuates growth, survival, migration, and metastatic spread of RCC cells *in vitro* and *in vivo*. Hence, these two HDACs present valid pharmacological targets in RCC treatment, that are assailable through the comparatively selective inhibitors VPA and MS-275.

5.1.8 Elucidation of the p53 status of Renca cells

In consideration of the, as described, entirely undefined p53 status of Renca cells, the conducted experiments were aimed to provide initial insight. Low basal and readily inducible total p53 expression both implied wild-type p53 expression in Renca cells (**Figure 43**, **Figure 44**). To further confirm this result, specific p53 mutation analysis could be performed using PCR and specific primers for all exons of the *Tp53* gene in Renca cells. Subsequent sequencing analysis would reveal potential mutations in p53 protein. Alternatively, p53 status might be elucidated by mutation load assay, mass spectrometric, functional, or microarray analysis as briefly described in (Robles and Harris 2010). However, the described analyses here suggest wild-type p53 expression in Renca cells which is a congruent result considering the low overall *Tp53* mutation rate of 2.4% in clear cell RCC (Wang and Sun 2017). Crucially, p53 mutation rates were shown to be significantly higher in cases with lymphatic metastasis, which indicates that tumors harboring mutant p53 display increased aggressiveness (Girgin et al. 2001; Zigeuner et al. 2004) and high p53 expression, possibly indicative for *Tp53* missense mutation, is associated with poor prognosis (Wang et al. 2017). As mutant, overexpressed p53 functions as negative apoptosis regulator in RCC (Tannapfel et al. 1997; Girgin et al. 2001), enhancement of aggressiveness and metastasis formation might be a combined result of reduced apoptosis and increased proliferation rate. Hence, the presented data in this work should putatively be reviewed in light of the assumed wild-type p53 expression in Renca cells. It might be worth to explore in future experiments, whether loss of wild-type p53 or expression of mutant p53 negatively influences HDACi induced apoptotic response. In general, reliable interpretation of data describing the implications of p53 mutation in RCC is complicated by the fact that the majority of studies of mutant p53 expression in clinical material from renal cancers relies on IHC detection of p53 and the assumption that mutations in p53 lead to its overexpression due to its inability to upregulate HDM2 rather than actual detection of mutations by PCR single-strand conformation polymorphism (SSCP) and sequence analysis (Noon et al. 2010). Moreover, this interpretational approach is only valid for missense mutations that enhance total protein expression, but not for the 10 – 20% of *Tp53* mutations that are nonsense or truncating mutations and lead to low level p53 expression (Noon et al. 2010). While other cancer types might confer this resistance by abrogating p53 tumor suppressor function, RCC's high intrinsic radiation and chemotherapy resistance and low p53 mutation frequency imply major roles for different resistance mechanisms like high levels of multidrug transporter expression (Gurova et al. 2004). It has also been suggested that resistance in RCC is conveyed by a tissue-specific mechanism that suppresses wild-type p53 mediated activation of target gene transcription (Gurova et al. 2004). However, the finding that doxorubicin treatment enhances BAX expression in Renca cells contradicts this theory (**Figure 44**). As around 97% of cancer-derived p53 missense mutations are located within exons encoding the p53 DNA binding domain, an existing mutation of p53 in Renca cells would likely prevent efficient BAX target gene activation (Olivier et al. 2002). Thus, the inducible BAX expression upon doxorubicin is in line with the strongly diminished expression of total p53 protein in Renca cells in comparison to a cell line that expresses mutated p53. In addition, p21 (*Cdkn1a*) expression was upregulated and Survivin (*Birc5*) expression was downregulated in response to MS-275 treatment according to mass spectrometric analysis (Kiweler et al. 2018). These data are coherent with the negative impact of p21 on the E2F-dependent expression of survivin in CRC cells (Rauch et al. 2018). Congruently, others describe intact wild-type p53 and HDM2 mediated signaling in response to UV induced DNA damage and thus argue against resistance mechanisms that are associated with p53-dependent gene activation (Warburton et al. 2005). In summary, these results indicate wild-type p53 expression in Renca cells and effective p53-dependent signaling induction in response to a toxic stimulus.

5.2 HDAC2 expression in colorectal cancer cells and the effects of HDAC2 sumoylation and HDAC inhibition

In consideration of the fact that next-generation sequencing studies in CRC revealed enormous inter- and intratumoral heterogeneity (Wood et al. 2007; Muzny et al. 2012), it is important to implement further biomarkers to streamline targeted treatment and patient stratification into prognostic subgroups to ultimately accomplish the most favorable therapeutic success for each individual patient. Interestingly, the expression levels of HDAC1, -2, -3, -5, and -7 were found to be significantly upregulated in human CRC and especially HDAC2 upregulation is described as early event in progression from adenoma to carcinoma (Zhu et al. 2004; Ashktorab et al. 2009; Stypula-Cyrus et al. 2013). While high HDAC class I expression has been described as being significantly associated with reduced CRC patient survival, HDAC2 expression is even considered to be a an independent prognostic factor (Weichert et al. 2008). Most publications consider the tumor promoting effect of HDAC overexpression to be mainly a consequence of overall changes in chromatin structure and subsequent transcriptional repression of tumor suppressor genes and other negative regulators of cell proliferation, migration, and metastasis (Minucci and Pelicci 2006; Weichert et al. 2008; Ashktorab et al. 2009; Stypula-Cyrus et al. 2013). As high expression of HDAC2 is sufficient to repress apoptosis in CRC cells while stably maintaining their transformed phenotype (Zhu et al. 2004), it is conceivable that distinct HDACs have defined roles in the regulation of specific carcinogenesis related signaling pathways. Appropriately, HDACs have been shown to catalyze the deacetylation of diverse transcription factors (e.g. p53, E2F, GATA-1, TCF, HMG-1, SP-1/-2, TFIIB, CREB) and to alter their DNA binding affinity and transcriptional activity (Minucci and Pelicci 2006; Mariadason 2008). Interestingly, preserved p53 functionality was found to be positively correlated with superior prognosis and treatment response in CRC whereas loss of p53 was predictive for aggressive phenotypes (Elsaleh et al. 2001; Sarasqueta et al. 2013; Cao et al. 2017). In consideration of the overexpression of HDACs in CRC, the subsequent sensitivity of CRCs to HDACi, and the relevance of p53 inactivation for CRC prognosis (Zhu et al. 2004; Sarasqueta et al. 2013; Stypula-Cyrus et al. 2013), our group reported a principle mechanisms that couples HDAC2 sumoylation, p53 activity, and dismal CRC prognosis (see **1.3.2**). To demonstrate the restrictive effect of HDAC2 sumoylation on p53-dependent cell death, RKO cells were comparatively subjected to doxorubicin treatment (Brandl et al. 2012). However, as doxorubicin has no relevance in CRC therapy, this initial experiment allowed no decisive predictive conclusions on the effect of HDAC2 sumoylation in common CRC treatment schemes. The following work was thus addressed to define the significance of HDAC2 sumoylation for CRC sensitivity towards 5-FU and to clarify whether HDAC2 sumoylation directly impacts further key enzymes and signaling pathways apart from p53 target gene expression.

5.2.1 Heterogenous HDAC2 expression in colorectal cancer cells

As described above, in the introduction of chapter **5.2**, the expression of HDACs and especially of HDAC2 is thought to have considerable impact on the carcinogenesis of CRC. Independent reports in literature show contradicting results concerning the HDAC2 status of the human colon cancer cell line RKO (Ropero et al. 2006; Hanigan et al. 2008; Ree et al. 2008). In short, MSI in RKO cells can result in a frameshift mutation in the A_9 coding repeat sequence in exon 1 of the *HDAC2* gene, which prompts the loss of HDAC2 expression and activity (Ropero et al. 2006). However, whereas Ropero and colleagues identify RKO cells as generally negative for HDAC2, Ree and colleagues state that authenticated RKO cells express HDAC2 and speculate that the RKO cell line investigated by Ropero represents a HDAC2 mutated subclone (Ropero et al. 2006; Ree et al. 2008). The analysis of our ATCC-derived RKO cell line by immunofluorescence staining and confocal microscopy confirmed the results by Ree and colleagues and furthermore, for the first time, proved the theory of heterogenous HDAC2 expression in RKO cells (**Figure 45**). In our understanding, HDAC2 negative cells represent a subpopulation of RKO cells, whose percentage can be increased upon beneficial culture conditions to give rise to a completely HDAC2 negative RKO cell line. This finding led to the implementation of a medical doctorate thesis conducted by [redacted]. This work reveals the possibility to select HDAC2 positive and negative subclones and the implications of HDAC2 expression for cellular sensitivity towards HDACi and selected chemotherapeutics relevant for CRC therapy. Furthermore, HDAC2 heterogeneity was verified for HCT116 cells (Hanigan et al. 2008) and additionally demonstrated for the human primary cancer cell line HROC24. This indicates that HDAC2 mutations occur frequently in different MSI CRC cell lines (**Figure 45**). This intratumoral heterogeneity of HDAC2 expression in CRC strongly argues for future research approaches that aim to examine cell fate decisions in direct relation to HDAC2 expression and activity. Such studies could lead the way to specific treatment recommendations for patients with HDAC(2)-positive or -negative tumors.

5.2.2 Characterization of RKO HDAC2^{wt} and RKO HDAC2^{K462R} cell lines

Sumoylation at lysine 462 regulates HDAC2 activity, as only K462-sumoylated HDAC2 binds and deacetylates p53 to reduce its transcriptional activity (see **1.3.2** and (Brandl et al. 2012)). To ensure reliable conditions in the utilized cell system, stable V5-tag expression in RKO HDAC2^{wt} and RKO HDAC2^{K462R} cell lines was confirmed by Western blot analysis (**Figure 46A**). Attachment of V5-tag allowed for regular analysis of stable recombinant protein expression in both cell lines. However, as RKO cells are MSI, occasional reduction of V5-expression was observed in both lines. This indicates that the recombinant *HDAC2* gene sequence is lost and/or prone to mutation over time alike endogenous *HDAC2* (**Figure 45**) (Ree et al. 2008). All results that are presented in this work have therefore been accompanied by a regular assessment of HDAC2 protein expression in reconstituted RKO cells. Furthermore, RKO HDAC2^{wt} and RKO HDAC2^{K462} cells can be discriminated by divergent p53 levels and p53-target gene expression (**Figure 46B**). Enhanced p53 protein levels in RKO HDAC2^{wt} cells indicate a reduced expression of HDM2, the p53-induced ubiquitin ligase for p53 (Brandl et al. 2012). In RKO HDAC2^{K462R} cells, increased activity of p53 induces the expression of its direct target genes and evokes augmented protein expression of BAX, p21, and HDM2 (**Figure 46B**) (Brandl et al. 2012). Growth properties of both cell lines were assessed to determine whether HDAC2 mutation had any influence on doubling times and to ensure that subsequent experiments were conducted under equal growth conditions for both cell lines (**Figure 47**). Doubling times were slightly divergent with RKO HDAC2^{K462R} displaying mildly enhanced growth rates (**Table 6**). The reason for this discrepancy might be the elevated standard deviation of the RKO HDAC2^{K462R} cell count at 72 h. Higher confidence in the obtained doubling times could be achieved by additional analysis of RKO cell number at later time points. However, the minor difference in doubling time together with the similar growth curve progression indicate that cell growth was equal and independent of HDAC2 mutation. This ensured the comparability of all subsequent experiments in these two cell lines. It would anyhow be more conceivable if RKO HDAC2^{K462R} displayed reduced proliferation rates compared to RKO HDAC2^{wt} cells considering their heightened expression of the crucial cell cycle inhibitor p21 (**Figure 46B**) (Xiong et al. 1993; Luo et al. 1995; El-Deiry 2016). Moreover, loss of wild-type HDAC2 expression through knockdown has been associated with reduced proliferation as described in the literature and during this work in renal cancer cells (**Figure 40B**) (Zhu et al. 2004; Harms and Chen 2007). Hence, the finding that RKO cells expressing the catalytically active, but sumoylation-deficient HDAC2^{K462R} mutant (Brandl et al. 2012) did not show substantial reduction of cell growth, indicates that loss of HDAC2 sumoylation, albeit sufficient to alter p53-dependent gene expression, does not phenocopy general loss of HDAC2 protein expression. Finally, the cell growth analysis provided a further benefit in clearly showing that experiments with both RKO cell lines should not be conducted earlier than 24 h post seeding, as exponential cell growth was not established prior to this time-point (**Figure 47**).

5.2.3 Sensitivity of RKO HDAC2^{wt} and RKO HDAC2^{K462R} to treatment with various chemotherapeutics

A constant mainstay of adjuvant CRC therapy over the past decades has been the application of fluoropyrimidines (**1.1.2**). As response rates for 5-FU monotherapy of advanced CRC reside at 10-20% and are only augmented in combination treatment schemes with OX and IRI to 40-50% (Douillard et al. 2000; Giacchetti et al. 2000; Johnston and Kaye 2001), understanding of resistance mechanisms to 5-FU is still of the utmost importance. Loss of HDAC2 sumoylation directly impacts p53-dependent expression of diverse proteins that are relevant for apoptosis and cell cycle arrest (**Figure 46B**) (Brandl et al. 2012) and might thus influence cell fate decisions in response toxic stimuli. Hence, both RKO cell lines were challenged with increasing concentrations of 5-FU and its DNA-damaging metabolite FdUrd (see **1.5.1**). Remarkably, RKO HDAC2^{K462R} cells were significantly sensitized to 5-FU but not to FdUrd (**Figure 48**). Consequently, absence of HDAC2 sumoylation might impact a 5-FU mechanism that has no or no significant value for FdUrd-mediated toxicity such as RNA integration of 5-FU. Unfortunately, the high versatility of 5-FU metabolism and subsequent toxic mechanisms aggravates the interpretation of these results (see **1.5.1**, **Figure 6**). As FdUrd mainly induces damage by TS inhibition, 5-FU-mediated DNA damage through false incorporation of FdUTP might present this independent pathway. It might thus be important to prospectively assess explicit DNA damage in response to both fluoropyrimidines either indirectly by comparing DNA strand break induction by COMET assay or directly by comparing the ratio of incorporated FdUTP by mass spectrometric approach (Noordhuis et al. 2004). Markedly, a previous study using the CRC cell line SW620 concluded, that 5-FU and FdUMP, the direct downstream metabolite of FdUrd, induce different types of primary DNA lesions that activate different cell cycle checkpoints and trigger different DNA repair pathways (Matuo et al. 2009). This finding could provide an explanation for the divergent cytotoxicity of 5-FU and FdUrd in dependence of HDAC2^{K462R} expression (**Figure 48**). Furthermore, neither RKO HDAC2^{wt} nor RKO HDAC2^{K462R} cells displayed significant changes in cell cycle distribution upon treatment with 5-FU (**Figure S 19A**). On the one hand, unaltered cell cycle might indicate that both cell lines were unable to detect damage induced by 5-FU and hence failed to initiate cell cycle arrest as a prerequisite of successful damage repair pathways. On the other hand, a trend towards increased G1-phase in RKO HDAC2^{wt} cells and towards increased G2-phase in RKO HDAC2^{K462R} cells might be considered as a sign for earlier cell cycle changes (**Figure S 19A**). Additional analysis of cell cycle distribution prior to 48 h treatment could result in the detection of cell cycle changes that preceded cell death induction. This insignificant but distinctive trend of divergent cell cycle regulation in both cell lines was most prominent in samples that coincidently displayed divergences in cell death induction (**Figure 48**, **Figure S 19A**). These small variations in cell cycle regulation in response to 5, 7.5, and 10 µM 5-FU could be associated with the different expression of p21 in these cell lines and suffice to alter DNA damage repair and cell death pathways. In contrast, significant cell cycle arrest in S-phase indicated that effective damage detection and subsequent signaling were induced equally in both cell lines in response to FdUrd (**Figure S 19B**). As described, enhanced 5-FU toxicity in RKO HDAC2^{K462R} cells might be either based on integration of its metabolites into RNA and/or DNA or on the inhibitory effect of FdUMP on TS (see **1.5.1**). To delimit accountable damage mechanisms, additional chemotherapeutics with comparable toxic mechanisms were used comparatively in RKO HDAC2^{wt} and RKO HDAC2^{K462R} cells. HU was chosen as it is, like 5-FU, an antimetabolite and furthermore a potential inhibitor of RNR. Comparable to 5-FU mediated TS inhibition, HU mediated RNR inhibition abolishes DNA synthesis through shortening of dNTP production and induction of replicative stress (Dobbelstein and Sørensen 2015). In contrast to 5-FU, HU evoked no different cell death response in both cell lines (**Figure 49A**). In conclusion, the 5-FU induced damage through TS inhibition and consecutive replicative stress response are unlikely to be modulated by HDAC2 sumoylation. Ola is a competitive inhibitor of the DNA damage sensor PARP and prevents successful PARP-dependent repair of endogenously occurring DNA SSBs (Caldecott 2008; O'Connor 2015). Inactivated PARP provokes stalling and/or collapsing of replication forks and consecutive generation of DSB. In cancer cells harboring profound deficiencies in effective DSB repair, PARP inhibition thus provokes lethal DNA damage termed synthetic lethality (O'Connor 2015). As RKO HDAC2^{wt} and RKO HDAC2^{K462R} cells display equal cell death induction in response to treatment with Ola (**Figure 49B**), there is no indication that sumoylation-defective HDAC2 results in severe defects in DSB. Noteworthy, this basic analysis of synthetic lethality is only suitable to exclude severe defects in DSB repair. To indubitably exclude minor changes in DSB repair, suitable reporter cassette assays should be executed to determine NHEJ and HR frequency (Seluanov et al. 2010; Krumm and Roos 2017). Finally, RKO HDAC2^{wt} and RKO HDAC2^{K462R} cells were submitted to ACNU. ACNU induces DNA damage by alkylation and crosslink formation amidst the two polynucleotide strands of DNA. These ICL avert fruitful strand separation during replication and ultimately result in DNA DSBs (see **1.5.2**) (Nikolova et al. 2017a; Nikolova et al. 2017b). Strikingly, RKO HDAC2^{K462R} cells responded to ACNU treatment with significant induction of cell death, whereas RKO HDAC2^{wt} cells displayed no toxic response (**Figure 49C**). This divergent reaction implies that, in contrast to RKO HDAC2^{K462R} cells, RKO cells expressing HDAC2^{wt} are capable of employing repair mechanisms to successfully prevent ICL- and DSB-related lethality. Cell cycle distribution in response to ACNU was comparable in RKO HDAC2^{wt} and RKO HDAC2^{K462R} following 24 and 48 h treatment (**Figure S 21**). Both cell lines were arrested in G2/M-phase after 24 h and this initial cell cycle blockage was resolved after 48 h treatment prior to induction of cell death at 72, 96, and 120 h (**Figure 49C**, **Figure S 21**). This chronology corresponds to the intricate mechanism of ICL formation that includes initial cell cycle blockage in G2-phase due to alkylating DNA adducts prior to the ultimate formation of lethal ICLs and DSBs (Nikolova et al. 2012). Thus, as misincorporated 5-FU- nucleotides and ACNU-mediated ICLs are both finally converted into DSBs, HDAC2 sumoylation might influence DSB repair processes like HR and NHEJ. Interestingly, comparable to 5-FU, ACNU-treated RKO HDAC2^{K462R} cells displayed a tendency for higher G2-phase and reduced G1-phase percentage when compared to RKO HDAC2^{wt} and this trend coincided with heightened cell death response (**Figure 49C**, **Figure S 20C**). These minor differences in cell cycle distribution that were measurable in response to 5-FU and ACNU, but not FdUrd, might thus be associated with the enhanced sensitivity of RKO HDAC2^{K462R}. To exclude dissimilarities in the complex mechanisms of ACNU-mediated ICL formation itself (see **1.5.2**), a modified COMET assay technique was employed to assess the extent of ICL strand formation in both cell lines. Retardation of COMET tail intensity of IR-induced DSBs was comparable in both cell lines, which indicates that equal amounts of ICL were formed 24 h post treatment (**Figure S 22**). It is furthermore noteworthy that RKO cells were tested for the enzyme activity of MGMT by radioactive MGMT activity assay as is routine in our lab (Preuss et al. 1995). Activity was found to be 694 fmol/mg in RKO HDAC2^{wt} and 684 fmol/mg in RKO HDAC2^{K462R} cells, which entails a higher MGMT activity than in the positive control of HeLa S3 cells with 494 fmol/mg. As the MGMT enzyme directly removes alkyl groups from the O^6-position of guanine, it successfully prevents initial DNA damage induction by alkylating agents (Preuss et al. 1995; Kaina et al. 2007). The MGMT reaction is stochiometric and can be prevented through suicide inhibition by pre-treatment with the substrate O^{6}BG (Kaina et al. 2007). Accordingly, MGMT activity was successfully abolished in all related experiments by equimolar pre-treatment with the MGMT inhibitor O^{6}BG.

5.2.4 p53-dependent gene expression in RKO HDAC2^{wt} and RKO HDAC2^{K462R} in response to 5-FU, FdUrd, and HU treatment

Basal p53-dependent gene expression differs in RKO HDAC2^{wt} and RKO HDAC2^{K462R} cells as sumoylation of HDAC2 affects the transcriptional activity of p53 (**Figure 46B**) (Brandl et al. 2012). In response to a cell's exposure to genotoxic stress, p53-dependent signaling is thought to either enhance cell survival by facilitating DNA repair through activation of cell cycle checkpoints or to induce apoptotic cell death as a matter of protection against genomic instability. However, recent studies suggest further roles for p53 in this context, such as regulation of cellular senescence and metabolism (Mirzayans et al. 2017). Further reports implicate that the initial role of p53 activation is to suppress apoptosis rather than promoting it, while concurrently initiating sustained blockage of cell cycle (Mirzayans et al. 2017). In either way, p53 represents a central hub in DNA damage response. In 5-FU-, FdUrd-, and HU-treated RKO HDAC2^{wt} and HDAC2^{K462R} cells, activation of p53 in response to the toxic stimulus is visible by p53 accumulation (**Figure 50**). The comparable extent of this initial reaction in both cell lines indicates equal initial damage response (**Figure 50**). Herein, RKO HDAC2^{wt} displayed a slightly higher absolute p53 expression after treatment (**Figure 50**) due to the heightened basal p53 expression in this cell line (**Figure 46B**, **Figure 50**). Selected studies propose a threshold mechanism in which low basal p53 expression triggers growth arrest and higher basal expression primes for apoptosis induction (Kracikova et al. 2013). This principle is not applicable in the RKO system, as it would implicate enhanced apoptotic response in RKO HDAC2^{wt} based on their augmented basal p53 expression (**Figure 46B**). In addition, this model is not compatible with the heightened transcriptional p53 activity for proapoptotic genes in RKO HDAC2^{K462R}, that is accompanied by a basal reduction of p53 (Brandl et al. 2012). Activation of p53 in the DNA damage response is accomplished by its phosphorylation at Ser15 by ATM and ATR protein kinases (Canman et al. 1998; Meek and Anderson 2009; Loughery et al. 2014). As initial focal point of p53-dependent DNA damage response, Ser15 phosphorylation prompts succeeding phosphorylation of p53 at Ser9, -20, -46, and Thr18 (Loughery et al. 2014). Furthermore, Ser15 phosphorylation diminishes interaction of p53 with its negative regulator HDM2 (Shieh et al. 1997; Loughery et al. 2014). Thus, the extent of this phosphorylation is suited to determine p53 activation. In RKO HDAC2^{wt} and RKO HDAC2^{K462R} cells, phosphorylation of p53 at Ser15 was comparable in response to 5-FU and HU (**Figure 51**). Moreover, expression of the p53 target protein PIG3 was induced evenly (**Figure 51**). Since PIG3 is critical for p53 upregulation in early DNA damage response (Lee et al. 2010b; Jin et al. 2017), comparable upregulation of PIG3 and p53 phosphoralytion indicate equal induction of p53-dependent damage response in both cell lines. Furthermore, upregulation of p21 in both cell lines demonstrates that p53-dependent target gene activation is also given in the presence of sumoylatable HDAC2 (**Figure 52**). Fittingly, HDAC2 sumoylation was demonstrated to be lost over time in response to genotoxic stress and to thus enable p53 stress response in HDAC2^{wt} cells (Brandl et al. 2012). Although p21 induction levels are seemingly higher in RKO HDAC2^{K462R} cells, fold-induction normalized to basal p21 expression is comparable in both cell lines (**Figure 52**, **Figure S 23**). This substantiates that p53-dependent gene expression is activated comparably irrespective of HDAC2 mutation and basal p53 expression levels. Due to p21's main role as a negative regulator of cell cycle in response to genotoxic events, it is also described as a repressor of apoptosis induction (Abbas and Dutta 2009). On the one hand, apoptosis is indirectly repressed by p21 because an active cell cycle is essential to recognize genotoxic damage and trigger apoptotic signaling (Abbas and Dutta 2009). On the other hand, high, cytoplasmic p21 levels directly inhibit the activity of procaspase 3, Caspase 8, Caspase 10, stress-activated protein caspases (SAPKs), and apoptosis signal-regulating kinase 1 (ASK1/MAP3K5) (Abbas and Dutta 2009). The seemingly higher p21 levels in RKO HDAC2^{K462R} should thus rather entail apoptosis repression than promote its activation. To fully elucidate if p53-dependent gene activation plays a role in 5-FU-mediated toxicity, it would be beneficial to combine 5-FU with the p53-activator nutlin-3 in RKO HDAC2^{wt} cells. Interestingly, substantial p21 upregulation was absent in both cell lines in response to FdUrd (**Figure 52**). This general lack of p21 upregulation at early timepoints corresponds to the observed FdUrd-induced S-phase arrest after 48 h, as initial p21 upregulation would have prevented transition to and arrest in S-phase (**Figure 52**, **Figure S 19**). In summary, analysis of selected p53 target proteins, p53 expression and phosphorylation gave no conclusive hint for divergent p53 regulation between both cell lines in response to 5-FU.

5.2.5 Thymidylate synthase inhibition in 5-FU-treated RKO HDAC2^{wt} and RKO HDAC2^{K462R}

Irreversible TS inhibition is believed to be the 5-FU-mediated damage mechanism with the highest clinical relevance as it effectively prevents synthesis of the essential DNA nucleotide precursor 2-deoxythymidine-5-monophosphate (dTMP) (see **1.5.1**) (Rustum 2004; Berger and Berger 2006). Clinical strategies are established to modulate 5-FU treatment to ameliorate the efficiency of TS inhibition (Rustum et al. 1997; Longley et al. 2003). These include, addition of leucovorin, a folinic acid that augments TS complex formation, and interferons, which inhibit acute TS induction and enhance 5-FU catabolism (Longley et al. 2003). TS inhibition is accomplished by stable complex formation between TS, the 5-FU metabolite FdUMP, and the folate cofactor CH_2THF (see **1.5.1**). As this complex (TS*) is a few kDa heavier than free TS and hence exhibits reduced mobility on SDS-PAGE, free TS and complexed TS* were successfully separated on Western blot and could be quantified independently. Efficiency of TS inhibition was comparable in short-term and long-term 5-FU-treated samples of RKO HDAC2^{wt} and RKO HDAC2^{K462R} cells (**Figure 53**). In both cell lines, free TS level resided around 20% of total TS after 24 h (**Figure 53A**) and increased to around 30% after 48 h (**Figure 53B**). This increase could be caused by compensatory marginal upregulation of TS expression. Nevertheless, TS inhibition was effective and, in any case, independent of HDAC2 sumoylation. As TS* complexes were shown to persist for up to 13 days in different cancer cell lines (Brody et al. 2006), it can be assumed that this comparable inhibition is stable and valid equally for longer 5-FU treatment times. In summary, uniform TS* complex formation in response to 5-FU treatment implies that differences in cell death induction in RKO HDAC2^{wt} and RKO HDAC2^{K462R} cells are not based on this damage mechanism and more likely dependent on down-stream DNA repair pathways.

5.2.6 Global protein expression analysis in RKO HDAC2^{wt} and RKO HDAC2^{K462R}

Global analysis of protein expression was performed in RKO HDAC2^{wt} and RKO HDAC2^{K462R} cells to identify significantly different regulated proteins, whose divergent expression could be causal for the deviation of 5-FU sensitivity. Mass spectrometric analysis of global protein expression in untreated RKO HDAC2^{wt} and RKO HDAC2^{K462R} cells provided quantitative data on the expression of 5901 proteins. A threshold was applied to only identify those proteins as differently expressed in RKO HDAC2^{wt} and RKO HDAC2^{K462R} cells that displayed a < -1.0 or > 1.0 deviation of log2 scale expression values, implicating a > 2-fold difference in protein expression in dependence of HDAC2 sumoylation. This approach yielded 54 differentially expressed proteins in untreated cells (**Figure 54**), which corresponds to 0.9% of all detected proteins. Expression levels of 17 proteins were downregulated and expression levels of 37 proteins were upregulated due to the abrogation of HDAC2 sumoylation (**Figure 55**). In consideration of the significance of HDAC2 sumoylation for p53 transcriptional activity (Brandl et al. 2012), the fraction of differently regulated proteins was screened for their dependence on p53 as a transcription factor using a record of 116 high-confidence p53-activated proteins that was compiled by (Fischer 2017) through examination of 16 high-throughput data sets, that studied p53 target genes in genome-wide analyses. Interestingly, Fischer concluded that p53 must be considered solely as transcriptional activator and not as repressor, for it was apparent that the clear majority of datasets exclusively identified target genes that were activated by p53 (Fischer 2017). This view is in accordance with further analyses of his group that challenge models of direct target gene repression by p53 and favor indirect suppression models that feature for instance p21 as mediator of p53 target gene repression (Fischer et al. 2014). Transferred to our proteome expression analysis, it is thus not surprising, that none of the 17 downregulated proteins in RKO HDAC2^{K462R} was identified as direct p53 target gene by (Fischer 2017). If their suppressed expression is related to the enhanced p53 activity in RKO HDAC2^{K462R}, it is more likely a result of enhanced p21 expression and subsequent signaling through the repressive p21-DREAM/RB pathway (Fischer et al. 2014; Engeland 2018). However, as only two of the upregulated proteins in RKO HDAC2^{K462R} could be identified as definite p53 target genes through comparison with Fischer's analysis (Fischer 2017), our proteome analysis suggests that the majority of protein upregulation in dependence of the loss of HDAC2 sumoylation is due to additional mechanisms that are independent of direct regulation by p53. Nevertheless, the two p53-activated proteins, the cell cycle regulator p21 (*CDKN1A*; nr. 32) and the ribonucleotide reductase p53R2 (*RRM2B*; nr. 24), were coincidentally also the only two proteins that were found by Fischer as most significantly regulated by p53 in 16 out of 16 datasets (Fischer 2017). Subsequent analysis of the molecular function of each of the 54 differentially regulated proteins provided candidates whose expression might have implications for 5-FU mediated DNA damage mechanisms, damage repair pathways, and general cytotoxicity. The first candidate is the class III NAD$^+$-dependent HDAC SIRT1 (*SIRT1*; nr. 39), whose expression was found to be 2-fold upregulated in RKO HDAC2^{K462R} cells (**Figure 55B**). This upregulation implies regulatory feedback loops between the deacetylases HDAC2 and SIRT1. Furthermore, SIRT1 activity is implicated in the regulation of DNA repair via BER as it interacts with TDG and modulates TDG activity through deacetylation (Madabushi et al. 2013). While deacetylated TDG has a higher activity for T/G, 5-formylcytosine/G, and 5-carboxycytosine/G, acetylated TDG has a higher activity for 5-FU/G mispairs (Madabushi et al. 2013). This would indicate reduced 5-FU excision rates in RKO HDAC2^{K462R} cells due to higher SIRT1 concentration. Hence, it has been theorized that low SIRT1 expression in CRC is tied to 5-FU resistance (Jang et al. 2012; Roos and Krumm 2016). However 5-FU excision by TDG is also associated with higher DNA damage than for instance excision by uracil DNA glycosylase (UDG) (Kunz et al. 2009). Thus, SIRT1 upregulation might in turn also protect RKO HDAC2^{K462R} from DNA damage by futile BER cycling. Moreover, HDAC2 sumoylation affected the expression of two structural components of the ribosome, RPS28 (*RPS28*; nr. 01) and RPL39 (*RPL39*; nr. 19). Whereas RPS28 was downregulated 2-fold in RKO HDAC2^{K462R}, RPL39 was upregulated 2-fold (**Figure 55**). In addition, a regulator of ribosomal assembly RRP12 (*RRP12*; nr. 18) was upregulated 2-fold in RKO HDAC2^{K462R} (**Figure 55B**). As other structural subunits of the ribosome have previously been shown to serve as inhibitors for HDM2 and to thus allow p53 activation in response to 5-FU-mediated ribosomal stress response, deregulation of RPS28 and RPL39 might have implications for 5-FU damage response (Sun et al. 2007). Moreover, misincorporation of FUTP into the diverse RNA types disrupts regular RNA function such as pre-rRNA processing, tRNA modification, pre-mRNA splicing, and mRNA polyadenylation (Longley et al. 2003). Additional differences in ribosome assembly due to the divergent expression of RPS28, RPL39, and RRP12 in RKO HDAC2^{K462R} might aggravate the toxicity of these RNA defects upon 5-FU treatment. Furthermore, expression levels of two proteins with direct implications in 5-FU metabolism were modulated: Expression of the ribonucleotide reductase p53R2 (*RRM2B*; nr. 24) was enhanced 2-fold, while expression of the nucleoside diphosphate kinase NME1 (*NME1*; nr. 02) was reduced 3-fold in RKO HDAC2^{K462R} cells (**Figure 55A, B**). p53R2 is a homologue of the small subunit of mammalian RNR and forms active RNR complexes with the RNR large subunit RRM1 to successfully catalyze the synthesis of deoxyribonucleotides. In contrast to its homologue RRM2, p53R2 expression is not restricted to mitosis and can be upregulated by p53 in response to DNA damage for repair in resting cells (Lozano and Elledge 2000; Tanaka et al. 2000; Guittet et al. 2001; Xue et al. 2003). Crucially, RNR complexes are also implicated in the conversion of FUDP to FdUDP (Aoki et al. 2013) and p53R2 upregulation in RKO HDAC2^{K462R} might thus enhance the abundance of FdUDP and potentially extend 5-FU mediated DNA damage. Difficulties to cope with this increased DNA damage, for instance due to additional defects in DNA repair, could consequently provoke the enhanced lethality of 5-FU in RKO HDAC2^{K462R} cells. Consistently, 5-FU resistant CRC cells displayed highly decreased RNR activity compared with non-resistant parental cells implicating that loss of RNR activity presents a protective mechanism to escape lethal DNA damage induction (Fukushima et al. 2001). NME1, on the other hand, is likewise involved in 5-FU metabolism. As its enzymatic activity is needed for the conversion of F(d)UDP to F(d)UTP, 3-fold downregulation of its expression implies that less nucleotides are available for integration into RNA and DNA (Muhale et al. 2011). However, loss of NME1 expression is counterintuitively associated with increased sensitivity towards 5-FU (Muhale et al. 2011). Additionally, NME1 upregulation has been reported in CRC patient tumor samples (Kidd et al. 2005) and in response to 5-FU treatment in breast cancer patients (Nordgard et al. 2008). Given that NME1 has various functions as transcription factor, transcriptional coregulator, and active participant in DSB repair alongside its kinase activity (Puts et al. 2017), it seems thus pointless to argue that NME1 downregulation influences RKO HDAC2^{K462R} sensitivity exclusively through loss of its kinase activity. Non-histone chromosomal protein HMG-14 (HMGN1; *HMGN1*; nr. 12), is downregulated 2-fold in RKO HDAC2^{K462R} cells (**Figure 55A**). High mobility group nucleosome-binding (HMGN) proteins destabilize and unfold heterochromatin and thereby improve DNA accessibility to facilitate repair (Reeves 2015). Albeit members of the HMGN protein family are mostly described for their role in the repair of UV-induced bulky DNA lesions via NER (Reeves and Adair 2005), HMGN1 also influences DSB repair in response to IR (Kim et al. 2008) and BER in response to MMS (Masaoka et al. 2012). Unfortunately, no studies have hitherto evaluated the value of HMGN1 expression for 5-FU cytotoxicity and DNA repair. Interestingly, HMGN1 has been shown to promote ATM activation in response to IR through modulation of histone H3 (H3K14) acetylation (Kim et al. 2008), which suggests functional interplay of HMGN1 and HDACs. Moreover, expression of the DNA helicase SMARCAD1 (*SMARCAD1*; nr. 11) was more than 4-fold decreased in RKO HDAC2^{K462R} (**Figure 55A**). SMARCAD1 is a member of the SNF2 helicase family and displays ATPase activity (Adra et al. 2000). SNF2 helicases serve as catalytical subunits of chromatin remodeling complexes, which are crucial regulators of DSB repair pathways (Brownlee et al. 2015; Rother and van Attikum 2017). Thus, HMGN1 and SMARCAD1 are implicated in the same regulatory mechanisms of chromatin structure, but contradictory reports exist as to whether these pathways affect each other or act independently (Hill et al. 2005; Rattner et al. 2009). In contrast to HMGN1, SMARCAD1 has a defined and essential role in HR as it has been shown to be recruited to DSBs to promote the initial HR step of 5’-3’ degradation of DNA ends (Costelloe et al. 2012). Furthermore, loss of SMARCAD1 affects IR-induced repair foci formation and DSB repair by HR (Chakraborty et al. 2018). In summary, the expression changes in the discussed proteins (RPS28, RPL39, RRP12, SIRT1, p53R2, NME1, HMGN1, SMARCAD1) might selectively, individually, or even in a collective fashion impact sensitivity of RKO HDAC2^{K462R} cells. Future analyses might thus comprise knockdown and overexpression experiments to evaluate the impact of RPS28, RPL39, RRP12, SIRT1, p53R2, NME1, and HMGN1 expression on 5-FU mediated toxicity. However, in consideration of the more than 4-fold reduced expression of SMARCAD1 in RKO HDAC2^{K462R} cells and its specific role in HR, subsequent analyses were thus far confined to the consequences of the loss of SMARCAD1 and potential further chromatin remodeling complex related helicases.

5.2.7 Expression of chromatin remodeling complex helicases in RKO HDAC2^{wt} and RKO HDAC2^{K462R}

Reduced expression of the DNA helicase SMARCAD1 in RKO HDAC2^{K462R} cells was confirmed by Western blot analysis (**Figure 56A**). Quantification of the Western blot signal intensity showed that SMARCAD1 expression was reduced almost 90% due to abrogation of HDAC2 sumoylation (**Figure 56B**). Albeit direct interaction and functional collaboration of SMARCAD1 and HDAC1/2 in chromatin remodeling complexes has been conjectured and described earlier (Jasencakova and Groth 2011; Mermoud et al. 2011; Rowbotham et al. 2011; Bi 2012; Al Kubaisy et al. 2016; Doiguchi et al. 2016), this clear regulation of SMARCAD1 expression by HDAC2, and specifically by a distinct PTM of HDAC2, is to our knowledge hitherto unreported. Noticeably, the significance of HDAC activity for the expression of chromatin remodeling factors has previously only once been suggested in a report that found a general depletion of BRD-containing proteins in HeLa cells in response to the HDACi VPA, NaB, and SAHA (Mackmull et al. 2015). The underlying mass spectrometric analysis showed downregulation of the BRD-containing chromatin remodeling factors hACF1 (*BAZ1A*), BAF180 (*PBRM1*), BRG1 (*SMARCA4*), BAZ1B (*BAZ1B*), and BRM (*SMARCA2*) (Mackmull et al. 2015). Our mass spectrometric analysis of global protein expression in murine renal cancer cells (see **4.1.2**, **5.1.2**) further validated the importance of HDAC class I activity for the expression of chromatin remodeling complexes. Central components of these complexes were found to be significantly downregulated in response to 48 h MS-275 treatment, including *Smarca1/5*, *Smarca2/4*, *Smarcad1*, *Smarcc1*, *Smarcc2*, *Smarcd1*, *Smarcd2*, *Smarce1*, *Baz1a/b*, *Baz2b*, *Arid1a/b*, *Arid2*, and *Actl6a/b* (Kiweler et al. 2018). Consequently, the GO terms *nucleosome disassembly* (GO:0006337), *nucleosome assembly* (GO:0006334), *chromosome organization* (GO:0051276), and *ATP-dependent chromatin remodeling* (GO:0043044) were found to be significantly regulated in the subsequent GO term enrichment analysis (**Figure 18**, **Table S 2**). Given these pleiotropic effects of HDAC class I activity and HDAC2 sumoylation on chromatin remodeling, expression levels of the two central SWI/SNF ATPases BRG1 (*SMARCA4*) and BRM (*SMARCA2*) were analyzed. Although expression of both ATPases was not quantifiable via mass spectrometry in RKO HDAC2^{wt} and RKO HDAC2^{K462R} cells, both proteins were detectable on Western blot (**Figure 57A**, **Figure S 24**). While BRM expression was not affected by HDAC2 sumoylation, BRG1 expression was strongly suppressed in RKO HDAC2^{K462R} cells to around 20% of the expression level in RKO HDAC2^{wt} (**Figure 57**, **Figure S 24**). Depletion of BRG1 is a crucial finding, as this helicase is a key catalytic component of the BAF and PBAF chromatin remodeling complex and thus exerts major roles in NHEJ and HR repair (Brownlee et al. 2015) (see **1.6.5**). Interestingly, studies showed that the BRM protein can be epigenetically silenced through posttranslational acetylation (Bourachot et al. 2003; Reisman et al. 2009). Accordingly, HDACi cause the accumulation of inactive, acetylated BRM (Bourachot et al. 2003; Glaros et al. 2007). Unaltered BRM expression in RKO HDAC2^{K462R} cells does thus not necessarily entail unchanged protein activity. As it is still unknown which HDACs are causally involved in this BRM inactivation (Reisman et al. 2009), it would be reasonable to prospectively resolve BRM acetylation and activity against the background of

HDAC2 sumoylation to clarify whether not only BRG1 but also BRM is silenced in RKO HDAC2^{K462R} cells. Notably, MS-275-treated tumor cell lines from various origins displayed reduced SMARCAD1 and BRG1 expression (**Figure 58**). ATPase depletion in response to abrogated HDAC2 sumoylation can thus be pharmacologically mimicked by HDACi. In addition, SMARCAD1 expression was also found to be affected by siRNA-mediated knockdown of HDAC2 (**Figure S 25**). However, HDAC2 siRNA mediated downregulation of SMARCAD1 was not as prominent as downregulation in RKO HDAC2^{K462R} or in response to HDACi (**Figure 56A**, **Figure 58D**, **Figure S 25**). Causative for this might be a compensatory effect of HDAC1 in the absence of HDAC2 expression, as seen in Renca cells (see **4.1.7**) and the literature (Jurkin et al. 2011). In contrast, sumoylation-deficient HDAC2 in RKO HDAC2^{K462R} might represent a dominant-negative protein isoform that does not trigger compensation by HDAC1. In summary, impairment of HDAC2 sumoylation results in the significant downregulation of the crucial DNA-helicases SMARCAD1 and BRG1. This effect can be mimicked by class I HDAC inhibition and partially by siRNA-mediated HDAC2 knockdown.

5.2.8 DNA damage response in 5-FU-treated RKO HDAC2^{wt} and RKO HDAC2^{K462R}

Due to the finding that the chromatin remodelers SMARCAD1 and BRG1 were crucially downregulated in 5-FU-sensitive RKO HDAC2^{K462R}, 5FU-associated DNA damage response was closer examined. DNA damage response is evoked by 5-FU via two of three of its cytotoxic mechanisms. On the one hand, FdUTP can be directly integrated into DNA. On the other hand, TS inhibition by FdUMP strongly diminishes dTTP concentration and augments dUTP integration into DNA (see **1.5.1**) (Longley et al. 2003). As both misincorporation mechanisms occur during DNA replication in S-phase, the central mediators of DNA damage response in S-phase, the PI3K-like kinases ATM and ATR, are thought to participate in sensing 5-FU mediated DNA damage (see **1.6.1**) (Wyatt and Wilson 2009; Smith et al. 2010). Fittingly, enhanced ATM Ser1981- and ATR Thr1989- phosphorylation indicated activation of the two kinases in response to 5-FU (**Figure 59**). Additionally, phosphorylation of the ATM and ATR downstream targets CHK1 and CHK2 was detectable (**Figure 59**, **Figure 61**). This upregulation was comparable at all time points in RKO HDAC2^{wt} and RKO HDAC2^{K462R}. FdUrd- and HU-mediated DNA damage in S-phase likewise led to comparable ATM, ATR, CHK1, and CHK2 activation in RKO HDAC2^{wt} and RKO HDAC2^{K462R} cells (**Figure 60**, **Figure 61**). As this shows that 5-FU-mediated nucleotide misincorporation was primarily sensed equally in RKO HDAC2^{wt} and RKO HDAC2^{K462R} cells, variations that account for divergent 5-FU sensitivity in these cell lines must occur in downstream damage repair pathways. Central DNA repair pathways responsible for the excision of misincorporated bases like 5-FU and uracil are the

BER and the MMR pathway. The latter would recognize misincorporated 5-FU and uracil as 5-FU:A and U:A mispairs or alternatively as 5-FU:G and U:G mispairs after cytosine deamination (Wyatt and Wilson 2009). However, in the RKO cell line, MMR is dispensable for 5-FU sensitivity as these cells display a hypermethylation of the *hMLH1* promoter. They thus lack expression of the central MMR protein MLH1, which confers a defect in MMR and renders RKO cells highly MSI (Suter et al. 2003; Vilar et al. 2008). Thus, in RKO cells, misincorporated 5-FU and uracil bases are likely exclusively excised by DNA glycosylases (e.g. UDG) during BER (Wyatt and Wilson 2009). However, downstream BER steps can presumably not convey faithful repair of the resulting AP sites and SSBs, as, during the final DNA resynthesis step, uracil or 5-FU are reintroduced into DNA due to high dUTP and 5-FU levels in the presence of TS* (see **1.6.2**) (Wyatt and Wilson 2009). The resulting futile cycling of BER gives increasing rise to unrepaired BER intermediates and has been shown to promote the generation of persistent DNA strand breaks due to 5-FU excision by TDG (Kunz et al. 2009). Consequently, HR is activated to deal with the repair of these lesions. Hence, disruption of HR leads to sensitization of CRC cells to genomically incorporated 5-FU (Huehls et al. 2016). Interestingly, failure to excise 5-FU and not uracil was the key determinant of 5-FU cytotoxicity in ovarian and CRC cell lines (Huehls et al. 2016). This finding indicates that specific inhibition of TS without additional DNA integration of fluorinated uracil is insufficient to profusely evoke maximum DNA damage. Furthermore, MMR deficiency might in part confer resistance towards 5-FU treatment by mediating a tolerance to the evoked DNA damage (Carethers et al. 1999; Meyers et al. 2001; Meyers et al. 2005; Wyatt and Wilson 2009). However, such a protective mechanism is solely applicable for low ranges of 5-FU mediated DNA damage, as higher DNA damage levels likely induce further surveillance pathways such as BER and HR (Liu et al. 2008). This would imply that the observed resistance of RKO HDAC2^{wt} cells towards 5-FU (**Figure 48A**) is mediated by MMR deficiency, while RNA integration does not significantly trigger cell death under the applied conditions. In turn, the sensitivity of RKO HDAC2^{K462R} cells (**Figure 48A**) might signify that DNA damage in this cell line exceeds the tolerated, MMR-deficiency-related threshold. Enhanced DNA damage in RKO HDAC2^{K462R} could possibly stem from additional alterations in BER and HR in response to the selective loss of specific HDAC2 activity. In agreement with this DNA damage threshold hypothesis, both RKO cell lines respond with similar sensitivity to treatment with FdUrd (**Figure 48B**), which indicates that FdUrd concentrations suffice to exceed the MMR-mediated DNA damage threshold in both cell lines. Higher nominal DNA damage in FdUrd-treated RKO cells, than in RKO cells that were treated with equimolar concentrations of 5-FU, is plausible, as in contrast to 5-FU, FdUrd molecules are almost entirely bound by TS or integrated into DNA while RNA integration is negligible. To test this threshold hypothesis, it would, as already proposed in **5.2.3**, be expedient to directly assess and quantify DNA damage in response to both fluoropyrimidines by COMET assay or to determine FdUTP and FUTP integration into DNA and RNA by HPLC-MS (Noordhuis et al. 2004). Markedly, studies do not convey any hints on a role of the NER pathway for prognosis after 5-FU treatment in CRC. This is consistent with the knowledge that the NER pathway mainly targets bulky, helix distorting DNA lesions (Kap et al. 2016). Repair via the NER pathway, was thus not included in deeper assessment throughout this discussion. Of notice, phosphorylation of CHK1 was especially induced by FdUrd-treatment after 16 and 24 h in both cell lines (**Figure 61**). This finding explains the lack of p21 upregulation in these S-phase-arrested cell (**Figure 52**, **Figure S 19**), as CHK1 activity obstructs transcriptional elongation of p21 mRNA during an arrest of DNA replication (Beckerman et al. 2009). In summary, initial DNA damage recognition in both cell lines was comparable in response to the various stimuli. This implies that downstream DNA repair pathways such as BER and HR are differentially regulated in dependence of HDAC2 sumoylation.

5.2.9 Effect of HDAC2^{K462R} expression on γH2AX formation

Phosphorylation of the histone H2A variant H2AX in response to the generation of DNA SSBs and DSBs is mediated by the kinases ATM and ATR (Smith et al. 2010). The resulting Ser-139 phosphorylated H2AX is termed γH2AX and serves as anchor point for the subsequent localization of essential components of the DNA damage response to the vicinity of strand breaks (Fernandez-Capetillo et al. 2004). Albeit migration of repair factors to damage sites is not abrogated in H2AX$^{-/-}$ cells, stable formation of essential irradiation induced foci (IRIF) is impeded in these cells, which indicates the importance of γH2AX formation for the local concentration of specific repair proteins and consecutive efficacy of DNA repair (Celeste et al. 2003; Fernandez-Capetillo et al. 2004). Accordingly, formation of extensive γH2AX domains in the DNA is established as quantitative and qualitative marker for strand break induction and successive repair (Rogakou et al. 1998; Rothkamm and Löbrich 2003). Effective phosphorylation of H2AX relies on chromatin remodeling complexes and especially on the activity of their core helicase subunits (Kwon et al. 2015). Chromatin remodeling complex helicases thus enable DNA repair processes and prevent apoptosis in response to genotoxic stress (Kwon et al. 2015). In this mechanism, abrogation of γH2AX formation due to downregulation of helicase expression is not accompanied by defects in the expression and activation of ATM, ATR, and DNA-PK (Kwon et al. 2015). This is consistent with the results in **4.2.8** that reveal no differences in ATM and ATR activation and signaling between RKO HDAC2^{wt} and RKO HDAC2^{K462R} cells. Analysis of γH2AX formation in response to 5-FU revealed significantly reduced phosphorylation in HDAC2 sumoylation-deficient cells (**Figure 62**, **Figure S 26**). The same effect was observed upon FdUrd and HU treatment (**Figure 63**). Accordingly, this comparatively reduced induction of H2AX phosphorylation in RKO HDAC2^{K462R} cells might be caused by the lowered expression of SMARCAD1 and BRG1 in this cell line (**Figure 56**, **Figure 57**). Surprisingly, lower levels of γH2AX were detected in 5-FU sensitive RKO HDAC2^{K462R} cells despite cell death induction and the associated DNA fragmentation (**Figure 48A**). Concurrent treatment with the caspase inhibitor Z-VAD-FMK proved that lower γH2AX levels did not result from apoptotic protein decay (**Figure 64**). Unfortunately, γH2AX detection at earlier timepoints was not successful in multiple Western blot experiments as γH2AX was not sufficiently induced to be reliably detectable (**Figure S 27**). These findings indicate that the loss of helicase expression in RKO HDAC2^{K462R} cells does have an impact on γH2AX formation comparable to data in the literature (Kwon et al. 2015).

5.2.10 Immunofluorescence analysis of H2AX phosphorylation and 53BP1 foci in dependence of SMARCAD1, HDAC2, and BRG1 expression

Loss of BRG1 activity or ectopic BRG1 expression were previously shown to inhibit γH2AX formation, to hamper 53BP1 localization to DSB sites, and to result in radiosensitization due to impairment of DSB repair (Park et al. 2006; Park et al. 2009; Kwon et al. 2015). Thus, in consideration of the strong reduction of BRG1 and additionally of SMARCAD1 expression in RKO HDAC2^{K462R} cells, it had to be expected, that a varying induction of γH2AX and 53BP1 foci would be measurable in RKO HDAC2^{wt} and RKO HDAC2^{K462R} cells upon DNA damage induction. In a first immunofluorescence experiment, RKO HDAC2^{wt} cells were transfected with siRNA directed against BRG1 and SMARCAD1 and subsequently treated with 5-FU (**Figure 65**). In contrast to previously published data by others (Park et al. 2006; Lee et al. 2010a; Kwon et al. 2015), the specific reduction of BRG1 and SMARCAD1 expression did not significantly reduce γH2AX formation in response to 5-FU-induced DNA damage (**Figure 65**). The observed reduction of γH2AX in RKO HDAC2^{K462R} cells in response to 5-FU (**Figure 62**, **Figure S 26**) can thus not be mimicked by distinct abrogation of SMARCAD1 and BRG1 expression in RKO HDAC2^{wt} cells. This finding implies that further differences in protein expression in both cell lines are essential for downregulation of γH2AX formation in response to 5-FU. These additional factors might for instance include any of the discussed candidate proteins that were found to be differentially regulated in both cell lines (**4.2.6**). Moreover, none of the published works describing the negative effect of either BRG1 or SMARCAD1 knockdown on H2AX phosphorylation was performed in CRC cells. In consideration of the fact that around 19% of tumors are mutated in different SWI/SNF subunits, RKO cells might differ from the hitherto described cell lines in the extent of their dependence on BRG1 and/or SMARCAD1 expression for effective DNA repair (Kadoch et al. 2013). Furthermore, as the time-dependency of DNA damage induction by 5-FU and the relative abundance of distinct DNA damage lesions are still not fully elucidated, the kinetics of γH2AX formation in combination with other repair markers, such as ATM, ATR, RPA, and 53BP1 should prospectively be assessed. Additionally, quantification of γH2AX was complicated by diffuse fluorescence staining due to the lack of distinct foci in response to 5-FU (**Figure 65**, **Figure S 28**). Hence, IR was used in the subsequent experiments. In contrast to 5-FU, IR is a commonly applied stimulus in the research of DNA damage response because of its precise induction of distinct DSB repair foci (Vignard et al. 2013). Accordingly, RKO HDAC2^{wt} and RKO HDAC2^{K462R} cells were subjected to IR. Both cell lines displayed a comparable mean fluorescence signal of γH2AX and equal amounts of γH2AX foci per cell (Figure **66A**, **B**, **Figure S 29**, **Figure S 30**). In contrast, 53BP1 foci formation differed and was slightly but nevertheless significantly diminished in RKO HDAC2^{K462R} (Figure **66A**, **C**). This finding indicates that BRG1 and SMARCAD1 deficiency, in conjunction with possible other DNA damage signaling alterations in RKO HDAC2^{K462R} cells, does impact DSB repair in response to IR. In addition, γH2AX and 53BP1 foci formation was determined by immunofluorescence in response to IR and BRG1 and/or SMARCAD1 knockdown in RKO HDAC2^{wt} cells (**Figure 67**, **Figure S 31**). Foci formation of γH2AX and 53BP1 was effectively induced by IR and colocalization of both DSB markers was apparent (**Figure 67**, **Figure S 31**). Quantification of γH2AX mean fluorescence and 53BP1 foci formation revealed slight but significant differences (**Figure 68**). Single knockdown of BRG1 led to an induction of γH2AX mean fluorescence and had no impact on 53BP1 foci formation in response to IR (**Figure 68**). In contrast, knockdown of SMARCAD1 did not affect γH2AX mean fluorescence but reduced 53BP1 foci formation in irradiated samples (**Figure 68**). Concerning this effect of SMARCAD1 depletion, it must be considered that SMARCAD1 knockdown also reduced basal 53BP1 foci formation (**Figure 68**). Strikingly, combined depletion of BRG1 and SMARCAD1 reduced γH2AX mean fluorescence as well as 53BP1 foci formation in response to IR (**Figure 68**). Mean γH2AX fluorescence was reduced from 3.59×10^5 AU to 3.19×10^5 AU from mock transfected to SMARCAD1- and BRG1-depleted samples. Considering that under both conditions basal γH2AX fluorescence was similar with 2.21×10^5 AU and 2.26×10^5 AU, the absolute reduction of 0.4×10^5 AU in response to SMARCAD1 and BRG1 depletion equates to a reduction of around 30% of the maximal IR-induced increase in γH2AX fluorescence (2.21×10^5 AU to 3.59×10^5 AU) in mock transfected cells. In addition, mean 53BP1 foci were reduced from 11.23 foci per cell to 8.70 foci per cell in response to SMARCAD1 and BRG1 depletion. Again, considering that basal 53BP1 foci formation was similar at both conditions with 3.67 foci per cell and 3.74 foci per cell, the reduction of 2.53 foci per cell in response to helicase depletion equates to a reduction of around 30% of the maximal IR induced increase in 53BP1 foci formation (3.67 foci per cell to 11.23 foci per cell) in mock transfected cells. Hence, γH2AX and 53BP1 were reduced to a comparable extent (- 30 %) in response to IR by the depletion of SMARCAD1 and BRG1. Optimization of IR dose and analysis timepoint might allow for improved visualization of this effect. In addition, the inhibition of DNA damage signaling due to combined BRG1 and SMARCAD1 depletion might not only be a quantitative effect but might also include different kinetics of H2AX-phosphorylation and -dephosphorylation as well as varying kinetics of the association and dissociation of other repair factors, such as 53BP1, RPA, BRCA1, and RAD51. For instance, knockdown of BRG1 by siRNA significantly reduced the initial induction of γH2AX foci in etoposide-treated U2OS cells and led to the persistence of these unrepaired foci over time (Qi et al. 2015). Strikingly, the enhanced initial γH2AX foci formation and subsequent repair kinetics in BRG1-proficient cells resulted in the observation that γH2AX levels were equivalent in BRG1-deficient and -proficient cells at intermediate timepoints (Qi et al. 2015). Furthermore, recently published data show, that loss of SMARCAD1, in contrast to loss of BRG1, might not result in an abrogation of γH2AX foci formation, but instead lead to prolonged retention of IR induced γH2AX foci (Chakraborty et al. 2018). Interpretation of γH2AX formation in RKO HDAC2^{K462R} cells might be complicated by these contrary effects of BRG1 and SMARCAD1 depletion on γH2AX kinetics. Moreover, as 53BP1 rapidly localizes to IR induced DSBs (Asaithamby and Chen 2009), highest 53BP1 foci formation might occur earlier than 1 h post IR. Hence, prospective determination of repair kinetics by assessing the expression and focal localization of various DNA repair proteins and their modifications seems to be indispensable to draw final and reliable conclusions. It might also be promising to combine SMARCAD1 and BRG1 knockdown with the stimulation of p53 activity by nutlin-3 treatment to more accurately mimic the RKO HDAC2^{K462R} phenotype. Furthermore, the present immunofluorescence protocol could be adjusted to improve transfection efficiency at the time point of irradiation. Hitherto, neither SMARCAD1 nor BRG1 depletion by siRNA was effective enough to mimic the extensive loss of expression that was observed in RKO HDAC2^{K462R} (**Figure 56**, **Figure 57**, **Figure S 32**). However, efficiency of BRG1 knockdown seems to depend on SMARCAD1 expression as a loss of SMARCAD1 resulted in an upregulation of BRG1 (**Figure S 32D**). This feedback mechanism causes a decrease of BRG1 knockdown efficiency from 50% upon single transfection to 25% upon combinatorial transfection (**Figure S 32A**). It might hence be difficult to enhance BRG1 transfection efficiency in combinatorial knockdown samples by accelerating siRNA concentration. Additional staining of immunofluorescence samples with primary antibodies against SMARCAD1 and BRG1 might provide a solution to allow the discrimination of helicase expressing cells throughout the quantitative analysis of γH2AX and 53BP1. In summary, these findings further indicate distinct alterations in DNA damage response in CRC cells upon downregulation of BRG1 and SMARCAD1 expression. However, prospective experiments assessing further repair factors and time kinetics are needed to fully evaluate the extent and impact of these alterations.

5.2.11 Effects of SMARCAD1, HDAC2, and BRG1 knockdown on cell death induction in HCT116, RKO, and RKO HDAC2^{wt}

Data in the literature indicates that single loss of SMARCAD1 or BRG1 expression are both sufficient to impair DNA damage recognition and repair and to sensitize diverse cell lines to DNA damage inducing drugs (Park et al. 2006; Zhang et al. 2009; Lee et al. 2010a; Costelloe et al. 2012; Kothandapani et al. 2012; O'Donnell et al. 2012; Kwon et al. 2015; Qi et al. 2015; Smith-Roe et al. 2015; Chakraborty et al. 2018). To examine the reproducibility of these data in our cell system, wild-type HDAC2-proficient CRC cells (HCT116 and RKO) were depleted for SMARCAD1 and/or HDAC2 and RKO HDAC2^{wt} were depleted for BRG1 and/or SMARCAD1 by siRNA-mediated knockdown. Effective knockdown of HDAC2 and SMARCAD1 in HCT116 and RKO cells and of SMARCAD1 and BRG1 in RKO HDAC2^{wt} was confirmed by Western blot (**Figure 69**, **Figure S 33**). Analysis of cell death induction revealed that neither individual nor combinatorial knockdown of SMARCAD1 and HDAC2 sensitized RKO or HCT116 cells to 5-FU or FdUrd treatment (**Figure 70**). Furthermore, neither single nor combinatorial reduction of SMARCAD1 and BRG1 did sensitize RKO HDAC2^{wt} cells to 5-FU or FdUrd (**Figure 71**, **Figure S 34**).These negative findings indicate for instance that, in contrast to data in the literature, the single loss of SMARCAD1 activity does not sensitize CRC cells to genotoxic damage. As previous experiments showed that only combined knockdown of SMARCAD1 and BRG1 was effective to introduce changes in IR mediated γH2AX and 53BP1 foci formation (**Figure 68**), one could assume that HCT116 and RKO cells might compensate the loss of SMARCAD1 by BRG1 activity. However, the finding that RKO HDAC2^{wt} cells were not sensitized by combinatorial knockdown of SMARCAD1 and BRG1 (**Figure 71**) contradicts this assumption. Interestingly, a recent study identified SMARCAD1 as an accessory factor in MMR. SMARCAD1 is recruited to mismatch-carrying DNA in an MSH2-dependent and MLH1-independent fashion and thereby enables the repair of mismatches in DNA-nucleosome complexes (Terui et al. 2018). RKO and HCT116 cells are MMR-deficient through loss of MLH1 activity and the loss of SMARCAD1 expression might thus have more extensive consequences in cells that rely on MMR as repair mechanism. Hence, the impact of SMARCAD1 depletion on 5-FU sensitivity could prospectively be examined in MMR-deficient HCT116 and MMR-proficient HCT116/3+6 cells, in which chromosome 3 containing the wild-type MLH1 was partially reintroduced (Vernole et al. 2011). Furthermore, with 28 SWI/SNF complex related genes known hitherto, determination of DNA repair mechanisms in CRC cells by other chromatin remodeling helicase family members, either in general or compensatory in the absence of BRG1 and/or SMARCAD1, are plausible (Kadoch et al. 2013). SWI/SNF complexes are constituted out of at least 14 core and accessory subunits, which indicates that in different cell lines, more than just the expression level of the central helicase subunit might determine cell fate decisions (Kadoch et al. 2013). Moreover, studies examining mutation frequencies of SWI/SNF subunits by means of whole-genome and exome sequencing show, that these subunits are mutated in high frequency in primary tumor tissues (Kadoch et al. 2013). Such mutations in chromatin remodeling complex subunits in CRC cells might additionally alter the consequences of reduced SMARCAD1 and/or BRG1 expression and account for the unexpected lack of sensitization to 5-FU-mediated DNA damage. Fittingly, cell lines in the discussed studies derived from embryonic fibroblasts, NSCLC, cervix adenocarcinoma, adrenal gland carcinoma, embryonic kidney, osteosarcoma, head and neck squamous carcinoma, breast adenocarcinoma, and lung carcinoma (Park et al. 2006; Zhang et al. 2009; Lee et al. 2010a; Costelloe et al. 2012; Kothandapani et al. 2012; Kwon et al. 2015; Qi et al. 2015; Smith-Roe et al. 2015; Chakraborty et al. 2018) and only one study was using the MMR-proficient colorectal adenocarcinoma cell line HT29 to demonstrate the effects of reduced BRG1 expression on the cytotoxicity of IR (Kwon et al. 2015). However, results in this study were achieved by ectopic overexpression of the bromodomain of BRG1 and are thus not reliably comparable to the knockdown experiments in this work. In addition, cell survival in response to the different stimuli in these studies was mainly determined by clonogenic survival assay. In comparison to cell death measurement using flow cytometry, this technique is focused on the reproductive viability rather than the immediate cell death induction in response to a stimulus. It thus allows to determine prolonged effects of genomic instability resulting from impaired DNA damage repair. A rerun of BRG1 and SMARCAD1 knockdown experiments in RKO HDAC2^{wt} cells and the assessment of colony formation ability might thus serve to undoubtedly achieve or exclude reproducibility of the published results. In addition, one or more of the other candidate proteins (RPS28, RPL39, RRP12, SIRT1, p53R2, NME1, HMGN1) (see **5.2.6**) could play a role in 5-FU toxicity. In addition, 5-FU-mediated RNA damage might be a major determinant of toxicity in RKO HDAC2^{K462R}, while 5-FU-mediated DNA-damage and even defects in DNA damage repair are neglectable (Pettersen et al. 2011). Otherwise, it is conceivable that a combination of the increased p53 proapoptotic target gene expression and the BRG1- and SMARCAD1-mediated DNA damage repair defects in RKO HDAC2^{K462R} is essential to enhance cell death in response to 5-FU. Future experiments including a combination of SMARCAD1 and BRG1 knockdown with nutlin-3 treatment might thus be successful to mimic the RKO HDAC2^{K462} phenotype and sensitize RKO HDAC2^{wt} cells. Interestingly, depletion of HDAC2 did neither sensitize HCT116 nor RKO cells (**Figure 70**). This finding further indicates that HDAC2^{K462R} represents a dominant-negative isoform of HDAC2 whose effects on cell fate could not be phenocopied by outright loss of HDAC2 expression.

5.2.12 HDACi and fluoropyrimidines: Combinatorial treatment as well as reversibility by Urd administration

Since HDAC2 sumoylation is so far not specifically targetable by pharmacologic intervention, the application of specific HDAC class I inhibitors represents the sole clinically relevant strategy to mimic the effects that were observed in the HDAC2^{K462R} mutant expressing CRC system. This approach is promising as the downregulation of the helicases BRG1 and SMARCAD1, that was seen in response to HDAC2^{K462R} expression and was shown to partially impair the IR-induced damage response, has also been detected in response to treatment with the HDACi MS-275 (**Figure 56**, **Figure 57**, **Figure 58**, **Figure 68**). RKO cells, that endogenously express HDAC2, were thus treated with 5-FU, FdUrd, and MS-275 and cell death was analyzed by flow cytometry. In contrast to data in the literature (Flis et al. 2010; Noro et al. 2010; Okada et al. 2016; Huang et al. 2017), HDAC inhibition did not sensitize RKO cells to 5-FU (**Figure 72A**). The observed combinatorial effect on cell death induction was merely additive and cell death was not significantly higher than in 5-FU single treatment (**Figure 72A**). In stark contrast, HCT116 cells were significantly sensitized towards 5-FU by MS-275 (**Figure S 35**). The divergent cell death induction in these two cell lines might stem from the finding that RKO cells, on the one hand, fail to increase Wnt-signaling via β-catenin dephosphorylation in response to HDACi (Bordonaro et al. 2007). On the other hand, HCT116 cells strongly induce this dephosphorylation of β-catenin and subsequently execute apoptosis through activation of Wnt-signaling (Bordonaro et al. 2007). Equivalent effects are observable upon FdUrd treatment in both cell lines. Whereas HCT116 cells were clearly sensitized to FdUrd by MS-275, RKO cells displayed no additive toxicity after combinatorial treatment (**Figure S 35**, **Figure 72**). Furthermore, it is still not fully understood to which extent RNA- and DNA-damaging 5-FU mechanisms contribute to overall cytotoxicity. On the one hand, it has been shown, that 5-FU integration into RNA occurs at 3.000- to 15.000-fold higher levels than integration into DNA in HeLa and SW480 cells and thus dominates cytotoxicity in these cells (Pettersen et al. 2011). This misincorporation into RNA may disrupt RNA function such as pre-rRNA processing, tRNA modification, pre-mRNA splicing, and mRNA polyadenylation (Longley et al. 2003). On the other hand, depletion of the HR protein XRCC2 (Zhang et al. 2017) as well as of the BER glycosylase SMUG1 (An et al. 2007) efficiently sensitizes to 5-FU-mediated DNA damage. Additionally, the development of 5-FU resistance in ovarian cancer *in vivo* is associated with decreased levels of integrated 5-FU in DNA (Chu et al. 1990). Strikingly, these controversial reports present just an excerpt of a multitude of data dealing with the relative contributions of RNA- and DNA-damaging 5-FU mechanisms. Thus, the reversibility of 5-FU cytotoxicity by addition of the nucleoside Urd was assessed in RKO cells. This approach has been frequently used to practically estimate whether 5-FU cytotoxicity can be abolished through reversion of FUTP integration into RNA by excessive Urd (Kufe and Major 1981; Pritchard et al. 1997;

Longley et al. 2002; Pettersen et al. 2011). Urd resulted in the significant reduction of 5-FU-mediated cell death induction (-75%) (**Figure 72**). In contrast, FdUrd-mediated cell death was not significantly reverted by Urd (-25%) (**Figure 72**). The effects were equally observable upon additional HDAC inhibition and thus independent of class I HDAC inhibition (**Figure 72**). In addition, RKO HDAC2^{K462R} cells were treated with combinations of 5-FU, FdUrd, and Urd (**Figure 73**). Comparable to RKO cells, 5-FU toxicity (- 60%), but not FdUrd toxicity (- 6%), was reverted by Urd in RKO HDAC2^{K462R} cells (**Figure 73**).To exclude that excessive Urd did not additionally revert DNA-damage due to enhanced substrate availability for TS and subsequent abrogation of TS inhibition, TS* formation was assessed in HCT116 and RKO cells (**Figure S 37**). Sole treatment with 5-FU and FdUrd led to effective inhibition of TS that was only marginally reduced by Urd in 5-FU-treated samples (**Figure S 37**). This finding indicates stable TS inhibition and dTTP-depletion upon both fluoropyrimidines. Additionally, FUrd, a second metabolite of 5-FU, was included in this experiment. In contrast to 5-FU and FdUrd, FUrd is described as a mimetic of 5-FU-mediated RNA damage (Longley et al. 2003; Pettersen et al. 2011). However, FUrd-treatment inhibited TS as efficiently as 5-FU and FdUrd (**Figure S 37**). As FUrd thus most likely exerts dTTP depletion and DNA damage comparable to the other two fluoropyrimidines, it can prospectively not be employed to study the RNA damage of 5-FU. Interestingly, TS inhibition upon FUrd was revertible by Urd (**Figure S 37**). This finding suggests that TS inhibition is likely achieved by 5-FU, FUrd, and FdUrd through two distinct metabolic pathways. First, 5-FU is conversed to FdUrd by TP. Whereas the inhibitory metabolite FdUMP is then build up from FdUrd through phosphorylation by TK, FdUMP from FUrd is generated through a multi-step process via RNR and finally arises from dephosphorylation of FdUDP (see **1.5.1**). It is thus possible, that Urd specifically prohibits the conversion of FUrd to FdUMP but not the conversion of 5-FU and FdUrd. In summary, the observed prevention of cell death by Urd demonstrates that the toxicity of 5-FU, but not of FdUrd, is mediated to a significant proportion by RNA-damage. This explanation is further affirmed by the exclusion of negative effects of excessive Urd on TS inhibition. RNA-associated toxicity of 5-FU explains why the downregulation of the DNA helicases BRG1 and SMARCAD1 affected DNA damage signaling but did simultaneously not suffice to sensitize CRC cells to 5-FU (**Figure 62**, **Figure 66**, **Figure 68**, **Figure 70**, **Figure 71**). Unfortunately, 5-FU is thus not a suitable stimulus to further examine the unveiled defects in DNA damage repair in response to the downregulation of central chromatin remodeling helicases in HDAC2 sumoylation-deficient RKO cells. Although constant TS inhibition upon 5-FU nevertheless implies persistent, yet nontoxic, DNA damage, future experiments should employ definite DNA-damaging stimuli such as IR to mechanistically affirm the implications of HDAC2 sumoylation in DNA damage pathways. Furthermore, sensitization of RKO HDAC2^{K462R} to 5-FU suggests a role for HDAC2 sumoylation in RNA-damage signaling that should be further investigated.

6 References

Abbas T, Dutta A. 2009. p21 in cancer: intricate networks and multiple activities. *Nat Rev Cancer* **9**: 400.

Adams H, Fritzsche FR, Dirnhofer S, Kristiansen G, Tzankov A. 2010. Class I histone deacetylases 1, 2 and 3 are highly expressed in classical Hodgkin's lymphoma. *Expert Opin Ther Targets* **14**: 577-584.

Adra CN, Donato J-L, Badovinac R, Syed F, Kheraj R, Cai H, Moran C, Kolker MT, Turner H, Weremowicz S et al. 2000. SMARCAD1, a Novel Human Helicase Family-Defining Member Associated with Genetic Instability: Cloning, Expression, and Mapping to 4q22–q23, a Band Rich in Breakpoints and Deletion Mutants Involved in Several Human Diseases. *Genomics* **69**: 162-173.

Agrawal A, Sahni S, Iftikhar A, Talwar A. 2015. Pulmonary manifestations of renal cell carcinoma. *Respir Med* **109**: 1505-1508.

Al Kubaisy E, Arafat K, De Wever O, Hassan AH, Attoub S. 2016. SMARCAD1 knockdown uncovers its role in breast cancer cell migration, invasion, and metastasis. *Expert Opin Ther Targets* **20**: 1035-1043.

Alao JP, Stavropoulou AV, Lam EW, Coombes RC, Vigushin DM. 2006. Histone deacetylase inhibitor, trichostatin A induces ubiquitin-dependent cyclin D1 degradation in MCF-7 breast cancer cells. *Mol Cancer* **5**: 8.

Alberts SR, Sargent DJ, Nair S, Mahoney MR, Mooney M, Thibodeau SN, Smyrk TC, Sinicrope FA, Chan E, Gill S et al. 2012. Effect of oxaliplatin, fluorouracil, and leucovorin with or without cetuximab on survival among patients with resected stage III colon cancer: a randomized trial. *JAMA* **307**: 1383-1393.

Allegra CJ, Yothers G, O'Connell MJ, Sharif S, Petrelli NJ, Lopa SH, Wolmark N. 2013. Bevacizumab in stage II-III colon cancer: 5-year update of the National Surgical Adjuvant Breast and Bowel Project C-08 trial. *J Clin Oncol* **31**: 359-364.

Allis CD, Berger SL, Cote J, Dent S, Jenuwien T, Kouzarides T, Pillus L, Reinberg D, Shi Y, Shiekhattar R et al. 2007. New Nomenclature for Chromatin-Modifying Enzymes. *Cell* **131**: 633-636.

An Q, Robins P, Lindahl T, Barnes DE. 2007. 5-Fluorouracil incorporated into DNA is excised by the Smug1 DNA glycosylase to reduce drug cytotoxicity. *Cancer Res* **67**: 940-945.

Andre T, de Gramont A, Vernerey D, Chibaudel B, Bonnetain F, Tijeras-Raballand A, Scriva A, Hickish T, Tabernero J, Van Laethem JL et al. 2015. Adjuvant Fluorouracil, Leucovorin, and Oxaliplatin in Stage II to III Colon Cancer: Updated 10-Year Survival and Outcomes According to BRAF Mutation and Mismatch Repair Status of the MOSAIC Study. *J Clin Oncol* **33**: 4176-4187.

Aoki Y, Sakogawa K, Hihara J, Emi M, Hamai Y, Kono K, Shi L, Sun J, Kitao H, Ikura T et al. 2013. Involvement of ribonucleotide reductase-M1 in 5-fluorouracilinduced DNA damage in esophageal cancer cell lines. *Int J Oncol* **42**: 1951-1960.

Aran V, Victorino AP, Thuler LC, Ferreira CG. 2016. Colorectal Cancer: Epidemiology, Disease Mechanisms and Interventions to Reduce Onset and Mortality. *Clin Colorectal Cancer* **15**: 195-203.

Asaithamby A, Chen DJ. 2009. Cellular responses to DNA double-strand breaks after low-dose gamma-irradiation. *Nucleic Acids Res* **37**: 3912-3923.

Ashburner M, The Gene Ontology C, Ball CA, Blake JA, Botstein D, Butler H, Cherry JM, Davis AP, Dolinski K, Dwight SS et al. 2000. Gene Ontology: tool for the unification of biology. *Nat Genet* **25**: 25-29.

Ashktorab H, Belgrave K, Hosseinkhah F, Brim H, Nouraie M, Takkikto M, Hewitt S, Lee EL, Dashwood RH, Smoot D. 2009. Global histone H4 acetylation and HDAC2 expression in colon adenoma and carcinoma. *Dig Dis Sci* **54**: 2109-2117.

Awasthi P, Foiani M, Kumar A. 2015. ATM and ATR signaling at a glance. *J Cell Sci* **128**: 4255-4262.

Aydin ÖZ, Vermeulen W, Lans H. 2014. ISWI chromatin remodeling complexes in the DNA damage response. *Cell Cycle* **13**: 3016-3025.

Azzam EI, Jay-Gerin J-P, Pain D. 2012. Ionizing radiation-induced metabolic oxidative stress and prolonged cell injury. *Cancer Lett* **327**: 48-60.

Bangert A, Cristofanon S, Eckhardt I, Abhari BA, Kolodziej S, Hacker S, Vellanki SH, Lausen J, Debatin KM, Fulda S. 2012. Histone deacetylase inhibitors sensitize glioblastoma cells to TRAIL-induced apoptosis by c-myc-mediated downregulation of cFLIP. *Oncogene* **31**: 4677-4688.

Barneda-Zahonero B, Parra M. 2012. Histone deacetylases and cancer. *Mol Oncol* **6**: 579-589.

Batlle E, Sancho E, Franci C, Dominguez D, Monfar M, Baulida J, Garcia De Herreros A. 2000. The transcription factor snail is a repressor of E-cadherin gene expression in epithelial tumour cells. *Nat Cell Biol* **2**: 84-89.

Beckerman R, Donner AJ, Mattia M, Peart MJ, Manley JL, Espinosa JM, Prives C. 2009. A role for Chk1 in blocking transcriptional elongation of p21 RNA during the S-phase checkpoint. *Genes Dev* **23**: 1364-1377.

Beltrao P, Bork P, Krogan NJ, Noort V. 2013. Evolution and functional cross-talk of protein post-translational modifications. *Mol Syst Biol* **9**: 714.

Berger FG, Berger SH. 2006. Thymidylate synthase as a chemotherapeutic drug target: where are we after fifty years? *Cancer Biol Ther* **5**: 1238-1241.

Beyer M, Kiweler N, Mahboobi S, Krämer OH. 2017. How to Distinguish Between the Activity of HDAC1-3 and HDAC6 with Western Blot. *Methods Mol Biol* **1510**: 355-364.

Bhalla S, Evens AM, Prachand S, Schumacker PT, Gordon LI. 2013. Paradoxical regulation of hypoxia inducible factor-1alpha (HIF-1alpha) by histone deacetylase inhibitor in diffuse large B-cell lymphoma. *PLoS One* **8**: e81333.

Bi X. 2012. Functions of chromatin remodeling factors in heterochromatin formation and maintenance. *Science China Life Sciences* **55**: 89-96.

Bienz M. 2005. β-Catenin: A Pivot between Cell Adhesion and Wnt Signalling. *Curr Biol* **15**: R64-R67.

Biterge B, Schneider R. 2014. Histone variants: key players of chromatin. *Cell Tissue Res* **356**: 457-466.

Blackford AN, Jackson SP. 2017. ATM, ATR, and DNA-PK: The Trinity at the Heart of the DNA Damage Response. *Mol Cell* **66**: 801-817.

Blaheta RA, Michaelis M, Driever PH, Cinatl J, Jr. 2005. Evolving anticancer drug valproic acid: insights into the mechanism and clinical studies. *Med Res Rev* **25**: 383-397.

Bolden JE, Shi W, Jankowski K, Kan CY, Cluse L, Martin BP, MacKenzie KL, Smyth GK, Johnstone RW. 2013. HDAC inhibitors induce tumor-cell-selective pro-apoptotic transcriptional responses. *Cell Death Dis* **4**: e519.

Booth L, Roberts JL, Poklepovic A, Dent P. 2018. Prior exposure of pancreatic tumors to [sorafenib + vorinostat] enhances the efficacy of an anti-PD-1 antibody. *Cancer Biol Ther*: 1-13.

Bordonaro M, Lazarova DL, Sartorelli AC. 2007. The activation of beta-catenin by Wnt signaling mediates the effects of histone deacetylase inhibitors. *Exp Cell Res* **313**: 1652-1666.

Bosshard M, Markkanen E, van Loon B. 2012. Base Excision Repair in Physiology and Pathology of the Central Nervous System. *IJMS* **13**: 16172.

Bourachot B, Yaniv M, Muchardt C. 2003. Growth inhibition by the mammalian SWI-SNF subunit Brm is regulated by acetylation. *EMBO J* **22**: 6505-6515.

Brabletz T. 2012. To differentiate or not — routes towards metastasis. *Nat Rev Cancer* **12**: 425.

Bradford MM. 1976. A rapid and sensitive method for the quantitation of microgram quantities of protein utilizing the principle of protein-dye binding. *Anal Biochem* **72**: 248-254.

Bradner JE, Mak R, Tanguturi SK, Mazitschek R, Haggarty SJ, Ross K, Chang CY, Bosco J, West N, Morse E et al. 2010. Chemical genetic strategy identifies histone deacetylase 1 (HDAC1) and HDAC2 as therapeutic targets in sickle cell disease. *Proc Natl Acad Sci U S A* **107**: 12617-12622.

Brandl A, Wagner T, Uhlig KM, Knauer SK, Stauber RH, Melchior F, Schneider G, Heinzel T, Krämer OH. 2012. Dynamically regulated sumoylation of HDAC2 controls p53 deacetylation and restricts apoptosis following genotoxic stress. *J Mol Cell Biol* **4**: 284-293.

Bray F, Ferlay J, Soerjomataram I, Siegel RL, Torre LA, Jemal A. 2018. Global cancer statistics 2018: GLOBOCAN estimates of incidence and mortality worldwide for 36 cancers in 185 countries. *CA Cancer J Clin*.

Brenner H, Chen C. 2018. The colorectal cancer epidemic: challenges and opportunities for primary, secondary and tertiary prevention. *Br J Cancer* **119**: 785-792.

Brenner H, Kloor M, Pox CP. 2014. Colorectal cancer. *The Lancet* **383**: 1490-1502.

Brenner W, Färber G, Herget T, Lehr H-A, Hengstler JG, Thüroff JW. 2002. Loss of tumor suppressor protein PTEN during renal carcinogenesis. *Int J Cancer* **99**: 53-57.

Briere D, Sudhakar N, Woods DM, Hallin J, Engstrom LD, Aranda R, Chiang H, Sodre AL, Olson P, Weber JS et al. 2018. The class I/IV HDAC inhibitor mocetinostat increases tumor antigen presentation, decreases immune suppressive cell types and augments checkpoint inhibitor therapy. *Cancer Immunol Immunother* **67**: 381-392.

Brody JR, Gallmeier E, Yoshimura K, Hucl T, Kulesza P, Canto MI, Hruban RH, Schulick RD, Kern SE. 2006. A proposed clinical test for monitoring fluoropyrimidine therapy: detection and stability of thymidylate synthase ternary complexes. *Cancer Biol Ther* **5**: 923-927.

Brownlee PM, Meisenberg C, Downs JA. 2015. The SWI/SNF chromatin remodelling complex: Its role in maintaining genome stability and preventing tumourigenesis. *DNA Repair* **32**: 127-133.

Buchbinder EI, Desai A. 2016. CTLA-4 and PD-1 Pathways: Similarities, Differences, and Implications of Their Inhibition. *Am J Clin Oncol* **39**: 98-106.

Burma S, Chen BP, Murphy M, Kurimasa A, Chen DJ. 2001. ATM phosphorylates histone H2AX in response to DNA double-strand breaks. *J Biol Chem* **276**: 42462-42467.

Burt R, Neklason DW. 2005. Genetic Testing for Inherited Colon Cancer. *Gastroenterology* **128**: 1696-1716.

Byler TK, Leocadio D, Shapiro O, Bratslavsky G, Stodgell CJ, Wood RW, Messing EM, Reeder JE. 2012. Valproic acid decreases urothelial cancer cell proliferation and induces thrombospondin-1 expression. *BMC Urol* **12**: 21-21.

Byles V, Zhu L, Lovaas JD, Chmilewski LK, Wang J, Faller DV, Dai Y. 2012. SIRT1 induces EMT by cooperating with EMT transcription factors and enhances prostate cancer cell migration and metastasis. *Oncogene* **31**: 4619-4629.

Cabanel M, Brand C, Oliveira-Nunes MC, Cabral-Piccin MP, Lopes MF, Brito JM, de Oliveira FL, El-Cheikh MC, Carneiro K. 2015. Epigenetic Control of Macrophage Shape Transition towards an Atypical Elongated Phenotype by Histone Deacetylase Activity. *PLoS One* **10**: e0132984.

Caldecott KW. 2008. Single-strand break repair and genetic disease. *Nat Rev Genet* **9**: 619.

Canman CE, Lim D-S, Cimprich KA, Taya Y, Tamai K, Sakaguchi K, Appella E, Kastan MB, Siliciano JD. 1998. Activation of the ATM Kinase by Ionizing Radiation and Phosphorylation of p53. *Science* **281**: 1677-1679.

Cano A, Perez-Moreno MA, Rodrigo I, Locascio A, Blanco MJ, del Barrio MG, Portillo F, Nieto MA. 2000. The transcription factor snail controls epithelial-mesenchymal transitions by repressing E-cadherin expression. *Nat Cell Biol* **2**: 76-83.

Cao DZ, Ou XL, Yu T. 2017. The association of p53 expression levels with clinicopathological features and prognosis of patients with colon cancer following surgery. *Oncol Lett* **13**: 3538-3546.

Carethers JM, Chauhan DP, Fink D, Nebel S, Bresalier RS, Howell SB, Boland CR. 1999. Mismatch repair proficiency and in vitro response to 5-fluorouracil. *Gastroenterology* **117**: 123-131.

Carew JS, Nawrocki ST, Kahue CN, Zhang H, Yang C, Chung L, Houghton JA, Huang P, Giles FJ, Cleveland JL. 2007. Targeting autophagy augments the anticancer activity of the histone deacetylase inhibitor SAHA to overcome Bcr-Abl-mediated drug resistance. *Blood* **110**: 313-322.

Cazzalini O, Scovassi AI, Savio M, Stivala LA, Prosperi E. 2010. Multiple roles of the cell cycle inhibitor p21CDKN1A in the DNA damage response. *Mutat Res* **704**: 12-20.

Ceccacci E, Minucci S. 2016. Inhibition of histone deacetylases in cancer therapy: lessons from leukaemia. *Br J Cancer* **114**: 605-611.

Celeste A, Fernandez-Capetillo O, Kruhlak MJ, Pilch DR, Staudt DW, Lee A, Bonner RF, Bonner WM, Nussenzweig A. 2003. Histone H2AX phosphorylation is dispensable for the initial recognition of DNA breaks. *Nat Cell Biol* **5**: 675.

Cha TL, Chuang MJ, Wu ST, Sun GH, Chang SY, Yu DS, Huang SM, Huan SK, Cheng TC, Chen TT et al. 2009. Dual degradation of aurora A and B kinases by the histone deacetylase inhibitor LBH589 induces G2-M arrest and apoptosis of renal cancer cells. *Clin Cancer Res* **15**: 840-850.

Chaabane W, User SD, El-Gazzah M, Jaksik R, Sajjadi E, Rzeszowska-Wolny J, Łos MJ. 2013. Autophagy, Apoptosis, Mitoptosis and Necrosis: Interdependence Between Those Pathways and Effects on Cancer. *Arch Immunol Ther Exp (Warsz)* **61**: 43-58.

Chakraborty S, Pandita RK, Hambarde S, Mattoo AR, Charaka V, Ahmed KM, Iyer SP, Hunt CR, Pandita TK. 2018. SMARCAD1 Phosphorylation and Ubiquitination Are Required for Resection during DNA Double-Strand Break Repair. *iScience* **2**: 123-135.

Chan LL-Y, Shen D, Wilkinson AR, Patton W, Lai N, Chan E, Kuksin D, Lin B, Qiu J. 2012. A novel image-based cytometry method for autophagy detection in living cells. *Autophagy* **8**: 1371-1382.

Chandrasekar T, Klaassen Z, Goldberg H, Kulkarni GS, Hamilton RJ, Fleshner NE. 2017. Metastatic renal cell carcinoma: Patterns and predictors of metastases-A contemporary population-based series. *Urol Oncol* **35**: 661.e667 - 661.e614.

Chang HHY, Pannunzio NR, Adachi N, Lieber MR. 2017. Non-homologous DNA end joining and alternative pathways to double-strand break repair. *Nat Rev Mol Cell Biol* **18**: 495.

Chapman JR, Taylor Martin RG, Boulton Simon J. 2012. Playing the End Game: DNA Double-Strand Break Repair Pathway Choice. *Mol Cell* **47**: 497-510.

Chappell C, Hanakahi LA, Karimi-Busheri F, Weinfeld M, West SC. 2002. Involvement of human polynucleotide kinase in double-strand break repair by non-homologous end joining. *EMBO J* **21**: 2827-2832.

Chatterjee N, Walker GC. 2017. Mechanisms of DNA damage, repair, and mutagenesis. *Environ Mol Mutag* **58**: 235-263.

Chiu HW, Yeh YL, Wang YC, Huang WJ, Ho SY, Lin P, Wang YJ. 2016. Combination of the novel histone deacetylase inhibitor YCW1 and radiation induces autophagic cell death through the downregulation of BNIP3 in triple-negative breast cancer cells in vitro and in an orthotopic mouse model. *Mol Cancer* **15**: 46.

Chiu L-Y, Gong F, Miller KM. 2017. Bromodomain proteins: repairing DNA damage within chromatin. *Philos Trans R Soc Lond B Biol Sci* **372**: 20160286.

Choi J-H, Kwon HJ, Yoon B-I, Kim J-H, Han SU, Joo HJ, Kim D-Y. 2001. Expression Profile of Histone Deacetylase 1 in Gastric Cancer Tissues. *Jap J Cancer Res* **92**: 1300-1304.

Choudhary C, Kumar C, Gnad F, Nielsen ML, Rehman M, Walther TC, Olsen JV, Mann M. 2009. Lysine Acetylation Targets Protein Complexes and Co-Regulates Major Cellular Functions. *Science* **325**: 834-840.

Chow WH, Gridley G, Fraumeni JF, Jr., Jarvholm B. 2000. Obesity, hypertension, and the risk of kidney cancer in men. *N Engl J Med* **343**: 1305-1311.

Christmann M, Tomicic MT, Roos WP, Kaina B. 2003. Mechanisms of human DNA repair: an update. *Toxicology* **193**: 3-34.

Christmann M, Verbeek B, Roos WP, Kaina B. 2011. O(6)-Methylguanine-DNA methyltransferase (MGMT) in normal tissues and tumors: enzyme activity, promoter methylation and immunohistochemistry. *Biochim Biophys Acta* **1816**: 179-190.

Chu E, Lai GM, Zinn S, Allegra CJ. 1990. Resistance of a human ovarian cancer line to 5-fluorouracil associated with decreased levels of 5-fluorouracil in DNA. *Mol Pharmacol* **38**: 410-417.

Chuh Kelly N, Batt Anna R, Pratt Matthew R. 2016. Chemical Methods for Encoding and Decoding of Posttranslational Modifications. *Cell Chemical Biology* **23**: 86-107.

Cimprich KA, Cortez D. 2008. ATR: an essential regulator of genome integrity. *Nat Rev Mol Cell Biol* **9**: 616.

Clapier CR, Cairns BR. 2009. The Biology of Chromatin Remodeling Complexes. *Annu Rev Biochem* **78**: 273-304.

Cohen HT, McGovern FJ. 2005. Renal-Cell Carcinoma. *N Engl J Med* **353**: 2477-2490.

Conacci-Sorrell M, Zhurinsky J, Ben-Ze'ev A. 2002. The cadherin-catenin adhesion system in signaling and cancer. *J Clin Invest* **109**: 987-991.

Connolly RM, Rudek MA, Piekarz R. 2017. Entinostat: a promising treatment option for patients with advanced breast cancer. *Future Oncol* **13**: 1137-1148.

Conradt L, Henrich A, Wirth M, Reichert M, Lesina M, Algul H, Schmid RM, Krämer OH, Saur D, Schneider G. 2013. Mdm2 inhibitors synergize with topoisomerase II inhibitors to induce p53-independent pancreatic cancer cell death. *Int J Cancer* **132**: 2248-2257.

Cooper AL, Greenberg VL, Lancaster PS, van Nagell JR, Zimmer SG, Modesitt SC. 2007. In vitro and in vivo histone deacetylase inhibitor therapy with suberoylanilide hydroxamic acid (SAHA) and paclitaxel in ovarian cancer. *Gynecol Oncol* **104**: 596-601.

Costelloe T, Louge R, Tomimatsu N, Mukherjee B, Martini E, Khadaroo B, Dubois K, Wiegant WW, Thierry A, Burma S et al. 2012. The yeast Fun30 and human SMARCAD1 chromatin remodellers promote DNA end resection. *Nature* **489**: 581-584.

National Research Council. 2006. *Health risks from exposure to low levels of ionizing radiation: BEIR VII phase 2*. National Academies Press.

Craene BD, Berx G. 2013. Regulatory networks defining EMT during cancer initiation and progression. *Nat Rev Cancer* **13**: 97.

Cunningham LA, Kahn RA. 2008. Cofactor D functions as a centrosomal protein and is required for the recruitment of the gamma-tubulin ring complex at centrosomes and organization of the mitotic spindle. *J Biol Chem* **283**: 7155-7165.

Damegunta SR. 2014. Time Matters!: When is the Right Time to Estimate Serum Valproic Acid Levels? *Indian J Psychol Med* **36**: 349-350.

Dave N, Guaita-Esteruelas S, Gutarra S, Frias À, Beltran M, Peiró S, de Herreros AG. 2011. Functional Cooperation between Snail1 and Twist in the Regulation of ZEB1 Expression during Epithelial to Mesenchymal Transition. *J Biol Chem* **286**: 12024-12032.

de Charette M, Marabelle A, Houot R. 2016. Turning tumour cells into antigen presenting cells: The next step to improve cancer immunotherapy? *Eur J Cancer* **68**: 134-147.

Dejung M, Subota I, Bucerius F, Dindar G, Freiwald A, Engstler M, Boshart M, Butter F, Janzen CJ. 2016. Quantitative Proteomics Uncovers Novel Factors Involved in Developmental Differentiation of Trypanosoma brucei. *PLoS Pathog* **12**: e1005439.

Deriano L, Roth DB. 2013. Modernizing the Nonhomologous End-Joining Repertoire: Alternative and Classical NHEJ Share the Stage. *Annu Rev Genet* **47**: 433-455.

Dietrich CS, Greenberg VL, DeSimone CP, Modesitt SC, van Nagell JR, Craven R, Zimmer SG. 2010. Suberoylanilide hydroxamic acid (SAHA) potentiates paclitaxel-induced apoptosis in ovarian cancer cell lines. *Gynecol Oncol* **116**: 126-130.

Dobbelstein M, Sørensen CS. 2015. Exploiting replicative stress to treat cancer. *Nat Rev Drug Discov* **14**: 405.

Doiguchi M, Nakagawa T, Imamura Y, Yoneda M, Higashi M, Kubota K, Yamashita S, Asahara H, Iida M, Fujii S et al. 2016. SMARCAD1 is an ATP-dependent stimulator of nucleosomal H2A acetylation via CBP, resulting in transcriptional regulation. *Sci Rep* **6**: 20179.

Dongre A, Weinberg RA. 2018. New insights into the mechanisms of epithelial–mesenchymal transition and implications for cancer. *Nat Rev Mol Cell Biol*.

Douillard JY, Cunningham D, Roth AD, Navarro M, James RD, Karasek P, Jandik P, Iveson T, Carmichael J, Alakl M et al. 2000. Irinotecan combined with fluorouracil compared with fluorouracil alone as first-line treatment for metastatic colorectal cancer: a multicentre randomised trial. *Lancet* **355**: 1041-1047.

Dovey OM, Foster CT, Conte N, Edwards SA, Edwards JM, Singh R, Vassiliou G, Bradley A, Cowley SM. 2013. Histone deacetylase 1 and 2 are essential for normal T-cell development and genomic stability in mice. *Blood* **121**: 1335-1344.

Dowdy SC, Jiang S, Zhou XC, Hou X, Jin F, Podratz KC, Jiang S-W. 2006. Histone deacetylase inhibitors and paclitaxel cause synergistic effects on apoptosis and microtubule stabilization in papillary serous endometrial cancer cells. *Mol Cancer Ther* **5**: 2767-2776.

Dronkert MLG, Kanaar R. 2001. Repair of DNA interstrand cross-links. *Mutat Res/DNA Repair* **486**: 217-247.

Dupere-Richer D, Kinal M, Menasche V, Nielsen TH, Del Rincon S, Pettersson F, Miller WH, Jr. 2013. Vorinostat-induced autophagy switches from a death-promoting to a cytoprotective signal to drive acquired resistance. *Cell Death Dis* **4**: e486.

Duschinsky R, Pleven E, Heidelberger C. 1957. The synthesis of 5-fluoropyrimidines. *J Am Chem Soc* **79**: 4559-4560.

Eberharter A, Becker PB. 2002. Histone acetylation: a switch between repressive and permissive chromatin. *EMBO Rep* **3**: 224-229.

Eid W, Steger M, El-Shemerly M, Ferretti LP, Peña-Diaz J, König C, Valtorta E, Sartori AA, Ferrari S. 2010. DNA end resection by CtIP and exonuclease 1 prevents genomic instability. *EMBO Rep* **11**: 962-968.

El-Deiry WS. 2016. p21(WAF1) Mediates Cell-Cycle Inhibition, Relevant to Cancer Suppression and Therapy. *Cancer Res* **76**: 5189-5191.

El-Khoury V, Pierson S, Szwarcbart E, Brons NH, Roland O, Cherrier-De Wilde S, Plawny L, Van Dyck E, Berchem G. 2014. Disruption of autophagy by the histone deacetylase inhibitor MGCD0103 and its therapeutic implication in B-cell chronic lymphocytic leukemia. *Leukemia* **28**: 1636-1646.

Elia Andrew EH, Boardman Alexander P, Wang David C, Huttlin Edward L, Everley Robert A, Dephoure N, Zhou C, Koren I, Gygi Steven P, Elledge Stephen J. 2015. Quantitative Proteomic Atlas of Ubiquitination and Acetylation in the DNA Damage Response. *Mol Cell* **59**: 867-881.

Elmore S. 2007. Apoptosis: A Review of Programmed Cell Death. *Toxicol Pathol* **35**: 495-516.

Elsaleh H, Powell B, McCaul K, Grieu F, Grant R, Joseph D, Iacopetta B. 2001. P53 alteration and microsatellite instability have predictive value for survival benefit from chemotherapy in stage III colorectal carcinoma. *Clin Cancer Res* **7**: 1343-1349.

Elsheikh SE, Green AR, Rakha EA, Powe DG, Ahmed RA, Collins HM, Soria D, Garibaldi JM, Paish CE, Ammar AA et al. 2009. Global Histone Modifications in Breast Cancer Correlate with Tumor Phenotypes, Prognostic Factors, and Patient Outcome. *Cancer Res* **69**: 3802-3809.

Engeland K. 2018. Cell cycle arrest through indirect transcriptional repression by p53: I have a DREAM. *Cell Death Differ* **25**: 114-132.

Eot-Houllier G, Fulcrand G, Magnaghi-Jaulin L, Jaulin C. 2009. Histone deacetylase inhibitors and genomic instability. *Cancer Lett* **274**: 169-176.

Esposti DD, Domart MC, Sebagh M, Harper F, Pierron G, Brenner C, Lemoine A. 2010. Autophagy is induced by ischemic preconditioning in human livers formerly treated by chemotherapy to limit necrosis. *Autophagy* **6**: 172-174.

Falcon S, Gentleman R. 2007. Using GOstats to test gene lists for GO term association. *Bioinformatics* **23**: 257-258.

Fearon ER. 2011. Molecular Genetics of Colorectal Cancer. *Annu Rev Pathol* **6**: 479-507.

Fearon ER, Vogelstein B. 1990. A genetic model for colorectal tumorigenesis. *Cell* **61**: 759-767.

Feng L, Pan M, Sun J, Lu H, Shen Q, Zhang S, Jiang T, Liu L, Jin W, Chen Y et al. 2013. Histone deacetylase 3 inhibits expression of PUMA in gastric cancer cells. *J Mol Med (Berl)* **91**: 49-58.

Feoktistova M, Leverkus M. 2015. Programmed necrosis and necroptosis signalling. *The FEBS Journal* **282**: 19-31.

Fernandez-Capetillo O, Lee A, Nussenzweig M, Nussenzweig A. 2004. H2AX: the histone guardian of the genome. *DNA Repair (Amst)* **3**: 959-967.

Finzer P, Kuntzen C, Soto U, zur Hausen H, Rosl F. 2001. Inhibitors of histone deacetylase arrest cell cycle and induce apoptosis in cervical carcinoma cells circumventing human papillomavirus oncogene expression. *Oncogene* **20**: 4768-4776.

Fischer M. 2017. Census and evaluation of p53 target genes. *Oncogene* **36**: 3943.

Fischer M, Steiner L, Engeland K. 2014. The transcription factor p53: not a repressor, solely an activator. *Cell cycle (Georgetown, Tex)* **13**: 3037-3058.

Flavahan WA, Gaskell E, Bernstein BE. 2017. Epigenetic plasticity and the hallmarks of cancer. *Science* **357**.

Flippot R, Escudier B, Albiges L. 2018. Immune Checkpoint Inhibitors: Toward New Paradigms in Renal Cell Carcinoma. *Drugs*.

Flis S, Gnyszka A, Flis K, Splawinski J. 2010. MS275 enhances cytotoxicity induced by 5-fluorouracil in the colorectal cancer cells. *Eur J Pharmacol* **627**: 26-32.

Forooghipour M, Mohammadpour AH, Mashhadian NV, Khayyat MH, Azarpajouh MR, Mokhber N, Aghebati T, Shamsara J. 2009. Therapeutic Drug Monitoring of Valproic Acid in Patients with Monotherapy at Steady State. *Iran J Basic Med Sci* **12**: 146-149.

Fraga MF, Ballestar E, Villar-Garea A, Boix-Chornet M, Espada J, Schotta G, Bonaldi T, Haydon C, Ropero S, Petrie K et al. 2005. Loss of acetylation at Lys16 and trimethylation at Lys20 of histone H4 is a common hallmark of human cancer. *Nat Genet* **37**: 391.

Francisco R, Perez-Perarnau A, Cortes C, Gil J, Tauler A, Ambrosio S. 2012. Histone deacetylase inhibition induces apoptosis and autophagy in human neuroblastoma cells. *Cancer Lett* **318**: 42-52.

Freed-Pastor WA, Prives C. 2012. Mutant p53: one name, many proteins. *Genes Dev* **26**: 1268-1286.

Fritzsche FR, Weichert W, Roske A, Gekeler V, Beckers T, Stephan C, Jung K, Scholman K, Denkert C, Dietel M et al. 2008. Class I histone deacetylases 1, 2 and 3 are highly expressed in renal cell cancer. *BMC Cancer* **8**: 381.

Fuchs Y, Steller H. 2015. Live to die another way: modes of programmed cell death and the signals emanating from dying cells. *Nat Rev Mol Cell Biol* **16**: 329.

Fukushima M, Fujioka A, Uchida J, Nakagawa F, Takechi T. 2001. Thymidylate synthase (TS) and ribonucleotide reductase (RNR) may be involved in acquired resistance to 5-fluorouracil (5-FU) in human cancer xenografts in vivo. *Eur J Cancer* **37**: 1681-1687.

Fulda S. 2008. Modulation of TRAIL-induced apoptosis by HDAC inhibitors. *Curr Cancer Drug Targets* **8**: 132-140.

Gameiro SR, Malamas AS, Tsang KY, Ferrone S, Hodge JW. 2016. Inhibitors of histone deacetylase 1 reverse the immune evasion phenotype to enhance T-cell mediated lysis of prostate and breast carcinoma cells. *Oncotarget* **7**: 7390-7402.

Gammoh N, Marks PA, Jiang X. 2012. Curbing autophagy and histone deacetylases to kill cancer cells. *Autophagy* **8**: 1521-1522.

Gandesiri M, Chakilam S, Ivanovska J, Benderska N, Ocker M, Di Fazio P, Feoktistova M, Gali-Muhtasib H, Rave-Frank M, Prante O et al. 2012. DAPK plays an important role in panobinostat-induced autophagy and commits cells to apoptosis under autophagy deficient conditions. *Apoptosis* **17**: 1300-1315.

Gao L, Sun X, Zhang Q, Chen X, Zhao T, Lu L, Zhang J, Hong Y. 2018. Histone deacetylase inhibitor trichostatin A and autophagy inhibitor chloroquine synergistically exert anti-tumor activity in H-ras transformed breast epithelial cells. *Mol Med Rep* **17**: 4345-4350.

Gebäck T, Schulz MM, Koumoutsakos P, Detmar M. 2009. TScratch: a novel and simple software tool for automated analysis of monolayer wound healing assays. *BioTechniques* **46**: 265-274.

Gelsomino F, Barbolini M, Spallanzani A, Pugliese G, Cascinu S. 2016. The evolving role of microsatellite instability in colorectal cancer: A review. *Cancer Treat Rev* **51**: 19-26.

Ghatalia P, Zibelman M, Geynisman DM, Plimack ER. 2017. Checkpoint Inhibitors for the Treatment of Renal Cell Carcinoma. *Curr Treat Options Oncol* **18**: 7.

Giacchetti S, Perpoint B, Zidani R, Le Bail N, Faggiuolo R, Focan C, Chollet P, Llory JF, Letourneau Y, Coudert B et al. 2000. Phase III multicenter randomized trial of oxaliplatin added to chronomodulated fluorouracil-leucovorin as first-line treatment of metastatic colorectal cancer. *J Clin Oncol* **18**: 136-147.

Gil J, Ramírez-Torres A, Encarnación-Guevara S. 2017. Lysine acetylation and cancer: A proteomics perspective. *J Proteomics* **150**: 297-309.

Gilardini Montani MS, Granato M, Santoni C, Del Porto P, Merendino N, D'Orazi G, Faggioni A, Cirone M. 2017. Histone deacetylase inhibitors VPA and TSA induce apoptosis and autophagy in pancreatic cancer cells. *Cell Oncol (Dordr)* **40**: 167-180.

Girgin C, Tarhan H, Hekimgil M, Sezer A, Gürel G. 2001. p53 Mutations and Other Prognostic Factors of Renal Cell Carcinoma. *Urol Int* **66**: 78-83.

Giudice FS, Pinto DS, Jr., Nor JE, Squarize CH, Castilho RM. 2013. Inhibition of histone deacetylase impacts cancer stem cells and induces epithelial-mesenchyme transition of head and neck cancer. *PLoS One* **8**: e58672.

Giuliani J, Bonetti A. 2018. First-line therapies in metastatic colorectal cancer: integrating clinical benefit with the costs of drugs. *Int J Colorectal Dis* **33**: 1505-1516.

Glaros S, Cirrincione GM, Muchardt C, Kleer CG, Michael CW, Reisman D. 2007. The reversible epigenetic silencing of BRM: implications for clinical targeted therapy. *Oncogene* **26**: 7058-7066.

Glozak MA, Seto E. 2007. Histone deacetylases and cancer. *Oncogene* **26**: 5420.

Göder A, Emmerich C, Nikolova T, Kiweler N, Schreiber M, Kuhl T, Imhof D, Christmann M, Heinzel T, Schneider G et al. 2018. HDAC1 and HDAC2 integrate checkpoint kinase phosphorylation and cell fate through the phosphatase-2A subunit PR130. *Nat Commun* **9**: 764.

Göder A, Mahendrarajah N, Krämer OH. 2017. Detection of Autophagy Induction After HDAC Inhibitor Treatment in Leukemic Cells. *Methods Mol Biol* **1510**: 3-10.

Gojo I, Jiemjit A, Trepel JB, Sparreboom A, Figg WD, Rollins S, Tidwell ML, Greer J, Chung EJ, Lee M-J et al. 2007. Phase 1 and pharmacologic study of MS-275, a histone deacetylase inhibitor, in adults with refractory and relapsed acute leukemias. *Blood* **109**: 2781-2790.

Gore L, Rothenberg ML, O'Bryant CL, Schultz MK, Sandler AB, Coffin D, McCoy C, Schott A, Scholz C, Eckhardt SG. 2008. A Phase I and Pharmacokinetic Study of the Oral Histone Deacetylase Inhibitor, MS-275, in Patients with Refractory Solid Tumors and Lymphomas. *Clin Cancer Res* **14**: 4517.

Goswami S, Sharma P. 2017. Genetic biomarker for cancer immunotherapy. *Science* **357**: 358-358.

Göttlicher M, Minucci S, Zhu P, Krämer OH, Schimpf A, Giavara S, Sleeman JP, Lo Coco F, Nervi C, Pelicci PG et al. 2001. Valproic acid defines a novel class of HDAC inhibitors inducing differentiation of transformed cells. *EMBO J* **20**: 6969-6978.

Grozinger CM, Schreiber SL. 2002. Deacetylase Enzymes: Biological Functions and the Use of Small-Molecule Inhibitors. *Chem Biol* **9**: 3-16.

Grynberg M, Jaroszewski L, Godzik A. 2003. Domain analysis of the tubulin cofactor system: a model for tubulin folding and dimerization. *BMC Bioinformatics* **4**: 46.

Guan JS, Haggarty SJ, Giacometti E, Dannenberg JH, Joseph N, Gao J, Nieland TJ, Zhou Y, Wang X, Mazitschek R et al. 2009. HDAC2 negatively regulates memory formation and synaptic plasticity. *Nature* **459**: 55-60.

Guirouilh-Barbat J, Lambert S, Bertrand P, Lopez BS. 2014. Is homologous recombination really an error-free process? *Front Genet* **5**: 175-175.

Guittet O, Hakansson P, Voevodskaya N, Fridd S, Graslund A, Arakawa H, Nakamura Y, Thelander L. 2001. Mammalian p53R2 protein forms an active ribonucleotide reductase in vitro with the R1 protein, which is expressed both in resting cells in response to DNA damage and in proliferating cells. *J Biol Chem* **276**: 40647-40651.

Guo S, Liang Y, Murphy SF, Huang A, Shen H, Kelly DF, Sobrado P, Sheng Z. 2015. A rapid and high content assay that measures cyto-ID-stained autophagic compartments and estimates autophagy flux with potential clinical applications. *Autophagy* **11**: 560-572.

Gurova KV, Hill JE, Razorenova OV, Chumakov PM, Gudkov AV. 2004. p53 Pathway in Renal Cell Carcinoma Is Repressed by a Dominant Mechanism. *Cancer Res* **64**: 1951-1958.

Hage-Sleiman R, Herveau S, Matera EL, Laurier JF, Dumontet C. 2010. Tubulin binding cofactor C (TBCC) suppresses tumor growth and enhances chemosensitivity in human breast cancer cells. *BMC Cancer* **10**: 135.

Hagelkruys A, Lagger S, Krahmer J, Leopoldi A, Artaker M, Pusch O, Zezula J, Weissmann S, Xie Y, Schofer C et al. 2014. A single allele of Hdac2 but not Hdac1 is sufficient for normal mouse brain development in the absence of its paralog. *Development* **141**: 604-616.

Halkidou K, Gaughan L, Cook S, Leung HY, Neal DE, Robson CN. 2004. Upregulation and Nuclear Recruitment of HDAC1 in Hormone Refractory Prostate Cancer. *The Prostate* **59**: 177-189.

Hanahan D, Weinberg RA. 2000. The Hallmarks of Cancer. *Cell* **100**: 57-70.

Hanahan D, Weinberg Robert A. 2011. Hallmarks of Cancer: The Next Generation. *Cell* **144**: 646-674.

Hanigan CL, van Engeland M, De Bruine AP, Wouters KA, Weijenberg MP, Eshleman JR, Herman JG. 2008. An Inactivating Mutation in HDAC2 Leads to Dysregulation of Apoptosis Mediated by APAF1. *Gastroenterology* **135**: 1654-1664.e1652.

Hao ZF, Su YM, Wang CM, Yang RY. 2015. Activating transcription factor 3 interferes with p21 activation in histone deacetylase inhibitor-induced growth inhibition of epidermoid carcinoma cells. *Tumour Biol* **36**: 1471-1476.

Harms KL, Chen X. 2007. Histone Deacetylase 2 Modulates p53 Transcriptional Activities through Regulation of p53-DNA Binding Activity. *Cancer Res* **67**: 3145-3152.

Hauer MH, Gasser SM. 2017. Chromatin and nucleosome dynamics in DNA damage and repair. *Genes Dev* **31**: 2204-2221.

He G, Wang Y, Pang X, Zhang B. 2014. Inhibition of autophagy induced by TSA sensitizes colon cancer cell to radiation. *Tumour Biol* **35**: 1003-1011.

Heggie GD, Sommadossi J-P, Cross DS, Huster WJ, Diasio RB. 1987. Clinical pharmacokinetics of 5-fluorouracil and its metabolites in plasma, urine, and bile. *Cancer Res* **47**: 2203-2206.

Heidelberger C, Chaudhuri NK, Danneberg P, Mooren D, Griesbach L, Duschinsky R, Schnitzer RJ, Pleven E, Scheiner J. 1957. Fluorinated Pyrimidines, A New Class of Tumour-Inhibitory Compounds. *Nature* **179**: 663.

Heideman MR, Wilting RH, Yanover E, Velds A, de Jong J, Kerkhoven RM, Jacobs H, Wessels LF, Dannenberg JH. 2013. Dosage-dependent tumor suppression by histone deacetylases 1 and 2 through regulation of c-Myc collaborating genes and p53 function. *Blood* **121**: 2038-2050.

Hientz K, Mohr A, Bhakta-Guha D, Efferth T. 2016. The role of p53 in cancer drug resistance and targeted chemotherapy. *Oncotarget* **8**: 8921-8946.

Hill DA, Peterson CL, Imbalzano AN. 2005. Effects of HMGN1 on chromatin structure and SWI/SNF-mediated chromatin remodeling. *J Biol Chem* **280**: 41777-41783.

Hodges C, Kirkland JG, Crabtree GR. 2016. The Many Roles of BAF (mSWI/SNF) and PBAF Complexes in Cancer. *Cold Spring Harb Perspect Med* **6**.

Hong L, Schroth GP, Matthews HR, Yau P, Bradbury EM. 1993. Studies of the DNA binding properties of histone H4 amino terminus. Thermal denaturation studies reveal that acetylation markedly reduces the binding constant of the H4 "tail" to DNA. *J Biol Chem* **268**: 305-314.

Hoshikawa H, Furuta H, Mori N, Sakai S. 1994a. Absorption activity and barrier properties in the endolymphatic sac. Ultrastructural and morphometric analysis. *Acta Otolaryngol* **114**: 40-47.

Hoshikawa Y, Kwon HJ, Yoshida M, Horinouchi S, Beppu T. 1994b. Trichostatin A induces morphological changes and gelsolin expression by inhibiting histone deacetylase in human carcinoma cell lines. *Exp Cell Res* **214**: 189-197.

Hu J, Colburn NH. 2005. Histone deacetylase inhibition down-regulates cyclin D1 transcription by inhibiting nuclear factor-kappaB/p65 DNA binding. *Mol Cancer Res* **3**: 100-109.

Huang T-H, Wu S-Y, Huang Y-J, Wei P-L, Wu AT, Chao T-Y. 2017. The identification and validation of Trichosstatin A as a potential inhibitor of colon tumorigenesis and colon cancer stem-like cells. *Am J Cancer Res* **7**: 1227-1237.

Huehls AM, Huntoon CJ, Joshi PM, Baehr CA, Wagner JM, Wang X, Lee MY, Karnitz LM. 2016. Genomically Incorporated 5-Fluorouracil that Escapes UNG-Initiated Base Excision Repair Blocks DNA Replication and Activates Homologous Recombination. *Mol Pharmacol* **89**: 53-62.

Hurwitz H, Fehrenbacher L, Novotny W, Cartwright T, Hainsworth J, Heim W, Berlin J, Baron A, Griffing S, Holmgren E et al. 2004. Bevacizumab plus irinotecan, fluorouracil, and leucovorin for metastatic colorectal cancer. *N Engl J Med* **350**: 2335-2342.

Insinga A, Monestiroli S, Ronzoni S, Gelmetti V, Marchesi F, Viale A, Altucci L, Nervi C, Minucci S, Pelicci PG. 2005. Inhibitors of histone deacetylases induce tumor-selective apoptosis through activation of the death receptor pathway. *Nat Med* **11**: 71-76.

Iyama T, Wilson DM, 3rd. 2013. DNA repair mechanisms in dividing and non-dividing cells. *DNA Repair* **12**: 620-636.

Jabbur JR, Huang P, Zhang W. 2000. DNA damage-induced phosphorylation of p53 at serine 20 correlates with p21 and Mdm-2 induction in vivo. *Oncogene* **19**: 6203-6208.

Jackson SP, Bartek J. 2009. The DNA-damage response in human biology and disease. *Nature* **461**: 1071.

Jain AK, Barton MC. 2017. Bromodomain Histone Readers and Cancer. *J Mol Biol* **429**: 2003-2010.

Jang SH, Min KW, Paik SS, Jang KS. 2012. Loss of SIRT1 histone deacetylase expression associates with tumour progression in colorectal adenocarcinoma. *J Clin Pathol* **65**: 735-739.

Jasencakova Z, Groth A. 2011. Broken Silence Restored—Remodeling Primes for Deacetylation at Replication Forks. *Mol Cell* **42**: 267-269.

Jass JR. 2007. Classification of colorectal cancer based on correlation of clinical, morphological and molecular features. *Histopathology* **50**: 113-130.

Jeon YJ, Ko SM, Cho JH, Chae JI, Shim JH. 2013. The HDAC inhibitor, panobinostat, induces apoptosis by suppressing the expresssion of specificity protein 1 in oral squamous cell carcinoma. *Int J Mol Med* **32**: 860-866.

Jiang G-M, Wang H-S, Zhang F, Zhang K-S, Liu Z-C, Fang R, Wang H, Cai S-H, Du J. 2013. Histone deacetylase inhibitor induction of epithelial–mesenchymal transitions via up-regulation of Snail facilitates cancer progression. *Biochim Biophys Acta* **1833**: 663-671.

Jin M, Park SJ, Kim SW, Kim HR, Hyun JW, Lee JH. 2017. PIG3 Regulates p53 Stability by Suppressing Its MDM2-Mediated Ubiquitination. *Biomol Ther (Seoul)* **25**: 396-403.

Joerger M, Koeberle D, Neumann HP, Gillessen S. 2005. Von Hippel-Lindau disease--a rare disease important to recognize. *Onkologie* **28**: 159-163.

Johnston PG, Kaye S. 2001. Capecitabine: a novel agent for the treatment of solid tumors. *Anticancer Drugs* **12**: 639-646.

Jones J, Juengel E, Mickuckyte A, Hudak L, Wedel S, Jonas D, Blaheta RA. 2009a. The histone deacetylase inhibitor valproic acid alters growth properties of renal cell carcinoma in vitro and in vivo. *J Cell Mol Med* **13**: 2376-2385.

Jones J, Juengel E, Mickuckyte A, Hudak L, Wedel S, Jonas D, Hintereder G, Blaheta RA. 2009b. Valproic acid blocks adhesion of renal cell carcinoma cells to endothelium and extracellular matrix. *J Cell Mol Med* **13**: 2342-2352.

Jorda M, Olmeda D, Vinyals A, Valero E, Cubillo E, Llorens A, Cano A, Fabra A. 2005. Upregulation of MMP-9 in MDCK epithelial cell line in response to expression of the Snail transcription factor. *J Cell Sci* **118**: 3371-3385.

Juengel E, Bhasin M, Libermann T, Barth S, Michaelis M, Cinatl J, Jr., Jones J, Hudak L, Jonas D, Blaheta RA. 2011. Alterations of the gene expression profile in renal cell carcinoma after treatment with the histone deacetylase-inhibitor valproic acid and interferon-alpha. *World J Urol* **29**: 779-786.

Juengel E, Nowaz S, Makarevi J, Natsheh I, Werner I, Nelson K, Reiter M, Tsaur I, Mani J, Harder S et al. 2014. HDAC-inhibition counteracts everolimus resistance in renal cell carcinoma in vitro by diminishing cdk2 and cyclin A. *Mol Cancer* **13**: 152.

Jung KH, Noh JH, Kim JK, Eun JW, Bae HJ, Xie HJ, Chang YG, Kim MG, Park H, Lee JY et al. 2012. HDAC2 overexpression confers oncogenic potential to human lung cancer cells by deregulating expression of apoptosis and cell cycle proteins. *J Cell Biochem* **113**: 2167-2177.

Jurkin J, Zupkovitz G, Lagger S, Grausenburger R, Hagelkruys A, Kenner L, Seiser C. 2011. Distinct and redundant functions of histone deacetylases HDAC1 and HDAC2 in proliferation and tumorigenesis. *Cell Cycle* **10**: 406-412.

Kadoch C, Hargreaves DC, Hodges C, Elias L, Ho L, Ranish J, Crabtree GR. 2013. Proteomic and bioinformatic analysis of mammalian SWI/SNF complexes identifies extensive roles in human malignancy. *Nat Genet* **45**: 592.

Kaina B, Christmann M, Naumann S, Roos WP. 2007. MGMT: Key node in the battle against genotoxicity, carcinogenicity and apoptosis induced by alkylating agents. *DNA Repair* **6**: 1079-1099.

Kakihana M, Ohira T, Chan D, Webster RB, Kato H, Drabkin HA, Gemmill RM. 2009. Induction of E-Cadherin in Lung Cancer and Interaction with Growth Suppression by Histone Deacetylase Inhibition. *J Thorac Oncol* **4**: 1455-1465.

Kanao K, Mikami S, Mizuno R, Shinojima T, Murai M, Oya M. 2008. Decreased acetylation of histone H3 in renal cell carcinoma: a potential target of histone deacetylase inhibitors. *J Urol* **180**: 1131-1136.

Kang R, Zeh HJ, Lotze MT, Tang D. 2011. The Beclin 1 network regulates autophagy and apoptosis. *Cell Death Differ* **18**: 571-580.

Kap EJ, Popanda O, Chang-Claude J. 2016. Nucleotide excision repair and response and survival to chemotherapy in colorectal cancer patients. *Pharmacogenomics* **17**: 755-794.

Keller SH, Nigam SK. 2003. Biochemical processing of E-cadherin under cellular stress. *Biochem Biophys Res Commun* **307**: 215-223.

Kelly AD, Issa J-PJ. 2017. The promise of epigenetic therapy: reprogramming the cancer epigenome. *Curr Opin Genet Dev* **42**: 68-77.

Kidd EA, Yu J, Li X, Shannon WD, Watson MA, McLeod HL. 2005. Variance in the Expression of 5-Fluorouracil Pathway Genes in Colorectal Cancer. *Clin Cancer Res* **11**: 2612-2619.

Kim JK, Noh JH, Eun JW, Jung KH, Bae HJ, Shen Q, Kim MG, Chang YG, Kim S-J, Park WS et al. 2013. Targeted Inactivation of HDAC2 Restores p16INK4a Activity and Exerts Antitumor Effects on Human Gastric Cancer. *Mol Cancer Res* **11**: 62-73.

Kim K, Skora AD, Li Z, Liu Q, Tam AJ, Blosser RL, Diaz LA, Papadopoulos N, Kinzler KW, Vogelstein B et al. 2014. Eradication of metastatic mouse cancers resistant to immune checkpoint blockade by suppression of myeloid-derived cells. *Proc Natl Acad Sci USA* **111**: 11774.

Kim Y-C, Gerlitz G, Furusawa T, Catez F, Nussenzweig A, Oh K-S, Kraemer KH, Shiloh Y, Bustin M. 2008. Activation of ATM depends on chromatin interactions occurring before induction of DNA damage. *Nat Cell Biol* **11**: 92.

Kiweler N, Brill B, Wirth M, Breuksch I, Laguna T, Dietrich C, Strand S, Schneider G, Groner B, Butter F et al. 2018. The histone deacetylases HDAC1 and HDAC2 are required for the growth and survival of renal carcinoma cells. *Arch Toxicol* **92**: 2227-2243.

Knorre DG, Kudryashova NV, Godovikova TS. 2009. Chemical and functional aspects of posttranslational modification of proteins. *Acta naturae* **1**: 29-51.

Koeneke E, Witt O, Oehme I. 2015. HDAC Family Members Intertwined in the Regulation of Autophagy: A Druggable Vulnerability in Aggressive Tumor Entities. *Cells* **4**: 135.

Kondo K, Kim WY, Lechpammer M, Kaelin WG, Jr. 2003. Inhibition of HIF2alpha is sufficient to suppress pVHL-defective tumor growth. *PLoS Biol* **1**: E83.

Kong D, Ahmad A, Bao B, Li Y, Banerjee S, Sarkar FH. 2012. Histone Deacetylase Inhibitors Induce Epithelial-to-Mesenchymal Transition in Prostate Cancer Cells. *PLoS One* **7**: e45045.

Kortazar D, Fanarraga ML, Carranza G, Bellido J, Villegas JC, Avila J, Zabala JC. 2007. Role of cofactors B (TBCB) and E (TBCE) in tubulin heterodimer dissociation. *Exp Cell Res* **313**: 425-436.

Kothandapani A, Gopalakrishnan K, Kahali B, Reisman D, Patrick SM. 2012. Downregulation of SWI/SNF chromatin remodeling factor subunits modulates cisplatin cytotoxicity. *Exp Cell Res* **318**: 1973-1986.

Kracikova M, Akiri G, George A, Sachidanandam R, Aaronson SA. 2013. A threshold mechanism mediates p53 cell fate decision between growth arrest and apoptosis. *Cell Death Differ* **20**: 576-588.

Krämer OH. 2009. HDAC2: a critical factor in health and disease. *Trends Pharmacol Sci* **30**: 647-655.

Krämer OH, Knauer SK, Zimmermann D, Stauber RH, Heinzel T. 2008a. Histone deacetylase inhibitors and hydroxyurea modulate the cell cycle and cooperatively induce apoptosis. *Oncogene* **27**: 732-740.

Krämer OH, Muller S, Buchwald M, Reichardt S, Heinzel T. 2008b. Mechanism for ubiquitylation of the leukemia fusion proteins AML1-ETO and PML-RARalpha. *FASEB J* **22**: 1369-1379.

Krämer OH, Zhu P, Ostendorff HP, Golebiewski M, Tiefenbach J, Peters MA, Brill B, Groner B, Bach I, Heinzel T et al. 2003. The histone deacetylase inhibitor valproic acid selectively induces proteasomal degradation of HDAC2. *The EMBO Journal* **22**: 3411-3420.

Krueger KE, Srivastava S. 2006. Posttranslational Protein Modifications: Current Implications for Cancer Detection, Prevention, and Therapeutics. *Mol Cell Proteomics* **5**: 1799-1810.

Krumm A, Roos WP. 2017. Assessing the Effect of Class I Histone Deacetylase Activity on DNA Double-Strand Break Repair by Homologous Recombination. *Methods Mol Biol* **1510**: 115-123.

Kruse J-P, Gu W. 2008. SnapShot: p53 posttranslational modifications. *Cell* **133**: 930-930.e931.

Kufe DW, Major PP. 1981. 5-Fluorouracil incorporation into human breast carcinoma RNA correlates with cytotoxicity. *J Biol Chem* **256**: 9802-9805.

Kunz C, Focke F, Saito Y, Schuermann D, Lettieri T, Selfridge J, Schar P. 2009. Base excision by thymine DNA glycosylase mediates DNA-directed cytotoxicity of 5-fluorouracil. *PLoS Biol* **7**: e91.

Kwon SH, Ahn SH, Kim YK, Bae GU, Yoon JW, Hong S, Lee HY, Lee YW, Lee HW, Han JW. 2002. Apicidin, a histone deacetylase inhibitor, induces apoptosis and Fas/Fas ligand expression in human acute promyelocytic leukemia cells. *J Biol Chem* **277**: 2073-2080.

Kwon SJ, Lee SK, Na J, Lee SA, Lee HS, Park JH, Chung JK, Youn H, Kwon J. 2015. Targeting BRG1 chromatin remodeler via its bromodomain for enhanced tumor cell radiosensitivity in vitro and in vivo. *Mol Cancer Ther* **14**: 597-607.

Lamouille S, Xu J, Derynck R. 2014. Molecular mechanisms of epithelial–mesenchymal transition. *Nat Rev Mol Cell Biol* **15**: 178.

Lawley PD, Phillips DH. 1996. DNA adducts from chemotherapeutic agents. *Mutat Res* **355**: 13-40.

Le DT, Durham JN, Smith KN, Wang H, Bartlett BR, Aulakh LK, Lu S, Kemberling H, Wilt C, Luber BS et al. 2017. Mismatch repair deficiency predicts response of solid tumors to PD-1 blockade. *Science* **357**: 409-413.

Lee HS, Park JH, Kim SJ, Kwon SJ, Kwon J. 2010a. A cooperative activation loop among SWI/SNF, gamma-H2AX and H3 acetylation for DNA double-strand break repair. *EMBO J* **29**: 1434-1445.

Lee JH, Kang Y, Khare V, Jin ZY, Kang MY, Yoon Y, Hyun JW, Chung MH, Cho SI, Jun JY et al. 2010b. The p53-inducible gene 3 (PIG3) contributes to early cellular response to DNA damage. *Oncogene* **29**: 1431-1450.

Lee YJ, Won AJ, Lee J, Jung JH, Yoon S, Lee BM, Kim HS. 2012. Molecular mechanism of SAHA on regulation of autophagic cell death in tamoxifen-resistant MCF-7 breast cancer cells. *Int J Med Sci* **9**: 881-893.

Levine JS, Ahnen DJ. 2006. Adenomatous Polyps of the Colon. *N Engl J Med* **355**: 2551-2557.

Li J, Liu R, Lei Y, Wang K, Lau QC, Xie N, Zhou S, Nie C, Chen L, Wei Y et al. 2010. Proteomic analysis revealed association of aberrant ROS signaling with suberoylanilide hydroxamic acid-induced autophagy in Jurkat T-leukemia cells. *Autophagy* **6**: 711-724.

Li LH, Zhang PR, Cai PY, Li ZC. 2016. Histone deacetylase inhibitor, Romidepsin (FK228) inhibits endometrial cancer cell growth through augmentation of p53-p21 pathway. *Biomed Pharmacother* **82**: 161-166.

Li Y, Kao GD, Garcia BA, Shabanowitz J, Hunt DF, Qin J, Phelan C, Lazar MA. 2006. A novel histone deacetylase pathway regulates mitosis by modulating Aurora B kinase activity. *Genes Dev* **20**: 2566-2579.

Li Y, Seto E. 2016. HDACs and HDAC Inhibitors in Cancer Development and Therapy. *Cold Spring Harb Perspect Med* **6**.

Linnebacher M, Maletzki C, Ostwald C, Klier U, Krohn M, Klar E, Prall F. 2010. Cryopreservation of human colorectal carcinomas prior to xenografting. *BMC Cancer* **10**: 362-362.

Lipworth L, Tarone RE, McLaughlin JK. 2006. The epidemiology of renal cell carcinoma. *J Urol* **176**: 2353-2358.

Liu A, Yoshioka K, Salerno V, Hsieh P. 2008. The mismatch repair-mediated cell cycle checkpoint response to fluorodeoxyuridine. *J Cell Biochem* **105**: 245-254.

Liu YL, Yang PM, Shun CT, Wu MS, Weng JR, Chen CC. 2010. Autophagy potentiates the anti-cancer effects of the histone deacetylase inhibitors in hepatocellular carcinoma. *Autophagy* **6**: 1057-1065.

Lomax ME, Folkes LK, O'Neill P. 2013. Biological Consequences of Radiation-induced DNA Damage: Relevance to Radiotherapy. *Clin Oncol* **25**: 578-585.

Longerich S, Li J, Xiong Y, Sung P, Kupfer GM. 2014. Stress and DNA repair biology of the Fanconi anemia pathway. *Blood* **124**: 2812-2819.

Longley DB, Boyer J, Allen WL, Latif T, Ferguson PR, Maxwell PJ, McDermott U, Lynch M, Harkin DP, Johnston PG. 2002. The role of thymidylate synthase induction in modulating p53-regulated gene expression in response to 5-fluorouracil and antifolates. *Cancer Res* **62**: 2644-2649.

Longley DB, Harkin DP, Johnston PG. 2003. 5-Fluorouracil: mechanisms of action and clinical strategies. *Nat Rev Cancer* **3**: 330.

Lopez G, Torres K, Liu J, Hernandez B, Young E, Belushov R, Bolshakov S, Lazar AJ, Slopis JM, McCutcheon IE et al. 2011. Autophagic survival in resistance to histone deacetylase inhibitors: novel strategies to treat malignant peripheral nerve sheath tumors. *Cancer Res* **71**: 185-196.

Los M, Wesselborg S, Schulze-Osthoff K. 1999. The Role of Caspases in Development, Immunity, and Apoptotic Signal Transduction: Lessons from Knockout Mice. *Immunity* **10**: 629-639.

Loughery J, Cox M, Smith LM, Meek DW. 2014. Critical role for p53-serine 15 phosphorylation in stimulating transactivation at p53-responsive promoters. *Nucleic Acids Res* **42**: 7666-7680.

Lozano G, Elledge SJ. 2000. p53 sends nucleotides to repair DNA. *Nature* **404**: 24.

Luo Y, Hurwitz J, Massagué J. 1995. Cell-cycle inhibition by independent CDK and PCNA binding domains in p21Cip1. *Nature* **375**: 159.

Ma J, Guo X, Zhang S, Liu H, Lu J, Dong Z, Liu K, Ming L. 2015. Trichostatin A, a histone deacetylase inhibitor, suppresses proliferation and promotes apoptosis of esophageal squamous cell lines. *Mol Med Rep* **11**: 4525-4531.

Ma P, Schultz RM. 2016. HDAC1 and HDAC2 in mouse oocytes and preimplantation embryos: Specificity versus compensation. *Cell Death Differ* **23**: 1119.

Mackmull M-T, Iskar M, Parca L, Singer S, Bork P, Ori A, Beck M. 2015. Histone Deacetylase Inhibitors (HDACi) Cause the Selective Depletion of Bromodomain Containing Proteins (BCPs). *Mol Cell Proteomics* **14**: 1350-1360.

Madabushi A, Hwang BJ, Jin J, Lu AL. 2013. Histone deacetylase SIRT1 modulates and deacetylates DNA base excision repair enzyme thymine DNA glycosylase. *Biochem J* **456**: 89-98.

Mahalingam D, Medina EC, Esquivel JA, 2nd, Espitia CM, Smith S, Oberheu K, Swords R, Kelly KR, Mita MM, Mita AC et al. 2010. Vorinostat enhances the activity of temsirolimus in renal cell carcinoma through suppression of survivin levels. *Clin Cancer Res* **16**: 141-153.

Mailand N, Falck J, Lukas C, Syljuåsen RG, Welcker M, Bartek J, Lukas J. 2000. Rapid Destruction of Human Cdc25A in Response to DNA Damage. *Science* **288**: 1425-1429.

Makhov P, Joshi S, Ghatalia P, Kutikov A, Uzzo RG, Kolenko VM. 2018. Resistance to Systemic Therapies in Clear Cell Renal Cell Carcinoma: Mechanisms and Management Strategies. *Mol Cancer Ther* **17**: 1355-1364.

Malet-Martino M, Jolimaitre P, Martino R. 2002. The Prodrugs of 5-Fluorouracil. *Curr Med Chem Anticancer Agents* **2**: 267-310.

Maletzki C, Stier S, Gruenert U, Gock M, Ostwald C, Prall F, Linnebacher M. 2012. Establishment, characterization and chemosensitivity of three mismatch repair deficient cell lines from sporadic and inherited colorectal carcinomas. *PLoS One* **7**: e52485.

Malkova A, Ira G. 2013. Break-induced replication: functions and molecular mechanism. *Curr Opin Genet Dev* **23**: 271-279.

Manchado E, Guillamot M, Malumbres M. 2012. Killing cells by targeting mitosis. *Cell Death Differ* **19**: 369-377.

Mani SA, Guo W, Liao MJ, Eaton EN, Ayyanan A, Zhou AY, Brooks M, Reinhard F, Zhang CC, Shipitsin M et al. 2008. The epithelial-mesenchymal transition generates cells with properties of stem cells. *Cell* **133**: 704-715.

Manuyakorn A, Paulus R, Farrell J, Dawson NA, Tze S, Cheung-Lau G, Hines OJ, Reber H, Seligson DB, Horvath S et al. 2010. Cellular Histone Modification Patterns Predict Prognosis and Treatment Response in Resectable Pancreatic Adenocarcinoma: Results From RTOG 9704. *J Clin Oncol* **28**: 1358-1365.

Mariadason JM. 2008. HDACs and HDAC inhibitors in colon cancer. *Epigenetics* **3**: 28-37.

Markowitz SD, Bertagnolli MM. 2009. Molecular Basis of Colorectal Cancer. *N Engl J Med* **361**: 2449-2460.

Markowitz SD, Dawson DM, Willis J, Willson JKV. 2002. Focus on colon cancer. *Cancer Cell* **1**: 233-236.

Martin AP, Park MA, Mitchell C, Walker T, Rahmani M, Thorburn A, Haussinger D, Reinehr R, Grant S, Dent P. 2009. BCL-2 family inhibitors enhance histone deacetylase inhibitor and sorafenib lethality via autophagy and overcome blockade of the extrinsic pathway to facilitate killing. *Mol Pharmacol* **76**: 327-341.

Masaoka A, Gassman NR, Kedar PS, Prasad R, Hou EW, Horton JK, Bustin M, Wilson SH. 2012. HMGN1 regulates PARP-1 self-PARylation in mouse fibroblasts. *J Biol Chem*.

Mateen S, Raina K, Jain AK, Agarwal C, Chan D, Agarwal R. 2012. Epigenetic modifications and p21-cyclin B1 nexus in anticancer effect of histone deacetylase inhibitors in combination with silibinin on non-small cell lung cancer cells. *Epigenetics* **7**: 1161-1172.

Matuo R, Sousa FG, Escargueil AE, Grivicich I, Garcia-Santos D, Chies JA, Saffi J, Larsen AK, Henriques JA. 2009. 5-Fluorouracil and its active metabolite FdUMP cause DNA damage in human SW620 colon adenocarcinoma cell line. *J Appl Toxicol* **29**: 308-316.

Maurer-Gebhard M, Schmidt M, Azemar M, Stocklin E, Wels W, Groner B. 1999. A novel animal model for the evaluation of the efficacy of drugs directed against the ErbB2 receptor on metastasis formation. *Hybridoma* **18**: 69-75.

McIlwain DR, Berger T, Mak TW. 2013. Caspase Functions in Cell Death and Disease. *Cold Spring Harb Perspect Biol* **5**.

Meek DW, Anderson CW. 2009. Posttranslational Modification of p53: Cooperative Integrators of Function. *Cold Spring Harb Perspect Biol* **1**.

Meidhof S, Brabletz S, Lehmann W, Preca BT, Mock K, Ruh M, Schuler J, Berthold M, Weber A, Burk U et al. 2015. ZEB1-associated drug resistance in cancer cells is reversed by the class I HDAC inhibitor mocetinostat. *EMBO Mol Med* **7**: 831-847.

Mermoud JE, Rowbotham SP, Varga-Weisz PD. 2011. Keeping chromatin quiet. *Cell Cycle* **10**: 4017-4025.

Meyers M, Wagner MW, Hwang HS, Kinsella TJ, Boothman DA. 2001. Role of the hMLH1 DNA mismatch repair protein in fluoropyrimidine-mediated cell death and cell cycle responses. *Cancer Res* **61**: 5193-5201.

Meyers M, Wagner MW, Mazurek A, Schmutte C, Fishel R, Boothman DA. 2005. DNA mismatch repair-dependent response to fluoropyrimidine-generated damage. *J Biol Chem* **280**: 5516-5526.

Mikami S, Oya M, Mizuno R, Kosaka T, Ishida M, Kuroda N, Nagashima Y, Katsube K-i, Okada Y. 2016. Recent advances in renal cell carcinoma from a pathological point of view. *Pathol Int* **66**: 481-490.

Minamiya Y, Ono T, Saito H, Takahashi N, Ito M, Mitsui M, Motoyama S, Ogawa J. 2011. Expression of histone deacetylase 1 correlates with a poor prognosis in patients with adenocarcinoma of the lung. *Lung Cancer* **74**: 300-304.

Minucci S, Pelicci PG. 2006. Histone deacetylase inhibitors and the promise of epigenetic (and more) treatments for cancer. *Nat Rev Cancer* **6**: 38.

Mirzayans R, Andrais B, Kumar P, Murray D. 2017. Significance of Wild-Type p53 Signaling in Suppressing Apoptosis in Response to Chemical Genotoxic Agents: Impact on Chemotherapy Outcome. *Int J Mol Sci* **18**.

Mizushima N, Komatsu M. 2011. Autophagy: renovation of cells and tissues. *Cell* **147**: 728-741.

Mizushima N, Yoshimori T. 2007. How to Interpret LC3 Immunoblotting. *Autophagy* **3**: 542-545.

Montgomery RL, Davis CA, Potthoff MJ, Haberland M, Fielitz J, Qi X, Hill JA, Richardson JA, Olson EN. 2007. Histone deacetylases 1 and 2 redundantly regulate cardiac morphogenesis, growth, and contractility. *Genes Dev* **21**: 1790-1802.

Morel AP, Lievre M, Thomas C, Hinkal G, Ansieau S, Puisieux A. 2008. Generation of breast cancer stem cells through epithelial-mesenchymal transition. *PLoS One* **3**: e2888.

Moser MA, Hagelkruys A, Seiser C. 2014. Transcription and beyond: the role of mammalian class I lysine deacetylases. *Chromosoma* **123**: 67-78.

Mrakovcic M, Kleinheinz J, Fröhlich LF. 2017. Histone Deacetylase Inhibitor-Induced Autophagy in Tumor Cells: Implications for p53. *IJMS* **18**: 1883.

Muhale FA, Wetmore BA, Thomas RS, McLeod HL. 2011. Systems pharmacology assessment of the 5-fluorouracil pathway. *Pharmacogenomics* **12**: 341-350.

Muller PAJ, Vousden KH. 2013. p53 mutations in cancer. *Nat Cell Biol* **15**: 2.

Müller S, Krämer OH. 2010. Inhibitors of HDACs--effective drugs against cancer? *Curr Cancer Drug Targets* **10**: 210-228.

Münster P, Marchion D, Bicaku E, Schmitt M, Lee JH, DeConti R, Simon G, Fishman M, Minton S, Garrett C et al. 2007. Phase I Trial of Histone Deacetylase Inhibition by Valproic Acid Followed by the Topoisomerase II Inhibitor Epirubicin in Advanced Solid Tumors: A Clinical and Translational Study. *J Clin Oncol* **25**: 1979-1985.

Muzny DM Bainbridge MN Chang K Dinh HH Drummond JA Fowler G Kovar CL Lewis LR Morgan MB Newsham IF et al. 2012. Comprehensive molecular characterization of human colon and rectal cancer. *Nature* **487**: 330.

Nam EA, Zhao R, Glick GG, Bansbach CE, Friedman DB, Cortez D. 2011. Thr-1989 phosphorylation is a marker of active ataxia telangiectasia-mutated and Rad3-related (ATR) kinase. *J Biol Chem* **286**: 28707-28714.

Nebbioso A, Clarke N, Voltz E, Germain E, Ambrosino C, Bontempo P, Alvarez R, Schiavone EM, Ferrara F, Bresciani F et al. 2005. Tumor-selective action of HDAC inhibitors involves TRAIL induction in acute myeloid leukemia cells. *Nat Med* **11**: 77-84.

Nieto MA, Huang Ruby Y-J, Jackson Rebecca A, Thiery Jean P. 2016. EMT: 2016. *Cell* **166**: 21-45.

Nikolova T, Hennekes F, Bhatti A, Kaina B. 2012. Chloroethylnitrosourea-induced cell death and genotoxicity: cell cycle dependence and the role of DNA double-strand breaks, HR and NHEJ. *Cell Cycle* **11**: 2606-2619.

Nikolova T, Kiweler N, Krämer OH. 2017a. Interstrand Crosslink Repair as a Target for HDAC Inhibition. *Trends Pharmacol Sci* **38**: 822-836.

Nikolova T, Roos WP, Krämer OH, Strik HM, Kaina B. 2017b. Chloroethylating nitrosoureas in cancer therapy: DNA damage, repair and cell death signaling. *Biochim Biophys Acta* **1868**: 29-39.

Noh EJ, Lee JS. 2003. Functional interplay between modulation of histone deacetylase activity and its regulatory role in G2-M transition. *Biochem Biophys Res Commun* **310**: 267-273.

Noon AP, Vlatković N, Polański R, Maguire M, Shawki H, Parsons K, Boyd MT. 2010. p53 and MDM2 in Renal Cell Carcinoma: Biomarkers for Disease Progression and Future Therapeutic Targets? *Cancer* **116**: 780-790.

Noordhuis P, Holwerda U, Van der Wilt CL, Van Groeningen CJ, Smid K, Meijer S, Pinedo HM, Peters GJ. 2004. 5-Fluorouracil incorporation into RNA and DNA in relation to thymidylate synthase inhibition of human colorectal cancers. *Ann Oncol* **15**: 1025-1032.

Nordgard SH, Alnæs GIG, Hihn B, Lingjærde OC, Liestøl K, Tsalenko A, Sørlie T, Lønning PE, Børresen-Dale A-L, Kristensen VN. 2008. Pathway based analysis of SNPs with relevance to 5-FU therapy: Relation to intratumoral mRNA expression and survival. *Int J Cancer* **123**: 577-585.

Noro R, Miyanaga A, Minegishi Y, Okano T, Seike M, Soeno C, Kataoka K, Matsuda K, Yoshimura A, Gemma A. 2010. Histone deacetylase inhibitor enhances sensitivity of non-small-cell lung cancer cells to 5-FU/S-1 via down-regulation of thymidylate synthase expression and up-regulation of p21(waf1/cip1) expression. *Cancer Sci* **101**: 1424-1430.

Nuti M, Zizzari IG, Botticelli A, Rughetti A, Marchetti P. 2018. The ambitious role of anti angiogenesis molecules: Turning a cold tumor into a hot one. *Cancer Treat Rev* **70**: 41-46.

O'Donnell PH, Stark AL, Gamazon ER, Wheeler HE, McIlwee BE, Gorsic L, Im HK, Huang RS, Cox NJ, Dolan ME. 2012. Identification of novel germline polymorphisms governing capecitabine sensitivity. *Cancer* **118**: 4063-4073.

O'Connor Mark J. 2015. Targeting the DNA Damage Response in Cancer. *Mol Cell* **60**: 547-560.

Ocker M, Schneider-Stock R. 2007. Histone deacetylase inhibitors: signalling towards p21cip1/waf1. *Int J Biochem Cell Biol* **39**: 1367-1374.

Oehme I, Linke J-P, Böck BC, Milde T, Lodrini M, Hartenstein B, Wiegand I, Eckert C, Roth W, Kool M et al. 2013. Histone deacetylase 10 promotes autophagy-mediated cell survival. *Proc Natl Acad Sci USA* **110**: E2592-E2601.

Ogiwara H, Ui A, Otsuka A, Satoh H, Yokomi I, Nakajima S, Yasui A, Yokota J, Kohno T. 2011. Histone acetylation by CBP and p300 at double-strand break sites facilitates SWI/SNF chromatin remodeling and the recruitment of non-homologous end joining factors. *Oncogene* **30**: 2135-2146.

Okada K, Hakata S, Terashima J, Gamou T, Habano W, Ozawa S. 2016. Combination of the histone deacetylase inhibitor depsipeptide and 5-fluorouracil upregulates major histocompatibility complex class II and p21 genes and activates caspase-3/7 in human colon cancer HCT-116 cells. *Oncol Rep* **36**: 1875-1885.

Olivier M, Eeles R, Hollstein M, Khan MA, Harris CC, Hainaut P. 2002. The IARC TP53 database: new online mutation analysis and recommendations to users. *Hum Mutat* **19**: 607-614.

Olzscha H, Bekheet ME, Sheikh S, La Thangue NB. 2016. HDAC Inhibitors. in *Histone Deacetylases: Methods and Protocols* (ed. S Sarkar), pp. 281-303. Springer New York, New York, NY.

Ouyang L, Shi Z, Zhao S, Wang F-T, Zhou T-T, Liu B, Bao J-K. 2012. Programmed cell death pathways in cancer: a review of apoptosis, autophagy and programmed necrosis. *Cell Prolif* **45**: 487-498.

Overman MJ, McDermott R, Leach JL, Lonardi S, Lenz HJ, Morse MA, Desai J, Hill A, Axelson M, Moss RA et al. 2017. Nivolumab in patients with metastatic DNA mismatch repair-deficient or microsatellite instability-high colorectal cancer (CheckMate 142): an open-label, multicentre, phase 2 study. *Lancet Oncol* **18**: 1182-1191.

Owonikoko TK, Ramalingam SS, Kanterewicz B, Balius TE, Belani CP, Hershberger PA. 2010. Vorinostat increases carboplatin and paclitaxel activity in non-small-cell lung cancer cells. *Int J Cancer* **126**: 743-755.

Pacheco M, Nielsen TO. 2011. Histone deacetylase 1 and 2 in mesenchymal tumors. *Mod Pathol* **25**: 222.

Påhlman LA, Hohenberger WM, Matzel K, Sugihara K, Quirke P, Glimelius B. 2016. Should the Benefit of Adjuvant Chemotherapy in Colon Cancer Be Re-Evaluated? *J Clin Oncol* **34**: 1297-1299.

Papamichos-Chronakis M, Peterson CL. 2012. Chromatin and the genome integrity network. *Nat Rev Genet* **14**: 62.

Park J-H, Park E-J, Hur S-K, Kim S, Kwon J. 2009. Mammalian SWI/SNF chromatin remodeling complexes are required to prevent apoptosis after DNA damage. *DNA Repair* **8**: 29-39.

Park JH, Park EJ, Lee HS, Kim SJ, Hur SK, Imbalzano AN, Kwon J. 2006. Mammalian SWI/SNF complexes facilitate DNA double-strand break repair by promoting gamma-H2AX induction. *EMBO J* **25**: 3986-3997.

Patard J-J, Leray E, Rodriguez A, Rioux-Leclercq N, Guillé F, Lobel B. 2003. Correlation between Symptom Graduation, Tumor Characteristics and Survival in Renal Cell Carcinoma. *Eur Urol* **44**: 226-232.

PDQ Adult Treatment Editorial Board. Colon Cancer Treatment (PDQ®): Health Professional Version. 2018a Aug 16. In: PDQ Cancer Information Summaries. Bethesda (MD): National Cancer Institute (US); 2002-. Available from: https://www.ncbi.nlm.nih.gov/books/NBK65858/

PDQ Screening and Prevention Editorial Board. Colorectal Cancer Prevention (PDQ®): Health Professional Version. 2018b Mar 1. In: PDQ Cancer Information Summaries. Bethesda (MD): National Cancer Institute (US); 2002-. Available from: https://www.ncbi.nlm.nih.gov/books/NBK65779/

PDQ Screening and Prevention Editorial Board. Colorectal Cancer Screening (PDQ®): Health Professional Version. 2018c Aug 2. In: PDQ Cancer Information Summaries. Bethesda (MD): National Cancer Institute (US); 2002-. Available from: https://www.ncbi.nlm.nih.gov/books/NBK65825/

PDQ Cancer Genetics Editorial Board. Genetics of Colorectal Cancer (PDQ®): Health Professional Version. 2018d Jun 14. In: PDQ Cancer Information Summaries. Bethesda (MD): National Cancer Institute (US); 2002-. Available from: https://www.ncbi.nlm.nih.gov/books/NBK126744/

PDQ Cancer Genetics Editorial Board. Genetics of Kidney Cancer (Renal Cell Cancer) (PDQ®): Health Professional Version. 2018e May 18. In: PDQ Cancer Information Summaries. Bethesda (MD): National Cancer Institute (US); 2002-. Available from: https://www.ncbi.nlm.nih.gov/books/NBK169222/

PDQ Adult Treatment Editorial Board. Rectal Cancer Treatment (PDQ®): Health Professional Version. 2018f Aug 17. In: PDQ Cancer Information Summaries. Bethesda (MD): National Cancer Institute (US); 2002-. Available from: https://www.ncbi.nlm.nih.gov/books/NBK65965/

PDQ Adult Treatment Editorial Board. Renal Cell Cancer Treatment (PDQ®): Health Professional Version. 2018g Apr 5. In: PDQ Cancer Information Summaries. Bethesda (MD): National Cancer Institute (US); 2002-. Available from: https://www.ncbi.nlm.nih.gov/books/NBK65815/

Peinado H, Ballestar E, Esteller M, Cano A. 2004. Snail mediates E-cadherin repression by the recruitment of the Sin3A/histone deacetylase 1 (HDAC1)/HDAC2 complex. *Mol Cell Biol* **24**: 306-319.

Peinado H, Olmeda D, Cano A. 2007. Snail, Zeb and bHLH factors in tumour progression: an alliance against the epithelial phenotype? *Nat Rev Cancer* **7**: 415.

Peserico A, Simone C. 2011. Physical and functional HAT/HDAC interplay regulates protein acetylation balance. *J Biomed Biotechnol* **2011**: 371832.

Pettersen HS, Visnes T, Vågbø CB, Svaasand EK, Doseth B, Slupphaug G, Kavli B, Krokan HE. 2011. UNG-initiated base excision repair is the major repair route for 5-fluorouracil in DNA, but 5-fluorouracil cytotoxicity depends mainly on RNA incorporation. *Nucleic Acids Res* **39**: 8430-8444.

Pili R, Salumbides B, Zhao M, Altiok S, Qian D, Zwiebel J, Carducci MA, Rudek MA. 2011. Phase I study of the histone deacetylase inhibitor entinostat in combination with 13-cis retinoic acid in patients with solid tumours. *Br J Cancer* **106**: 77.

Pinkerneil M, Hoffmann MJ, Deenen R, Köhrer K, Arent T, Schulz WA, Niegisch G. 2016. Inhibition of Class I Histone Deacetylases 1 and 2 Promotes Urothelial Carcinoma Cell Death by Various Mechanisms. *Mol Cancer Ther* **15**: 299-312.

Pino MS, Chung DC. 2010. The Chromosomal Instability Pathway in Colon Cancer. *Gastroenterology* **138**: 2059-2072.

Preuss I, Eberhagen I, Haas S, Eibl RH, Kaufmann M, Minckwitz GV, Kaina B. 1995. O6-methylguanine-DNA methyltransferase activity in breast and brain tumors. *Int J Cancer* **61**: 321-326.

Price Brendan D, D'Andrea Alan D. 2013. Chromatin Remodeling at DNA Double-Strand Breaks. *Cell* **152**: 1344-1354.

Pritchard DM, Watson AJ, Potten CS, Jackman AL, Hickman JA. 1997. Inhibition by uridine but not thymidine of p53-dependent intestinal apoptosis initiated by 5-fluorouracil: evidence for the involvement of RNA perturbation. *Proc Natl Acad Sci U S A* **94**: 1795-1799.

Przybycin CG, Harper HL, Reynolds JP, Magi-Galluzzi C, Nguyen JK, Wu A, Sangoi AR, Liu PS, Umar S, Mehra R et al. 2018. Acquired Cystic Disease-associated Renal Cell Carcinoma (ACD-RCC): A Multiinstitutional Study of 40 Cases With Clinical Follow-up. *Am J Surg Pathol* **42**: 1156-1165.

Punt CJA, Koopman M, Vermeulen L. 2016. From tumour heterogeneity to advances in precision treatment of colorectal cancer. *Nat Rev Clin Oncol* **14**: 235.

Puts GS, Leonard MK, Pamidimukkala NV, Snyder DE, Kaetzel DM. 2017. Nuclear functions of NME proteins. *Lab Invest* **98**: 211.

Qi W, Wang R, Chen H, Wang X, Xiao T, Boldogh I, Ba X, Han L, Zeng X. 2015. BRG1 promotes the repair of DNA double-strand breaks by facilitating the replacement of RPA with RAD51. *J Cell Sci* **128**: 317-330.

Radcliffe PA, Hirata D, Vardy L, Toda T. 1999. Functional dissection and hierarchy of tubulin-folding cofactor homologues in fission yeast. *Mol Biol Cell* **10**: 2987-3001.

Rao R, Balusu R, Fiskus W, Mudunuru U, Venkannagari S, Chauhan L, Smith JE, Hembruff SL, Ha K, Atadja P et al. 2012. Combination of pan-histone deacetylase inhibitor and autophagy inhibitor exerts superior efficacy against triple-negative human breast cancer cells. *Mol Cancer Ther* **11**: 973-983.

Rattner BP, Yusufzai T, Kadonaga JT. 2009. HMGN Proteins Act in Opposition to ATP-Dependent Chromatin Remodeling Factors to Restrict Nucleosome Mobility. *Mol Cell* **34**: 620-626.

Rauch A, Carlstedt A, Emmerich C, Mustafa AM, Göder A, Knauer SK, Linnebacher M, Heinzel T, Krämer OH. 2018. Survivin antagonizes chemotherapy-induced cell death of colorectal cancer cells. *Oncotarget* **9**: 27835-27850.

Rauch A, Hennig D, Schäfer C, Wirth M, Marx C, Heinzel T, Schneider G, Krämer OH. 2014. Survivin and YM155: How faithful is the liaison? *Biochim Biophys Acta* **1845**: 202-220.

Ravikumar B, Sarkar S, Davies JE, Futter M, Garcia-Arencibia M, Green-Thompson ZW, Jimenez-Sanchez M, Korolchuk VI, Lichtenberg M, Luo S et al. 2010. Regulation of Mammalian Autophagy in Physiology and Pathophysiology. *Physiol Rev* **90**: 1383-1435.

Ree AH, Folkvord S, Flatmark K. 2008. HDAC2 deficiency and histone acetylation. *Nat Genet* **40**: 812-813; author reply 813.

Reeves R. 2015. High mobility group (HMG) proteins: Modulators of chromatin structure and DNA repair in mammalian cells. *DNA Repair* **36**: 122-136.

Reeves R, Adair JE. 2005. Role of high mobility group (HMG) chromatin proteins in DNA repair. *DNA Repair* **4**: 926-938.

Reisman D, Glaros S, Thompson EA. 2009. The SWI/SNF complex and cancer. *Oncogene* **28**: 1653.

Rhodes LV, Tate CR, Segar HC, Burks HE, Phamduy TB, Hoang V, Elliott S, Gilliam D, Pounder FN, Anbalagan M et al. 2014. Suppression of triple-negative breast cancer metastasis by pan-DAC inhibitor panobinostat via inhibition of ZEB family of EMT master regulators. *Breast Cancer Res Treat* **145**: 593-604.

Richon VM, Sandhoff TW, Rifkind RA, Marks PA. 2000. Histone deacetylase inhibitor selectively induces p21WAF1 expression and gene-associated histone acetylation. *Proc Natl Acad Sci USA* **97**: 10014-10019.

Robert C, Rassool FV. 2012. Chapter Three - HDAC Inhibitors: Roles of DNA Damage and Repair. in *Adv Cancer Res* (ed. S Grant), pp. 87-129. Academic Press.

Robins P, Harris AL, Goldsmith I, Lindahl T. 1983. Cross-linking of DNA induced by chloroethylnitrosourea is presented by O6-methylguanine-DNA methyltransferase. *Nucleic Acids Res* **11**: 7743-7758.

Robles AI, Harris CC. 2010. Clinical Outcomes and Correlates of TP53 Mutations and Cancer. *Cold Spring Harb Perspect Biol* **2**.

Rodgers K, McVey M. 2016. Error-Prone Repair of DNA Double-Strand Breaks. *J Cell Physiol* **231**: 15-24.

Rogakou EP, Boon C, Redon C, Bonner WM. 1999. Megabase chromatin domains involved in DNA double-strand breaks in vivo. *J Cell Biol* **146**: 905-916.

Rogakou EP, Pilch DR, Orr AH, Ivanova VS, Bonner WM. 1998. DNA Double-stranded Breaks Induce Histone H2AX Phosphorylation on Serine 139. *J Biol Chem* **273**: 5858-5868.

Roos WP, Kaina B. 2013. DNA damage-induced cell death: From specific DNA lesions to the DNA damage response and apoptosis. *Cancer Lett* **332**: 237-248.

Roos WP, Krumm A. 2016. The multifaceted influence of histone deacetylases on DNA damage signalling and DNA repair. *Nucleic Acids Res* **44**: 10017-10030.

Roos WP, Thomas AD, Kaina B. 2015. DNA damage and the balance between survival and death in cancer biology. *Nat Rev Cancer* **16**: 20.

Ropero S, Fraga MF, Ballestar E, Hamelin R, Yamamoto H, Boix-Chornet M, Caballero R, Alaminos M, Setien F, Paz MF et al. 2006. A truncating mutation of HDAC2 in human cancers confers resistance to histone deacetylase inhibition. *Nat Genet* **38**: 566-569.

Rother MB, van Attikum H. 2017. DNA repair goes hip-hop: SMARCA and CHD chromatin remodellers join the break dance. *Philos Trans R Soc Lond B Biol Sci* **372**: 20160285.

Rothkamm K, Löbrich M. 2003. Evidence for a lack of DNA double-strand break repair in human cells exposed to very low x-ray doses. *Proc Natl Acad Sci USA* **100**: 5057-5062.

Rowbotham Samuel P, Barki L, Neves-Costa A, Santos F, Dean W, Hawkes N, Choudhary P, Will WR, Webster J, Oxley D et al. 2011. Maintenance of Silent Chromatin through Replication Requires SWI/SNF-like Chromatin Remodeler SMARCAD1. *Mol Cell* **42**: 285-296.

Roy SS, Gonugunta VK, Bandyopadhyay A, Rao MK, Goodall GJ, Sun LZ, Tekmal RR, Vadlamudi RK. 2014. Significance of PELP1/HDAC2/miR-200 regulatory network in EMT and metastasis of breast cancer. *Oncogene* **33**: 3707-3716.

Ruefli AA, Ausserlechner MJ, Bernhard D, Sutton VR, Tainton KM, Kofler R, Smyth MJ, Johnstone RW. 2001. The histone deacetylase inhibitor and chemotherapeutic agent suberoylanilide hydroxamic acid (SAHA) induces a cell-death pathway characterized by cleavage of Bid and production of reactive oxygen species. *Proc Natl Acad Sci U S A* **98**: 10833-10838.

Ruscetti M, Dadashian EL, Guo W, Quach B, Mulholland DJ, Park JW, Tran LM, Kobayashi N, Bianchi-Frias D, Xing Y et al. 2016. HDAC inhibition impedes epithelial-mesenchymal plasticity and suppresses metastatic, castration-resistant prostate cancer. *Oncogene* **35**: 3781-3795.

Rustum YM. 2004. Thymidylate synthase: a critical target in cancer therapy? *Front Biosci* **9**: 2467-2473.

Rustum YM, Harstrick A, Cao S, Vanhoefer U, Yin MB, Wilke H, Seeber S. 1997. Thymidylate synthase inhibitors in cancer therapy: direct and indirect inhibitors. *J Clin Oncol* **15**: 389-400.

Rutman RJ, Cantarow A, Paschkis KE. 1954. Studies in 2-Acetylaminofluorene Carcinogenesis. III. The Utilization of Uracil-2-C14 by Preneoplastic Rat Liver and Rat Hepatoma. *Cancer Res* **14**: 119-123.

Ryan QC, Headlee D, Acharya M, Sparreboom A, Trepel JB, Ye J, Figg WD, Hwang K, Chung EJ, Murgo A et al. 2005. Phase I and pharmacokinetic study of MS-275, a histone deacetylase inhibitor, in patients with advanced and refractory solid tumors or lymphoma. *J Clin Oncol* **23**: 3912-3922.

Sanchez-Tillo E, Lazaro A, Torrent R, Cuatrecasas M, Vaquero EC, Castells A, Engel P, Postigo A. 2010. ZEB1 represses E-cadherin and induces an EMT by recruiting the SWI/SNF chromatin-remodeling protein BRG1. *Oncogene* **29**: 3490-3500.

Sandor V, Senderowicz A, Mertins S, Sackett D, Sausville E, Blagosklonny MV, Bates SE. 2000. P21-dependent g(1)arrest with downregulation of cyclin D1 and upregulation of cyclin E by the histone deacetylase inhibitor FR901228. *Br J Cancer* **83**: 817-825.

Santoro F, Botrugno OA, Dal Zuffo R, Pallavicini I, Matthews GM, Cluse L, Barozzi I, Senese S, Fornasari L, Moretti S et al. 2013. A dual role for Hdac1: oncosuppressor in tumorigenesis, oncogene in tumor maintenance. *Blood* **121**: 3459-3468.

Sarasqueta AF, Forte G, Corver WE, de Miranda NF, Ruano D, van Eijk R, Oosting J, Tollenaar RAEM, van Wezel T, Morreau H. 2013. Integral analysis of p53 and its value as prognostic factor in sporadic colon cancer. *BMC Cancer* **13**: 277-277.

Sartori AA, Lukas C, Coates J, Mistrik M, Fu S, Bartek J, Baer R, Lukas J, Jackson SP. 2007. Human CtIP promotes DNA end resection. *Nature* **450**: 509-514.

Schech A, Kazi A, Yu S, Shah P, Sabnis G. 2015. Histone Deacetylase Inhibitor Entinostat Inhibits Tumor-Initiating Cells in Triple-Negative Breast Cancer Cells. *Mol Cancer Ther* **14**: 1848-1857.

Schneider G, Henrich A, Greiner G, Wolf V, Lovas A, Wieczorek M, Wagner T, Reichardt S, von Werder A, Schmid RM et al. 2010. Cross talk between stimulated NF-κB and the tumor suppressor p53. *Oncogene* **29**: 2795.

Schuler S, Fritsche P, Diersch S, Arlt A, Schmid RM, Saur D, Schneider G. 2010. HDAC2 attenuates TRAIL-induced apoptosis of pancreatic cancer cells. *Mol Cancer* **9**: 80.

Schuster-Böckler B, Lehner B. 2012. Chromatin organization is a major influence on regional mutation rates in human cancer cells. *Nature* **488**: 504.

Sebesta M, Burkovics P, Haracska L, Krejci L. 2011. Reconstitution of DNA repair synthesis in vitro and the role of polymerase and helicase activities. *DNA Repair (Amst)* **10**: 567-576.

Seligson DB, Horvath S, McBrian MA, Mah V, Yu H, Tze S, Wang Q, Chia D, Goodglick L, Kurdistani SK. 2009. Global Levels of Histone Modifications Predict Prognosis in Different Cancers. *Am J Pathol* **174**: 1619-1628.

Seligson DB, Horvath S, Shi T, Yu H, Tze S, Grunstein M, Kurdistani SK. 2005. Global histone modification patterns predict risk of prostate cancer recurrence. *Nature* **435**: 1262.

Seluanov A, Mao Z, Gorbunova V. 2010. Analysis of DNA double-strand break (DSB) repair in mammalian cells. *J Vis Exp*: 2002.

Shao Y, Gao Z, Marks PA, Jiang X. 2004. Apoptotic and autophagic cell death induced by histone deacetylase inhibitors. *Proc Natl Acad Sci U S A* **101**: 18030-18035.

Shen X, Li L. 2010. Mutagenic repair of DNA interstrand crosslinks. *Environ Mol Mutag* **51**: 493-499.

Shieh SY, Ikeda M, Taya Y, Prives C. 1997. DNA damage-induced phosphorylation of p53 alleviates inhibition by MDM2. *Cell* **91**: 325-334.

Shinagawa T, Tanaka T, Nozawa H, Emoto S, Murono K, Kaneko M, Sasaki K, Otani K, Nishikawa T, Hata K et al. 2018. Comparison of the guidelines for colorectal cancer in Japan, the USA and Europe. *Ann Gastroenterol Surg* **2**: 6-12.

Shuch B, Amin A, Armstrong AJ, Eble JN, Ficarra V, Lopez-Beltran A, Martignoni G, Rini BI, Kutikov A. 2015. Understanding Pathologic Variants of Renal Cell Carcinoma: Distilling Therapeutic Opportunities from Biologic Complexity. *Eur Urol* **67**: 85-97.

Sidhar SK, Clark J, Gill S, Hamoudi R, Crew AJ, Gwilliam R, Ross M, Linehan WM, Birdsall S, Shipley J et al. 1996. The t(X;1)(p11.2;q21.2) translocation in papillary renal cell carcinoma fuses a novel gene PRCC to the TFE3 transcription factor gene. *Hum Mol Genet* **5**: 1333-1338.

Siegel RL, Miller KD, Jemal A. 2018. Cancer statistics, 2018. *CA Cancer J Clin* **68**: 7-30.

Sinicrope FA, Okamoto K, Kasi PM, Kawakami H. 2016. Molecular Biomarkers in the Personalized Treatment of Colorectal Cancer. *Clin Gastroenterol Hepatol* **14**: 651-658.

Smith-Roe SL, Nakamura J, Holley D, Chastain PD, 2nd, Rosson GB, Simpson DA, Ridpath JR, Kaufman DG, Kaufmann WK, Bultman SJ. 2015. SWI/SNF complexes are required for full activation of the DNA-damage response. *Oncotarget* **6**: 732-745.

Smith J, Tho LM, Xu N, Gillespie DA. 2010. The ATM-Chk2 and ATR-Chk1 pathways in DNA damage signaling and cancer. *Adv Cancer Res* **108**: 73-112.

Sonnemann J, Marx C, Becker S, Wittig S, Palani CD, Krämer OH, Beck JF. 2014. p53-dependent and p53-independent anticancer effects of different histone deacetylase inhibitors. *Br J Cancer* **110**: 656-667.

Srivastava RK, Kurzrock R, Shankar S. 2010. MS-275 sensitizes TRAIL-resistant breast cancer cells, inhibits angiogenesis and metastasis, and reverses epithelial-mesenchymal transition in vivo. *Mol Cancer Ther* **9**: 3254-3266.

Stankov MV, El Khatib M, Kumar Thakur B, Heitmann K, Panayotova-Dimitrova D, Schoening J, Bourquin JP, Schweitzer N, Leverkus M, Welte K et al. 2014. Histone deacetylase inhibitors induce apoptosis in myeloid leukemia by suppressing autophagy. *Leukemia* **28**: 577-588.

Steinhusen U, Weiske J, Badock V, Tauber R, Bommert K, Huber O. 2001. Cleavage and Shedding of E-cadherin after Induction of Apoptosis. *J Biol Chem* **276**: 4972-4980.

Stiff T, Walker SA, Cerosaletti K, Goodarzi AA, Petermann E, Concannon P, O'Driscoll M, Jeggo PA. 2006. ATR-dependent phosphorylation and activation of ATM in response to UV treatment or replication fork stalling. *The EMBO Journal* **25**: 5775-5782.

Strano S, Dell'Orso S, Di Agostino S, Fontemaggi G, Sacchi A, Blandino G. 2007. Mutant p53: an oncogenic transcription factor. *Oncogene* **26**: 2212.

Stypula-Cyrus Y, Damania D, Kunte DP, Cruz MD, Subramanian H, Roy HK, Backman V. 2013. HDAC up-regulation in early colon field carcinogenesis is involved in cell tumorigenicity through regulation of chromatin structure. *PLoS One* **8**: e64600.

Sun X-X, Dai M-S, Lu H. 2007. 5-Fluorouracil Activation of p53 Involves an MDM2-Ribosomal Protein Interaction. *J Biol Chem* **282**: 8052-8059.

Supek F, Lehner B. 2015. Differential DNA mismatch repair underlies mutation rate variation across the human genome. *Nature* **521**: 81.

Suter CM, Norrie M, Ku SL, Cheong KF, Tomlinson I, Ward RL. 2003. CpG island methylation is a common finding in colorectal cancer cell lines. *British Journal Of Cancer* **88**: 413.

Suzuki T, Terao S, Acharya B, Naoe M, Yamamoto S, Okamura H, Gotoh A. 2010. The antitumour effect of gamma-delta T-cells is enhanced by valproic acid-induced up-regulation of NKG2D ligands. *Anticancer Res* **30**: 4509-4513.

Swenberg JA, Lu K, Moeller BC, Gao L, Upton PB, Nakamura J, Starr TB. 2011. Endogenous versus Exogenous DNA Adducts: Their Role in Carcinogenesis, Epidemiology, and Risk Assessment. *Toxicol Sci* **120**: S130-S145.

Swift LH, Golsteyn RM. 2014. Genotoxic anti-cancer agents and their relationship to DNA damage, mitosis, and checkpoint adaptation in proliferating cancer cells. *Int J Mol Sci* **15**: 3403-3431.

Symington LS. 2014. End Resection at Double-Strand Breaks: Mechanism and Regulation. *Cold Spring Harb Perspect Biol* **6**.

Tanaka H, Arakawa H, Yamaguchi T, Shiraishi K, Fukuda S, Matsui K, Takei Y, Nakamura Y. 2000. A ribonucleotide reductase gene involved in a p53-dependent cell-cycle checkpoint for DNA damage. *Nature* **404**: 42-49.

Tang HM, Kuay KT, Koh PF, Asad M, Tan TZ, Chung VY, Lee SC, Thiery JP, Huang RJ. 2016. An epithelial marker promoter induction screen identifies histone deacetylase inhibitors to restore epithelial differentiation and abolishes anchorage independence growth in cancers. *Cell Death Discov* **2**: 16041.

Tanida I, Ueno T, Kominami E. 2004. LC3 conjugation system in mammalian autophagy. *Int J Biochem Cell Biol* **36**: 2503-2518.

Tannapfel A, Hahn HA, Katalinic A, Fietkau RJ, Kuhn R, Wittekind CW. 1997. Incidence of apoptosis, cell proliferation and P53 expression in renal cell carcinomas. *Anticancer Res* **17**: 1155-1162.

Terranova-Barberio M, Thomas S, Ali N, Pawlowska N, Park J, Krings G, Rosenblum MD, Budillon A, Munster PN. 2017. HDAC inhibition potentiates immunotherapy in triple negative breast cancer. *Oncotarget* **8**: 114156-114172.

Terranova-Barberio M, Thomas S, Munster PN. 2016. Epigenetic modifiers in immunotherapy: a focus on checkpoint inhibitors. *Immunotherapy* **8**: 705-719.

Terui R, Nagao K, Kawasoe Y, Taki K, Higashi TL, Tanaka S, Nakagawa T, Obuse C, Masukata H, Takahashi TS. 2018. Nucleosomes around a mismatched base pair are excluded via an Msh2-dependent reaction with the aid of SNF2 family ATPase Smarcad1. *Genes Dev* **32**: 806-821.

Thiery JP, Acloque H, Huang RYJ, Nieto MA. 2009. Epithelial-Mesenchymal Transitions in Development and Disease. *Cell* **139**: 871-890.

Torgersen ML, Engedal N, Boe SO, Hokland P, Simonsen A. 2013. Targeting autophagy potentiates the apoptotic effect of histone deacetylase inhibitors in t(8;21) AML cells. *Blood* **122**: 2467-2476.

Torre LA, Bray F, Siegel RL, Ferlay J, Lortet-Tieulent J, Jemal A. 2015. Global cancer statistics, 2012. *CA Cancer J Clin* **65**: 87-108.

Toyota M, Ahuja N, Ohe-Toyota M, Herman JG, Baylin SB, Issa JP. 1999. CpG island methylator phenotype in colorectal cancer. *Proc Natl Acad Sci U S A* **96**: 8681-8686.

Tse JWT, Jenkins LJ, Chionh F, Mariadason JM. 2017. Aberrant DNA Methylation in Colorectal Cancer: What Should We Target? *Trends in Cancer* **3**: 698-712.

Van Cutsem E, Tabernero J, Lakomy R, Prenen H, Prausova J, Macarulla T, Ruff P, van Hazel GA, Moiseyenko V, Ferry D et al. 2012. Addition of aflibercept to fluorouracil, leucovorin, and irinotecan improves survival in a phase III randomized trial in patients with metastatic colorectal cancer previously treated with an oxaliplatin-based regimen. *J Clin Oncol* **30**: 3499-3506.

Vernole P, Muzi A, Volpi A, Terrinoni A, Dorio AS, Tentori L, Shah GM, Graziani G. 2011. Common fragile sites in colon cancer cell lines: role of mismatch repair, RAD51 and poly(ADP-ribose) polymerase-1. *Mutat Res* **712**: 40-48.

Vignard J, Mirey G, Salles B. 2013. Ionizing-radiation induced DNA double-strand breaks: A direct and indirect lighting up. *Radiother Oncol* **108**: 362-369.

Vilar E, Scaltriti M, Balmaña J, Saura C, Guzman M, Arribas J, Baselga J, Tabernero J. 2008. Microsatellite instability due to hMLH1 deficiency is associated with increased cytotoxicity to irinotecan in human colorectal cancer cell lines. *Br J Cancer* **99**: 1607-1612.

Vilenchik MM, Knudson AG. 2003. Endogenous DNA double-strand breaks: Production, fidelity of repair, and induction of cancer. *Proc Natl Acad Sci USA* **100**: 12871-12876.

Vogelstein B, Fearon ER, Hamilton SR, Kern SE, Preisinger AC, Leppert M, Smits AMM, Bos JL. 1988. Genetic Alterations during Colorectal-Tumor Development. *N Engl J Med* **319**: 525-532.

Vrana JA, Decker RH, Johnson CR, Wang Z, Jarvis WD, Richon VM, Ehinger M, Fisher PB, Grant S. 1999. Induction of apoptosis in U937 human leukemia cells by suberoylanilide hydroxamic acid (SAHA) proceeds through pathways that are regulated by Bcl-2/Bcl-XL, c-Jun, and p21CIP1, but independent of p53. *Oncogene* **18**: 7016-7025.

Wagner T, Brand P, Heinzel T, Krämer OH. 2014. Histone deacetylase 2 controls p53 and is a critical factor in tumorigenesis. *Biochim Biophys Acta* **1846**: 524-538.

Wagner T, Kiweler N, Wolff K, Knauer SK, Brandl A, Hemmerich P, Dannenberg JH, Heinzel T, Schneider G, Krämer OH. 2015. Sumoylation of HDAC2 promotes NF-kappaB-dependent gene expression. *Oncotarget* **6**: 7123-7135.

Walther A, Johnstone E, Swanton C, Midgley R, Tomlinson I, Kerr D. 2009. Genetic prognostic and predictive markers in colorectal cancer. *Nat Rev Cancer* **9**: 489.

Wang J, Xu MQ, Jiang XL, Mei XY, Liu XG. 2018. Histone deacetylase inhibitor SAHA-induced epithelial-mesenchymal transition by upregulating Slug in lung cancer cells. *Anticancer Drugs* **29**: 80-88.

Wang X, Sun Q. 2017. TP53 mutations, expression and interaction networks in human cancers. *Oncotarget* **8**: 624-643.

Wang YL, Liui HL, Fu RG, Wang ZW, Ren HT, Dai ZJ, Jing YY, Li Y. 2016. HDAC Inhibitor Oxamflatin Induces Morphological Changes and has Strong Cytostatic Effects in Ovarian Cancer Cell Lines. *Curr Mol Med* **16**: 232-242.

Wang Z, Peng S, Jiang N, Wang A, Liu S, Xie H, Guo L, Cai Q, Niu Y. 2017. Prognostic and clinicopathological value of p53 expression in renal cell carcinoma: a meta-analysis. *Oncotarget* **8**: 102361-102370.

Wapenaar H, Dekker FJ. 2016. Histone acetyltransferases: challenges in targeting bi-substrate enzymes. *Clin Epigenetics* **8**: 59.

Warburton HE, Brady M, Vlatković N, Linehan WM, Parsons K, Boyd MT. 2005. p53 Regulation and Function in Renal Cell Carcinoma. *Cancer Res* **65**: 6498-6503.

Ward IM, Chen J. 2001. Histone H2AX is phosphorylated in an ATR-dependent manner in response to replicational stress. *J Biol Chem* **276**: 47759-47762.

Ward JF. 1988. DNA Damage Produced by Ionizing Radiation in Mammalian Cells: Identities, Mechanisms of Formation, and Reparability. in *Prog Nucleic Acid Res Mol Biol* (eds. WE Cohn, K Moldave), pp. 95-125. Academic Press.

Wei Y, Kadia T, Tong W, Zhang M, Jia Y, Yang H, Hu Y, Tambaro FP, Viallet J, O'Brien S et al. 2010. The combination of a histone deacetylase inhibitor with the Bcl-2 homology domain-3 mimetic GX15-070 has synergistic antileukemia activity by activating both apoptosis and autophagy. *Clin Cancer Res* **16**: 3923-3932.

Weichert W. 2009. HDAC expression and clinical prognosis in human malignancies. *Cancer Lett* **280**: 168-176.

Weichert W, Röske A, Niesporek S, Noske A, Buckendahl A-C, Dietel M, Gekeler V, Boehm M, Beckers T, Denkert C. 2008. Class I Histone Deacetylase Expression Has Independent Prognostic Impact in Human Colorectal Cancer: Specific Role of Class I Histone Deacetylases In vitro and In vivo *Clin Cancer Res* **14**: 1669-1677.

White E. 2012. Deconvoluting the context-dependent role for autophagy in cancer. *Nat Rev Cancer* **12**: 401.

Wiencke JK, Wiemels J. 1995. Genotoxicity of 1,3-bis(2-chloroethyl)-1-nitrosourea (BCNU). *Mutat Res* **339**: 91-119.

Winter M, Moser MA, Meunier D, Fischer C, Machat G, Mattes K, Lichtenberger BM, Brunmeir R, Weissmann S, Murko C et al. 2013. Divergent roles of HDAC1 and HDAC2 in the regulation of epidermal development and tumorigenesis. *EMBO J* **32**: 3176-3191.

Wood LD, Parsons DW, Jones S, Lin J, Sjöblom T, Leary RJ, Shen D, Boca SM, Barber T, Ptak J et al. 2007. The Genomic Landscapes of Human Breast and Colorectal Cancers. *Science* **318**: 1108-1113.

Woods DM, Sodre AL, Villagra A, Sarnaik A, Sotomayor EM, Weber J. 2015. HDAC Inhibition Upregulates PD-1 Ligands in Melanoma and Augments Immunotherapy with PD-1 Blockade. *Cancer Immunol Res* **3**: 1375-1385.

Woods DM, Woan K, Cheng F, Wang H, Perez-Villarroel P, Lee C, Lienlaf M, Atadja P, Seto E, Weber J et al. 2013. The antimelanoma activity of the histone deacetylase inhibitor panobinostat (LBH589) is mediated by direct tumor cytotoxicity and increased tumor immunogenicity. *Melanoma Res* **23**: 341-348.

Wu MZ, Tsai YP, Yang MH, Huang CH, Chang SY, Chang CC, Teng SC, Wu KJ. 2011. Interplay between HDAC3 and WDR5 is essential for hypoxia-induced epithelial-mesenchymal transition. *Mol Cell* **43**: 811-822.

Wu S, Luo Z, Yu PJ, Xie H, He YW. 2016a. Suberoylanilide hydroxamic acid (SAHA) promotes the epithelial mesenchymal transition of triple negative breast cancer cells via HDAC8/FOXA1 signals. *Biol Chem* **397**: 75-83.

Wu Y, Lyu H, Liu H, Shi X, Song Y, Liu B. 2016b. Downregulation of the long noncoding RNA GAS5-AS1 contributes to tumor metastasis in non-small cell lung cancer. *Sci Rep* **6**: 31093.

Wyatt HDM, West SC. 2014. Holliday Junction Resolvases. *Cold Spring Harb Perspect Biol* **6**.

Wyatt MD, Wilson DM. 2009. Participation of DNA repair in the response to 5-fluorouracil. *Cell Mol Life Sci* **66**: 788-799.

Xiong Y, Hannon GJ, Zhang H, Casso D, Kobayashi R, Beach D. 1993. p21 is a universal inhibitor of cyclin kinases. *Nature* **366**: 701.

Xu L, Tong R, Cochran DM, Jain RK. 2005. Blocking platelet-derived growth factor-D/platelet-derived growth factor receptor beta signaling inhibits human renal cell carcinoma progression in an orthotopic mouse model. *Cancer Res* **65**: 5711-5719.

Xue L, Zhou B, Liu X, Qiu W, Jin Z, Yen Y. 2003. Wild-type p53 regulates human ribonucleotide reductase by protein-protein interaction with p53R2 as well as hRRM2 subunits. *Cancer Res* **63**: 980-986.

Yamada T, Horinaka M, Shinnoh M, Yoshioka T, Miki T, Sakai T. 2013. A novel HDAC inhibitor OBP-801 and a PI3K inhibitor LY294002 synergistically induce apoptosis via the suppression of survivin and XIAP in renal cell carcinoma. *Int J Oncol* **43**: 1080-1086.

Yamaguchi T, Cubizolles F, Zhang Y, Reichert N, Kohler H, Seiser C, Matthias P. 2010. Histone deacetylases 1 and 2 act in concert to promote the G1-to-S progression. *Genes Dev* **24**: 455-469.

Yang K, Guo R, Xu D. 2016. Non-homologous end joining: advances and frontiers. *Acta Biochimica et Biophysica Sinica* **48**: 632-640.

Yang X-J, Seto E. 2008. The Rpd3/Hda1 family of lysine deacetylases: from bacteria and yeast to mice and men. *Nat Rev Mol Cell Biol* **9**: 206.

Yao X, Ireland SK, Pham T, Temple B, Chen R, Raj MH, Biliran H. 2014. TLE1 promotes EMT in A549 lung cancer cells through suppression of E-cadherin. *Biochem Biophys Res Commun* **455**: 277-284.

Ye Y, Xiao Y, Wang W, Yearsley K, Gao JX, Shetuni B, Barsky SH. 2010. ERalpha signaling through slug regulates E-cadherin and EMT. *Oncogene* **29**: 1451-1462.

Yoo CB, Yun SM, Jo C, Koh YH. 2012. gamma-Secretase-dependent cleavage of E-cadherin by staurosporine in breast cancer cells. *Cell Commun Adhes* **19**: 11-16.

Yu L, Lenardo MJ, Baehrecke EH. 2004. Autophagy and caspases: a new cell death program. *Cell Cycle* **3**: 1124-1126.

Zeisberg M, Neilson EG. 2009. Biomarkers for epithelial-mesenchymal transitions. *J Clin Invest* **119**: 1429-1437.

Zhang J, Ng S, Wang J, Zhou J, Tan SH, Yang N, Lin Q, Xia D, Shen HM. 2015. Histone deacetylase inhibitors induce autophagy through FOXO1-dependent pathways. *Autophagy* **11**: 629-642.

Zhang J, Zhong Q. 2014. Histone deacetylase inhibitors and cell death. *Cell Mol Life Sci* **71**: 3885-3901.

Zhang L, Zhang Q, Jones K, Patel M, Gong F. 2009. The chromatin remodeling factor BRG1 stimulates nucleotide excision repair by facilitating recruitment of XPC to sites of DNA damage. *Cell Cycle* **8**: 3953-3959.

Zhang XD, Gillespie SK, Borrow JM, Hersey P. 2004. The histone deacetylase inhibitor suberic bishydroxamate regulates the expression of multiple apoptotic mediators and induces mitochondria-dependent apoptosis of melanoma cells. *Mol Cancer Ther* **3**: 425-435.

Zhang YZ, An JH, Liu YX, Wu XC, Han SS, Ren XQ, Qin CJ. 2017. XRCC2-Deficient Cells are Highly Sensitive to 5-Fluorouracil in Colorectal Cancer. *Cell Physiol Biochem* **43**: 1207-1219.

Zhang Z, Yamashita H, Toyama T, Sugiura H, Ando Y, Mita K, Hamaguchi M, Hara Y, Kobayashi S, Iwase H. 2005. Quantitation of HDAC1 mRNA Expression in Invasive Carcinoma of the Breast. *Breast Cancer Res Treat* **94**: 11-16.

Zhao L, Li L, Xu J, Zhong R. 2014. Comparative investigation of the DNA inter-strand crosslinks induced by ACNU, BCNU, CCNU and FTMS using high-performance liquid chromatography–electrospray ionization tandem mass spectrometry. *Int J Mass spectrom* **368**: 30-36.

Zhao Y, Lu S, Wu L, Chai G, Wang H, Chen Y, Sun J, Yu Y, Zhou W, Zheng Q et al. 2006. Acetylation of p53 at lysine 373/382 by the histone deacetylase inhibitor depsipeptide induces expression of p21(Waf1/Cip1). *Mol Cell Biol* **26**: 2782-2790.

Zhao Y, Tan J, Zhuang L, Jiang X, Liu ET, Yu Q. 2005. Inhibitors of histone deacetylases target the Rb-E2F1 pathway for apoptosis induction through activation of proapoptotic protein Bim. *Proc Natl Acad Sci U S A* **102**: 16090-16095.

Zhou Y, Lee J-H, Jiang W, Crowe JL, Zha S, Paull TT. 2017. Regulation of the DNA Damage Response by DNA-PKcs Inhibitory Phosphorylation of ATM. *Mol Cell* **65**: 91-104.

Zhu P, Martin E, Mengwasser J, Schlag P, Janssen K-P, Göttlicher M. 2004. Induction of HDAC2 expression upon loss of APC in colorectal tumorigenesis. *Cancer Cell* **5**: 455-463.

Zigeuner R, Ratschek M, Rehak P, Schips L, Langner C. 2004. Value of p53 as a prognostic marker in histologic subtypes of renal cell carcinoma: a systematic analysis of primary and metastatic tumor tissue. *Urology* **63**: 651-655.

Zimmer M, Doucette D, Siddiqui N, Iliopoulos O. 2004. Inhibition of hypoxia-inducible factor is sufficient for growth suppression of VHL-/- tumors. *Mol Cancer Res* **2**: 89-95.

Zuco V, De Cesare M, Cincinelli R, Nannei R, Pisano C, Zaffaroni N, Zunino F. 2011. Synergistic antitumor effects of novel HDAC inhibitors and paclitaxel in vitro and in vivo. *PLoS One* **6**: e29085.

7 Supplement

7.1 Supplementary Figures

7.1.1 Effects of HDAC inhibition in renal carcinoma cells

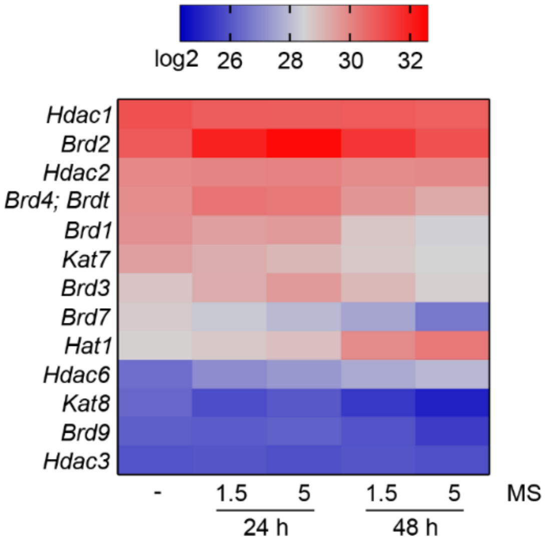

Figure S 1: Protein expression of prominent regulators of histone acetylation. Renca cells were treated with the indicated concentrations of MS-275 (µM) for 24–48 h. Four independent replicates were analyzed for global protein expression by LFQ via mass spectrometry. Heatmap lists changes in LFQ expression levels of the indicated proteins.

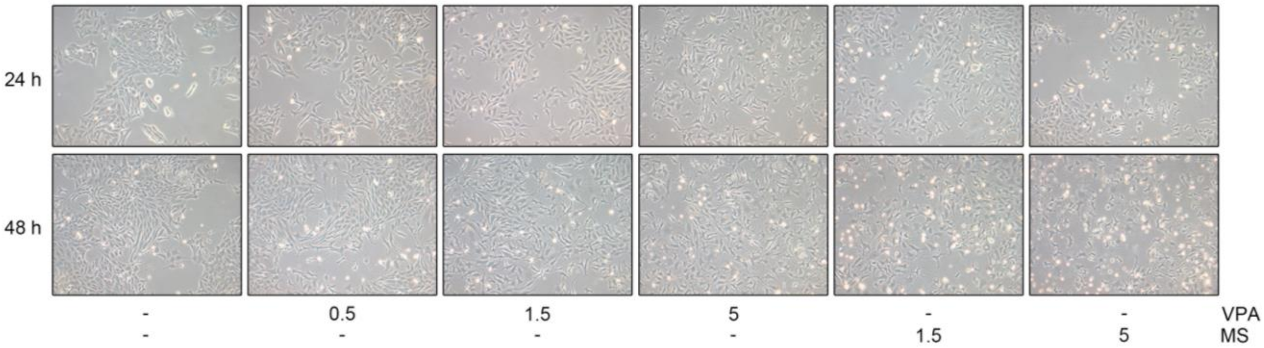

Figure S 2: Cell morphology of HDACi-treated Renca cells. Cells were treated with the indicated concentrations of VPA (mM) and MS-275 (µM) for 24 h and 48 h. Respective complete images of **Figure 16**, obtained using phase-change light microscopy. Images are representative for four independent experiments.

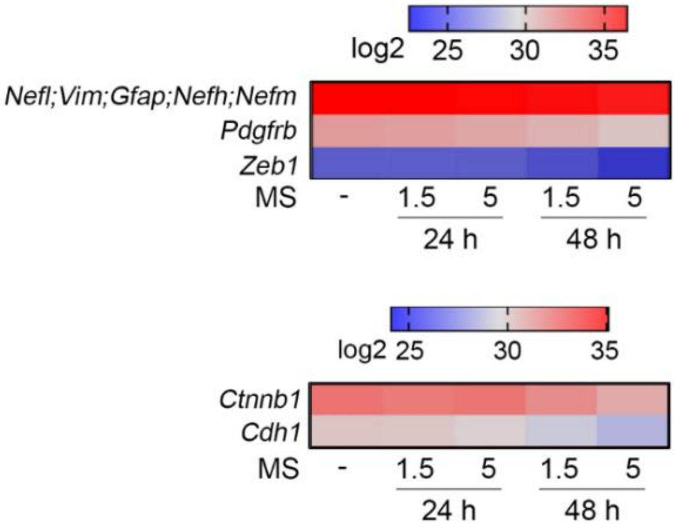

Figure S 3: Heatmap of protein expression of EMT signature proteins. Renca cells were treated with the indicated concentrations of MS-275 (µM) for 24–48 h. Four independent replicates were analyzed for global protein expression by LFQ via mass spectrometry. Heatmap lists changes in LFQ expression levels of the indicated proteins.

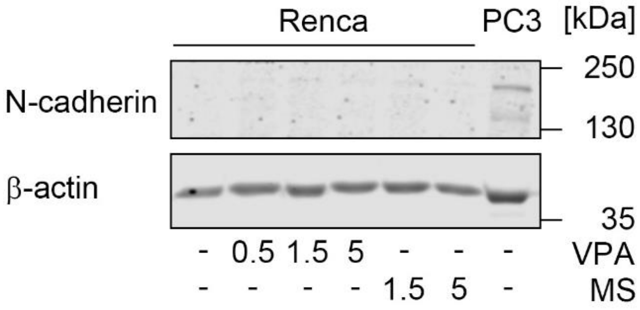

Figure S 4: N-cadherin expression in Renca cells in response to HDACi treatment. Cells were treated with the indicated concentrations of VPA (mM) and MS-275 (µM) for 48 h. Whole cell lysate of untreated PC3 cells was added as positive control. N-Cadherin expression was determined via Western Blot; β-actin, loading control.

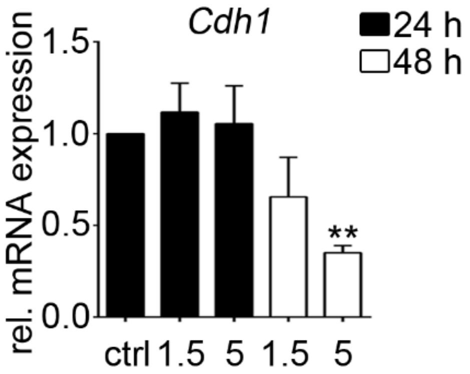

Figure S 5: mRNA expression of E-cadherin (*Cdh1*) in HDACi-treated Renca cells. Cells were treated with 1.5 µM and 5 µM MS-275 for 24 h and 48 h. Independent triplicates were analyzed for quantitative mRNA expression of *Cdh1* gene by qPCR analysis. qPCR analysis was kindly performed by [redacted], LMU Munich. Graph shows mean ± SD (n=3; one-way ANOVA; Dunnett multiple comparison test; $^{**}P<0.01$).

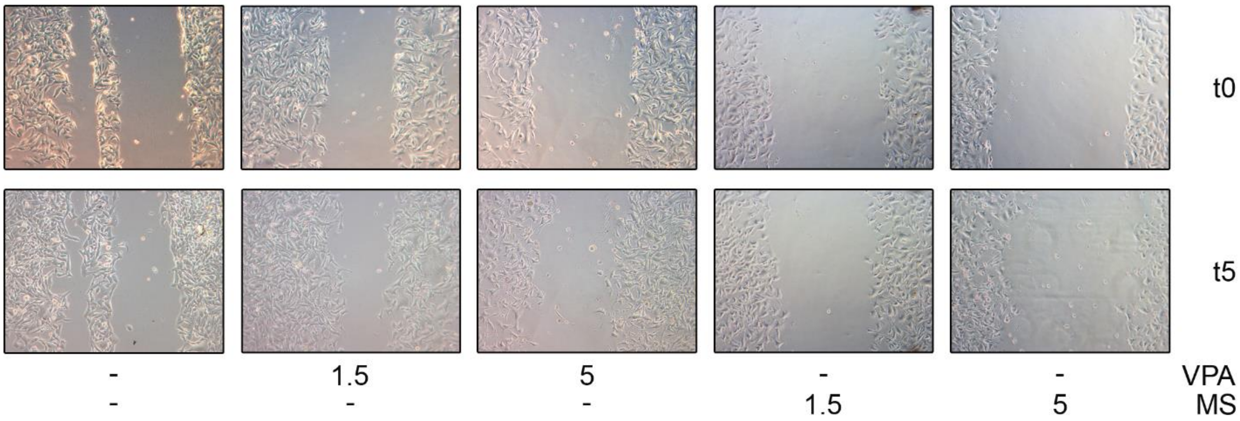

Figure S 6: Images of Scratch assay in HDACi-treated Renca cells. Confluent cells were pre-treated for 14 h with the indicated concentrations of VPA (mM) and MS-275 (µM). Upper panel shows images at timepoint t0 that were taken immediately after application of scratches. Lower panel shows images at timepoint t5 that were taken 10 h after application of scratches.

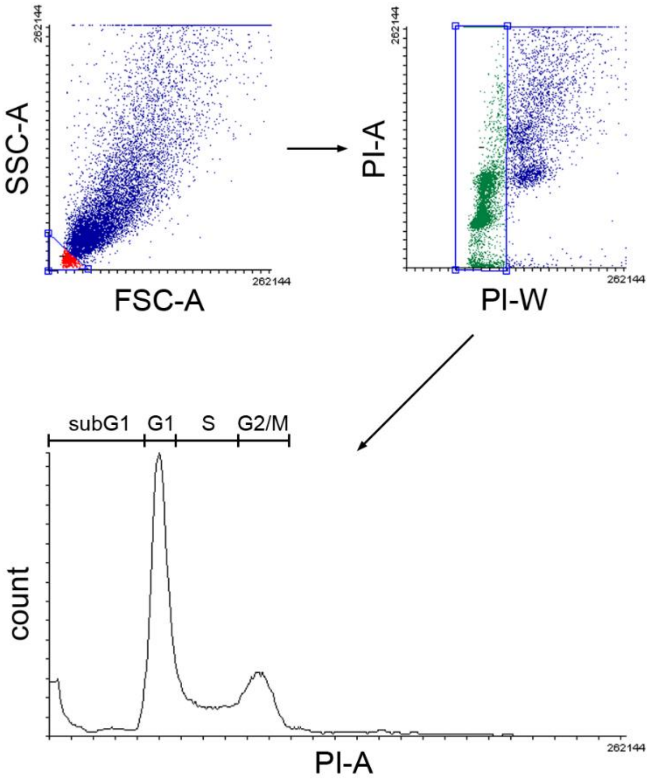

Figure S 7: Gating scheme of flow cytometric measurement of cell death as subG1 fraction. Debris was excluded in forward and sideward scatter (SSC/FSC). Cells were stained with PI to identify cell cycle distribution. Duplicates were excluded by gating in PI-area (PI-A) vs. PI-wide (PI-W) dot blot. Cell cycle phase separation was accomplished by gating the subsequent cell population in a count vs. PI-A histogram. Gating scheme is representative for all subG1 analyses in this work.

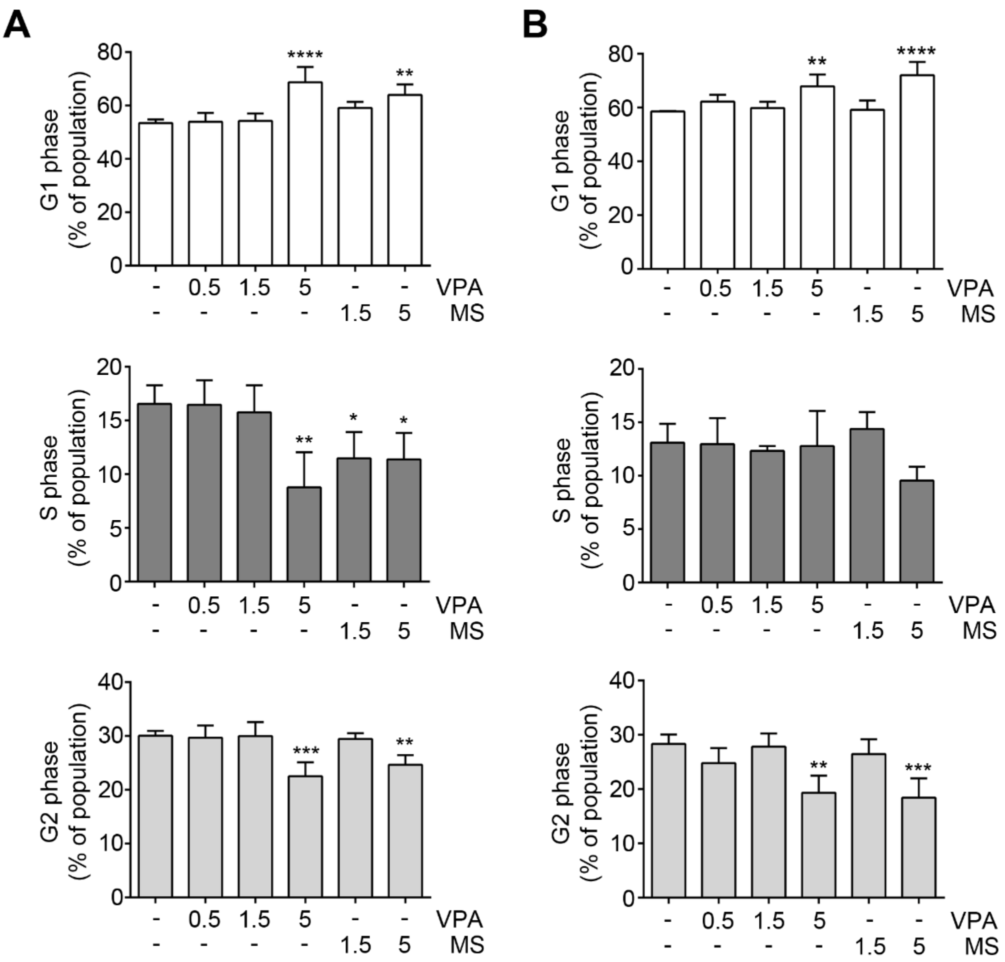

Figure S 8: Cell cycle phase alterations in Renca cells in response to HDACi. Cells were treated with the indicated concentrations of VPA (mM) and MS-275 (µM) for 24 h (**A**) and 48 h (**B**). Cell cycle distribution was determined by flow cytometry analysis of fixed and PI stained cells. Cells with fractionated DNA (subG1 fraction) were excluded to receive the cell cycle distribution of the viable cell population. Graphs show mean ± SD (n=4; one-way ANOVA; Dunnett's multiple comparison test; **P*<0.05, ***P*<0.01, ****P*<0.001, *****P*<0.0001). Figure shows statistical analysis of cell cycle distribution presented in **Figure 29**.

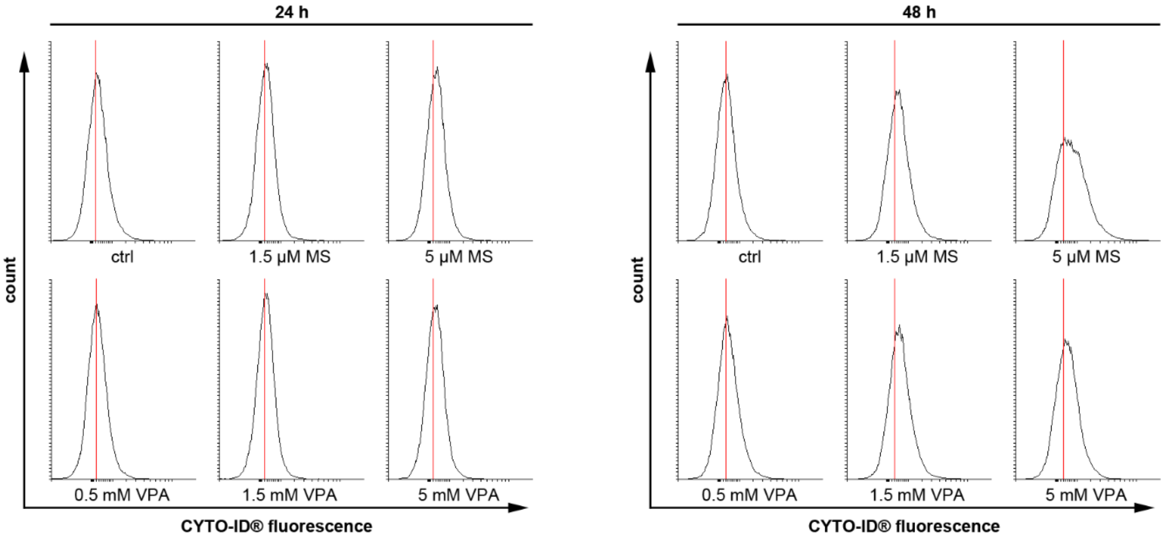

Figure S 9: Exemplary CYTO-ID® histograms of autophagy measurement in Renca cells. Cells were treated with the indicated concentrations of VPA (mM) and MS-275 (µM) for 24-48h. Autophagy was determined by flowcytometry detection of mean fluorescence of CYTO-ID® stained cells. Figure shows exemplary histograms to illustrate differences in CYTO-ID® mean fluorescence. Red line indicates maximum of fluorescence intensity in untreated samples.

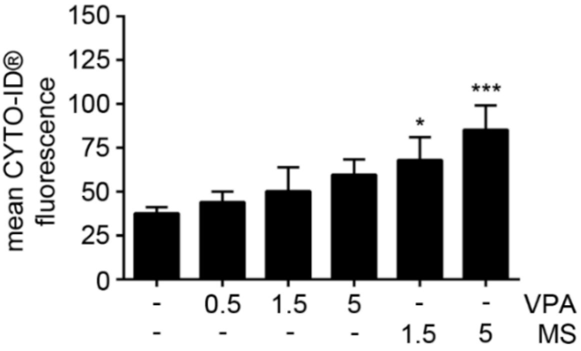

Figure S 10: Mean CYTO-ID® fluorescence of 48 h HDACi-treated Renca cells – total signal. Cells were treated with the indicated concentrations of VPA (mM) and MS-275 (µM). Autophagy was determined by flowcytometry detection of mean fluorescence of CYTO-ID® stained cells. Graph depicts mean ± SD (n=4; one-way ANOVA; Dunnett's multiple comparison test; **P*<0.05, ****P*<0.001). Corresponds to fold induction presented in **Figure 32A**.

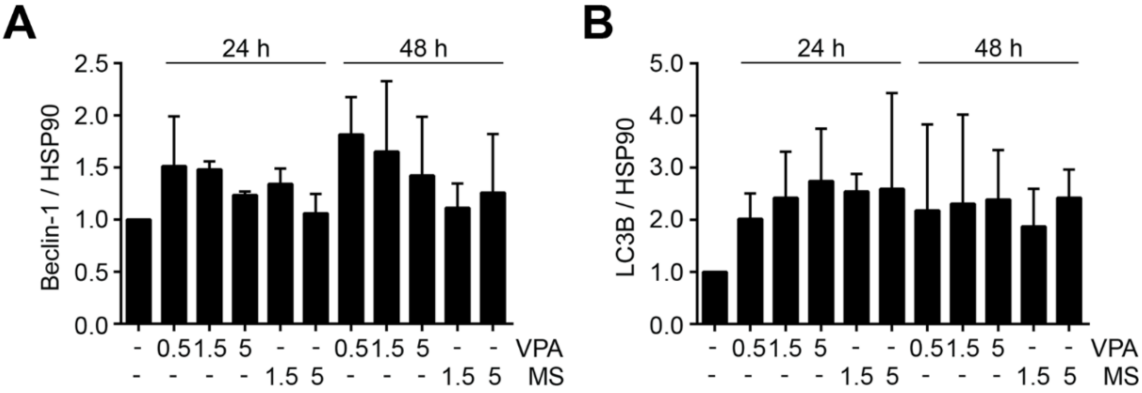

Figure S 11: Quantification of Beclin-1 and LC3B expression in HDACi-treated Renca cells. Cells were treated with the indicated concentrations of VPA (mM) and MS-275 (µM) for 24 h and 48 h. Beclin-1 (**A**) and LC3B (**B**) expression was determined by Western blot (**Figure 32 B**) and quantification of the respective proteins was achieved by densitometric analysis of protein signal intensities and normalization to respective loading control signal intensities. Graph depicts relative levels of Beclin-1 (**A**) and LC3B (**B**) expression as mean ± SD (n=3; one-way ANOVA; Tukey's multiple comparison test; no treatment led to significant changes in protein expression).

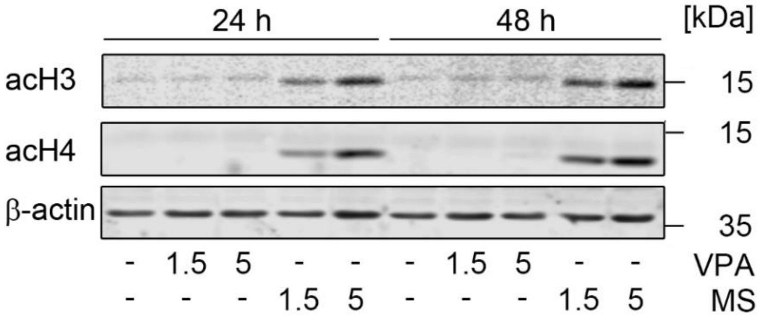

Figure S 12: HDAC class I inhibition induced histone hyperacetylation in MZ-ccRCC2 cells. Cells were treated with the indicated concentrations of VPA (mM) and MS-275 (µM) for 24 h and 48 h. Hyperacetylation of the histones H3 and H4 was analyzed in Western blot. β-actin serves as loading control.

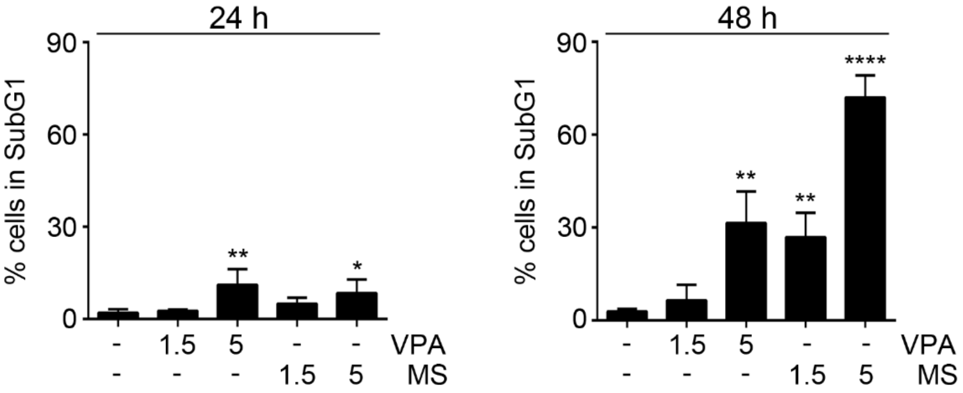

Figure S 13: Cell death induction in HDACi-treated Mz-ccRCC2 cells. Cells were treated with the indicated concentrations of VPA (mM) and MS-275 (µM) for 24 h and 48 h. Cell death was analyzed by flow cytometry of fixed and PI-stained cells as fraction of cells with fragmented DNA (subG1 fraction). Graph shows mean ± SD (n=4 for 24 h; n=3 for 48 h; one-way ANOVA; Dunnett's multiple comparison test; *P<0.05, **P<0.01 ****P<0.0001).

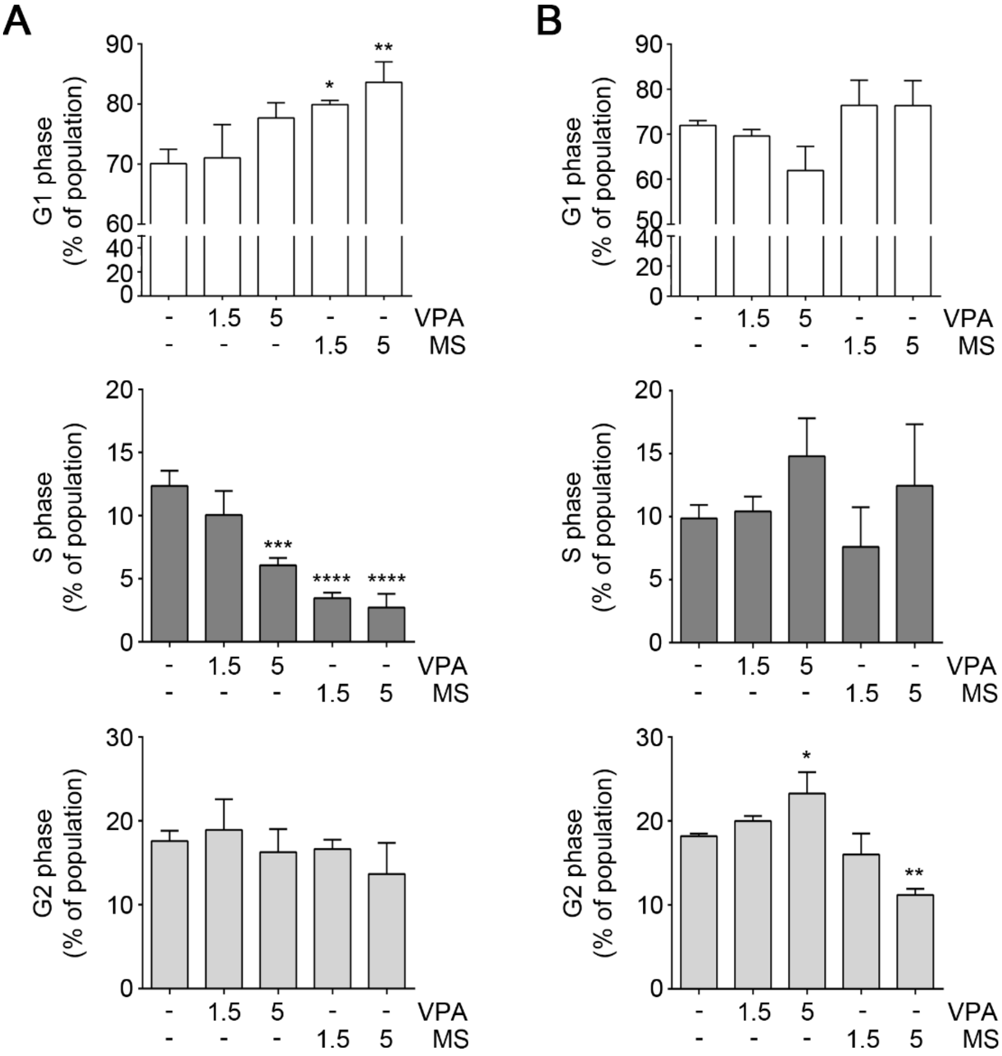

Figure S 14: Cell cycle phase alterations in Mz-ccRCC1 cells in response to HDACi. Cells were treated with the indicated concentrations of VPA (mM) and MS-275 (µM) for 48 h (**A**) and 72 h (**B**). Cell cycle distribution was determined by flow cytometry analysis of fixed and PI stained cells. Cells with fractionated DNA (subG1 fraction) were excluded to receive the cell cycle distribution of the viable cell population. Graphs show mean ± SD (n=3; one-way ANOVA; Dunnett's multiple comparison test; *P<0.05, **P<0.01, ***P<0.001, ****P<0.0001). Figure shows statistical analysis of cell cycle distribution presented in **Figure 35**.

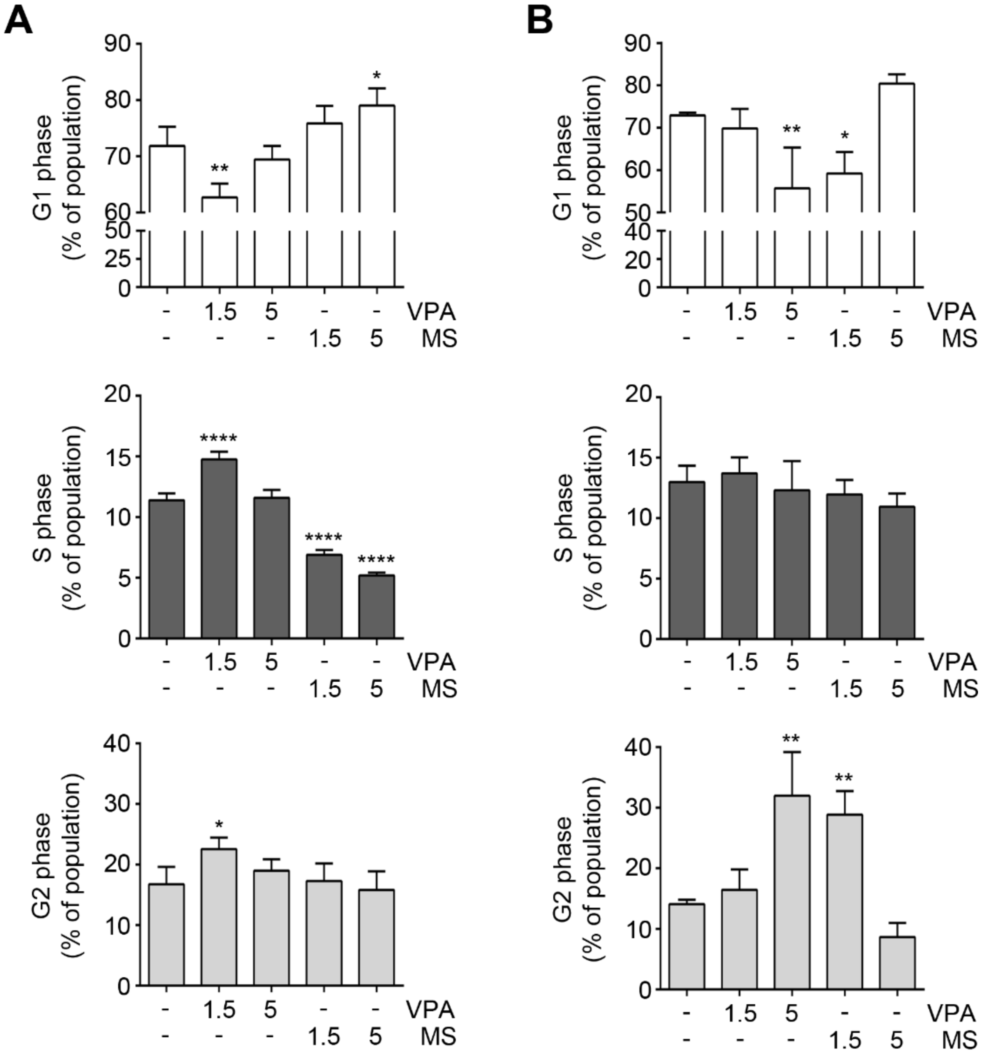

Figure S 15: Cell cycle phase alterations in Mz-ccRCC2 cells in response to HDACi. Cells were treated with the indicated concentrations of VPA (mM) and MS-275 (µM) for 24 h (**A**) and 48 h (**B**). Cell cycle distribution was determined by flow cytometry analysis of fixed and PI stained cells. Cells with fractionated DNA (subG1 fraction) were excluded to receive the cell cycle distribution of the viable cell population. Graphs show mean ± SD (n=4 for 24 h; n=3 for 48 h; one-way ANOVA; Dunnett's multiple comparison test; *P<0.05, **P<0.01, ****P<0.0001).

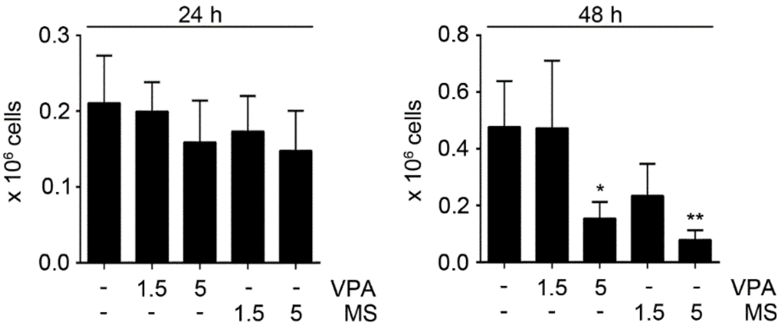

Figure S 16: Viable Mz-ccRCC2 cell number in response to HDACi treatment. Cells were treated with the indicated concentrations of VPA (mM) and MS-275 (µM) for 24 h and 48 h. Dead cells were excluded by trypan blue staining and viable cell population was counted in a Neubauer chamber. Graph depicts mean ± SD (n=4; one-way ANOVA; Dunnett's multiple comparisons test; *P<0.05, ****P<0.0001).

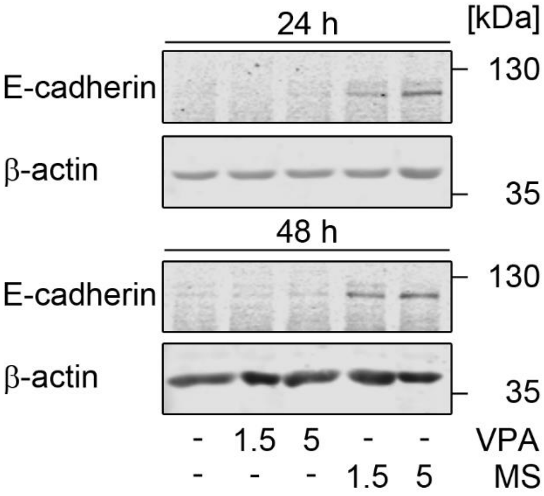

Figure S 17: E-Cadherin expression in HDACi-treated MZ-ccRCC2 cells. Cells were treated with the indicated concentrations of VPA (mM) and MS-275 (µM) for 24 – 48 h and analyzed for E-cadherin expression in Western blot. β-actin served as loading control.

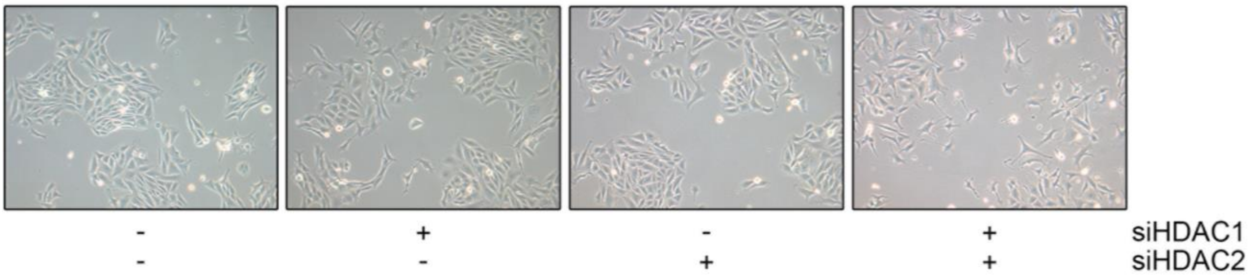

Figure S 18: Morphological alterations in Renca cells upon HDAC1 and HDAC2 knockdown. Cells were transfected with siRNA as indicated and images were taken 72 h post transfection. Respective complete images of **Figure 39**, obtained using phase-change light microscopy. Images are representative for three independent experiments.

7.1.2 HDAC2 expression in colorectal cancer cells and the effects of HDAC2 sumoylation and HDAC inhibition

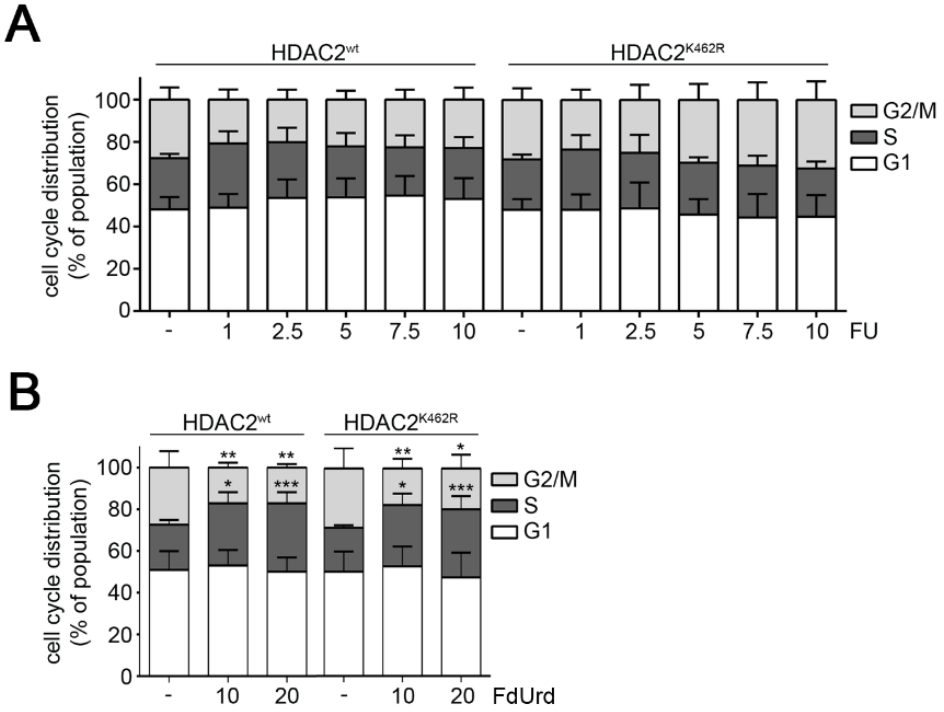

Figure S 19: Cell cycle of 5-FU- and FdUrd-treated RKO HDAC2^{wt} and RKO HDAC2^{K462R}. Cells were treated with the indicated concentrations of FU (µM) (**A**) and FdUrd (µM) (**B**) for 48 h. Cell cycle distribution was determined by flow cytometric analysis of fixed and PI stained cells. Graph shows mean ± SD (n=5 for (**A**); n=5 for (**B**); two-way ANOVA; Tukey's multiple comparisons test, **P*<0.05, ***P*<0.01, ****P*<0.001, *****P*<0.0001).

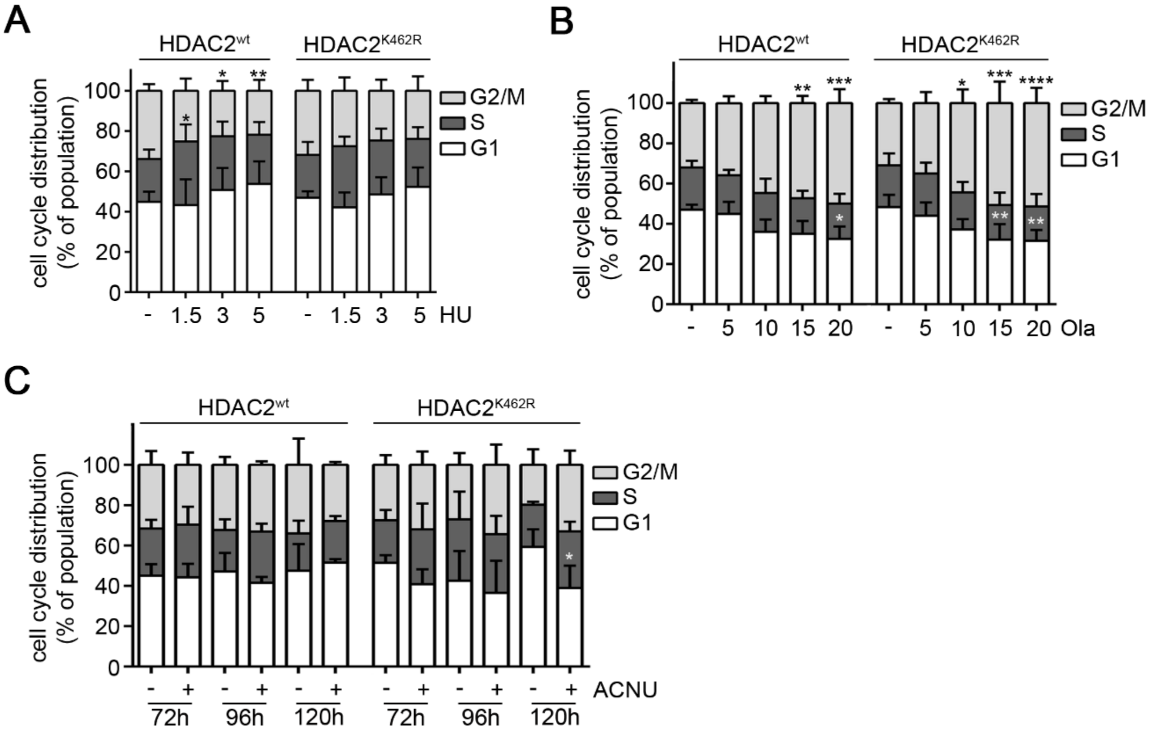

Figure S 20: Cell cycle of HU, olaparib, and ACNU-treated RKO HDAC2^{wt} and RKO HDAC2^{K462R}. Cells were treated with the indicated concentrations of HU (mM) (**A**) and olaparib (µM) (**B**) for 48 h. Cells were treated with 5 µM ACNU (**C**) for the indicated period. Cell cycle distribution was determined by flow cytometric analysis of fixed and PI stained cells. Graph shows mean ± SD (n=10 for (**A**); n=4 for (**B**); n=4-5 for (**C**); two-way ANOVA; Tukey's multiple comparisons test, **P*<0.05, ***P*<0.01, ****P*<0.001).

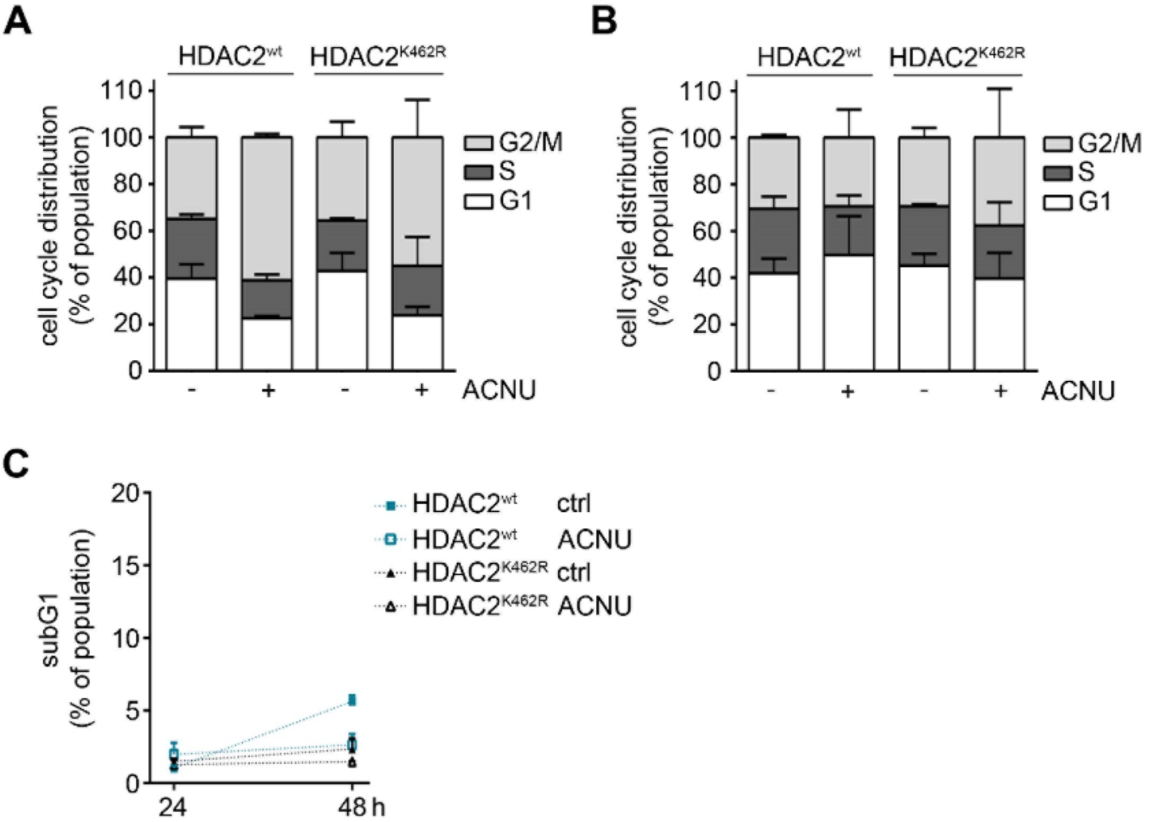

Figure S 21: Cell cylce and cell death of ACNU-treated RKO HDAC2^{wt} and RKO HDAC2^{K462R}. Cells were treated with 5 µM ACNU and cell cycle distribution was determined by flow cytometric analysis of fixed and PI stained cells after 24 h (**A**) and 48 h (**B**). (**C**) Cells were treated with 5 µM ACNU for 24 h and 48 h. Cell death induction was measured by flow cytometry analysis of fixed and PI-stained cells as induction of the fraction of cells with fragmented DNA (subG1 fraction). (**A**), (**B**), (**C**) Graphs depict mean ± SD (n=2).

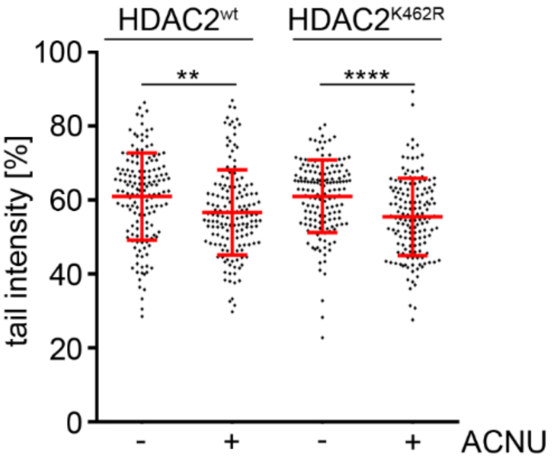

Figure S 22: ACNU induced ICLs in RKO HDAC2^{wt} and RKO HDAC2^{K462R}. Cells were treated with 5 µM ACNU and 5 µM O^{6}BG for 24 h. Treated and untreated cells were then irradiated with 6 Gy and immediately submitted to alkaline COMET assay to detect DNA ICLs. Graph shows tail intensity of 151 to 154 individual cells per sample that were derived from n=4 independent experiments (one-way ANOVA; Tukey's multiple comparisons test, ***P*<0.01, *****P*<0.0001).

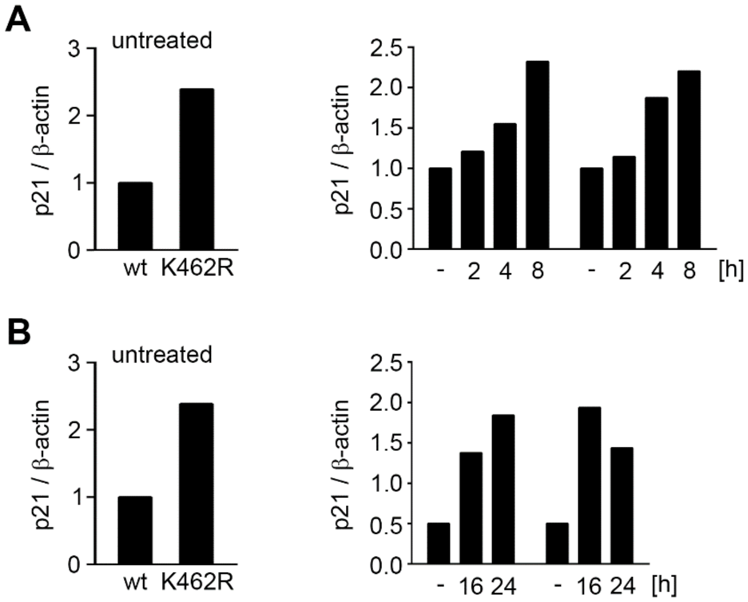

Figure S 23: Quantification of p21 expression in 5-FU-treated RKO HDAC2^{wt} and RKO HDAC2^{K462R}. (**A**) Quantification of p21 expression after 2, 4, and 8 h in 5-FU-treated cells in Western blot analysis in **Figure 52 A**. Left panel shows the difference in p21 expression in untreated controls. (**B**) Quantification of p21 expression after 16 and 24 h in 5-FU-treated cells in Western blot analysis in **Figure 52 B**. Left panel shows the difference in p21 expression in untreated controls.

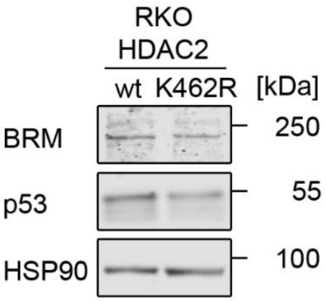

Figure S 24: BRM expression in RKO HDAC2^{wt} and RKO HDAC2^{K462R}. Expression of the indicated proteins was analyzed in untreated cells. HSP90 served as loading control.

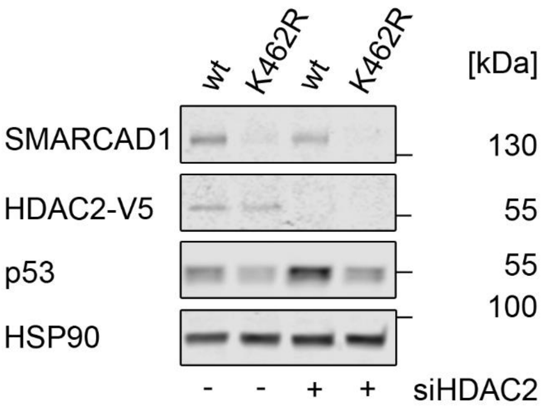

Figure S 25: SMARCAD1 expression in RKO HDAC2^{wt} and RKO HDAC2^{K462R} following HDAC2 knockdown. Cells were transfected with siRNA directed against SMARCAD1 mRNA. Expression of the indicated proteins was determined by Western blot. HSP90 served as loading control.

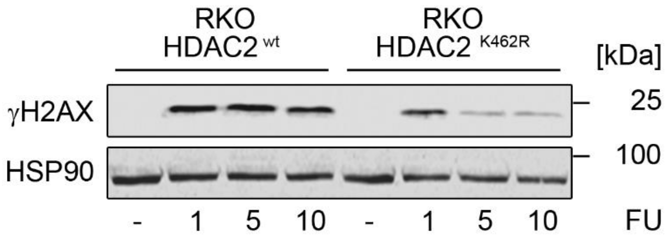

Figure S 26: Phosphorylation of histone H2AX in RKO HDAC2^{wt} and RKO HDAC2^{K462R} in response to 48 h 5-FU. Cells were treated with the indicated concentrations of 5-FU (µM) for 48 h. Phosphorylation of histone H2AX was determined by Western blot analysis. HSP90 served as loading control.

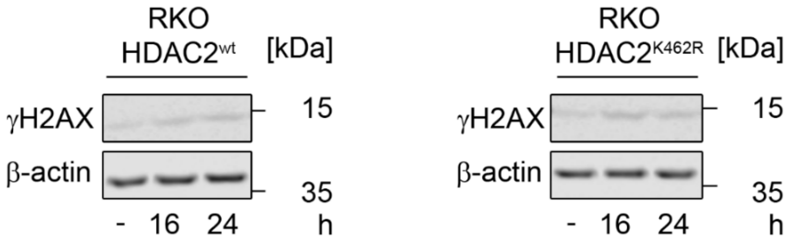

Figure S 27: Phosphorylation of histone H2AX in RKO HDAC2^{wt} and RKO HDAC2^{K462R} in response to 16 h and 24 h 5-FU. Cells were treated with 10 µM 5-FU for 16 h and 24 h. Phosphorylation of histone H2AX was determined by Western blot analysis. β-actin served as loading control.

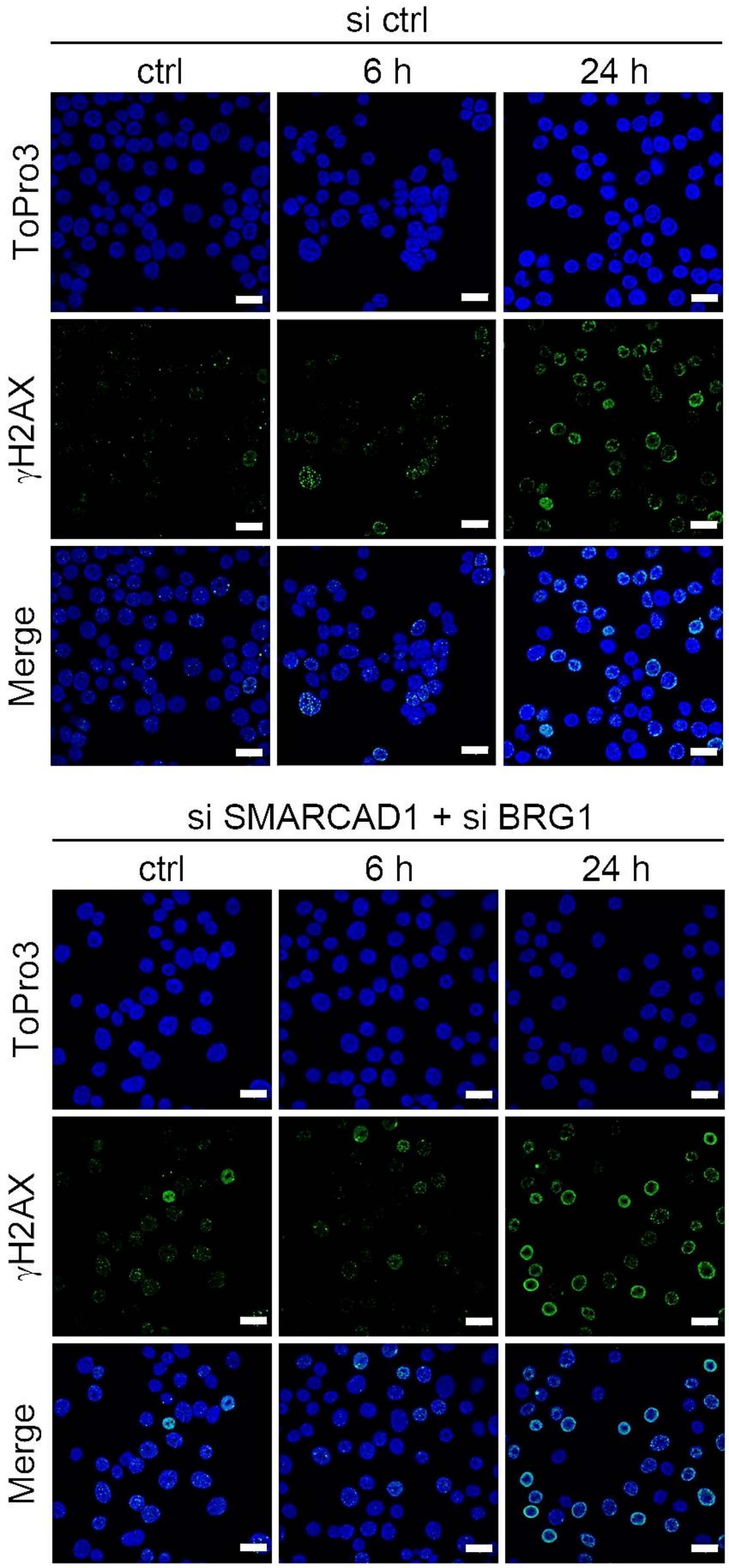

Figure S 28: Immunofluorescence analysis of 5-FU-induced γH2AX formation in SMARCAD1- and BRG1-depleted RKO HDAC2^{wt}. Cells were transfected with siRNA directed against SMARCAD1 and BRG1 and subsequently treated with 10 µM 5-FU for 6 h and 24 h prior to fixation and staining with γH2AX primary antibody and immunofluorescence analysis. Representative immunofluorescence images of all samples. Sections are shown in **Figure 65**. Scale bar represents 20 µm.

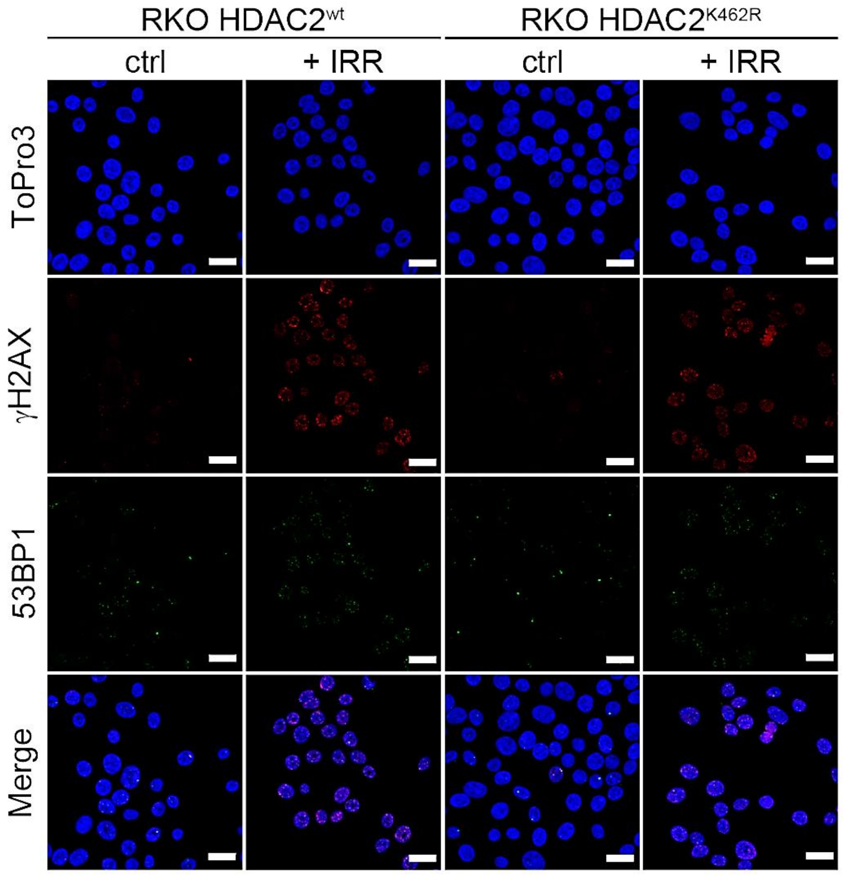

Figure S 29: Immunofluorescence analysis of γH2AX and 53BP1 in irradiated RKO HDAC2^{wt} and RKO HDAC2^{K462R}. Cells were irradiated with 6 Gy and incubated for 1 h prior to fixation and staining with γH2AX and 53BP1 primary antibodies. Representative full immunofluorescence images of all samples. Sections are shown in Figure 66. Scale bar represents 20 µm.

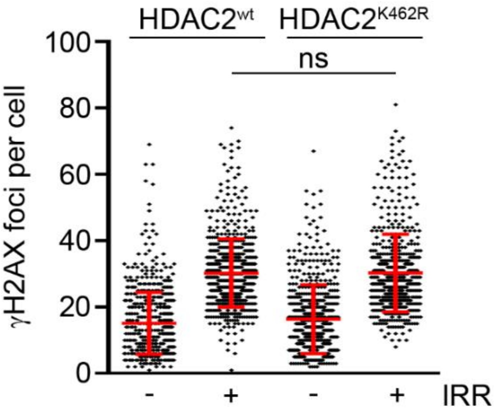

Figure S 30: γH2AX foci formation in response to irradiation of RKO HDAC2^{wt} and RKO HDAC2^{K462R}. Cells were irradiated with 6 Gy and incubated for 1 h prior to fixation and staining with γH2AX primary antibody. Number of γH2AX foci per cell was determined using Image J. Each dot represents the amount of foci measured in a single cell. 112 - 212 cells were counted per sample (n=4; one-way ANOVA; Tukey's multiple comparisons test; no significant difference).

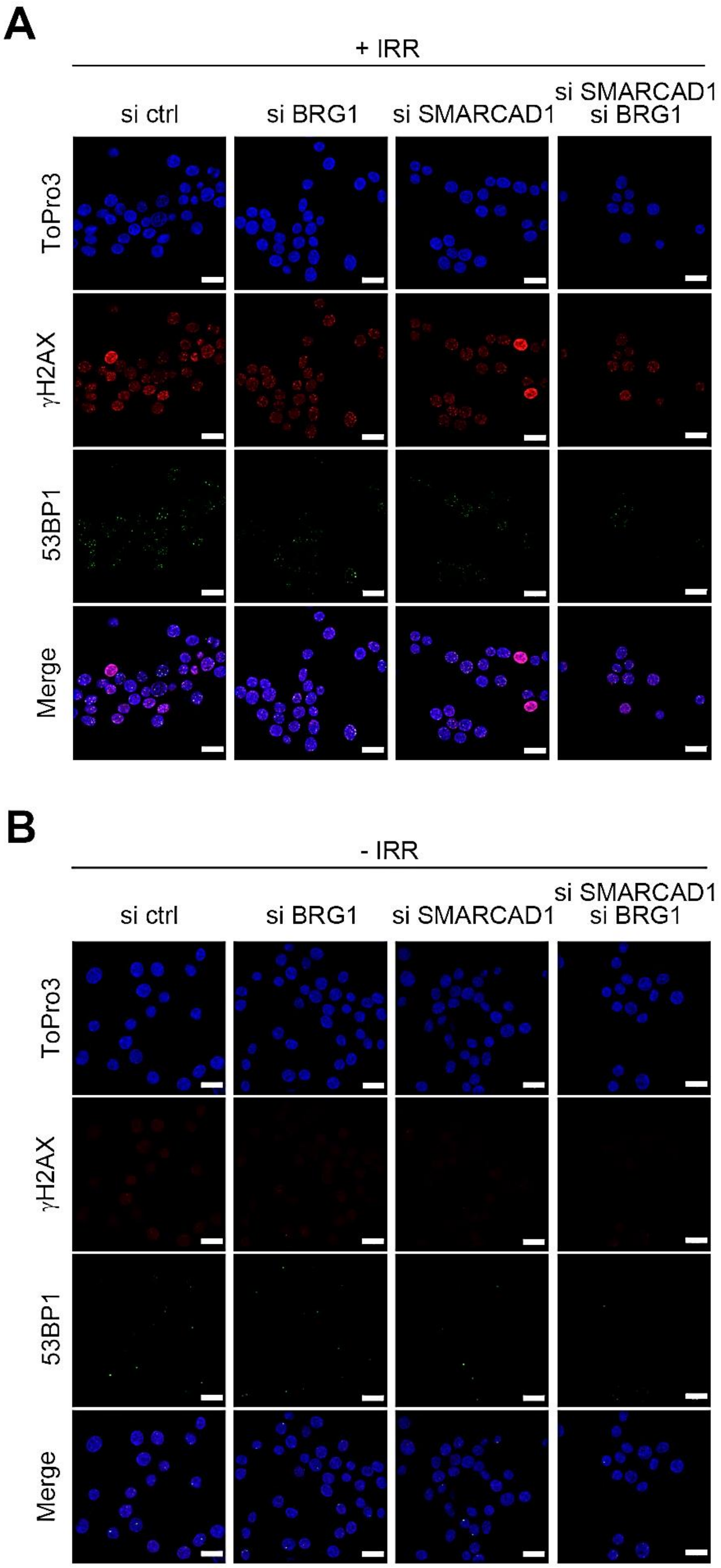

Figure S 31: Immunofluorescence analysis of ionizing radiation induced γH2AX and 53BP1 foci formation in BRG1-, SMARCAD1-, and HDAC2-depleted RKO HDAC2^{wt}. Cells were transfected with the indicated combinations of siRNA directed against BRG1, SMARCAD1, and HDAC2, subsequently irradiated with 6 Gy and incubated for 1 h prior to fixation and staining with γH2AX and 53BP1 primary antibody and immunofluorescence analysis. Figure shows representative immunofluorescence images of irradiated samples (**A**) and unirradiated controls (**B**). Sections of irradiated samples are shown in **Figure 67.** Scale bar represents 20 µm.

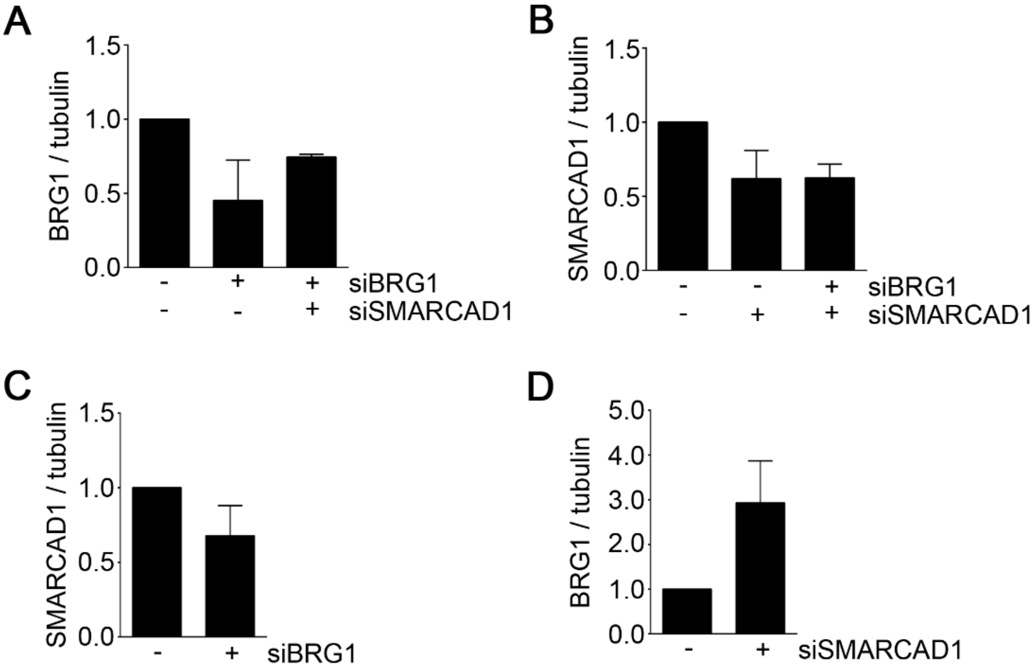

Figure S 32: Immunofluorescence analysis - BRG1 and SMARCAD1 expression in response to siRNA mediated knockdown in RKO HDAC2^{wt}. Cells were transfected with siRNA directed against SMARCAD1 and BRG1 mRNA as indicated prior to immunofluorescence analysis (**Figure 67**, **Figure 68**, **Figure S 31**). (**A**) Quantification of BRG1 expression in BRG1 and SMARCAD1 siRNA transfected cells by measurement of BRG1 signal intensity in Western blot analysis. Signal intensities were normalized to the corresponding Western blot loading controls. Graph shows mean ± SD (n=3). (**B**) Quantification of SMARCAD1 expression in BRG1 and SMARCAD1 siRNA transfected cells by measurement of SMARCAD1 signal intensity in Western blot analysis. Signal intensities were normalized to the corresponding Western blot loading controls. Graph shows mean ± SD (n=3). (**C**) Quantification of SMARCAD1 expression in BRG1 siRNA transfected cells by measurement of SMARCAD1 signal intensity in Western blot analysis. Signal intensities were normalized to the corresponding Western blot loading controls. Graph shows mean ± SD (n=3). (**D**) Quantification of BRG1 expression in SMARCAD1 siRNA transfected cells by measurement of SMARCAD1 signal intensity in Western blot analysis. Signal intensities were normalized to the corresponding Western blot loading controls. Graph shows mean ± SD (n=3).

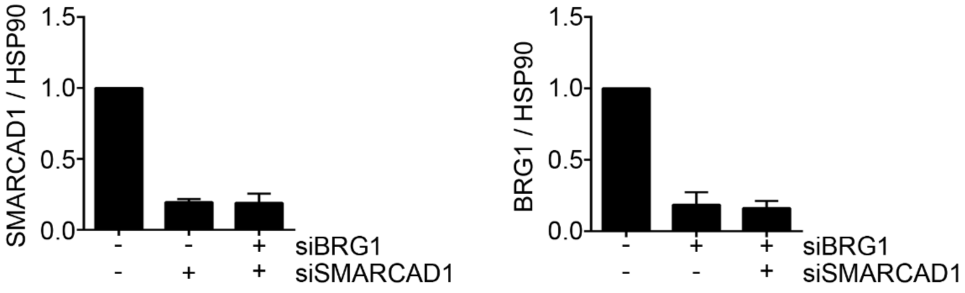

Figure S 33: Cell death analysis - BRG1 and SMARCAD1 expression in response to siRNA mediated knockdown in RKO HDAC2^{wt}. Cells were transfected with siRNA directed against SMARCAD1 and BRG1 mRNA as indicated prior to cell death analysis (**Figure 71, Figure S 34**). Quantification of SMARCAD1 and BRG1 expression in transfected RKO HDAC2^{wt} cells was performed by measurement of SMARCAD1 and BRG1 signal intensity in Western blot analysis. Signal intensities were normalized to the corresponding Western blot loading controls. Graphs show mean ± SD (n=2).

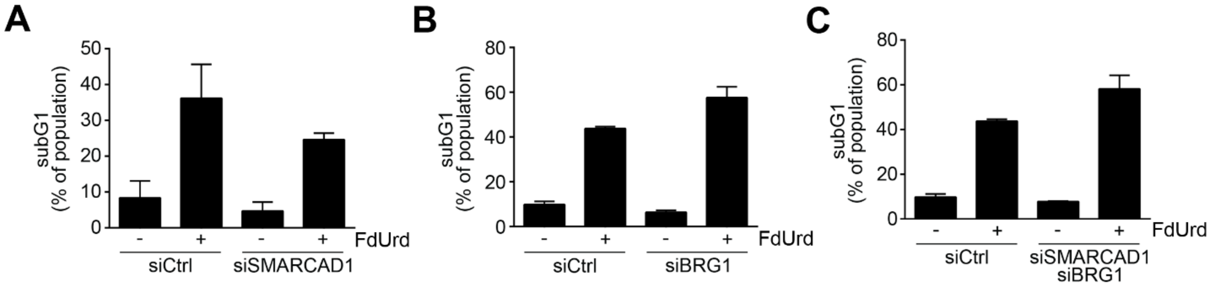

Figure S 34: Effect of SMARCAD1 and BRG1 knockdown on cell death induction in FdUrd-treated RKO HDAC2^{wt}. (**A**) Cells were transfected with siRNA directed against SMARCAD1 and treated with 2 µM FdUrd for 48 h. Graph shows mean ± SD (n=4; one-way ANOVA; Tukey's multiple comparisons test; no significant difference). (**B**) Cells were transfected with siRNA directed against BRG1 and treated with 2 µM FdUrd for 48 h. Graph shows mean ± SD (n=2). (**C**) Cells were transfected with siRNA directed against SMARCAD1 and BRG1 and treated with 2 µM FdUrd for 48 h. Graph shows mean ± SD (n=2). Cell death was determined by flow cytometric analysis of fixed and PI-stained cells as fraction of cells with fragmented DNA (subG1 fraction).

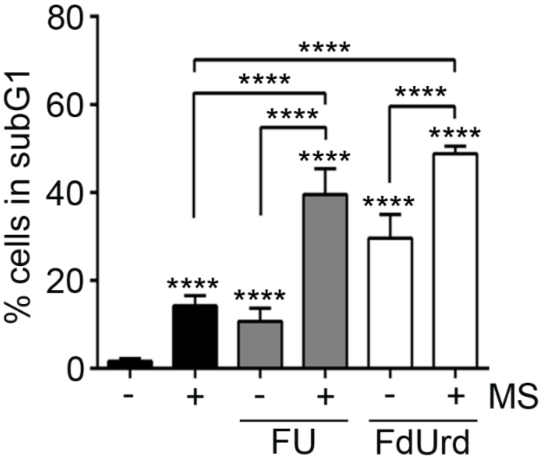

Figure S 35: Cell death induction in HCT116 treated with MS-275, 5-FU, and FdUrd. Cells were treated with 2 µM MS-275, 5 µM 5-FU, and 2 µM FdUrd for 48h. Cell death induction was determined by flow cytometric analysis of fixed and PI stained samples. Graphs show mean ± SD (n=3-10; one-way ANOVA; Tukey's multiple comparisons test; ns: no significant difference, *****P*<0.0001).

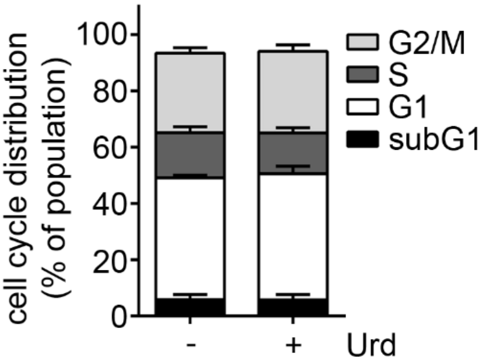

Figure S 36: Cell cycle distribution in uridine-treated RKO. RKO cells were treated with 10 mM Urd for 48 h. Cell cycle distribution was determined by flow cytometric analysis of fixed and PI stained cells. Graph shows mean ± SD (n=5; one-way ANOVA, Sidak's multiple comparisons test; no significant difference).

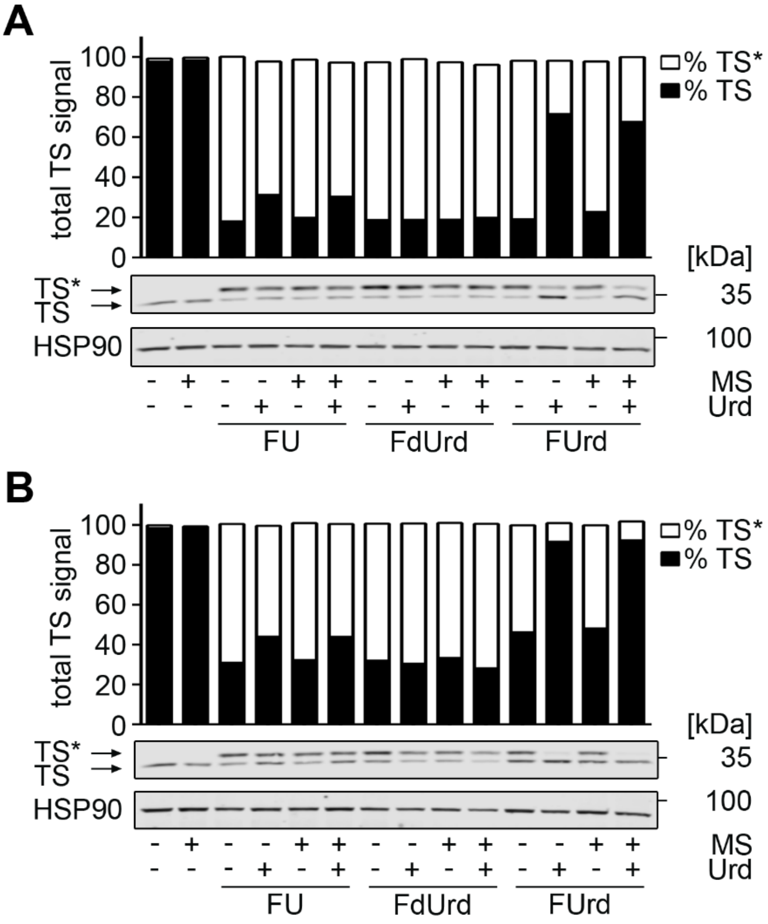

Figure S 37: Thymidylate synthase inhibition in 5-FU- and FdUrd-treated RKO and HCT116. (**A**) RKO and (**B**) HCT116 cells were treated with 2 µM MS-275, 10 mM Urd, 5 µM 5-FU and 2 µM FdUrd for 24 h. Expression of free thymidylate synthase protein (TS) and the FdUMP-CH_2THF-TS complex (TS*) was determined by Western blot. HSP90 and β-actin served as loading control. Quantification was performed by measurement of signal intensity of both TS bands and normalization to the respective loading control.

7.2 Supplementary Tables

Table S 1: GO-term enrichment in response to all applied treatment conditions. (complete list) The significant set of proteins considered for analysis was obtained through unpaired Students t-test analysis by selecting those proteins that were significantly regulated in samples treated with 5 µM MS-275 for 48 h.

GOBPID	Term	Exp Count	Count	Size	neg log10 (p)	Odds Ratio
GO:0098609	cell-cell adhesion	60	89	342	4,45	1,71
GO:0043094	cellular metabolic compound salvage	3	10	16	4,11	7,88
GO:0051156	glucose 6-phosphate metabolic process	2	9	14	3,87	8,50
GO:0006048	UDP-N-acetylglucosamine biosynthetic process	1	5	5	3,78	Inf
GO:0007021	tubulin complex assembly	1	5	5	3,78	Inf
GO:0009225	nucleotide-sugar metabolic process	4	11	20	3,77	5,78
GO:0006796	phosphate-containing compound metabolic process	82	111	482	3,62	1,52
GO:0044262	cellular carbohydrate metabolic process	14	27	81	3,40	2,39
GO:0044283	small molecule biosynthetic process	32	50	181	3,36	1,83
GO:0005996	monosaccharide metabolic process	17	31	98	3,34	2,21

GO:0046939	nucleotide phosphorylation	7	16	39	3,31	0,33
GO:0006749	glutathione metabolic process	6	14	32	3,30	3,68
GO:0006739	NADP metabolic process	4	11	22	3,30	4,73
GO:0009069	serine family amino acid metabolic process	3	10	19	3,27	0,00
GO:0050852	T cell receptor signaling pathway	3	9	16	3,26	6,07
GO:0045116	protein neddylation	1	6	8	3,23	14,14
GO:0019362	pyridine nucleotide metabolic process	13	25	75	3,17	2,38
GO:0036211	protein modification process	206	244	1172	3,13	1,31
GO:0044724	single-organism carbohydrate catabolic process	9	19	52	3,08	2,73
GO:2000379	positive regulation of reactive oxygen species metabolic process	7	15	37	3,07	3,23
GO:0031115	negative regulation of microtubule polymerization	1	5	6	3,07	23,55
GO:0042537	benzene-containing compound metabolic process	1	5	6	3,07	23,55
GO:0046500	S-adenosylmethionine metabolic process	1	5	6	3,07	23,55
GO:0019320	hexose catabolic process	2	7	11	3,06	8,25
GO:1990748	cellular detoxification	2	7	11	3,06	8,25
GO:0006081	cellular aldehyde metabolic process	4	10	20	3,06	4,75
GO:0022610	biological adhesion	84	110	477	3,06	1,46
GO:0009719	response to endogenous stimulus	67	91	383	3,04	1,51
GO:0051240	positive regulation of multicellular organismal process	69	93	394	3,03	1,50
GO:0006000	fructose metabolic process	1	4	4	3,02	Inf
GO:0006166	purine ribonucleoside salvage	1	4	4	3,02	Inf
GO:0009052	pentose-phosphate shunt, non-oxidative branch	1	4	4	3,02	Inf
GO:0034310	primary alcohol catabolic process	1	4	4	3,02	Inf
GO:0044282	small molecule catabolic process	23	37	128	3,02	1,94
GO:0051186	cofactor metabolic process	7	15	38	3,01	3,16
GO:0002695	negative regulation of leukocyte activation	6	14	34	2,98	3,31
GO:0006757	ATP generation from ADP	6	14	34	2,98	3,31
GO:0019751	polyol metabolic process	6	14	34	2,98	3,31
GO:1901607	alpha-amino acid biosynthetic process	6	14	34	2,98	3,31
GO:0042398	cellular modified amino acid biosynthetic process	4	10	21	2,84	4,29
GO:0061615	glycolytic process through fructose-6-phosphate	2	6	9	2,82	9,42
GO:0045861	negative regulation of proteolysis	15	26	83	2,82	2,17
GO:0071356	cellular response to tumor necrosis factor	5	12	28	2,81	3,55
GO:0045429	positive regulation of nitric oxide biosynthetic process	3	9	18	2,78	4,72
GO:0001782	B cell homeostasis	2	7	12	2,75	6,60
GO:0031663	lipopolysaccharide-mediated signaling pathway	2	7	12	2,75	6,60
GO:0046632	alpha-beta T cell differentiation	3	8	15	2,75	5,39
GO:0051403	stress-activated MAPK cascade	11	21	63	2,75	2,37
GO:0043085	positive regulation of catalytic activity	59	80	337	2,72	1,50
GO:0006082	organic acid metabolic process	68	90	387	2,70	1,46
GO:0071396	cellular response to lipid	23	37	133	2,69	1,84
GO:0006470	protein dephosphorylation	16	27	89	2,68	2,07
GO:0046434	organophosphate catabolic process	7	15	40	2,67	2,84
GO:0052547	regulation of peptidase activity	19	31	107	2,64	1,94
GO:0035556	intracellular signal transduction	122	149	691	2,62	1,34
GO:0003008	system process	54	73	305	2,62	1,51
GO:0006002	fructose 6-phosphate metabolic process	1	5	7	2,59	11,77

GO:0051409	response to nitrosative stress	1	5	7	2,59	11,77
GO:0007169	transmembrane receptor protein tyrosine kinase signaling pathway	25	39	144	2,57	1,77
GO:0008652	cellular amino acid biosynthetic process	5	11	26	2,56	3,46
GO:0010033	response to organic substance	129	157	736	2,54	1,32
GO:0002757	immune response-activating signal transduction	10	19	57	2,54	2,37
GO:0090087	regulation of peptide transport	9	18	53	2,53	2,44
GO:0019752	carboxylic acid metabolic process	62	82	352	2,53	1,46
GO:0009116	nucleoside metabolic process	32	47	182	2,53	1,66
GO:0048864	stem cell development	3	8	16	2,52	4,72
GO:0010646	regulation of cell communication	133	161	758	2,51	1,32
GO:0044248	cellular catabolic process	108	133	615	2,50	1,35
GO:0009636	response to toxic substance	5	12	30	2,50	3,15
GO:0032770	positive regulation of monooxygenase activity	2	6	10	2,49	7,07
GO:0046040	IMP metabolic process	2	6	10	2,49	7,07
GO:0046185	aldehyde catabolic process	2	6	10	2,49	7,07
GO:1903037	regulation of leukocyte cell-cell adhesion	12	22	70	2,49	2,17
GO:0006298	mismatch repair	2	7	13	2,49	5,50
GO:0032024	positive regulation of insulin secretion	4	10	23	2,47	3,63
GO:0032496	response to lipopolysaccharide	11	20	62	2,45	2,26
GO:0034728	nucleosome organization	10	19	58	2,44	2,31
GO:0009179	purine ribonucleoside diphosphate metabolic process	7	15	42	2,43	2,63
GO:0070663	regulation of leukocyte proliferation	9	17	50	2,42	2,44
GO:0044700	single organism signaling	222	255	1265	2,41	1,25
GO:0050868	negative regulation of T cell activation	5	11	27	2,40	3,25
GO:0050865	regulation of cell activation	20	32	115	2,40	1,83
GO:0023051	regulation of signaling	135	162	768	2,40	1,30
GO:0000103	sulfate assimilation	1	4	5	2,39	18,82
GO:0030878	thyroid gland development	1	4	5	2,39	18,82
GO:0044597	daunorubicin metabolic process	1	4	5	2,39	18,82
GO:0044598	doxorubicin metabolic process	1	4	5	2,39	18,82
GO:0046887	positive regulation of hormone secretion	6	13	35	2,34	2,79
GO:0006730	one-carbon metabolic process	3	8	17	2,32	4,19
GO:0010035	response to inorganic substance	26	39	149	2,29	1,69
GO:0006732	coenzyme metabolic process	26	39	150	2,27	1,68
GO:0006059	hexitol metabolic process	1	3	3	2,27	Inf
GO:0007023	post-chaperonin tubulin folding pathway	1	3	3	2,27	Inf
GO:0019401	alditol biosynthetic process	1	3	3	2,27	Inf
GO:0033499	galactose catabolic process via UDP-galactose	1	3	3	2,27	Inf
GO:0035872	nucleotide-binding domain, leucine rich repeat containing receptor signaling pathway	1	3	3	2,27	Inf
GO:0038026	reelin-mediated signaling pathway	1	3	3	2,27	Inf
GO:0042473	outer ear morphogenesis	1	3	3	2,27	Inf
GO:0043096	purine nucleobase salvage	1	3	3	2,27	Inf
GO:0046102	inosine metabolic process	1	3	3	2,27	Inf
GO:0046121	deoxyribonucleoside catabolic process	1	3	3	2,27	Inf
GO:0061622	glycolytic process through glucose-1-phosphate	1	3	3	2,27	Inf
GO:0070257	positive regulation of mucus secretion	1	3	3	2,27	Inf
GO:0070431	nucleotide-binding oligomerization domain containing 2 signaling pathway	1	3	3	2,27	Inf

GO:0071637	regulation of monocyte chemotactic protein-1 production	1	3	3	2,27	Inf
GO:0002793	positive regulation of peptide secretion	5	11	28	2,26	3,06
GO:0044710	single-organism metabolic process	245	277	1412	2,26	1,23
GO:0016051	carbohydrate biosynthetic process	11	19	60	2,26	2,19
GO:0007156	homophilic cell adhesion via plasma membrane adhesion molecules	2	7	14	2,26	4,71
GO:0046835	carbohydrate phosphorylation	1	5	8	2,23	7,85
GO:0006301	postreplication repair	2	6	11	2,22	5,65
GO:0043243	positive regulation of protein complex disassembly	2	6	11	2,22	5,65
GO:0046112	nucleobase biosynthetic process	2	6	11	2,22	5,65
GO:0007052	mitotic spindle organization	4	9	21	2,22	3,54
GO:0009262	deoxyribonucleotide metabolic process	4	9	21	2,22	3,54
GO:0018958	phenol-containing compound metabolic process	4	9	21	2,22	3,54
GO:0031110	regulation of microtubule polymerization or depolymerization	4	9	21	2,22	3,54
GO:0050670	regulation of lymphocyte proliferation	8	16	48	2,22	2,37
GO:0010951	negative regulation of endopeptidase activity	7	14	40	2,21	2,55
GO:0051261	protein depolymerization	7	14	40	2,21	2,55
GO:0032943	mononuclear cell proliferation	11	20	65	2,19	2,11
GO:0030098	lymphocyte differentiation	13	22	74	2,17	2,01
GO:0046148	pigment biosynthetic process	4	10	25	2,16	3,15
GO:1901617	organic hydroxy compound biosynthetic process	10	18	57	2,15	2,18
GO:0055086	nucleobase-containing small molecule metabolic process	17	27	98	2,14	1,84
GO:0019748	secondary metabolic process	3	8	18	2,13	3,77
GO:0060324	face development	3	8	18	2,13	3,77
GO:1901575	organic substance catabolic process	114	137	656	2,13	1,30
GO:1903050	regulation of proteolysis involved in cellular protein catabolic process	14	23	79	2,12	1,95
GO:1903426	regulation of reactive oxygen species biosynthetic process	6	12	33	2,11	2,70
GO:0019220	regulation of phosphate metabolic process	82	102	467	2,10	1,35
GO:0043270	positive regulation of ion transport	11	19	62	2,09	2,09
GO:0008283	cell proliferation	100	122	571	2,09	1,31
GO:0032268	regulation of cellular protein metabolic process	136	160	771	2,09	1,27
GO:0050790	regulation of catalytic activity	37	51	216	2,06	1,52
GO:0009063	cellular amino acid catabolic process	4	9	22	2,06	3,27
GO:0006801	superoxide metabolic process	3	7	15	2,05	4,12
GO:0006468	protein phosphorylation	87	107	495	2,04	1,33
GO:0048562	embryonic organ morphogenesis	12	20	67	2,04	2,01
GO:0009132	nucleoside diphosphate metabolic process	9	16	50	2,03	2,23
GO:0002768	immune response-regulating cell surface receptor signaling pathway	5	10	26	2,02	2,95
GO:2000378	negative regulation of reactive oxygen species metabolic process	5	10	26	2,02	2,95
GO:0051402	neuron apoptotic process	18	28	103	2,02	1,77
GO:0045766	positive regulation of angiogenesis	5	11	30	2,00	2,73
GO:0048584	positive regulation of response to stimulus	85	105	486	2,00	1,33

Table S 2: GO-term enrichment in response to 48 h 5 µM MS-275. (complete list) The significant set of proteins considered for analysis was obtained through one-way ANOVA analysis by selecting those proteins that were significantly regulated in at least four of the total ten comparisons (treatment conditions: 0 µM, 1.5 µM, and 5 µM MS-275 for 24 – 48h).

GOBPID	Term	Exp Count	Count	Size	neg log10 (p)	Odds Ratio
GO:0098609	cell-cell adhesion	38	64	149	5,85	2,28
GO:1901605	alpha-amino acid metabolic process	21	40	83	5,21	2,76
GO:0006304	DNA modification	9	22	37	4,90	4,32
GO:0008652	cellular amino acid biosynthetic process	7	17	26	4,67	5,55
GO:0006725	cellular aromatic compound metabolic process	531	594	2082	4,35	1,28
GO:0001775	cell activation	54	80	213	4,24	1,79
GO:1903405	protein localization to nuclear body	2	7	7	4,15	Inf
GO:1904871	positive regulation of protein localization to Cajal body	2	7	7	4,15	Inf
GO:0042221	response to chemical	245	293	959	4,10	1,35
GO:0032984	macromolecular complex disassembly	19	34	74	3,96	2,51
GO:0051186	cofactor metabolic process	50	73	194	3,95	1,79
GO:0046483	heterocycle metabolic process	506	564	1994	3,92	1,27
GO:0006337	nucleosome disassembly	2	8	9	3,90	23,39
GO:0006333	chromatin assembly or disassembly	17	31	66	3,88	2,61
GO:0046939	nucleotide phosphorylation	10	21	39	3,83	3,43
GO:0043981	histone H4-K5 acetylation	3	10	13	3,82	9,76
GO:0043982	histone H4-K8 acetylation	3	10	13	3,82	9,76
GO:0006757	ATP generation from ADP	9	19	34	3,80	3,72
GO:0051276	chromosome organization	63	88	245	3,80	1,67
GO:0022610	biological adhesion	122	156	477	3,78	1,46
GO:0006306	DNA methylation	7	16	27	3,68	4,27
GO:0071214	cellular response to abiotic stimulus	20	35	79	3,67	2,35
GO:0071310	cellular response to organic substance	140	175	546	3,67	1,42
GO:0090287	regulation of cellular response to growth factor stimulus	13	25	51	3,60	2,83
GO:2000377	regulation of reactive oxygen species metabolic process	18	32	71	3,57	2,42
GO:0030388	fructose 1,6-bisphosphate metabolic process	2	6	6	3,56	Inf
GO:0046500	S-adenosylmethionine metabolic process	2	6	6	3,56	Inf
GO:0080090	regulation of primary metabolic process	449	502	1755	3,54	1,25
GO:0043984	histone H4-K16 acetylation	4	11	16	3,46	6,44
GO:0043044	ATP-dependent chromatin remodeling	7	16	28	3,43	3,91
GO:0051716	cellular response to stimulus	402	451	1586	3,35	1,25
GO:1901360	organic cyclic compound metabolic process	523	576	2066	3,34	1,24
GO:0006457	protein folding	30	47	119	3,27	1,93
GO:0019752	carboxylic acid metabolic process	90	117	352	3,25	1,49
GO:0036211	protein modification process	300	344	1172	3,24	1,27
GO:1901998	toxin transport	6	14	24	3,18	4,10
GO:0071824	protein-DNA complex subunit organization	21	35	83	3,18	2,15
GO:0016573	histone acetylation	20	33	77	3,18	2,21
GO:0018210	peptidyl-threonine modification	9	19	37	3,18	3,10
GO:0006793	phosphorus metabolic process	247	288	967	3,18	1,29

GO:0032963	collagen metabolic process	4	11	17	3,12	5,37
GO:0043543	protein acylation	27	42	105	3,12	1,97
GO:0006749	glutathione metabolic process	8	17	32	3,11	3,32
GO:0071822	protein complex subunit organization	152	185	595	3,09	1,36
GO:0008152	metabolic process	971	1019	3793	3,08	1,23
GO:0044236	multicellular organism metabolic process	6	13	22	3,06	4,23
GO:0055086	nucleobase-containing small molecule metabolic process	72	95	280	3,06	1,53
GO:0050790	regulation of catalytic activity	141	173	553	3,06	1,37
GO:0050789	regulation of biological process	759	810	2965	3,04	1,21
GO:0051054	positive regulation of DNA metabolic process	28	43	109	3,03	1,92
GO:0045597	positive regulation of cell differentiation	64	86	250	3,03	1,56
GO:1901701	cellular response to oxygen-containing compound	68	91	267	3,02	1,54
GO:0071495	cellular response to endogenous stimulus	81	105	315	3,02	1,49
GO:0044724	single-organism carbohydrate catabolic process	13	24	52	2,99	2,52
GO:0034654	nucleobase-containing compound biosynthetic process	317	359	1237	2,97	1,25
GO:0006048	UDP-N-acetylglucosamine biosynthetic process	1	5	5	2,96	Inf
GO:1905332	positive regulation of morphogenesis of an epithelium	1	5	5	2,96	Inf
GO:0032846	positive regulation of homeostatic process	21	34	82	2,95	2,09
GO:0070661	leukocyte proliferation	17	29	67	2,94	2,24
GO:0010799	regulation of peptidyl-threonine phosphorylation	3	9	13	2,93	6,58
GO:0009408	response to heat	8	17	33	2,91	3,12
GO:0060341	regulation of cellular localization	86	110	335	2,87	1,46
GO:0007339	binding of sperm to zona pellucida	3	8	11	2,86	7,79
GO:0018193	peptidyl-amino acid modification	73	95	287	2,85	1,50
GO:0018209	peptidyl-serine modification	22	35	86	2,85	2,02
GO:0032880	regulation of protein localization	92	117	360	2,84	1,44
GO:0010948	negative regulation of cell cycle process	19	31	74	2,82	2,12
GO:0006418	tRNA aminoacylation for protein translation	10	19	39	2,82	2,79
GO:0006002	fructose 6-phosphate metabolic process	2	6	7	2,82	17,52
GO:0021819	layer formation in cerebral cortex	2	6	7	2,82	17,52
GO:0009070	serine family amino acid biosynthetic process	2	7	9	2,81	10,22
GO:0061615	glycolytic process through fructose-6-phosphate	2	7	9	2,81	10,22
GO:0009179	purine ribonucleoside diphosphate metabolic process	11	20	42	2,79	2,67
GO:0043038	amino acid activation	11	20	42	2,79	2,67
GO:0071901	negative regulation of protein serine/threonine kinase activity	9	17	34	2,73	2,93
GO:0006475	internal protein amino acid acetylation	21	33	81	2,72	2,02
GO:0007166	cell surface receptor signaling pathway	132	160	515	2,72	1,35
GO:0006323	DNA packaging	19	31	75	2,71	2,07
GO:0016053	organic acid biosynthetic process	26	40	103	2,71	1,87
GO:0016569	chromatin modification	71	92	276	2,71	1,49
GO:0002757	immune response-activating signal transduction	15	25	57	2,71	2,29
GO:0043279	response to alkaloid	5	12	21	2,69	3,90
GO:0014070	response to organic cyclic compound	55	74	215	2,69	1,55
GO:0046434	organophosphate catabolic process	10	19	40	2,66	2,65
GO:0031323	regulation of cellular metabolic process	431	474	1701	2,63	1,21
GO:0018394	peptidyl-lysine acetylation	21	33	82	2,62	1,98
GO:0006110	regulation of glycolytic process	4	9	14	2,60	5,26

GO:0007156	homophilic cell adhesion via plasma membrane adhesion molecules	4	9	14	2,60	5,26
GO:0009988	cell-cell recognition	4	9	14	2,60	5,26
GO:0046651	lymphocyte proliferation	16	27	64	2,58	2,14
GO:0048523	negative regulation of cellular process	252	287	1000	2,56	1,25
GO:0070848	response to growth factor	41	57	160	2,56	1,63
GO:0005975	carbohydrate metabolic process	53	71	207	2,56	1,55
GO:0051259	protein oligomerization	54	72	211	2,52	1,53
GO:0010605	negative regulation of macromolecule metabolic process	189	220	738	2,52	1,28
GO:0044248	cellular catabolic process	160	189	625	2,51	1,30
GO:0072524	pyridine-containing compound metabolic process	20	31	77	2,50	1,98
GO:0001782	B cell homeostasis	3	8	12	2,49	5,84
GO:0009067	aspartate family amino acid biosynthetic process	3	8	12	2,49	5,84
GO:0021799	cerebral cortex radially oriented cell migration	3	8	12	2,49	5,84
GO:0006334	nucleosome assembly	11	20	44	2,49	2,44
GO:0006081	cellular aldehyde metabolic process	8	15	30	2,47	2,93
GO:0009132	nucleoside diphosphate metabolic process	13	22	50	2,46	2,31
GO:0045778	positive regulation of ossification	6	12	22	2,46	3,51
GO:0030162	regulation of proteolysis	53	71	209	2,44	1,52
GO:0006541	glutamine metabolic process	4	10	17	2,43	4,18
GO:0006730	one-carbon metabolic process	4	10	17	2,43	4,18
GO:0008219	cell death	80	101	318	2,42	1,41
GO:0014003	oligodendrocyte development	3	7	10	2,40	6,81
GO:0022030	telencephalon glial cell migration	3	7	10	2,40	6,81
GO:0034502	protein localization to chromosome	9	17	36	2,40	2,62
GO:0033138	positive regulation of peptidyl-serine phosphorylation	6	13	25	2,39	3,17
GO:0006041	glucosamine metabolic process	1	4	4	2,37	Inf
GO:0010424	DNA methylation on cytosine within a CG sequence	1	4	4	2,37	Inf
GO:0060314	regulation of ryanodine-sensitive calcium-release channel activity	1	4	4	2,37	Inf
GO:0010660	regulation of muscle cell apoptotic process	2	6	8	2,33	8,80
GO:0009225	nucleotide-sugar metabolic process	5	11	20	2,33	3,57
GO:0010243	response to organonitrogen compound	44	59	171	2,33	1,56
GO:0070202	regulation of establishment of protein localization to chromosome	2	6	8	2,32	8,76
GO:1904851	positive regulation of establishment of protein localization to telomere	2	6	8	2,32	8,76
GO:0097190	apoptotic signaling pathway	62	80	242	2,32	1,46
GO:0048584	positive regulation of response to stimulus	124	149	486	2,32	1,32
GO:0006801	superoxide metabolic process	4	9	15	2,31	4,38
GO:0046164	alcohol catabolic process	4	9	15	2,31	4,38
GO:0060997	dendritic spine morphogenesis	4	9	15	2,31	4,38
GO:0010647	positive regulation of cell communication	103	126	404	2,30	1,35
GO:0042440	pigment metabolic process	8	15	31	2,29	2,74
GO:0002313	mature B cell differentiation involved in immune response	2	5	6	2,29	14,59
GO:0009113	purine nucleobase biosynthetic process	2	5	6	2,29	14,59
GO:0010224	response to UV-B	2	5	6	2,29	14,59
GO:0017144	drug metabolic process	2	5	6	2,29	14,59
GO:0042537	benzene-containing compound metabolic process	2	5	6	2,29	14,59
GO:0046498	S-adenosylhomocysteine metabolic process	2	5	6	2,29	14,59
GO:0046654	tetrahydrofolate biosynthetic process	2	5	6	2,29	14,59

GO:0048566	embryonic digestive tract development	2	5	6	2,29	14,59
GO:0042692	muscle cell differentiation	28	40	108	2,28	1,73
GO:0033993	response to lipid	50	66	195	2,26	1,51
GO:0032024	positive regulation of insulin secretion	6	12	23	2,25	3,19
GO:0071479	cellular response to ionizing radiation	6	12	23	2,25	3,19
GO:0006468	protein phosphorylation	127	151	495	2,25	1,31
GO:0000723	telomere maintenance	16	25	61	2,23	2,04
GO:0051289	protein homotetramerization	10	18	40	2,23	2,40
GO:0042787	protein ubiquitination involved in ubiquitin-dependent protein catabolic process	15	24	58	2,22	2,07
GO:0060255	regulation of macromolecule metabolic process	251	283	1008	2,22	1,23
GO:0019220	regulation of phosphate metabolic process	119	143	467	2,22	1,31
GO:0031399	regulation of protein modification process	132	156	514	2,22	1,30
GO:2000026	regulation of multicellular organismal development	122	146	478	2,21	1,31
GO:0040029	regulation of gene expression, epigenetic	25	36	96	2,20	1,76
GO:0010656	negative regulation of muscle cell apoptotic process	5	10	18	2,19	3,65
GO:0032212	positive regulation of telomere maintenance via telomerase	5	10	18	2,19	3,65
GO:0006213	pyrimidine nucleoside metabolic process	3	8	13	2,19	4,67
GO:0070229	negative regulation of lymphocyte apoptotic process	3	8	13	2,19	4,67
GO:0016337	single organismal cell-cell adhesion	49	65	193	2,18	1,50
GO:0060548	negative regulation of cell death	96	117	375	2,18	1,35
GO:0043067	regulation of programmed cell death	133	157	519	2,17	1,29
GO:0090304	nucleic acid metabolic process	454	492	1774	2,16	1,18
GO:0003008	system process	78	97	305	2,14	1,38
GO:0048588	developmental cell growth	17	26	65	2,14	1,96
GO:0042398	cellular modified amino acid biosynthetic process	5	11	21	2,12	3,22
GO:0042113	B cell activation	15	24	59	2,12	2,01
GO:0023056	positive regulation of signaling	105	126	409	2,11	1,32
GO:0048660	regulation of smooth muscle cell proliferation	11	19	44	2,09	2,23
GO:0019941	modification-dependent protein catabolic process	62	79	243	2,09	1,42
GO:1900180	regulation of protein localization to nucleus	23	34	91	2,08	1,75
GO:0046496	nicotinamide nucleotide metabolic process	19	29	75	2,08	1,85
GO:0019400	alditol metabolic process	3	7	11	2,07	5,11
GO:0043243	positive regulation of protein complex disassembly	3	7	11	2,07	5,11
GO:0048010	vascular endothelial growth factor receptor signaling pathway	3	7	11	2,07	5,11
GO:1904814	regulation of protein localization to chromosome, telomeric region	3	7	11	2,07	5,11
GO:1990748	cellular detoxification	3	7	11	2,07	5,11
GO:0009394	2'-deoxyribonucleotide metabolic process	4	9	16	2,06	3,76
GO:0010659	cardiac muscle cell apoptotic process	4	9	16	2,06	3,76
GO:0043094	cellular metabolic compound salvage	4	9	16	2,06	3,76
GO:0044093	positive regulation of molecular function	113	135	443	2,05	1,30
GO:0032269	negative regulation of cellular protein metabolic process	83	102	325	2,04	1,36
GO:0034641	cellular nitrogen compound metabolic process	585	623	2304	2,03	1,16
GO:0043434	response to peptide hormone	28	39	108	2,03	1,66
GO:1901214	regulation of neuron death	30	42	118	2,02	1,63
GO:0002694	regulation of leukocyte activation	27	38	105	2,01	1,67
GO:0002684	positive regulation of immune system process	46	60	179	2,01	1,49

Danksagung

[redacted]

[redacted]

[redacted]

[redacted]

[redacted]

[redacted]

[redacted]

Erklärung

Die in der vorliegenden Arbeit vorgestellten Experimente wurden in der Zeit von Januar 2013 bis Juni 2018 am Institut für Toxikologie an der Universitätsmedizin der Johannes Gutenberg-Universität Mainz unter der Betreuung von [redacted] durchgeführt.

Teilaspekte der Arbeit wurden bereits veröffentlicht. Die Publikationen hierzu sind im Kapitel Curriculum Vitae aufgelistet.

Hiermit versichere ich die jetzt als Dissertation vorgelegte Arbeit mit dem Titel

“Impact of class I HDACs and their inhibitors on renal and colorectal tumor cell fate decisions”

selbstständig angefertigt und alle benutzten Hilfsmittel in der Arbeit angegeben zu haben.

Mainz, Januar 2019

Nicole Kiweler

Curriculum Vitae

[redacted]

[redacted]

[redacted]

[redacted]

Publications

1. Wagner T, **Kiweler N**, Wolff K, Knauer SK, Brandl A, Hemmerich P et al (2015). Sumoylation of HDAC2 promotes NF-kappaB-dependent gene expression. Oncotarget **6:** 7123-7135.
2. Beyer M, **Kiweler N**, Mahboobi S, Krämer OH (2017). How to Distinguish Between the Activity of HDAC1-3 and HDAC6 with Western Blot. Methods in molecular biology **1510:** 355-364.
3. Schäfer C, Göder A, Beyer M, **Kiweler N**, Mahendrarajah N, Rauch A et al (2017). Class I histone deacetylases regulate p53/NF-kappaB crosstalk in cancer cells. Cellular signalling **29:** 218-225.
4. Nikolova T, **Kiweler N**, Krämer OH (2017). Interstrand Crosslink Repair as a Target for HDAC Inhibition. Trends in pharmacological sciences **38:** 822-836.
5. **Kiweler N**, Krämer OH (2018). PNUTS at the crossroads of tumorigenesis and metastasis formation. J Thorac Dis **10:** 560-563.
6. Göder A, Emmerich C, Nikolova T, **Kiweler N**, Schreiber M, Kuhl T et al (2018). HDAC1 and HDAC2 integrate checkpoint kinase phosphorylation and cell fate through the phosphatase-2A subunit PR130. Nature communications **9:** 764.
7. **Kiweler N**, Brill B, Wirth M, Breuksch I, Laguna T, Dietrich C et al (2018). The histone deacetylases HDAC1 and HDAC2 are required for the growth and survival of renal carcinoma cells. Archives of toxicology 92: 2227-2243.
8. Pons M, Reichardt CM, Hennig D, Nathan A, **Kiweler N**, Stocking C et al (2018). Loss of Wilms tumor 1 protein is a marker for apoptosis in response to replicative stress in leukemic cells. Archives of toxicology 92: 2119-2135.